

NORT 65-126

FINAL SUMMARY REPORT

ANALYTICAL AND EXPERIMENTAL INVESTIGATIONS INTO
PROBLEMS ASSOCIATED WITH GYRO-STABILIZED
PLATFORM-MOUNTED OPTICAL SENSING ELEMENTS

Contract No. NAS 8-20193
George C. Marshall Space Flight Center
Huntsville, Alabama

15 July 1966

Prepared by

E. H. Kong, Jr.
W. H. Schuck

N 66 35238

Approved by



D. E. Conklin, Chief
Tracking & Display Systems

ABSTRACT

35238

The use of a star tracker with the ST124-M platform to provide long-term drift compensation is considered. The accuracy with which platform alignment can be made is determined for different platform-star tracker mounting configurations. The coordinate relationships between the star tracker triad, the inertial triad and the terrestrial triad are presented, and the utilization of a star tracker, inertial platform and a horizon sensor for orbital navigation and attitude control are considered.

Fundamental design concepts relating to optical tracking systems, including considerations of different optical systems, detectors of visible energy, and several optical modulation methods are presented. The utilization of optical equipment in a spacecraft is discussed, and three types of optical experiments, star tracker-platform, scientific and engineering experiments are evaluated.

The causes and methods of reducing off-axis and background radiance in an optical system are examined. Some techniques considered, include use of a sun shade or multiple-celled sun shield, baffling, and the operation of the star tracker in a space environment.

Circuit modifications to improve the performance of the Celestial Body Tracker, built by Nortronics for the George C. Marshall Space Flight Center are presented in Appendix A.

FOREWORD

The Analytical and Experimental Investigations into Problems Associated with Gyro-Stabilized Platform-Mounted Optical Sensing Elements at Nortronics, was authorized under the National Aeronautics and Space Administration Contract No. NAS8-20193 by the George C. Marshall Space Flight Center. The control number is DCN 1-5-40-56222-01(1F), S1(1F). The study was carried out over a period of twelve months, and was made possible through the contributions of specialist in many technical areas. Mr. E. H. Kong and Mr. W. H. Schuck were the principal investigators during the program. Mr. Kong was the Project Engineer, and Mr. Schuck conducted the study concerning the use of a star tracker with the ST 124-M platform. Other contributors were Mr. P. T. Glankowski, in the investigation concerning the use of a multiple-celled sun shield; Mr. R. E. Cornwell, in the study of vacuum bearing lubrication; and Mr. J. M. Sacks, who is responsible for the circuit modifications for the Celestial Body Tracker.

The guidance and direction of Mr. Clyde Jones, Mr. George Doane, and Mr. Joseph Parker of the Astrionics Division, George C. Marshall Space Flight Center, Huntsville, Alabama, are gratefully acknowledged.

CONTENTS

<u>Section</u>	<u>Page</u>
1 Study of Utilization of Astro-Inertial System Using ST-124M Inertial Platform	2
1.1 Analysis of Improvement in Navigation System Accuracy with Use of A Star Tracker	3
1.1.1 Characteristic Error Growth For Pure Inertial System and Star Tracker Aided Inertial System	3
1.1.2 Utilization of Astrotracker Data for Navigation (Terrestrial Position Determination) and Attitude Control	11
1.1.2.1 Frames of Reference	11
1.1.2.2 Terrestrial Navigation Using A Star Tracker	16
1.1.2.3 Vehicle Attitude Correction With A Star Tracker	19
1.1.2.3.1 Derivation of Equations for Removal of Platform Tilt Error with Star Tracker	19
1.1.2.3.2 Derivation of Correction Equations for Removal of Platform Error in Three Axes with Star Tracker	20
1.2 Description and Analysis of An Orbital Navigation System Using The ST124-M Inertial Platform	27
1.2.1 System Configuration and Analysis	27
1.2.2 Computer Function C_1 (Star Tracker Pointing)	27
1.2.3 Computer Function C_2 (Star Tracker Correction to IMU)	30
1.2.3.1 Removal of Constant Gyro Drift with Star Tracker	36
1.2.3.2 Bounding of Random Gyro Drift with Star Tracker	39
1.2.3.2.1 Random Gyro Drift Error Calculation	39
1.2.3.2.2 Fixed Platform Drift Errors	43
1.2.3.3 Platform Error Due to Star Tracker Error	44
1.2.3.4 Final Platform Angle Error	45
1.2.4 Computer Function C_3 (Relationship Between Craft Attitude and Inertial Space)	49
1.2.5 Computer Function C_4 (Local Vertical Determination)	49
1.2.6 Computer Function C_5 (Craft Position Determination)	50
1.2.7 Computer Function C_6 (Spacecraft Altitude)	51
1.2.8 Computer Function C_7 (Initial Condition for Horizon Scanner)	52
1.2.9 Computer Function C_8 (Spacecraft Attitude with respect to Earth)	52
1.2.9.1 Orbital Gyrocompass	52
1.2.10 Summary and Conclusions, Orbital Guidance and Navigation System	57

CONTENTS (Cont'd)

<u>Section</u>	<u>Page</u>
1.3 Comparison of Static Pointing Accuracy for Star Tracker Mounted On and Off The Platform	58
1.3.1 Derivation of Error Equations	59
1.3.1.1 Preliminary Definitions	59
1.3.1.2 Case 1 - Tracker on Platform	60
1.3.1.3 Second Case - Tracker Off Platform But No Flexure Errors	62
1.3.1.4 Third Case - Tracker Off Platform With Craft Flexure	63
1.3.2 Numerical Evaluation of Platform Gimbal Errors - Platform Gimbal Pickoff Errors	64
1.3.3 Pointing Angle Errors	67
1.4 Coordinate Transformation for Tracker Mounted Off The Platform	71
2 Basic Optical Tracking System Design Concepts	76
2.1 Optical System	76
2.1.1 Field Lens	83
2.2 Basic Detector Types	86
2.2.1 Single Element Detectors	86
2.2.1.1 Photomultipliers	87
2.2.1.2 Semiconductor Detectors	90
2.2.1.2.1 Silicon	92
2.2.1.2.2 Cadmium Sulfide	92
2.2.2 Extended Area Detector	92
2.2.2.1 Image Dissector	92
2.2.2.2 Radiation Tracking Transducer	92
2.2.3 Extended Area Detectors with Storage	94
2.2.3.1 Vidicon	94
2.2.3.2 Image Orthicon	97
2.3 Mechanical Modulation Methods	100
2.3.1 Radiation Balance System	100
2.3.2 Mechanical Optical Field Dither	102
2.3.3 Amplitude and Frequency Modulated Reticule System	103
3 Utilization of Optical Sensing Elements in a Space Vehicle	107
3.1 Monitoring of Platform Drift with a Star Tracker	107

<u>Section</u>	<u>CONTENTS (Cont'd)</u>	<u>Page</u>
	3.1.1 Platform Drift During Launch	107
	3.1.2 Platform Drift in Earth Orbit or in Deep Space	107
	3.1.3 Equipment Required For Platform Drift Measurements	108
	3.1.3.1 Use of the Vidicon Star Tracker to Monitor Platform Drift During Vehicle Launch	109
	3.1.3.2 Star Tracker Description and Accuracy	109
	3.1.3.3 Brightness of the Daytime Background	112
	3.1.3.4 Star Availability During the Launch Period	115
	3.1.3.5 Effects Caused by Vented Gases and Rocket Plume	122
3.2	Optical Instrumentation for Orbital Navigation and for Attitude Control	123
	3.2.1 Earth-Oriented Orbital System Using A Horizon Sensor and A Gyrocompass	123
	3.2.2 Inertially Oriented System Using Solar-Inertial or Sun-Star Alignment	124
	3.2.3 Earth Oriented Orbital System Using A Horizon Sensor and A Star Field Scanner	125
	3.2.4 Autonomous Navigation System Using a Horizon Sensor and Star Trackers	125
	3.2.5 Precision Orbital Navigation System Using A Landmark Tracker	127
	3.2.6 Attitude Control of A Space Vehicle	127
	3.2.6.1 Spin Stabilization	128
	3.2.6.2 Celestial Body Tracking	128
	3.2.7 Accuracy of Autonomous Navigation System	131
3.3	Considerations of Experiments That Can Be Performed From An Orbiting Satellite	133
	3.3.1 Thermal Ocean Mapping	134
	3.3.1.1 Scanning Spectrometer	135
	3.3.1.2 Dual Radiometer	138
	3.3.1.3 Choice of System For Thermal Ocean Mapping	140
	3.3.2 Geophysical Background Information	140
	3.3.3 Mapping By Photographic Techniques	142
	3.3.4 Cold Star Detection	142
	3.3.5 Atmospheric Refraction Measurements	143
	3.3.6 Contamination of Spacecraft Window	143
4	Reduction of Effects of Off-Axis and Background Illuminance In A Star Tracker	145
	4.1 Sunshade	145
	4.2 Multiple-Celled Sun Shield	146

<u>Section</u>	<u>CONTENTS (Cont'd)</u>	<u>Page</u>
4.3	Reduction of Glare	150
4.3.1	Optical Glare	152
4.3.1.1	Bubbles	152
4.3.1.2	Scratches	153
4.3.2	Mechanical Glare	153
4.4	Operation Of A Star Tracker Without A Window	154
4.4.1	Bearing and Brush Wear Under Space Conditions	154
4.4.1.1	Oils and Greases	155
4.4.1.2	Laminar Solids	156
4.4.1.3	Soft Metals	157
4.4.1.4	Plastics	158
4.4.1.5	Ceramics and Cermet Materials	159
4.4.2	Space Lubricant Suppliers	159
4.4.2.1	Vac-Kote Process By Ball Brothers	159
4.4.2.2	CBS	160
4.4.2.3	Electrofilm Incorporated	160
4.4.2.4	Lubeco Incorporated	160
4.4.3	Summary of Application of Bearing Lubrication For Space	161
Appendix A	Modification of Electronic Circuitry to Improve Performance of Quadrant Photomultiplier Celestial Body Tracker	162
	Component Parts List for Celestial Body Tracker Electronic Modification	178
Appendix B	Bibliography	181

ILLUSTRATIONS

<u>Figure</u>		<u>Page</u>
1.1	Typical Single-Axis Undamped Inertial Loop	4
1.2	Typical Single-Axis Inertial Loop With Star Tracker Input	6
1.3	Random Tracker Error	7
1.4	Comparison of Mean-Squared Position Error As A Function Of Time For Pure Inertial System and Stellar-Inertial System	10
1.5	Celestial Sphere Model	12
1.6	Inertial and Earth Triad Relationship	13
1.7	Location of Vector \bar{Z} with Respect To Earth Triad	14
1.8	Projection of \bar{N} into (\bar{g}, \bar{a}) Plane	15
1.9	Line of Sight (LOS) To Star With Respect To Observer's Triad	16
1.10	Rotation of Coordinate System Due To Verticality Error	20
1.11	Resolver Implementation To Determine E_a and E_h	23
1.12	Orbital Navigation and Guidance System ^a Functional Block Diagram	28
1.13	Rate Stabilization Servo	29
1.14	Single Axis Platform Stabilization Loop	31
1.15	Signal Flow Graph of Single Axis Stabilization Loop	32
1.16	Block Diagram of Relationship of Platform Gimbal Angle Error to Gyro Drift	33
1.17	Gyro Stabilization Loop With Star Tracker Correction (Error Model)	34
1.18	Sampling Switch Input and Output Waveforms	35
1.19	Variation in Star Tracker Output Due To Constant Gyro Drift	38
1.20	Error Model For Calculation of Random Errors	39
1.21	Vidicon Star Tracker Error Profile	44
1.22	Misaligned Orbital Gyrocompass	53
1.23	Aligned Orbital Gyrocompass	53
1.24	Block Diagram of Orbital Gyrocompass (not gimbal mounted) Precessing to Null	54
1.25	Block Diagram of Gimbal Mounted Orbital Gyrocompass	55
1.26	Signal Flow Graph For Gimbal Mounted Orbital Gyrocompass	55
1.27	Location of Pointing Vector \bar{R} with Respect To True Inertial Triad	67
1.28	Gimbal Arrangement For 3-Axis Stable Platform and Two Axis Star Tracker Mount	72
1.29	Coordinate Change Due To Rotation About ϕ Axis of Platform Gimbal	72
2.1	Representative Optical Tracking System Block Diagram	76
2.2	Field Lens System	83
2.3	Spectral Response of Five Representative Photoemissive Surfaces	88
2.4	Silicon Photovoltaic Detector	90
2.5	Spectral Response of Silicon Photovoltaic Detector	91
2.6a	Spectral Response of Several Types of Clairex CdS and CdSe Detectors	93
2.6b	Variation of Resistance of CdS and CdSe with Illumination	93
2.7	Spectral Response (RCA C-73496) and Equivalent Circuit of Vidicon	95

ILLUSTRATIONS (Cont'd)

<u>Figure</u>		<u>Page</u>
2.8a	Image Orthicon Schematic Arrangement	98
2.8b	Spectral response of Westinghouse WL-7611 Image Orthicon	98
2.9	Three and Four Detector Radiometric Balance Sensors	101
2.10	Operating Diagram - Amplitude and Frequency Modulated Scanning Systems	105
3.1	Optical Head of Vidicon Star Tracker	110
3.2	Isolume Plot Showing Brightness of Sky at 20,000-Foot Altitude	113
3.3	Isolume Plot Showing Brightness of Sky at 40,000-Foot Altitude	114
3.4	Star Chart Showing Primary and Secondary Navigation Stars	116
3.5	Star Tracker Field of View and Solar Exclusion Zone	118
3.6	Overlay Number 3 - Orientation of Center of the Field of View With World Star Chart Right Ascension and Declination Plus Upper Atmosphere Obscuration	121
4.1	Sunshade Length As A Function of Angle of Incidence of Stray Illumination	146
4.2	Cell Length of Multi-Celled Sun Shield As A Function of The Angle of Incidence of Stray Illumination	146
4.3	Multiple-Cell Glare Shield	148
4.4	Diffraction Patterns Produced By Multiple Apertures	151
A1	Electronic Block Diagram	168
A2	Important Waveforms	169
A3	Cathode Switch Array	170
A4	High Voltage Rectifier	171
A5	Synchronous Detector	172
A6	Preamplifier	173
A7	A.G.C. Rectifier	174
A8	A.G.C. Amplifier	175
A9	Master Oscillator and Counter Chain	176
A10	Synchronous Detector Driver	177

TABLES

	<u>Page</u>
1.1 One Star Tracker Mounted On The Platform	46
1.2 One Star Tracker Off The Platform (No Craft Flexure)	47
1.3 One Star Tracker Off The Platform (With Craft Flexure)	47
1.4 Two Star Trackers Off The Platform (No Craft Flexure)	48
1.5 Two Star Trackers Off The Platform (With Craft Flexure)	48
1.6 Summary of Platform Gimbal Angle Error For Three Different Mounting Configurations	65
1.7 Summary of RMS Pointing Angle Errors With Respect To An Absolute Reference For Three Different Pointing Vectors	70
2.1 Representative Optical Systems	pp 78, 79, 80
2.2 Energy Distribution of Star Image	81
3.1 Vidicon Star Tracker Accuracy	111
3.2 Right Ascension Monthly Schedule	117
3.3 Spacecraft Attitude Control Systems	129, 130
3.4 Axes of Equi-Probability Ellipsoid	131
3.5 Autonomous Navigation Accuracy Estimate	132
3.6 Sensor Performance Capability Estimate	133
3.7 Peak of Blackbody Curve For Different Temperatures	135
3.8 Design Parameter For Scanning Spectrometer To Measure Ocean Temperatures	136
3.9 Percentage of Blackbody Energy in Different Spectral Bands As A Function of Temperature	139
3.10 Design Parameters For Dual Radiometer Ocean Temperature Determination System	139

INTRODUCTION

The purpose of the contract was to perform analytical and experimental investigations into alignment problems associated with gyro-stabilized platform-mounted optical sensing elements. Specific areas that were to be investigated included:

1. Examination of the problems and development of techniques for aligning a stabilized platform sensing axis with the reference frame of the platform.
2. Examination and recommendation of solutions for interference problems caused by direct sunlight on a space vehicle optical window, when the sensing elements utilize the visible light spectrum.
3. Design changes for the celestial body tracker, produced by Nortronics under Contract NAS8-5393, that will eliminate the apparent (warm-up) time delay, decrease the error signal crosstalk, and improve the tracker accuracy.

The study effort was divided into five distinct areas. The first was an investigation into the use of a star tracker with a stable platform, to provide an absolute alignment reference for the platform. The second was a brief treatment of fundamental system concepts involved in the design of optical tracking systems. The third was a consideration of applications in which optical equipment can be utilized in a spacecraft. The fourth was an examination of the effects caused by stray illumination in an optical system and methods in which these effects can be minimized. The fifth was the modification of electronic circuitry required to provide the desired improvement in the performance of the Celestial Body Tracker. The study effort is reported in Sections One through Four, and in Appendix A of this report.

SECTION 1

STUDY OF ASTRO-INERTIAL SYSTEM USING ST-124M INERTIAL PLATFORM

In the following section, the technical considerations involved in using a star tracker in conjunction with the ST124-M inertial platform will be discussed and analyzed.

There exist several fairly broad areas of interest in stellar-inertial systems toward which technical effort may be directed to achieve fruitful results. The major areas are summarized by the following breakdown:

- A) Potential improvements in navigational and guidance capability of stellar-inertial systems over pure inertial systems: a) For intermittent alignment and b) continuous updating.
- B) Optimum interface between star tracker and inertial platform. This area encompasses: a) comparison of system capability with the star tracker mounted directly on the platform and with the star tracker mounted on separate gimbals, and b) the design of "optimum" information filtering and processing schemes to derive the maximum use from the star tracker information.
- C) Component Capability and Accuracy. The cost, weight, power requirements, reliability, and accuracy of available components such as resolvers, torquers, separate star tracker gimbal system, etc., place constraints upon the overall improvement in a guidance system that is attainable with a star tracker. The computer space required for processing the star tracker information is also a consideration. Furthermore, the star tracker itself may be considered as a component with limitations in accuracy, sensitivity, search time and acquisition time.
- D) Final stellar-inertial system accuracy versus pure inertial system accuracy and cost versus accuracy considerations.

Items A, B and C above are reasonably independent of one another; however, in order to determine the final system accuracy (Item D), it is necessary to perform a somewhat detailed analysis of Items A through C.

In order to arrive at perhaps two or three different system mechanizations and perform a detailed error analysis on each system, it is necessary to apply some system constraints to narrow the field of possible mechanizations. It is anticipated that even a general analysis performed on Items A through C will negate some system configurations. However, some system constraints must be derived from the type of mission or class of missions for which the system is intended. Therefore the system to be considered in this study will be assumed to be intended for earth orbital type of missions.

1.1 ANALYSIS OF IMPROVEMENTS IN NAVIGATIONAL SYSTEM ACCURACY WITH STAR TRACKER

1.1.1 Characteristic Error Growth for Pure Inertial Systems and Star Tracker Aided Inertial Systems

It is characteristic of pure inertial navigational systems that the inertial reference tends to degrade as a function of time. The primary reason for this being the fact that the random components of gyro drift cannot be removed. Over a long mission, with relatively low acceleration inputs over the major part of the mission, the gyro drift errors will greatly predominate over the errors due to accelerometer noise. A pure inertial system responds to random gyro drift components with a mean-squared error that grows with time and is unbounded. Hence, for long missions it is generally necessary to augment the inertial system with independent velocity or position information. Aids such as doppler velocity, altimeter altitude, magnetic heading, etc., are frequently used examples of external aids for inertial systems operating close to earth. However, although it is possible to limit the growth of random noise errors with the aids mentioned above, the only way to bound the overall system error independent of flight time or distance traveled is to use a celestial reference. There exist two schemes by which true inertial position fixes may be utilized to bound inertial errors. One way is to track the guided vehicle with earth-based tracking networks that telemeter position fixes to the vehicle. The other scheme is to incorporate a star tracker in the vehicle and use its outputs to directly correct the inertial system. This report is directed toward the latter scheme.

In order to illustrate the capability of a star tracker in bounding inertial errors due to random gyro drift, consider the sample single-axis undamped inertial loop shown in Figure 1.1.

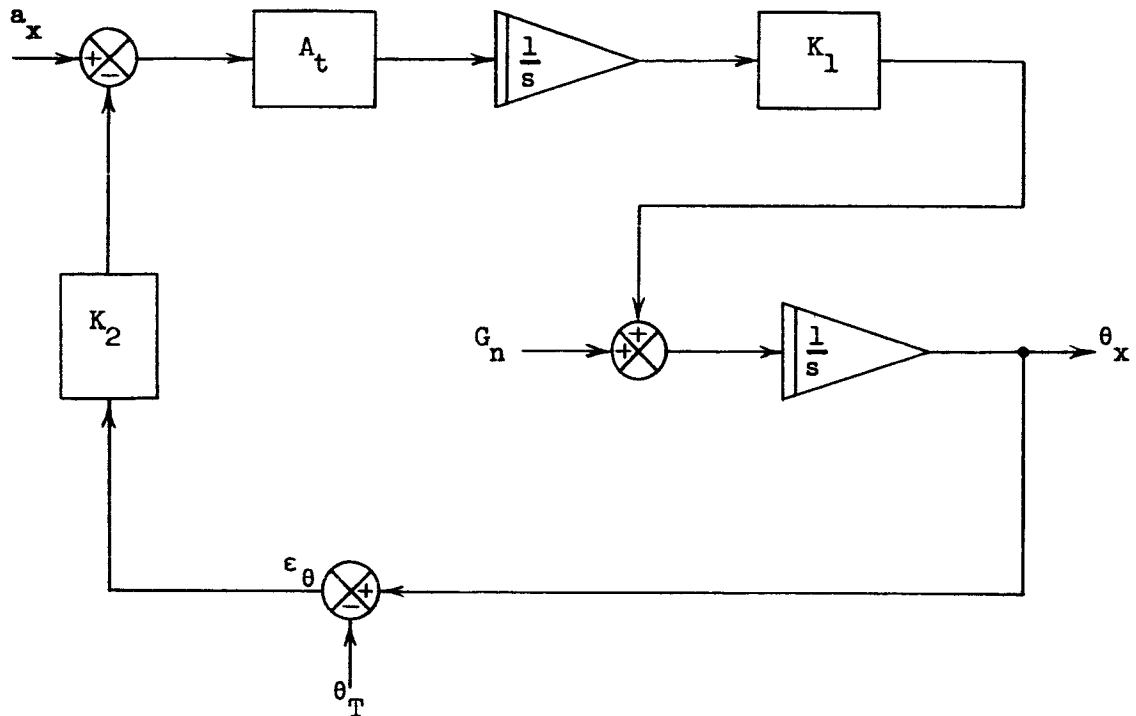
The platform error, ϵ_θ , due to random gyro drift, G_n , will be calculated to demonstrate the time growth of error in an inertial system.

The transfer function $\epsilon_\theta(s)/G_n(s)$ is given by equation 1.1 below:

$$\frac{\epsilon_\theta(s)}{G_n(s)} = H(s) = \frac{s}{s^2 + K_1 K_2} \quad (1.1)$$

Writing the system impulse response in the time domain:

$$h(t) = \mathcal{L}^{-1} [H(s)] = \cos \sqrt{K_1 K_2} \, t \quad (1.2)$$



- a_x = vehicle acceleration
 θ_x = platform angle which contains an error
 θ_T = true inertial angle
 $\epsilon_\theta = \theta_x - \theta_T$
 G_n = random gyro drift input
 A_t = accelerometer with a unity transfer function
 K_1, K_2 = constants

FIGURE 1.1 TYPICAL SINGLE-AXIS UNDAMPED INERTIAL LOOP

The mean-squared position error $\overline{\epsilon_\theta^2}$ as a function of time is given by equation 1.3 below:

$$\overline{\epsilon_\theta^2}(t) = \int_0^t h(\tau) d\tau \int_0^t h(\lambda) \phi_{gn}(\tau-\lambda) d\lambda \quad (1.3)$$

where $\phi_{gn}(\tau-\lambda)$ = autocorrelation function of the random gyro drift noise

For simplicity the random gyro drift noise will be assumed to have a white frequency distribution over the system bandwidth. Thus, the autocorrelation function $\phi(\tau-\lambda)$ becomes:

$$\phi_{gn}(\tau-\lambda) = N_{gn} \delta(\tau-\lambda) \quad (1.4)$$

where N_{gn} = power density of the noise in watts/cps

$\delta(-)$ = impulse function.

Substituting equations 1.2 and 1.4 into equation 1.3,

$$\overline{\epsilon_\theta^2}(t) = N_{gn} \int_0^t \cos \sqrt{K_1 K_2} \tau d\tau \int_0^t \cos \sqrt{K_1 K_2} \lambda \delta(\tau-\lambda) d\lambda \quad (1.5)$$

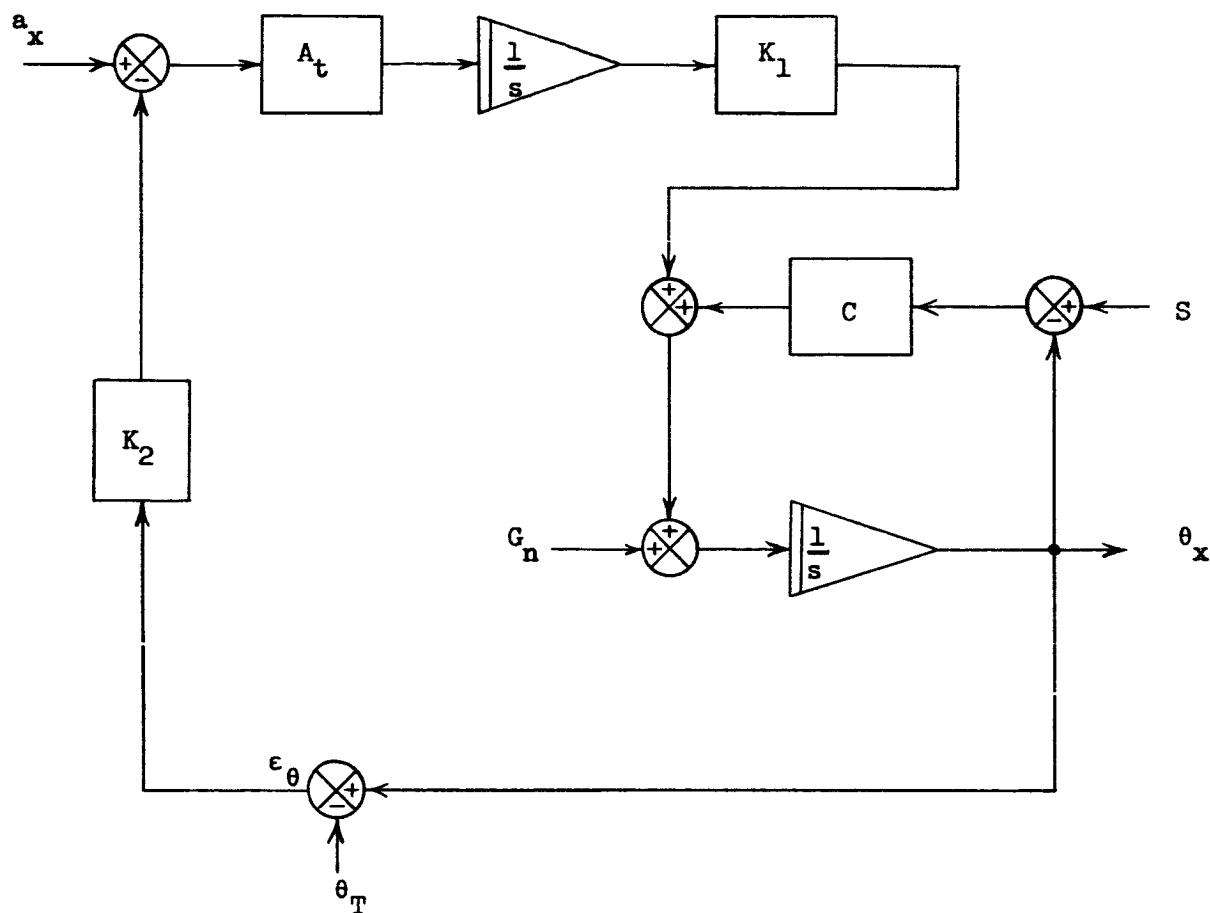
Performing the first integration yields,

$$\overline{\epsilon_\theta^2}(t) = N_{gn} \int_0^t \cos^2 \sqrt{K_1 K_2} \tau d\tau \quad (1.6)$$

Integrating again,

$$\overline{\epsilon_\theta^2}(t) = N_{gn} \left[\frac{t}{2} + \frac{1}{4\sqrt{K_1 K_2}} \sin 2\sqrt{K_1 K_2} t \right] \quad (1.7)$$

Now consider the same inertial loop with an external position input supplied by a star tracker. A block diagram of this loop is shown in Figure 1.2.



- S = star tracker input
 C = constant
 a_x = vehicle acceleration
 θ_T = true inertial angle
 $\epsilon_\theta = \theta_x - \theta_T$
 G_n = random gyro drift
 A_t = accelerometer with a unity transfer function
 K_1, K_2 = constants
 θ_x = platform angle which contains an error

FIGURE 1.2 TYPICAL SINGLE-AXIS INERTIAL LOOP WITH STAR TRACKER INPUT

The star tracker input S may be characterized by the true position parameter S_o and an error term S_n ,

$$S = S_o + S_n \quad (1.8)$$

S_n represents the component of tracker error that occurs at each star sighting. The form of S_n depends upon the particular type of tracker and the tracking format. However, for a typical case the tracker error may be described by the square wave with random amplitude and period shown in Figure 1.3 below.

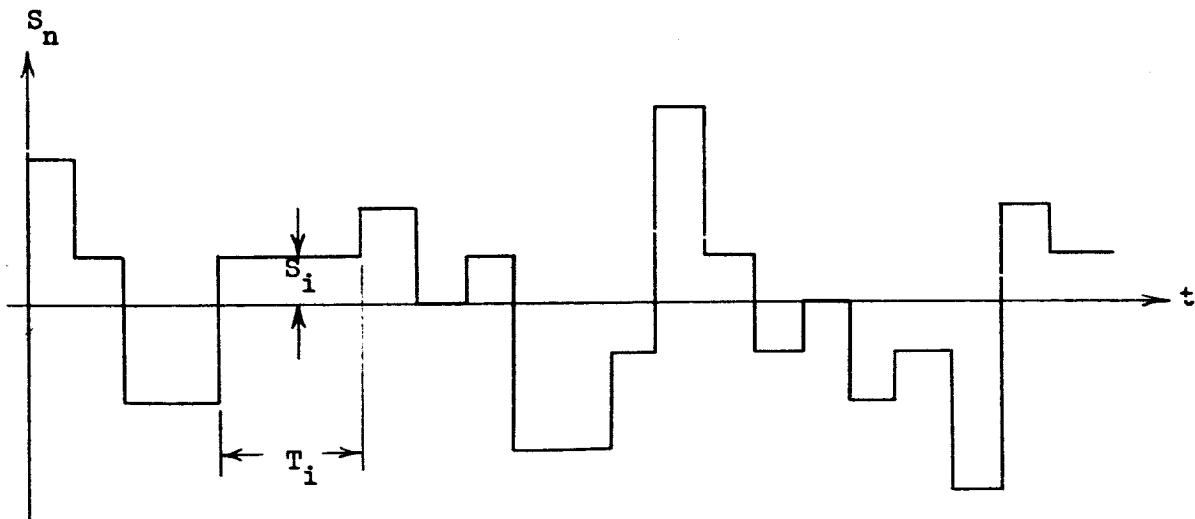


FIGURE 1.3 RANDOM TRACKER ERROR

If the period between star readouts, T_i , is smaller than the inverse of the system bandwidth, then the star tracker error S_n may be assumed to have a white frequency distribution. This assumption will be made in the following analysis to simplify the calculations. Thus, the autocorrelation function of the tracker error is given by,

$$\phi_{sn}(\tau-\lambda) = N_{sn} \delta(\tau-\lambda) \quad (1.9)$$

where N_{sn} = power density of the tracker error in watts/cps.

The net position error, $\overline{\epsilon_\theta^2}$, for the system shown in Figure 1.2 is composed of a random gyro drift component and a star tracker error component. The system transfer functions between the position output and the gyro drift noise, $\theta_p(s)/G_n(s)$, and the star tracker input $\theta_p(s)/S(s)$ are given by:

$$\frac{\theta_p(s)}{G_n(s)} = \frac{s}{s^2 + sc + K_1 K_2} \quad (1.10)$$

$$\frac{\theta_p(s)}{S(s)} = \frac{sC}{s^2 + sc + K_1 K_2} \quad (1.11)$$

For true stellar-inertial operation of the system, the gain C should be much higher than $K_1 K_2$. Thus, if $C \gg K_1 K_2$, equations 1.10 and 1.11 reduce to:

$$\frac{\theta_p(s)}{G_n(s)} = H_1(s) = \frac{1}{s + C} \quad (1.12)$$

$$\frac{\theta_p(s)}{S(s)} = H_2(s) = \frac{C}{s + C} \quad (1.13)$$

Transforming equations 1.12 and 1.13 into the time domain yields the system impulse responses,

$$h_1(t) = e^{-ct} \quad (1.14)$$

$$h_2(t) = Ce^{-ct} \quad (1.15)$$

The mean-squared position error, $\overline{\epsilon_\theta^2}(t)$, due to gyro drift and star tracker error is given by equation 1.16,

$$\overline{\epsilon_\theta^2}(t) = \int_0^t h_1(\tau) d\tau \int_0^t h_1(\lambda) \phi_{gn}(\tau-\lambda) d\lambda + \int_0^t h_2(\tau) d\tau \int_0^t h_2(\lambda) \phi_{sn}(\tau-\lambda) d\lambda \quad (1.16)$$

Substituting equations 1.4, 1.9, 1.14, and 1.15 into equation 1.16,

$$\begin{aligned} \overline{\epsilon_{\theta}^2}(t) = & N_{gn} \int_0^t e^{-c\tau} d\tau \int_0^t e^{-c\lambda} \delta(\tau-\lambda) d\lambda \\ & + N_{sn} C \int_0^t e^{-c\tau} d\tau \int_0^t e^{-c\lambda} \delta(\tau-\lambda) d\lambda \end{aligned} \quad (1.17)$$

Performing the first integration,

$$\overline{\epsilon_{\theta}^2}(t) = N_{gn} \int_0^t e^{-2c\tau} d\tau + N_{sn} C \int_0^t e^{-2c\tau} d\tau \quad (1.18)$$

Integrating again,

$$\overline{\epsilon_{\theta}^2}(t) = \frac{N_{gn}(1 - e^{-2ct})}{2c} + \frac{N_{sn}(1 - e^{-2ct})}{2} \quad (1.19)$$

Letting $t \rightarrow \infty$ in equation 1.19 yields,

$$\overline{\epsilon_{\theta}^2}(\infty) = \frac{N_{gn}}{2c} + \frac{N_{sn}}{2} \quad (1.20)$$

Thus, it is seen from equation 1.20 that, when an inertial loop is aided by a star tracker, the position error is bounded.

A comparison of the position error growth for a pure inertial system and a stellar inertial system is shown in Figure 1.4 where equations 1.7 and 1.9 are plotted.

It may be noted here that the choice of C as much greater than $K_1 K_2$ is somewhat arbitrary. In designing a specific system the value of C would be chosen to yield an "optimum" system. That is, C would be defined by a criterion that yields the smallest mean-squared system error. The methods of choosing the optimum system parameters for integrating the star tracker outputs into the overall system will be discussed and analyzed in more detail in a subsequent report where a star tracker will be integrated with the specific inertial platform of interest (i.e., the ST124-M platform).

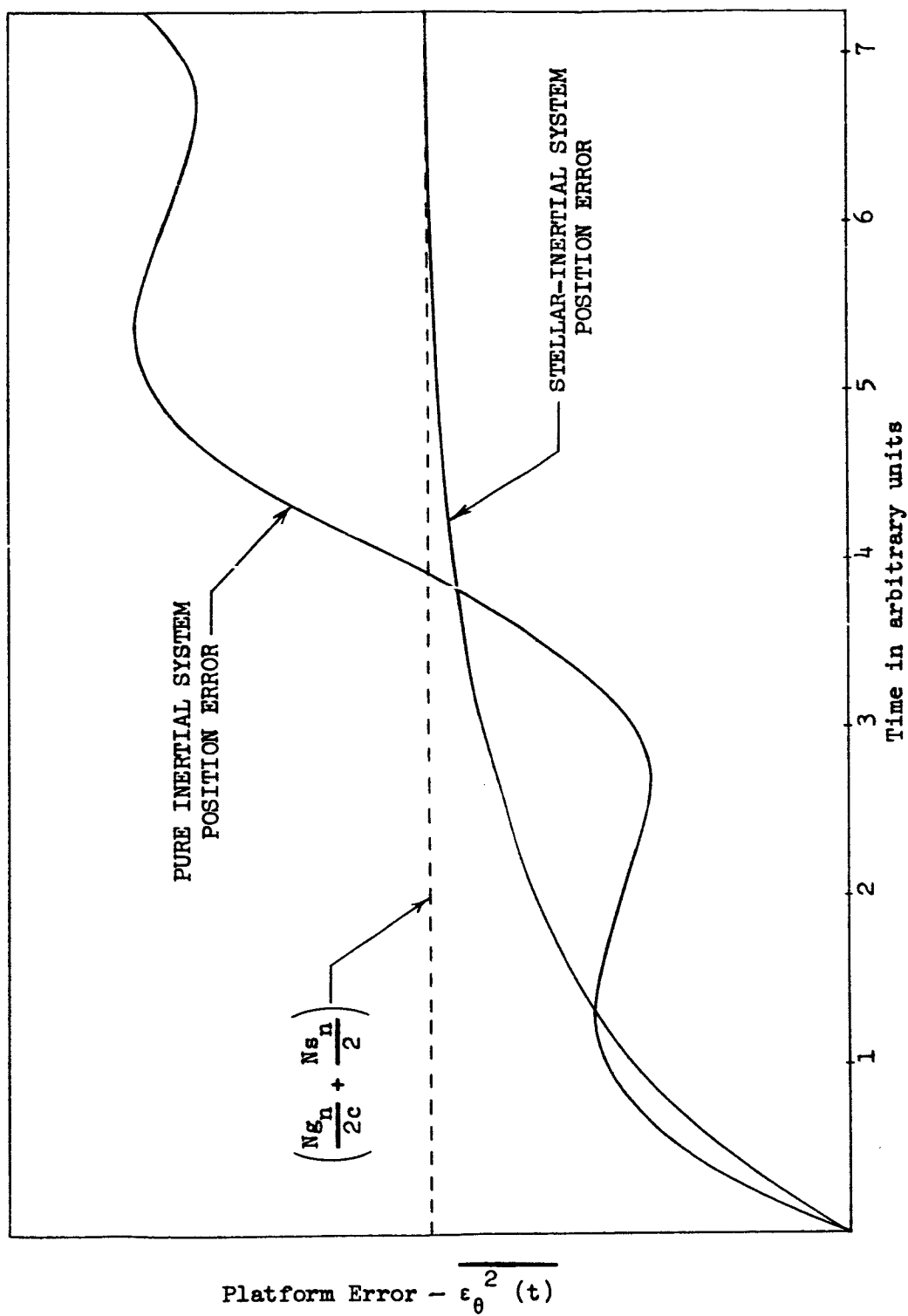


FIGURE 1.4 COMPARISON OF MEAN-SQUARED POSITION ERROR AS A FUNCTION OF TIME
FOR PURE INERTIAL AND STELLAR-INERTIAL SYSTEM

1.1.2 UTILIZATION OF ASTROTRACKER DATA FOR NAVIGATION (TERRESTRIAL POSITION DETERMINATION) AND ATTITUDE CONTROL

For purposes of celestial navigation the earth is conceived of as the center of a celestial sphere of infinite radius. The stars are all considered to exist on the surface of the celestial sphere. The enormity of the distance between the stars and the earth as compared to the radius of the earth is the basic justification for this celestial model.

A pictorial representation of this celestial model is given in Figure 1.5.

The following definitions of terrestrial and celestial terms are given before deriving the equations for navigation in earth coordinates and attitude reference.

L = latitude

Lo = longitude (measured west from the Greenwich meridian)

GHA = Greenwich hour angle (measured west from Greenwich)

γ = first point of Aries, is defined by the intersection of the celestial equator and the ecliptic.

Ecliptic = plane defined by the revolution of the earth about the sun.

GHA γ = the hour angle measured westward from Greenwich to γ

LHA = local hour angle = GHA - Lo (west)

δ = declination = angle measured along the star's meridian from the celestial equator to the star

1.1.2.1 Frames of Reference

In order to derive the necessary relationships for vehicle navigation and attitude control, several triads, or coordinate systems existent within the celestial sphere, will be defined.

Among the various possibilities available for an inertial triad, perhaps the simplest choice for navigation close to earth is the inertial triad composed of the following unit vectors:

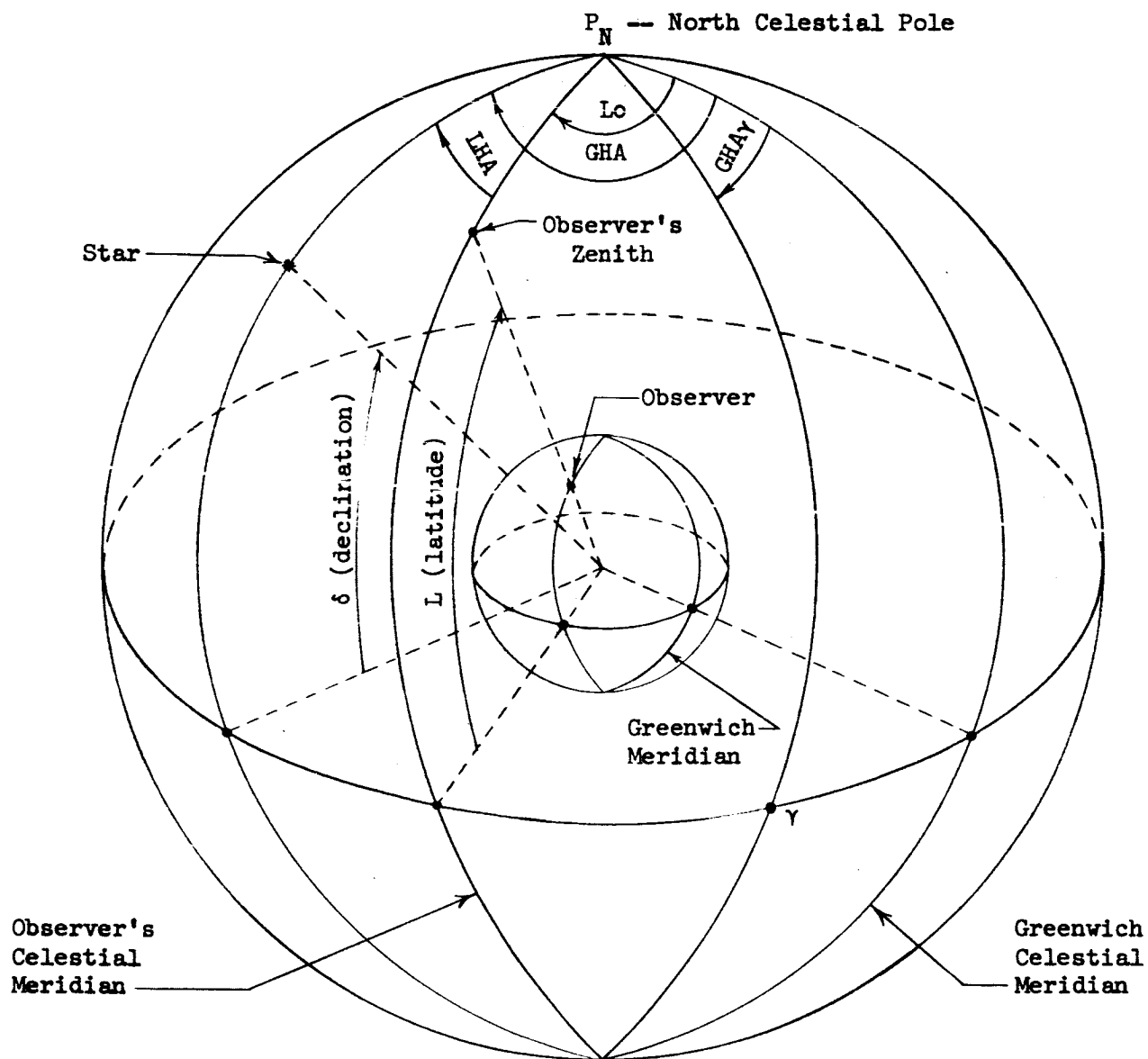


FIGURE 1.5 CELESTIAL SPHERE MODEL

Inertial Triad ($\bar{\gamma}$, \bar{n} , \bar{p}):

$\bar{\gamma}$ = unit vector pointing from the center of the earth to the first point of Aries on the celestial equator

\bar{p} = unit vector pointing from the center of the earth to the north celestial pole

\bar{n} = unit vector normal to $\bar{\gamma}$ and \bar{p} and given by: $\bar{p} \times \bar{\gamma}$

An earth triad may be defined by the following:

Earth Triad (\bar{g} , \bar{a} , \bar{p})

\bar{g} = unit vector pointing from center of the earth to the intersection of the Greenwich meridian and the equator.

\bar{p} = identical to the inertial triad unit vector \bar{p}

\bar{a} = unit vector normal to \bar{g} and \bar{p} and given by: $\bar{p} \times \bar{g}$

The relationship between the inertial triad ($\bar{\gamma}$, \bar{n} , \bar{p}) and the earth triad (\bar{g} , \bar{a} , \bar{p}) is shown in Figure 1.6.

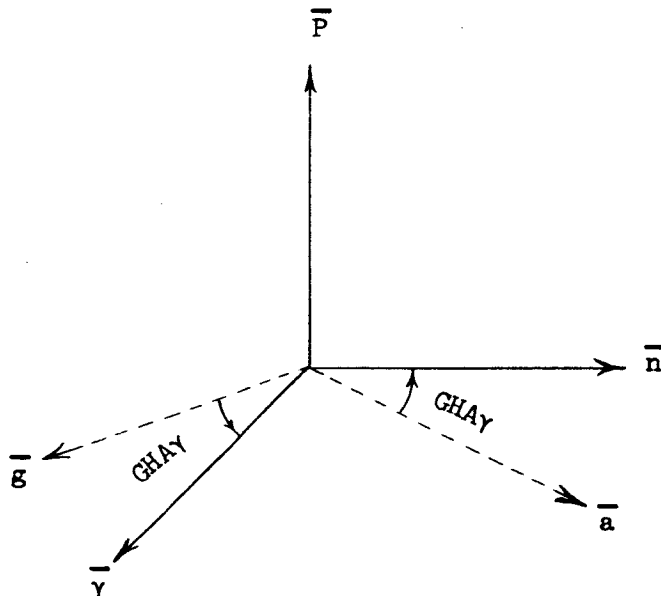


FIGURE 1.6 INERTIAL AND EARTH TRIAD RELATIONSHIP

As seen from Figure 1.6, the relationship between the inertial and earth triads is given by the matrix in equation 1.21 below.

$$\begin{bmatrix} \bar{g} \\ \bar{a} \\ \bar{p} \end{bmatrix} = \begin{bmatrix} \cos GHAY & -\sin GHAY & 0 \\ \sin GHAY & \cos GHAY & 0 \\ 0 & 0 & 1 \end{bmatrix} \begin{bmatrix} \bar{\gamma} \\ \bar{n} \\ \bar{p} \end{bmatrix} \quad (1.21)$$

Conversely the above matrix may be inverted to yield the expression for the inertial triad ($\bar{\gamma}$, \bar{n} , \bar{p}) in terms of the earth triad (\bar{g} , \bar{a} , \bar{p}):

$$\begin{bmatrix} \bar{\gamma} \\ \bar{n} \\ \bar{p} \end{bmatrix} = \begin{bmatrix} \cos GHAY & \sin GHAY & 0 \\ -\sin GHAY & \cos GHAY & 0 \\ 0 & 0 & 1 \end{bmatrix} \begin{bmatrix} \bar{g} \\ \bar{a} \\ \bar{p} \end{bmatrix} \quad (1.22)$$

Another important triad is the observer's triad. A convenient choice for the observer's triad is defined by the following three unit vectors,

- \bar{e} = unit vector tangent to the observer's latitude parallel and pointing eastward from the observer's position
- \bar{N} = unit vector tangent to the observer's meridian and pointing northward from the observer's position
- \bar{z} = unit vector pointing from the center of the earth to the observer's position (i.e., the zenith vector)

The vector \bar{z} may be derived in terms of the earth triad (\bar{g} , \bar{a} , \bar{p}) by reference to Figures 1.5 and 1.7

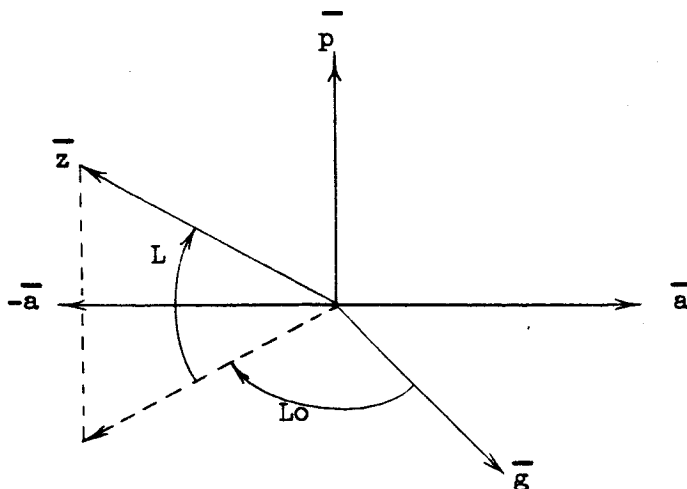


FIGURE 1.7 LOCATION OF VECTOR \bar{z} WITH RESPECT TO EARTH TRIAD

Thus \bar{z} is given by:

$$\bar{z} = \cos L \cos Lo \bar{g} - \cos L \sin Lo \bar{a} + \sin L \bar{p} \quad (1.23)$$

Figure 1.8 below may be helpful in visualizing the resolving of the vector \bar{N} into its components along the earth triad unit vectors.

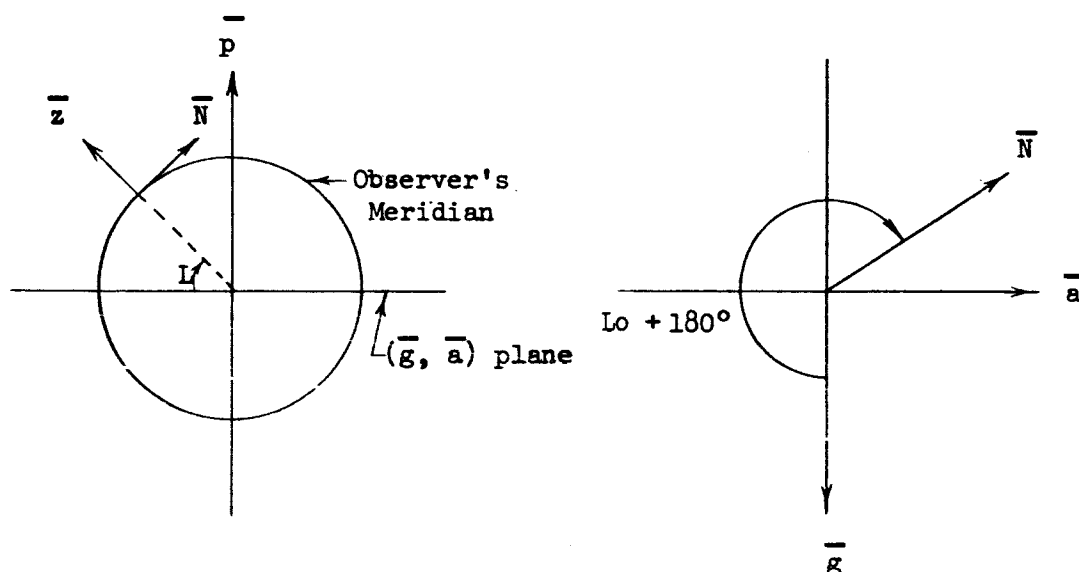


FIGURE 1.8 PROJECTION OF \bar{N} INTO (\bar{g}, \bar{a}) PLANE

From Figure 1.8 it is seen that \bar{N} is given by:

$$\bar{N} = -\sin L \cos Lo \bar{g} + \sin L \sin Lo \bar{a} + \cos L \bar{p} \quad (1.24)$$

Now since \bar{e} forms a right-hand system with \bar{z} and \bar{N} , it is given by:

$$\bar{e} = \bar{N} \times \bar{z} = \begin{bmatrix} \bar{g} & \bar{a} & \bar{p} \\ -\sin L \cos Lo & \sin L \sin Lo & \cos L \\ \cos L \cos Lo & -\cos L \sin Lo & \sin L \end{bmatrix}$$

$$\bar{e} = \sin Lo \bar{g} + \cos Lo \bar{a} \quad (1.25)$$

Equations 1.23, 1.24, and 1.25 may be summarized by the matrix relationship given by equation 1.26 below:

$$\begin{bmatrix} \bar{e} \\ \bar{N} \\ \bar{z} \end{bmatrix} = \begin{bmatrix} \sin L_o & \cos L_o & 0 \\ -\sin L \cos L_o & \sin L \sin L_o & \cos L \\ \cos L \cos L_o & -\cos L \sin L_o & \sin L \end{bmatrix} \begin{bmatrix} \bar{g} \\ \bar{a} \\ \bar{p} \end{bmatrix} \quad (1.26)$$

1.1.2.2 Terrestrial Navigation Using a Star Tracker

Referring to Figure 1.5 it is seen that the unit vector (\bar{S}) pointing from the center of the earth to the star is given in terms of the star's declination (δ) and Greenwich hour angle (GHA) by:

$$\bar{S} = \cos \delta \cos \text{GHA} \bar{g} - \cos \delta \sin \text{GHA} \bar{a} + \sin \delta \bar{p} \quad (1.27)$$

The line of sight unit vector ($\overline{\text{LOS}}$) from the observer to the star may be derived from Figure 1.9 below,

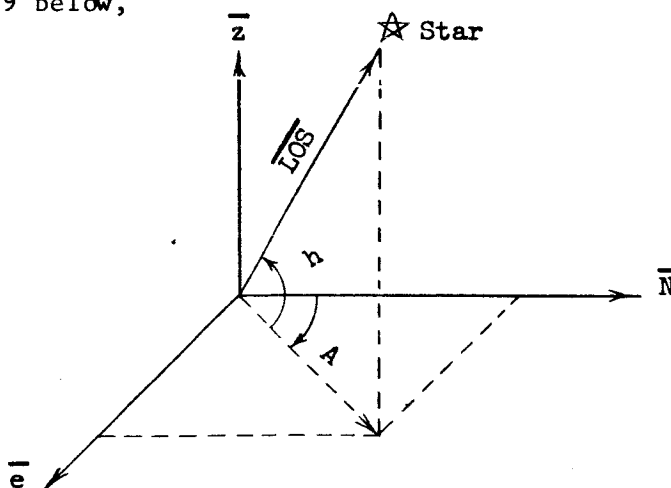


FIGURE 1.9 LINE OF SIGHT (LOS) TO STAR WITH RESPECT TO OBSERVER'S TRIAD

where h = elevation angle of the star

A = azimuth angle of the star

Thus the vector $\overline{\text{LOS}}$ is given by:

$$\overline{\text{LOS}} = \cos h \sin A \bar{e} + \cos h \cos A \bar{N} + \sin h \bar{z} \quad (1.28)$$

Now since the star is very far from the earth compared to the radius of the earth, the vectors \bar{S} and \bar{LOS} may be equated with only a negligible parallax error of less than 0.1 arc-second. Equating equations 1.27 and 1.28,

$$\cos h \sin A \bar{e} + \cos h \cos A \bar{N} + \sin h \bar{z} = \cos \delta \cos GHA \bar{g} - \cos \delta \sin GHA \bar{a} + \sin \delta \bar{p} \quad (1.29)$$

We can now express the vectors \bar{g} , \bar{a} , and \bar{p} on the right side of equation 1.29 by inverting the matrix relationship given by equation 1.26

$$\begin{bmatrix} \bar{g} \\ \bar{a} \\ \bar{p} \end{bmatrix} = \begin{bmatrix} \sin L_o & -\sin L \cos L_o & \cos L \cos L_o \\ \cos L_o & \sin L \sin L_o & -\cos L \sin L_o \\ 0 & \cos L & \sin L \end{bmatrix} \begin{bmatrix} \bar{e} \\ \bar{N} \\ \bar{z} \end{bmatrix} \quad (1.30)$$

Substituting the expressions for \bar{g} , \bar{a} , and \bar{p} given by equation 1.30 into equation 1.29 and equating coefficients of the \bar{e} , \bar{N} and \bar{z} vectors yields:

$$\cos h \sin A = (\sin L_o \cos GHA - \cos L_o \sin GHA) \cos \delta \quad (1.31a)$$

$$\cos h \cos A = \sin \delta \cos L - \cos \delta \sin L (\cos L_o \cos GHA + \sin L_o \sin GHA) \quad (1.31b)$$

$$\sin h = \sin \delta \sin L + \cos \delta \cos L (\cos L_o \cos GHA + \sin L_o \sin GHA) \quad (1.31c)$$

Noting that $LHA = GHA - L_o$ (west), we can simplify equations 1.31a, 1.31b, and 1.31c to the following:

$$\cos h \sin A = -\cos \delta \sin LHA \quad (1.32a)$$

$$\cos h \cos A = -(\cos \delta \sin L \cos LHA - \sin \delta \cos L) \quad (1.32b)$$

$$\sin h = \sin \delta \sin L + \cos \delta \cos L \cos LHA \quad (1.32c)$$

Equations 1.32a, 1.32b, and 1.32c form the basic relationship between 1) the observer's position on earth [L and L_o], 2) the star's position on the celestial sphere [δ and GHA], and 3) the star's position with respect to the observer [h and A].

The closed form expressions for h and A are derived from 1.32a, 1.32b, and 1.32c as follows:

Dividing equation 1.32a by 1.32b yields the expression for A:

$$\tan A = \frac{\cos \delta \sin LHA}{\cos \delta \sin L \cos LHA - \sin \delta \cos L} \quad (1.33)$$

Equation 1.33 is in a form that is readily solvable by resolver chain computer.

Now the expression for h given by Equation 1.32c, although quite simple, requires some further manipulation in order to solve for h with a resolver chain. An expression for h, derivable from equation 1.32c by trigonometric rearrangement, that is solvable with a resolver chain is given by equation 1.34 below.

$$\tan h = \frac{\sin \delta \sin L + \cos \delta \cos L \cos LHA}{[(\cos \delta \sin LHA)^2 + (\cos \delta \sin L \cos LHA - \sin \delta \cos L)^2]^{1/2}} \quad (1.34)$$

If a digital computer is used for solving for h, then it is more expedient to use Equation 1.32c rather than Equation 1.34.

We can now solve for the observer's position on earth (L and Lo) in terms of the star's celestial coordinates (δ and GHA) and the measured azimuth (A) and elevation (h) angles in the following manner:

Solving for LHA = GHA - Lo from Equation 1.32a,

$$\sin LHA = \sin (GHA - Lo) = - \frac{\cos h \sin A}{\cos \delta}$$

and

$$Lo = GHA + \sin^{-1} \frac{\cos h \sin A}{\cos \delta} \quad (1.35)$$

Multiplying Equation 1.32b by cos L and Equation 1.32c by sin L; adding the two new equations yields:

$$\sin \delta = \cos h \cos A \cos L + \sin h \sin L$$

Applying the transformation: $a \cos x + b \sin x = \sqrt{a^2 + b^2} \sin(x + \tan^{-1} a/b)$:

$$\sin \delta = (\cos^2 h \cos^2 A + \sin^2 h)^{1/2} \sin (L + \tan^{-1} \cot h \cos A)$$

$$L = \sin^{-1} \frac{\sin \delta}{(\cos^2 h \cos^2 A + \sin^2 h)^{1/2}} - \tan^{-1} \cot h \cos A \quad (1.36)$$

Using the two identities on Equation 1.36:

$$\tan^{-1} x = \sin^{-1} \frac{x}{\sqrt{1 + x^2}}$$

and

$$\sin^{-1} x - \sin^{-1} y = \sin^{-1} [x \sqrt{1 - y^2} - y \sqrt{1 - x^2}]$$

$$L = \sin^{-1} \left[\frac{\sin \delta \sin h - \cos h \cos A (\cos^2 \delta - \cos^2 h \sin^2 A)^{1/2}}{\cos^2 h \cos^2 A + \sin^2 h} \right] \quad (1.37)$$

In summarizing the results of this section it is seen that the basic relationships between the navigational variables (h , A , L , Lo , δ , GHA) are given by Equations 1.32a, 1.32b, and 1.32c. Equations 1.33, 1.34, 1.35, and 1.37 give an explicit equation for azimuth (A), elevation (h), longitude (Lo), and L (latitude) respectively. It may also be noted that these equations can be rearranged quite readily by the use of trigonometric identities to take on a form that lends itself best to the particular computational scheme in the system.

1.1.2.3 Vehicle Attitude Correction with a Star Tracker

This topic is treated in two sections. The first of the following sections considers the information required of a star tracker to correct a stabilization or attitude control system that has an error in two axes. It is shown that only one star fix is required to uniquely correct the error in the two axes. Furthermore, it is shown that the correction equations require only the functional characteristic of a single resolver for their solution.

In the second section it is shown that two star fixes are required for attitude correction when there exists an error in all three of the stabilization axes.

1.1.2.3.1 Derivation of Equations for Removal of Platform Tilt Error with a Star Tracker

A platform tilt, or verticality error is characterized by two consecutive rotations about the two axes that define the plane of tilt. Thus taking the plane defined by the east and north unit vectors (\bar{e} , \bar{N}) to be the plane of tilt, and rotating an angle α about the \bar{e} axes and on angle β about the \bar{N} axis, a tilted coordinate system is formed.

The unrotated coordinate system is shown in Figure 1.10 below,

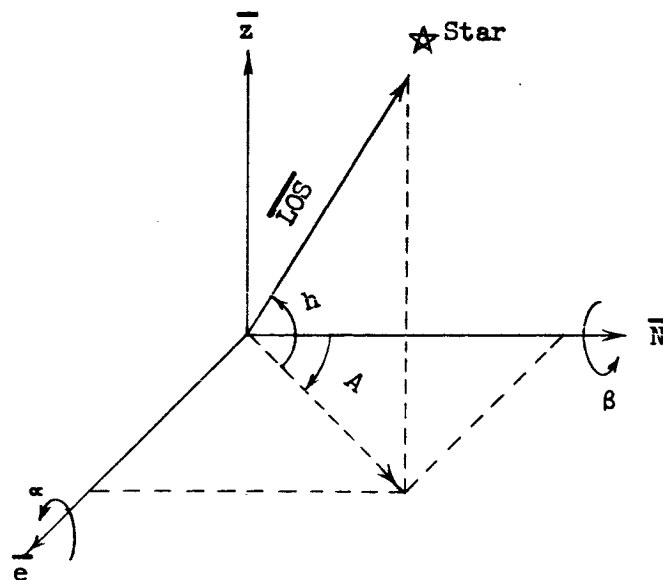


FIGURE 1.10 ROTATION OF COORDINATE SYSTEM DUE TO VERTICALITY ERROR

The axes of the rotated triad are given by the coordinate transformation:

$$\begin{bmatrix} \bar{e}^1 \\ \bar{N}^1 \\ \bar{z}^1 \end{bmatrix} = \begin{bmatrix} \cos \beta & 0 & -\sin \beta \\ 0 & 1 & 0 \\ \sin \beta & 0 & \cos \beta \end{bmatrix} \begin{bmatrix} 1 & 0 & 0 \\ 0 & \cos \alpha & \sin \alpha \\ 0 & -\sin \alpha & \cos \alpha \end{bmatrix} \begin{bmatrix} \bar{e} \\ \bar{N} \\ \bar{z} \end{bmatrix} \quad (1.38)$$

Multiplying the matrices in Equation 1.38 yields

$$\begin{bmatrix} \bar{e}^1 \\ \bar{N}^1 \\ \bar{z}^1 \end{bmatrix} = \begin{bmatrix} \cos \beta & \sin \alpha \sin \beta & -\cos \alpha \sin \beta \\ 0 & \cos \alpha & \sin \alpha \\ \sin \beta & -\sin \alpha \cos \beta & \cos \alpha \cos \beta \end{bmatrix} \begin{bmatrix} \bar{e} \\ \bar{N} \\ \bar{z} \end{bmatrix} \quad (1.39)$$

The line of sight vector from the coordinate origin to the star can be written in terms of the unrotated triad as:

$$\overline{LOS} = \cos h \sin A \overline{e} + \cos h \cos A \overline{N} + \sin h \overline{z} \quad (1.40)$$

The line of sight vector in terms of the rotated triad is given by:

$$\overline{LOS} = \cos h' \sin A' \overline{e'} + \cos h' \cos A' \overline{N'} + \sin h' \overline{z'} \quad (1.41)$$

Substituting the expressions for $\overline{e'}$, $\overline{N'}$ and $\overline{z'}$ given by Equation 1.39 into Equation 1.41 yields:

$$\begin{aligned} \overline{LOS} = & (\cos \beta \cos h' \sin A' + \sin \beta \sin h') \overline{e} \\ & + (\sin \alpha \sin \beta \cos h' \sin A' + \cos \alpha \cos h' \cos A' - \sin \alpha \cos \beta \sin h') \overline{N} \\ & + (-\cos \alpha \sin \beta \cos h' \sin A' + \sin \alpha \cos h' \cos A' + \cos \alpha \cos \beta \sin h') \overline{z} \end{aligned} \quad (1.42)$$

Now equating the coefficients of \overline{e} , \overline{N} , and \overline{z} of Equations 1.40 and 1.42 yields the following three equations:

$$\cos h \sin A = \cos \beta \cos h' \sin A' + \sin \beta \sin h' \quad (1.43a)$$

$$\cos h \cos A = \sin \alpha \sin \beta \cos h' \sin A' + \cos \alpha \cos h' \cos A' - \sin \alpha \cos \beta \sin h' \quad (1.43b)$$

$$\sin h = -\cos \alpha \sin \beta \cos h' \sin A' + \sin \alpha \cos h' \cos A' + \cos \alpha \cos \beta \sin h' \quad (1.43c)$$

Defining the following:

$E_h = h - h' =$ difference between true elevation and elevation measured from the platform

$E_a = A - A' =$ difference between true azimuth and azimuth measured from the platform

In general the angles α and β are small such that the following approximations are valid:

$$\sin \alpha \approx \alpha \text{ radians}$$

$$\sin \beta \approx \beta \text{ radians}$$

$$\cos \alpha \approx 1$$

$$\cos \beta \approx 1$$

This assumption is quite practical since, if the angles α and β are large, the star tracker would not be able to find the star during its search mode.

Now subtracting $\sin h'$ from both sides of Equation 1.43c and using the small angle approximations:

$$\sin h - \sin h' = -\beta \cos h' \sin A' + \alpha \cos h' \cos A'$$

Using the identity: $\sin x - \sin y = 2 \sin \frac{1}{2}(x-y) \cos \frac{1}{2}(x+y)$, and noting that small angle approximations hold for Eh and Ea since α and β are small.

$$Eh = -\beta \sin A' + \alpha \cos A' \quad (1.44)$$

The expression for Ea is obtained by first applying the small angle approximation and dividing Equation 1.43a by Equation 1.43b.

$$\tan A = \frac{\cos h' \sin A' + \beta \sin h'}{\alpha \beta \cos h' \sin A' + \cos h' \cos A' - \alpha \sin h'}$$

Subtracting $\tan A'$ from both sides of the above equation yields:

$$\tan A - \tan A' = \frac{Ea}{\cos^2 A'} = \frac{\beta \sin h' \cos A' - \alpha \beta \cos h' \sin^2 A' + \alpha \sin h' \sin A'}{\cos A' (\alpha \beta \cos h' \sin A' + \cos h' \cos A' - \alpha \sin h')}$$

We now make the further approximations:

$$\beta \sin h' \cos A' + \alpha \sin h' \sin A' \gg \alpha \beta \cos h'$$

and $\cos h' \cos A \gg \alpha \beta \cos h' \sin A' - \alpha \sin h'$

Again these approximations are valid if α and β are small. The expression for Ea is finally given by:

$$Ea = (\alpha \sin A' + \beta \cos A') \tan h' \quad (1.45)$$

By rewriting Equations 1.44 and 1.45 in the following form, it is seen that a single resolver and a tangent potentiometer represent the only computer function required to relate α and β to Ea and Eh . Equations 1.44 and 1.45 are written as:

$$E_h = \alpha \cos A' - \beta \sin A' \quad (1.46)$$

$$\frac{E_a}{\tan h'} = \alpha \sin A' + \beta \cos A' \quad (1.47)$$

Figure 1.11 shows the resolver method of solving these equations. Since a digital computer would probably be available aboard the vehicle, the use of a resolver may be unnecessary, especially if high accuracy is required.

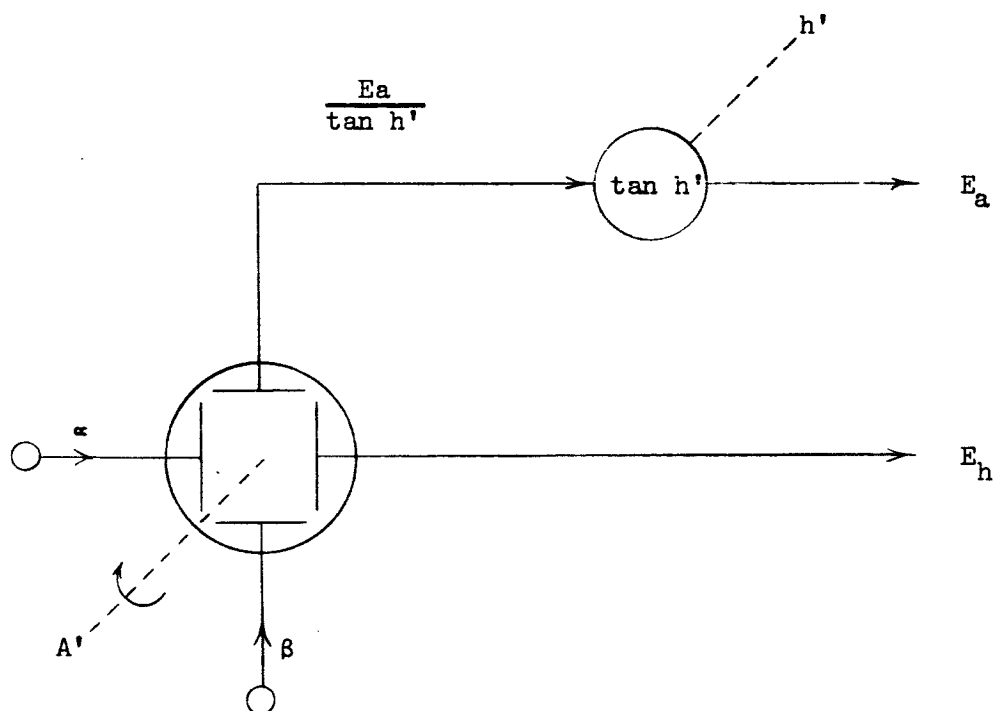


FIGURE 1.11 RESOLVER IMPLEMENTATION TO DETERMINE E_a AND E_h

1.1.2.3.2 Derivation of Correction Equations for Removal of Platform Error in Three Axes with a Star Tracker

Denoting the true triad by: $(\bar{e}, \bar{N}, \bar{z})$, we form the rotated triad by consecutively rotating an angle α about the \bar{e} axis, an angle β about the new north axis (i.e., \bar{N}_1), and an angle γ about the new zenith axis (i.e., \bar{z}_2). Denoting the rotated triad by: $(\bar{e}', \bar{N}', \bar{z}')$, the relationship between the two triads takes the form of a standard Euler coordinate transformation: (1.48)

$$\begin{bmatrix} \bar{e}' \\ \bar{N}' \\ \bar{z}' \end{bmatrix} = \begin{bmatrix} \cos\beta \cos\gamma & \cos\alpha \sin\gamma + \sin\alpha \sin\beta \cos\gamma & \sin\alpha \sin\gamma - \cos\alpha \sin\beta \cos\gamma \\ -\cos\beta \sin\gamma & \cos\alpha \cos\gamma - \sin\alpha \sin\beta \sin\gamma & \sin\alpha \cos\gamma + \cos\alpha \sin\beta \sin\gamma \\ \sin\beta & -\sin\alpha \cos\beta & \cos\alpha \cos\beta \end{bmatrix} \begin{bmatrix} \bar{e} \\ \bar{N} \\ \bar{z} \end{bmatrix}$$

Now assuming that the small angle approximation is valid and that the product of two or more sine terms is negligible, the approximate relationship between the two triads becomes

$$\begin{bmatrix} \bar{e}' \\ \bar{N}' \\ \bar{z}' \end{bmatrix} = \begin{bmatrix} 1 & \gamma & -\beta \\ -\gamma & 1 & \alpha \\ \beta & -\alpha & 1 \end{bmatrix} \begin{bmatrix} \bar{e} \\ \bar{N} \\ \bar{z} \end{bmatrix} \quad (1.49)$$

The line of sight vector to the star in terms of the $(\bar{e}, \bar{N}, \bar{z})$ triad is

$$\overline{LOS} = \cos h \sin A \bar{e} + \cos h \cos A \bar{N} + \sin h \bar{z} \quad (1.50)$$

The line of sight vector to the star in terms of the $(\bar{e}', \bar{N}', \bar{z}')$ triad is

$$\overline{LOS} = \cos h' \sin A' \bar{e}' + \cos h' \cos A' \bar{N}' + \sin h' \bar{z}' \quad (1.51)$$

Substituting Equation 1.49 into 1.50,

$$\begin{aligned} \overline{LOS} = & (\cos h' \sin A' - \gamma \cos h' \cos A' + \beta \sin h') \bar{e} \\ & + (\gamma \cos h' \sin A' + \cos h' \cos A' - \alpha \sin h') \bar{N} \\ & + (-\beta \cos h' \sin A' + \alpha \cos h' \cos A' + \sin h') \bar{z} \end{aligned} \quad (1.52)$$

Equating coefficients of \bar{e} , \bar{N} , and \bar{z} in Equations 1.50 and 1.52 yields,

$$\cos h \sin A = \cos h' \sin A' - \gamma \cos h' \cos A' + \beta \sin h' \quad (1.53a)$$

$$\cos h \cos A = \gamma \cos h' \sin A' + \cos h' \cos A' - \alpha \sin h' \quad (1.53b)$$

$$\sin h = -\beta \cos h' \sin A' + \alpha \cos h' \cos A' + \sin h' \quad (1.53c)$$

The expressions for $E_h = h - h'$ and $E_a = A - A'$ may be derived from Equations 1.53a, 1.53b, and 1.53c with the same procedure as in Section 1.1.2.4. These expressions are,

$$E_h = \alpha \cos A' - \beta \sin A' \quad (1.54)$$

$$E_a = (\alpha \sin A' + \beta \cos A') \tan h' - \gamma \quad (1.55)$$

Equations 1.54 and 1.55 show that it is not possible to obtain a unique solution for α , β , and γ since there are only two equations and three unknowns. This is due to the fact that, if all three axes are allowed to rotate, then any rotations about the star tracker's line of sight do not require the tracking loop to reposition the tracker gimbals. Thus, two different stars must be tracked to obtain a unique solution for α , β , and γ . The method for obtaining α , β , and γ from a two star fix is as follows:

On the first star fix two equations are obtained:

First Star Fix:

$$E_{h1} = \alpha \cos A'_1 - \beta \sin A'_1 \quad (1.56)$$

$$E_{a1} = (\alpha \sin A'_1 + \beta \cos A'_1) \tan h'_1 - \gamma \quad (1.57)$$

Now assuming that the second star fix occurs immediately after the first star fix such that α , β , and γ are the same for the second star fix:

Second Star Fix:

$$E_{h2} = \alpha \cos A'_2 - \beta \sin A'_2 \quad (1.58)$$

$$E_{a2} = (\alpha \sin A'_2 + \beta \cos A'_2) \tan h'_2 - \gamma \quad (1.59)$$

Solving Equations 1.56 and 1.58 for α and β by matrix inversion

$$\begin{bmatrix} E_{h1} \\ E_{h2} \end{bmatrix} = \begin{bmatrix} \cos A'_1 - \sin A'_1 \\ \cos A'_2 - \sin A'_2 \end{bmatrix} \begin{bmatrix} \alpha \\ \beta \end{bmatrix}$$

$$\begin{bmatrix} \alpha \\ \beta \end{bmatrix} = \frac{1}{\sin A'_1 \cos A'_2 - \cos A'_1 \sin A'_2} \begin{bmatrix} -\sin A'_2 & \sin A'_1 \\ -\cos A'_2 & \cos A'_1 \end{bmatrix} \begin{bmatrix} E_{h1} \\ E_{h2} \end{bmatrix}$$

Letting $\Delta A' = A'_1 - A'_2$, α and β become:

$$\alpha = -\frac{\sin A'_2}{\sin \Delta A'} E_{h1} + \frac{\sin A'_1}{\sin \Delta A'} E_{h2} \quad (1.60)$$

$$\beta = -\frac{\cos A'_2}{\sin \Delta A'} E_{h1} + \frac{\cos A'_1}{\sin \Delta A'} E_{h2} \quad (1.61)$$

We can now solve for γ by substituting Equations 1.60 and 1.61 into either Equation 1.57 or Equation 1.59. First using 1.57, we obtain for γ ,

$$\gamma = (-E_{h1} \cot \Delta A' + E_{h2} \csc \Delta A') \tan h'_1 - E_{a1} \quad (1.62)$$

Now using Equation 1.59, we obtain for γ ,

$$\gamma = (-E_{h1} \csc \Delta A' + E_{h2} \cot \Delta A') \tan h'_2 - E_{a2} \quad (1.63)$$

Thus, γ is given by either Equation 1.62 or Equation 1.63.

1.2 DESCRIPTION AND ANALYSIS OF AN ORBITAL NAVIGATION SYSTEM USING THE ST124-M INERTIAL PLATFORM

A navigational and guidance system for earth orbital type missions such as that anticipated for the S-IV Saturn Booster Stage is described. The system considered uses the ST124-M inertial platform as the prime inertial reference. The remainder of the system consists of one or two star trackers, a horizon scanner, an orbital gyro compass, and a digital computer. The overall system function is to provide the following information: 1) spacecraft attitude with respect to inertial space, 2) spacecraft attitude with respect to earth, 3) spacecraft heading, and 4) spacecraft position (including altitude) with respect to earth.

The following analyses present a derivation of the system equations and error analyses of the coupling between the inertial platform (ST124-M) and the star tracker. It is shown that with the inertial platform oriented to an inertial triad the star tracker will limit both the coherent and random gyro drift errors.

1.2.1 System Configuration and Analysis

The functional block diagram of the system under consideration is shown in Figure 1.12. The various components of the system are shown linked together by computer functions symbolically represented by the letter C with a subscript. In the actual system all the computer functions are combined into one digital computer. However, for purposes of simplicity in describing the system, the computer functions have been separated. Each of the computer functions will be discussed in turn, and the system equations will be derived.

1.2.2 Computer Function C_1 (Star Tracker Pointing)

Function C_1 serves to point the star tracker by converting the gimbal angles of the platform and the star ephemeris data stored in the computer into pointing angles. The inertial platform is oriented to an inertial triad defined by the following unit vectors:

$\bar{\gamma}$ = Unit vector pointing from the center of the earth to the first point of Aries on the celestial equator

\bar{p} = Unit vector pointing from the center of the earth to the north celestial pole

\bar{n} = Unit vector normal to $\bar{\gamma}$ and \bar{p} and given by:

$$\bar{n} = \bar{p} \times \bar{\gamma}$$

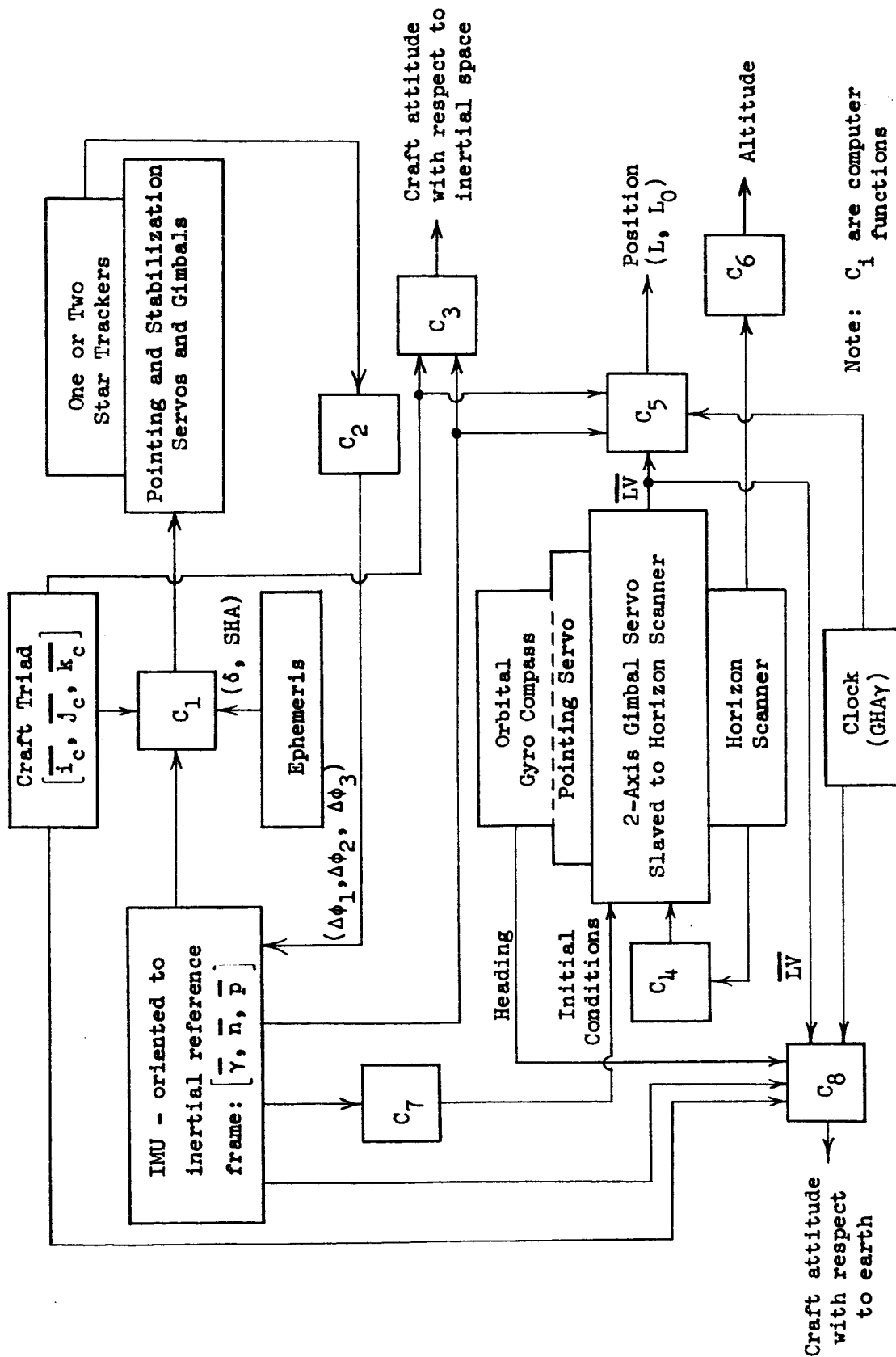


FIGURE 1.12 ORBITAL NAVIGATION AND GUIDANCE SYSTEM FUNCTIONAL BLOCK DIAGRAM

The ephemeris consists of the declination (δ) and the sidereal hour angle (SHA) of the stars. The star tracker is pointed by driving the star tracker gimbals to given angles as determined by the computer. These gimbal angles will vary depending upon the star tracker gimbal configuration, and whether the star tracker is mounted on or off the platform. If the star tracker is located on the platform, and an altitude-azimuth gimbal is used, then the δ and SHA angles of the star can be used directly to position the star tracker gimbals. If the star tracker is off the platform, then two different basic system configurations for the star tracker are possible. The star tracker may be mounted in a two-gimbal system with two rate (or rate integrating) gyros mounted perpendicular to the line of sight in order to remove relative rates between the star and the star tracker. The other possible configuration is the star tracker mounted in a four-gimbal system, where rate stabilization is derived from the inertial platform (IMU). In this configuration, the two base or outer gimbals of the star tracker are slaved to the ecliptic as are the IMU gimbals. The two axes that define the plane of the ecliptic are $\bar{\gamma}$ and \bar{n} . Thus these two star tracker gimbals can be slaved directly to the IMU gimbals. The star tracker is then mounted within these two outer gimbals, in an SHA gimbal and a declination (δ) gimbal. No rate stabilization is required for the δ gimbal because the γ and n gimbals provide a stable base. The SHA loop does require rate stabilization which can be derived directly from the p gimbal of the IMU. The gimbal follow-up servo of the SHA channel would be of the form shown in Figure 1.13.

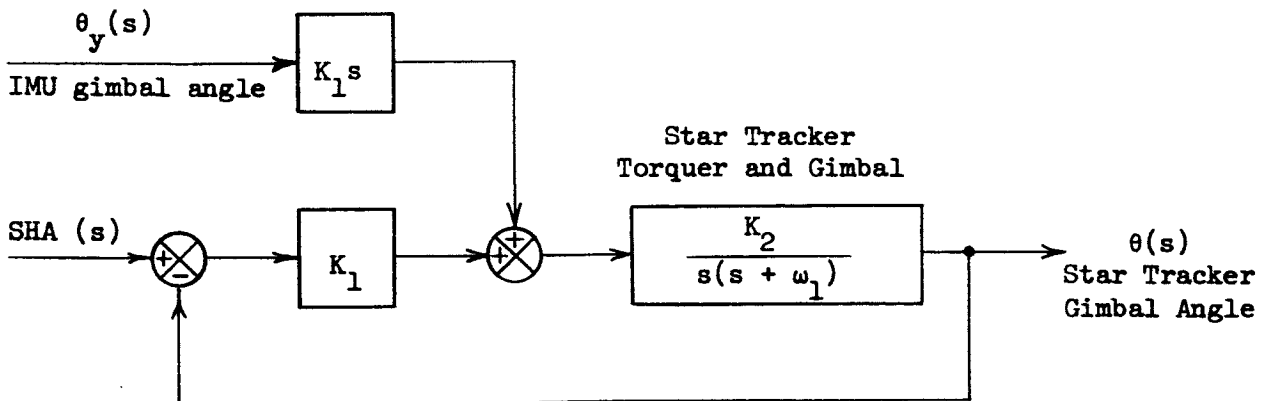


FIGURE 1.13 RATE STABILIZATION SERVO

The expression for $\theta(s)$ in terms of $SHA(s)$ and $\theta_y(s)$ is given by:

$$\theta(s) = \left(\frac{K_1 K_2}{s^2 + s\omega_1 + K_1 K_2} \right) \left(SHA(s) + s \theta_y(s) \right) \quad (1.64)$$

The SHA(s) function will be a step command of magnitude SHA. Thus, after a period of time greater than the servo time constants, the output $\theta(t)$ will be given by:

$$\lim_{t \gg \tau_1, \tau_2} \theta(t) = SHA + \dot{\theta}_y(t) \quad (1.65)$$

Depending upon the field of view of the star tracker and the initial uncertainty in craft attitude, C_1 may also be required to generate a search pattern.

Other gimbal configurations for the star tracker may be devised but will not be treated here.

1.2.3 Computer Function C_2 (Star Tracker Correction to IMU)

The function of computer element C_2 is to use the star tracker(s) outputs to correct the inertial platform. If the platform is used in a strapped-down configuration, then the correction to the inertial reference is performed in the computer rather than to the gimbals of the platform. In either case the basic correction equations are the same.

In Section 1.1.2 the equations for correcting the platform's inertial triad with a star tracker were derived. Since the platform considered here is referenced to a space fixed triad $(\bar{\gamma}, \bar{n}, \bar{p})$ rather than a local vertical triad, the pointing angles to the star are denoted by their celestial coordinates declination (δ) and sidereal hour angle (SHA), rather than elevation and azimuth. The correction equations written in terms of celestial coordinates (δ and SHA) are given by:

First Star Fix

$$E_{\delta 1} = \Delta\phi_1 \cos SHA'_1 - \Delta\phi_2 \sin SHA'_1 \quad (1.66)$$

$$E_{SHA_1} = (\Delta\phi_1 \sin SHA'_1 + \Delta\phi_2 \cos SHA'_1) \tan \delta'_1 - \Delta\phi_3 \quad (1.67)$$

Second Star Fix

$$E_{\delta 1} = \Delta\phi_1 \cos SHA'_2 - \Delta\phi_2 \sin SHA'_2 \quad (1.68)$$

$$E_{SHA_2} = (\Delta\phi_1 \sin SHA'_2 + \Delta\phi_2 \cos SHA'_2) \tan \delta'_2 - \Delta\phi_3 \quad (1.69)$$

where

SHA = computed sidereal hour angle

SHA' = star tracker output sidereal hour angle

δ = computed declination

δ' = star tracker output declination

$E_{SHA} = SHA - SHA'$

$E_{\delta} = \delta - \delta'$

$\Delta\phi_1, \Delta\phi_2$, and $\Delta\phi_3$ = correction angles about the platform's $\bar{\gamma}, \bar{n}$, and \bar{p} axes, respectively

Solving Equations 1.64, 1.65, 1.66 and 1.67 for $\Delta\phi_1, \Delta\phi_2$, and $\Delta\phi_3$ yields:

$$\Delta\phi_1 = -\frac{\sin SHA'_2}{\sin(SHA'_1 - SHA'_2)} E_{\delta 1} + \frac{\sin SHA'_1}{\sin(SHA'_1 - SHA'_2)} E_{\delta 2} \quad (1.70)$$

$$\Delta\phi_2 = -\frac{\cos SHA'_2}{\sin(SHA'_1 - SHA'_2)} E_{\delta 1} + \frac{\cos SHA'_1}{\sin(SHA'_1 - SHA'_2)} E_{\delta 2} \quad (1.71)$$

$$\Delta\phi_3 = \left[-E_{\delta 1} \cotn(SHA'_1 - SHA'_2) + E_{\delta 2} \csc(SHA'_1 - SHA'_2) \right] \tan \delta'_1 - E_{SHA_1} \quad (1.72)$$

Thus the computer generates the required corrections to the inertial platform from two star fixes. The star tracker correction angles ($\Delta\phi_1, \Delta\phi_2$, and $\Delta\phi_3$) remove constant gyro drift and bound the errors due to random gyro drift. The manner in which the star tracker accomplishes this function is derived in the following paragraphs.

The single axis gyro stabilization loop block diagram for the ST124-M inertial platform as given by NASA TN D-2983 is shown in Figure 1.14 below.

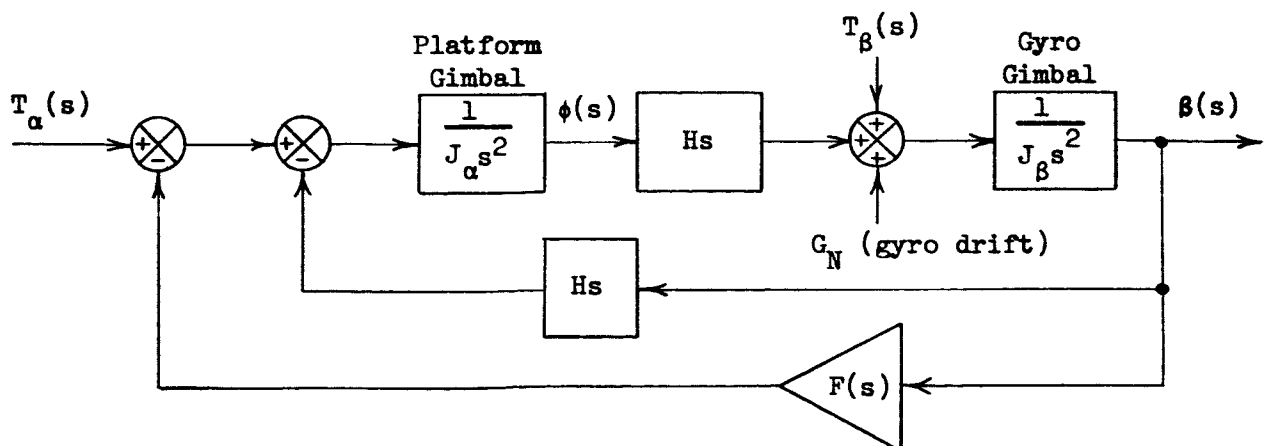


FIGURE 1.14 SINGLE AXIS PLATFORM STABILIZATION LOOP

The signal flow graph for the system shown in Figure 1.14 is shown in Figure 1.15 below:

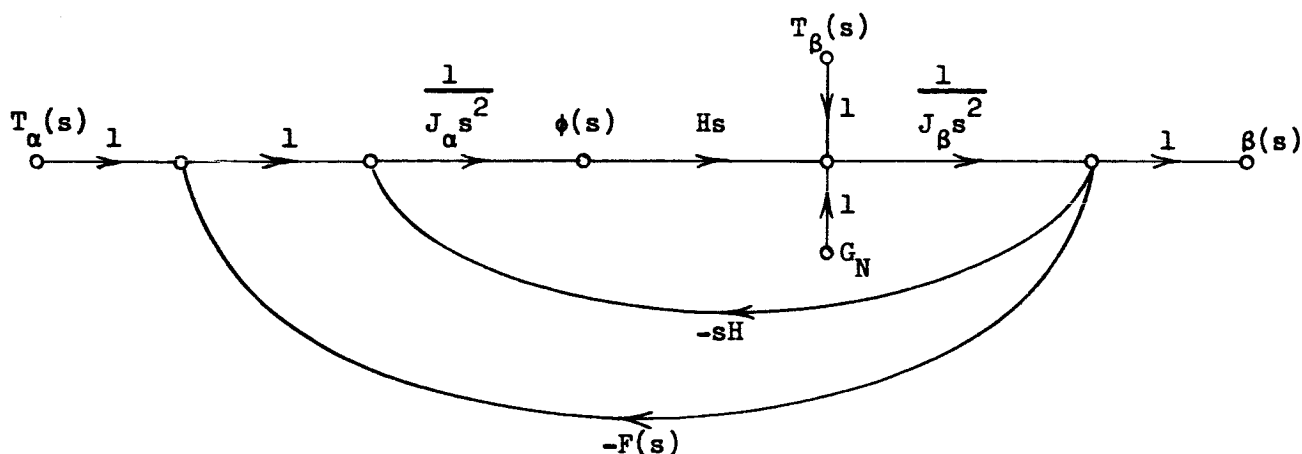


FIGURE 1.15 SIGNAL FLOW GRAPH OF SINGLE AXIS STABILIZATION LOOP

The star tracker output platform correction angles ($\Delta\phi_1, \Delta\phi_2, \Delta\phi_3$) are used to correct the orientation of the platform by applying a torquing signal at the $T_\beta(s)$ input. Thus the transfer function of interest is $\phi(s)/T_\beta(s)$; where $\phi(s)$ is the gimbal output angle. This transfer function is readily derived from the signal flow graph in Figure 1.15 and is given by:

$$\frac{\phi(s)}{T_\beta(s)} = - \frac{sH + F(s)}{s \left[J_\alpha J_\beta s^3 + sH^2 + HF(s) \right]} \quad (1.73)$$

Since the system errors that exist after a fairly long period of time are of interest rather than the errors after a few seconds, the transfer function given by Equation 1.73 may be approximated by:

$$\left. \frac{\phi(s)}{T_\beta(s)} \right|_{\substack{t \rightarrow \infty \\ s \rightarrow 0}} \rightarrow \frac{F}{s H F} = \frac{1}{sH} \quad (1.74)$$

where

$$F = \lim_{s \rightarrow 0} F(s)$$

The error due to gyro drift (G_N) can be computed from Equation 1.74.

Figure 1.16 below shows the block diagram relationship of platform gimbal angle error to gyro drift.

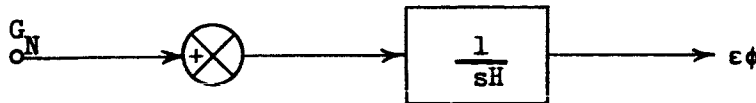


FIGURE 1.16 BLOCK DIAGRAM OF RELATIONSHIP OF PLATFORM GIMBAL ANGLE ERROR TO GYRO DRIFT

where $\epsilon\phi$ = platform gimbal error

G_N = gyro drift

The constant drift component may be represented by letting G_N equal a step function ($G_N = \frac{K}{s}$). The output $\epsilon\phi$ for $G_N = \frac{K}{s}$ is a ramp function ($\epsilon\phi(t) = \frac{K}{H} t$). Thus a constant gyro drift rate results in an unbounded attitude error when no velocity or position damping information is available.

The effect of random gyro drift, in general, may be characterized by a correlation function of the form:

$$R_{gg}(\tau) = \sigma_N^2 e^{-\omega_c |\tau|} \quad (1.75)$$

where $R_{gg}(\tau)$ = random gyro drift correlation function

σ_N^2 = mean-squared value of random gyro drift

ω_c = bandwidth of gyro drift noise

The impulse response of $\epsilon\phi$ to G_N is given by:

$$h_{\phi g}(t) = \mathcal{L}^{-1} \left[\frac{\phi(s)}{G_N(s)} \right] = \frac{1}{H} \quad (1.76)$$

Thus the mean-squared error ($\overline{\epsilon\phi^2}$) growth as a function of time is given in terms of the noise autocorrelation function (Equation 1.75) and the impulse response (Equation 1.76) as:

$$\begin{aligned}\overline{\epsilon\phi^2} &= \frac{\sigma_N^2}{H^2} \int_0^t d\tau \int_0^t e^{-\omega_c |\tau-\lambda|} d\lambda \\ &= \frac{\sigma_N^2}{H^2} \int_0^t d\tau \left[e^{-\omega_c \tau} \int_0^\tau e^{\omega_c \lambda} d\lambda + e^{\omega_c \tau} \int_\tau^t e^{-\omega_c \lambda} d\lambda \right] \quad (1.77)\end{aligned}$$

Evaluating the integrals in the above equation yields the following expression for the mean-squared platform error:

$$\overline{\epsilon\phi^2} = \frac{2 \sigma_N^2}{\omega_c^2 H^2} \left[\omega_c t + e^{-\omega_c t} - 1 \right] \quad (1.78)$$

From Equation 1.78, it is apparent from the $\omega_c t$ term that the platform error is unbounded.

A star tracker's capability to reduce and bound platform errors due to gyro drift (both constant and random) will be considered next.

The star tracker correction data would be inserted into the platform stabilization loop at the $T_\beta(s)$ input node as shown in Figures 1.14 and 1.15; that is, the star tracker data is used to torque the platform gyros to a corrected position. Thus the functional block diagram of the gyro stabilization loop with star tracker correction takes a form as shown in Figure 1.17 below,

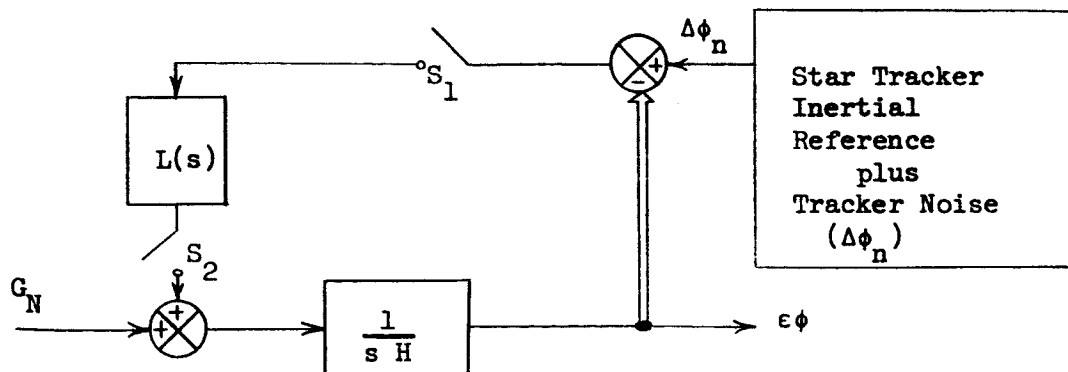


FIGURE 1.17 GYRO STABILIZATION LOOP WITH STAR TRACKER CORRECTION (ERROR MODEL)

where $\Delta\phi_n$ = star tracker noise (i.e., correction signal error)

S_1, S_2 = synchronized switches

$L(s)$ = optimum filter or simple gain

In the error model of Figure 1.17 the star tracker output is composed of the instantaneous platform error $-\epsilon\phi$ and a noise term $\Delta\phi_n$ which represents the tracker error. The $-\epsilon\phi$ term of the star tracker output is represented by a feedback path from the gimbal output with a double line. The double line is used to denote that the path is functional rather than wired.

The switches shown in Figure 1.17 are necessary to allow the gyro stabilization loop to respond to craft rates whose frequency content are higher than the inherent star tracker sampling frequency. If the switch remains closed continuously (that is, if the last star tracker output is held), the loop response to craft rates would be insufficient to prevent the star image from smearing due to image motion. Image motion with respect to the tracker line of sight causes a loss of both detectivity and accuracy. Furthermore, the Sampling Theorem states that in order to retrieve information from a sampled signal without loss it is necessary to sample the signal at a rate which is at least twice the highest frequency component of the signal. Since the star tracker output (for image forming and flying spot scanning types of star trackers) is inherently of a sampled nature, with a period equal to the tracker acquisition and readout time, certain components of craft motion will not appear in the tracker output at the readout times. Thus, the inertial platform serves to stabilize for craft rates that occur in the middle to high frequency range while the star tracker removes the low frequency errors that accumulate due to platform drift.

Mathematically the switch is assumed to be ideal, such that its output is an impulse with a weighting equal to the amplitude of the input signal at the sampling instant. This is illustrated in Figure 1.18.

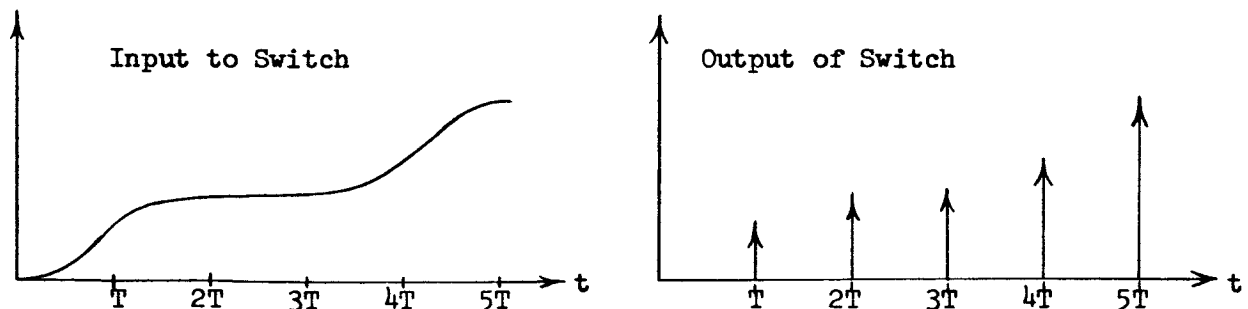


FIGURE 1.18 SAMPLING SWITCH INPUT AND OUTPUT WAVEFORMS

If the input function to the switch is denoted by $f_i(t)$, then the output of the switch (f_o) is given by:

$$f_o(nT) = f_i(nT) \delta(t - nT)$$

where $\delta(t)$ = impulse function

The expressions for $\epsilon\phi(s)$ and $\epsilon\phi^*(s)$ are given by Equations 1.79 and 1.80 below:

$$\epsilon\phi(s) = \frac{1}{sH} G_N(s) - \left(\frac{1}{sH}\right) \frac{L^*(s) \left[\frac{G_N(s)}{sH}\right]^*}{1 + L^*(s) \left(\frac{1}{sH}\right)^*} + \left(\frac{1}{sH}\right) \frac{L^*(s) \Delta\phi_n^*(s)}{1 + L^*(s) \left(\frac{1}{sH}\right)^*} \quad (1.79)$$

$$\epsilon\phi^*(s) = \left[\frac{G_N(s)}{sH}\right]^* - \left(\frac{1}{sH}\right)^* \frac{L^*(s) \left[\frac{G_N(s)}{sH}\right]^*}{1 + L^*(s) \left(\frac{1}{sH}\right)^*} + \left(\frac{1}{sH}\right)^* \frac{L^*(s) \Delta\phi_n^*(s)}{1 + L^*(s) \left(\frac{1}{sH}\right)^*} \quad (1.80)$$

Note that the asterisk (*) denotes the pulse transform.

We can now write the Z transform of $\epsilon\phi(s)$ as follows:

$$\epsilon\phi(Z) = \left[\frac{(Z-1)}{H(Z-1) + ZL(Z)}\right] Z \left[\frac{G_N(s)}{s}\right] + \frac{ZL(Z)}{H(Z-1) + ZL(Z)} \Delta\phi_n(Z) \quad (1.81)$$

1.2.3.1 Removal of Constant Gyro Drift with Star Tracker

In general, the constant, or coherent component of gyro drift, is considerably greater than either the random gyro drift or star tracker noise. If constant gyro drift is removed dynamically (i.e., with the loop configuration shown in Figure 1.17), the drift rate is damped but a constant offset may exist in the platform gimbal angle output unless $L(Z)$ is properly chosen. This may be seen by letting $G_N(s) = \frac{K}{s}$ (i.e., setting G_N equal to a step function corresponds to a constant gyro drift rate) and letting the star tracker noise term $\Delta\phi_n$ go to zero. Inserting these quantities into Equation 1.81 yields,

$$\epsilon\phi(Z) \Big|_{\substack{\text{constant gyro} \\ \text{drift rate}}} = \frac{KTZ}{(Z-1)[H(Z-1) + ZL(Z)]} \quad (1.82)$$

where T = sampling period (i.e., star tracker acquisition time)

Applying the final value theorem to Equation 1.80,

$$\begin{aligned} \lim_{n \rightarrow \infty} \epsilon \phi(nT) &= \lim_{Z \rightarrow 1} \frac{Z-1}{Z} \frac{KTZ}{(Z-1)[H(Z-1) + ZL(Z)]} \\ \lim_{n \rightarrow \infty} \epsilon \phi(nT) &= \lim_{Z \rightarrow 1} \frac{KT}{[H(Z-1) + ZL(Z)]} \end{aligned} \quad (1.83)$$

Thus, it is seen from Equation 1.83 that, if the steady state error $\epsilon \phi(nT)$ is to be zero, the denominator of the right hand side of Equation 1.83 must be of the form:

$$H(Z-1) + ZL(Z) = \frac{F(Z)}{Z-1} \quad (1.84)$$

where $F(Z)$ = polynomial in Z with no roots at $Z = 1$.

Solving for $L(Z)$ from Equation 1.84,

$$L(Z) = \frac{F(Z) - H(Z-1)^2}{Z(Z-1)}$$

Now choosing $F(Z) = aZ$,

$$L(Z) = \frac{-HZ^2 + (a + 2H)Z - H}{Z(Z-1)} \quad (1.85)$$

Note that $L(Z)$ is a physically realizable transfer function. Inserting this value of $L(Z)$ into Equation 1.82 yields:

$$\epsilon \phi(Z) \left| \begin{array}{l} \text{constant gyro} \\ \text{drift rate} \end{array} \right. = \frac{KT}{a} \quad (1.86)$$

Equation 1.86 indicates that the error exists only at the first sampling instant and is zero thereafter assuming that the drift rate remains constant.

Although the proper choice of $L(s)$ has eliminated platform error due to constant gyro drift rate, the platform error due to random gyro drift rate and star tracker noise, or error, remains. Furthermore, by choosing $L(s)$ to eliminate constant gyro drift rate, the platform response to the random error sources will not be optimum. One solution to this problem is to alter $L(s)$ to yield an optimum system by minimizing the platform mean-squared error due to all error sources. Another, perhaps better, solution depending on the particular hardware utilized, is to

let the system operate open loop (i.e., without star tracker correction), determine from the star tracker output the constant gyro drift rate (after the orbital angular rates are removed with the computer), then apply a trim signal to the gyro torquer to eliminate the drift. The star tracker output after being resolved into equivalent rotations about the three inertial axes ($\bar{\gamma}$, \bar{n} , \bar{p}) would exhibit a pattern as shown in Figure 1.19 if there existed a constant gyro drift rate.

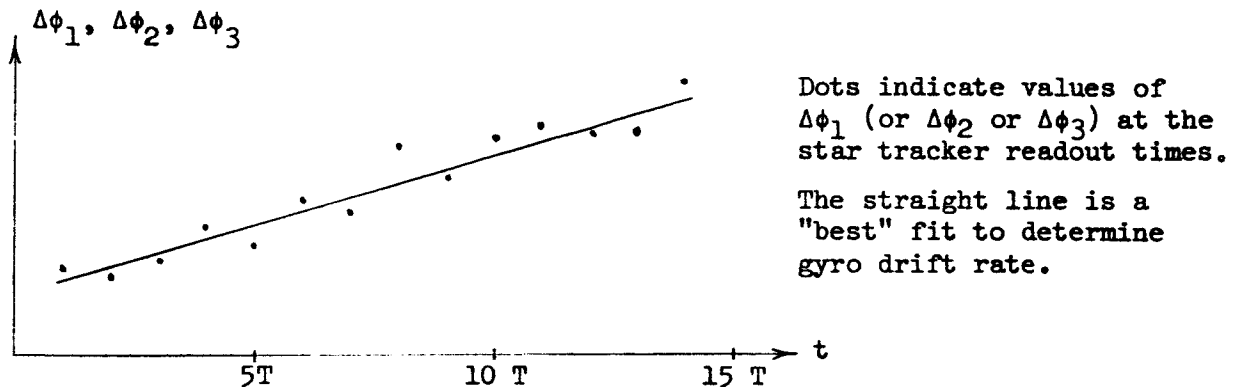


FIGURE 1.19 VARIATION IN STAR TRACKER OUTPUT
DUE TO CONSTANT GYRO DRIFT

Thus, with the system operating open loop, a set of star tracker readouts are stored. Then the data is smoothed by any of the following three methods:

- 1) Least Squares Fit
- 2) Frequency Filtering
- 3) Kalman Filter

The smoothed data yields a straight line fit to the star tracker data. Now a trim signal (derived from the straight line fit) is applied to the gyro torquer to remove the constant component of gyro drift. After the trim signal is applied to the gyro, the loop is closed around the platform with the star tracker as shown in Figure 1.17. With the loop closed the errors due to random error sources become bounded as will be shown below. If the system is operated in this manner, it is necessary to periodically adjust the gyro trim signal since changes in the constant gyro drift rate will tend to occur.

1.2.3.2 Bounding of Random Gyro Drift with Star Tracker

To simplify the following analysis, the filter network $L(s)$ will be assumed to have a constant gain (L). The error model block diagram used to compute the system errors due to gyro drift and tracker error is the same as that shown in Figure 1.17, except for the shifting of the pole at the origin. The pole is shifted into the left half s -plane in order to avoid ambiguities in the correlation function equations of the system. After the mean-squared error of the system is determined, the limit as $a \rightarrow 0$ is taken to yield the true mean-squared system error. The error model block diagram used in the following calculations is shown in Figure 1.20.

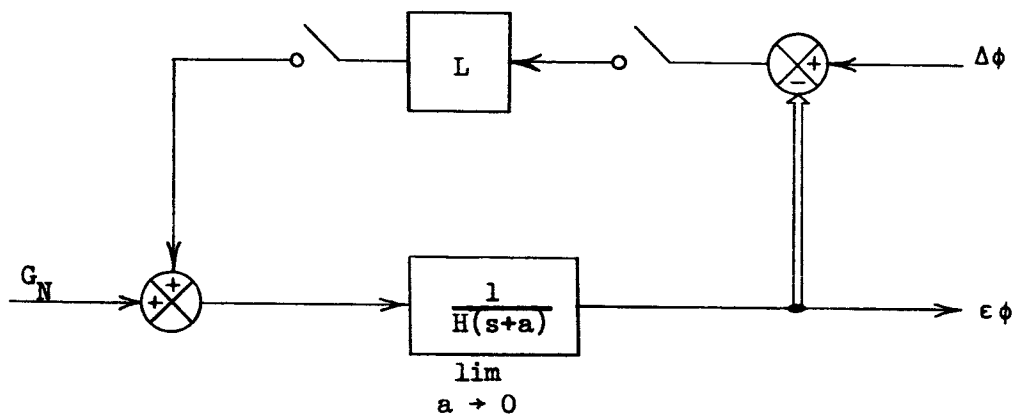


FIGURE 1.20 ERROR MODEL FOR CALCULATION OF RANDOM ERRORS

1.2.3.2.1 Random Gyro Drift Error Calculation: The transfer function relating the platform error, $\epsilon\phi$, to gyro drift, G_N , in terms of the Z -transform is given by:

$$\epsilon\phi(Z) = \frac{Z - e^{-aT}}{(L+H)Z - He^{-aT}} Z \left[\frac{G_N}{(s+a)} \right] \quad (1.87)$$

The system correlation function equation may be written from Equation 1.87 as:

$$R_{\epsilon\phi}(Z) = \left(\frac{Z - e^{-aT}}{(L+H)Z - He^{-aT}} \right) \left(\frac{Z^{-1} - e^{-aT}}{(L+H)Z^{-1} - He^{-aT}} \right) R_{gg}(Z) \quad (1.88)$$

where $R_{gg}(Z)$ is the autocorrelation function of $\frac{G_N}{s+a}$ in the Z -domain.

Assuming the gyro drift noise to be white with a spectral density equal to $\eta_g/2$, we can write $R_{gg}(s)$ as:

$$R_{gg}(s) = \frac{\eta_g/2}{-s+a} = \frac{\eta_g/4a}{s+a} + \frac{\eta_g/4a}{-s+a} \quad (1.89)$$

Now taking the Z-transform of $R_{gg}(s)$:

$$R_{gg}(Z) = \mathcal{Z}[R_{gg}(s)] = \frac{1}{T} \mathcal{Z} \left[R_{gg}^+(s) + R_{gg}^-(s) - R_{gg}(0) \right] \quad (1.90)$$

where $R_{gg}^+(s) = \frac{\eta_g/4a}{s+a}$

$$R_{gg}^-(s) = \frac{\eta_g/4a}{-s+a}$$

$$R_{gg}(0) = \mathcal{L}^{-1} \left[R_{gg}^+(s) \right]_{\tau=0} = \eta_g/4a$$

Substituting these expressions into Equation 1.90 and taking the Z-transform yields:

$$R_{gg}(Z) = \frac{\eta_g}{4aT} \frac{(1 - e^{-2aT})Z}{(Z - e^{-aT})(1 - e^{-aT}Z)} \quad (1.91)$$

Substituting Equation 1.91 into Equation 1.88 and simplifying yields:

$$R_{\epsilon\phi}(Z) = \frac{\eta_g}{4aT(L+H)^2} \frac{(1 - e^{-2aT})Z}{\left(Z - \frac{He^{-aT}}{L+H} \right) \left(1 - \frac{He^{-aT}}{L+H} Z \right)} \quad (1.92)$$

The mean-squared error of the sampled output sequence, $\epsilon\phi^*$, is given by:

$$\begin{aligned} \overline{\epsilon\phi^2} &= \text{Residue of } \left[R_{\epsilon\phi}(Z) Z^{-1} \right]; Z = \frac{He^{-aT}}{L+H} \\ &= \left[\frac{\eta_g}{4aT(L+H)^2} \right] \left[\frac{1 - e^{-2aT}}{1 - \frac{H^2 e^{-2aT}}{(L+H)^2}} \right] \end{aligned} \quad (1.93)$$

The asterisk(*) denotes that the sampled output sequence ($\epsilon\phi$) is implied rather than the continuous output.

Now taking the limit as $a \rightarrow 0$ and multiplying by T in Equation 1.93 yields the final expression for the mean-squared continuous output error due to random gyro drift noise.

$$\overline{\epsilon\phi^2} = \frac{\eta_g T}{2L(L + 2H)} \quad (1.94)$$

Note that, if the feedback term L is reduced to zero (i.e., no star tracker input), the error due to gyro drift becomes infinite.

In general gyro drift may be characterized by specifying the RMS drift rate and the bandwidth. For the gyros used in the ST124-M platform it will be assumed that the random and fixed drift rates are as follows:

$$\text{Random drift (RMS)} = 0.01^\circ/\text{hr} = 0.01 \text{ } \widehat{\text{sec}}/\text{sec}$$

$$\text{Quasi fixed drift} = 0.2^\circ/\text{hr} = 0.2 \text{ } \widehat{\text{sec}}/\text{sec}$$

The torquer noise (G_N) corresponding to a platform drift rate of $0.01 \text{ } \widehat{\text{sec}}/\text{sec}$ RMS is given by:

$$\overline{G_N^2} = \sigma_g^2 = H^2 (0.01 \text{ } \widehat{\text{sec}}/\text{sec})^2$$

The AB5-K8 gyro used on the ST124-M platform has an angular momentum, H , equal to $2.6 \times 10^6 \text{ gm cm}^2/\text{sec}$. Thus σ_g^2 is given by:

$$\sigma_g^2 = (2.6 \times 10^6)^2 (0.01)^2 \frac{\text{gm}^2 \text{ cm}^4 \text{ sec}^2}{\text{sec}^4}$$

$$\sigma_g^2 = 6.76 \times 10^8 \frac{\text{gm}^2 \text{ cm}^4 \text{ sec}^2}{\text{sec}^4}$$

Now assuming the random torque noise to have a frequency distribution given by:

$$|G_N(j\omega)|^2 = \frac{\eta_g/2}{1 + (\omega/\omega_0)^2}$$

The relationship between η_g and σ_g^2 for this type of frequency distribution is:

$$\frac{\eta_g}{2} = \frac{2 \sigma_g^2}{\omega_o}$$

Assuming a bandwidth of 10 cps, $\omega_o = 20\pi$, η_g is given by:

$$\eta_g = \frac{4(6.76 \times 10^8)}{20 \pi} \frac{\text{gm}^2 \text{ cm}^4 \text{ sec}^2}{\text{sec}^3}$$

$$\eta_g = 0.43 \times 10^8 \frac{\text{gm}^2 \text{ cm}^4 \text{ sec}^2}{\text{sec}^3}$$

Substituting this value of η_g into Equation 1.94 yields:

$$\overline{\epsilon \phi^2} = \frac{0.43 \times 10^8 T}{2L(L + 5.2 \times 10^6)} \text{ sec}^2 \quad (1.95)$$

In order to determine the numerical value of $\overline{\epsilon \phi^2}$ it is necessary to select the values for T and L. If reasonably accurate data were available for the various dynamic platform inputs, L [or L(s)] could be chosen by using an optimum synthesis technique such as the Wiener method modified for sampled data systems. Since such data is not at present available, L will be chosen equal to H such that the correction signal from the star tracker reflects as a one-to-one rotation of the platform. The period, T, between star tracker correction inputs is dependent upon the type of star tracker employed and whether one or two star trackers are available. Assuming that a vidicon tracker with a field of view equal to 30 min x 15 min. is used, the values of T for two consecutive star shots with one star tracker and for two simultaneous star shots with two star trackers are given as:

$$T (2 \text{ star trackers}) = 5.0 \text{ sec.}$$

$$T (1 \text{ star tracker}) = 5 + 5 + 5 = 15 \text{ sec.}$$

It is assumed that 5 seconds are required to slew the star tracker to the second star. Inserting these quantities into Equation 1.95, the mean-squared platform error due to random gyro drift becomes:

$$\overline{\epsilon\phi^2} \text{ (2 star trackers)} = 0.053 \times 10^{-4} \text{ sec}^2 \quad (1.96a)$$

$$\epsilon\phi \text{ (2 star trackers)}_{\text{RMS}} = 0.0023 \text{ sec} \quad (1.96b)$$

$$\overline{\epsilon\phi^2} \text{ (1 star tracker)} = 0.16 \times 10^{-4} \text{ sec}^2 \quad (1.96c)$$

$$\epsilon\phi \text{ (1 star tracker)}_{\text{RMS}} = 0.004 \text{ sec} \quad (1.96d)$$

Thus the star tracker results in a negligible amount of platform error due to random gyro drift.

1.2.3.2.2 Fixed Platform Drift Errors: Now consider the platform error due to quasi fixed drift. The torquer noise that characterizes this type of drift is given by:

$$G_N \text{ (fixed drift)} = \frac{(0.2 \text{ sec/sec})H}{s}$$

The expression for $\epsilon\phi$ in terms of G_N is given by (note that the pole "a" is set equal to zero since it is not necessary to use correlation functions for fixed drift):

$$\begin{aligned} \epsilon\phi(Z) &= \frac{Z-1}{(L+H)Z-H} Z \left[\frac{0.2 H}{s^2} \right] \\ \epsilon\phi(Z) &= \left[\frac{0.2 H T}{L+H} \right] \left[\frac{Z}{\left(Z - \frac{H}{L+H} \right) (Z-1)} \right] \end{aligned} \quad (1.97)$$

Applying the final value theorem for the Z-transform to Equation 1.97 yields the steady state platform error:

$$\epsilon\phi(\text{steady state}) = \lim_{Z \rightarrow 1} \frac{Z-1}{Z} \left[\frac{0.2 H T}{L+H} \right] \left[\frac{Z}{\left(Z - \frac{H}{L+H} \right) (Z-1)} \right]$$

For $L = H$ this becomes,

$$\epsilon\phi(\text{steady state}) = 0.2 T \text{ sec}$$

Now using $T = 5$ sec. for two star trackers and $T = 15$ sec. for one star tracker, the fixed drift platform errors are:

$$\epsilon\phi \text{ (2 star trackers)} = 1.0 \text{ sec} \quad (1.98a)$$

$$\epsilon\phi \text{ (1 star tracker)} = 3.0 \text{ sec} \quad (1.98b)$$

1.2.3.3 Platform Error Due To Star Tracker Error

A star tracker error torques the platform as does the star tracker correction signal. The error that is reflected into the platform angle due to star tracker error is dependent upon the statistics of the star tracker error source. For purposes of analysis, a vidicon star tracker will be assumed to be used in the system, since performance information for this type of star tracker is readily available. With a vidicon star tracker, the error is dependent upon the location of the star image in the field of view of the tracker, which results from the fact that the major sources of error in the vidicon star tracker are coherent rather than random in nature. The predominant errors in the vidicon star tracker are 1) scanning sweep non-linearity, 2) quantizing errors, and 3) mechanical misalignment errors. Thus, the error input to the platform loop from the star tracker will consist of a series of impulses that are fixed for a period of time. The period of time that the amplitude of the error impulses remain fixed is dependent upon the specific tracking format. As a first order approximation, it will be assumed that the period of fixed amplitude error impulses is long with respect to the time constant of the loop. Figure 1.21 illustrates a typical star tracker error pattern.

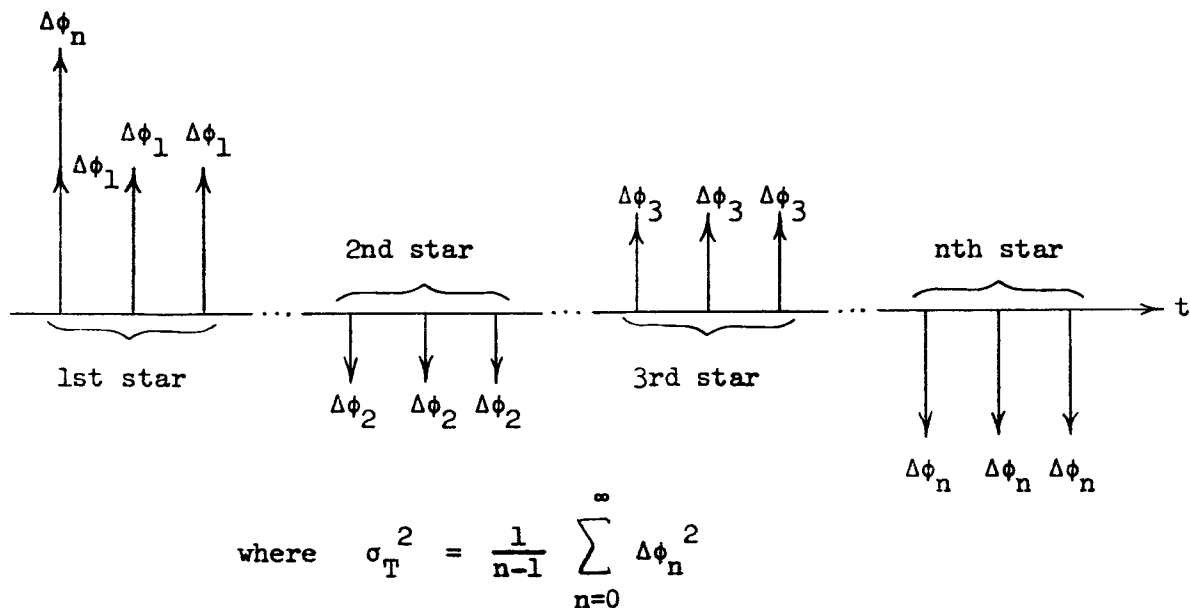


FIGURE 1.21 VIDICON STAR TRACKER ERROR PROFILE

The transfer function between the star tracker error input, $\Delta\phi$, and the platform angle output, $\epsilon\phi$, is given in terms of the Z-transform as:

$$\epsilon\phi(Z) = \frac{ZL}{(L+H)Z - H} \Delta\phi(Z)$$

Now for $L = H$ and $\Delta\phi(Z)$ represented by a train of impulses of RMS amplitude σ_T over a period of time which is long with respect to T , the platform output error is given by:

$$\epsilon\phi = \frac{1}{2} \left[\frac{Z}{Z-1/2} \right] \left[\frac{\sigma_T Z}{Z-1} \right] = \frac{\sigma_T}{2} \left[\frac{Z^2}{(Z-1/2)(Z-1)} \right] \quad (1.99)$$

Applying the final value theorem to obtain the steady-state value of $\epsilon\phi$ yields:

$$\begin{aligned} \epsilon\phi \text{ (steady state)} &= \lim_{Z \rightarrow 1} \frac{Z-1}{Z} \left[\frac{\sigma_T}{2} \right] \left[\frac{Z^2}{(Z-1/2)(Z-1)} \right] \\ \epsilon\phi \text{ (steady state)} &= \sigma_T \end{aligned} \quad (1.100)$$

Thus, the star tracker error reflects directly into an error in platform angle for the particular circumstances given above.

1.2.3.4 Final Platform Angle Error

The final platform angle error is a root-sum-square summation of the following error sources:

- 1) Random Gyro Drift Error -- $\overline{\epsilon\phi_g^2}$ -- given by Equations 1.96a through 1.96d.
- 2) Quasi-Fixed Gyro Drift -- $\overline{\epsilon\phi_d^2}$ -- given by Equations 1.98 a and 1.98b.
- 3) Star Tracker Error -- $\overline{\epsilon\phi_s^2}$ -- given functionally by Equation 1.100 and numerically in Section 1.3.
- 4) Star Tracker Gimbal Pickoff Error -- $\overline{\epsilon\phi_{ps}^2}$ -- given in Section 1.3.
- 5) Platform Gimbal Pickoff Error (this only applies if the star tracker(s) is located off the platform) -- $\overline{\epsilon\phi_p^2}$ -- given in Section 1.3.
- 6) Craft Flexure Errors (This only applies if the star tracker(s) is located off the platform.) -- $\overline{\epsilon\phi_f^2}$ -- given in Section 1.3.

The final platform gimbal error is given by:

$$\left(\overline{\epsilon \phi^2} \right)^{1/2} = \left[\overline{\epsilon \phi_g^2} + \overline{\epsilon \phi_d^2} + \overline{\epsilon \phi_s^2} + \overline{\epsilon \phi_{ps}^2} + \overline{\epsilon \phi_p^2} + \overline{\epsilon \phi_f^2} \right]^{1/2} \quad (1.101)$$

Tables 1.1 through 1.5 present a summary of the platform gimbal angle errors for various system configurations. The star tracker errors are based upon a two-star fix with the celestial angles of the stars given by: δ_1 (declination) = 45° , SHA_1 (Sidereal Hour Angle) = 90° , $\delta_2 = 45^\circ$, $SHA_2 = 45^\circ$. Details about the star tracker errors, pickoff errors, and craft flexure errors may be found in Section 1.3.

TABLE 1.1 ONE STAR TRACKER MOUNTED ON THE PLATFORM

ERROR SOURCES	GIMBAL ERROR		
	OUTER	MIDDLE	INNER
	$(\epsilon \phi_1)_{RMS}$	$(\epsilon \phi_2)_{RMS}$	$(\epsilon \phi_3)_{RMS}$
	sec.	sec.	sec.
Random Gyro Drift	0.004	0.004	0.004
Quasi Fixed Gyro Drift	3.0	3.0	3.0
Star tracker Error for 2 star fix, including tracker's gimbal pick-off error.	14.2	8.2	18.3
Platform Gimbal Pickoff Error	N.A.	N.A.	N.A.
Craft Flexure Error	N.A.	N.A.	N.A.
Net RSS Error	14.5	8.8	18.6

N.A. - not applicable

TABLE 1.2 ONE STAR TRACKER OFF THE PLATFORM (NO CRAFT FLEXURE)

ERROR SOURCES	GIMBAL ERROR		
	OUTER	MIDDLE	INNER
	$(\epsilon\phi_1)_{\text{RMS}}$	$(\epsilon\phi_2)_{\text{RMS}}$	$(\epsilon\phi_3)_{\text{RMS}}$
	sec	sec	sec
Random Gyro Drift	0.004	0.004	0.004
Quasi Fixed Gyro Drift	3.0	3.0	3.0
Star Tracker Error - for 2 star fix, including tracker's gimbal pickoff error	14.2	8.2	18.3
Platform Gimbal Pickoff Error	6.5	6.5	6.5
Craft Flexure Error	N.A.	N.A.	N.A.
Net RSS Error	15.9	10.9	19.6

TABLE 1.3 ONE STAR TRACKER OFF THE PLATFORM (WITH CRAFT FLEXURE)

Random Gyro Drift	0.004	0.004	0.004
Quasi Fixed Gyro Drift	3.0	3.0	3.0
Star Tracker Error - for 2 star fix, including tracker's gimbal pickoff error	14.2	8.2	18.3
Platform Gimbal Pickoff Error	6.5	6.5	6.5
Craft Flexure Error	$\epsilon\phi_{f1}$	$\epsilon\phi_{f2}$	$\epsilon\phi_{f3}$
Net RSS Error	$(253.2 + \epsilon\phi_{f1}^2)^{1/2}$	$(118.4 + \epsilon\phi_{f2}^2)^{1/2}$	$(386.2 + \epsilon\phi_{f3}^2)^{1/2}$

TABLE 1.4 TWO STAR TRACKERS OFF THE PLATFORM (NO CRAFT FLEXURE)

ERROR SOURCES	GIMBAL ERROR		
	OUTER	MIDDLE	INNER
	$(\epsilon\phi_1)$ RMS	$(\epsilon\phi_2)$ RMS	$(\epsilon\phi_3)$ RMS
	sec	sec	sec
Random Gyro Drift	0.0023	0.0023	0.0023
Quasi Fixed Gyro Drift	1.0	1.0	1.0
Star Tracker Error - for 2 star fix, including tracker's gimbal pickoff error	14.2	8.2	18.3
Platform Gimbal Pickoff Error	6.5	6.5	6.5
Craft Flexure Error	N.A.	N.A.	N.A.
Net RSS Error	15.7	10.5	19.4

TABLE 1.5 TWO STAR TRACKERS OFF THE PLATFORM (WITH CRAFT FLEXURE)

Random Gyro Drift	0.0023	0.0023	0.0023
Quasi Fixed Gyro Drift	1.0	1.0	1.0
Star Tracker Error - for 2 star fix, including tracker's gimbal pickoff error	14.2	8.2	18.3
Platform Gimbal Pickoff Error	6.5	6.5	6.5
Craft Flexure Error	$\epsilon\phi_{f1}$	$\epsilon\phi_{f2}$	$\epsilon\phi_{f3}$
Net RSS Error	$(245.2 + \epsilon\phi_{f1}^2)^{1/2}$	$(110.4 + \epsilon\phi_{f2}^2)^{1/2}$	$(378.2 + \epsilon\phi_{f3}^2)^{1/2}$

1.2.4 Computer Function C_3 (Relationship Between Craft Attitude and Inertial Space)

Computer function C_3 is essentially a matrix relationship that relates the craft attitude to inertial space. The angles of rotation between the craft triad and the inertial triad are derived from gimbal pickoffs (or from the gyro outputs if a strapped-down configuration is used.)

Denoting the craft triad by $(\bar{i}_c, \bar{j}_c, \bar{k}_c)$ and the inertial triad by $(\bar{\gamma}, \bar{n}, \bar{p})$ the relationship between the two triads is given by:

$$\begin{bmatrix} \bar{\gamma} \\ \bar{n} \\ \bar{p} \end{bmatrix} = \begin{bmatrix} M_1 \\ M_F \end{bmatrix} \begin{bmatrix} \bar{i}_c \\ \bar{j}_c \\ \bar{k}_c \end{bmatrix} \quad (1.102)$$

where the matrix $[M_1]$ is given by:

(1.103)

$$[M_1] = \begin{bmatrix} \cos \phi_2 \cos \phi_3 & \begin{pmatrix} \sin \phi_1 \sin \phi_2 \cos \phi_3 + \\ \cos \phi_1 \sin \phi_3 \end{pmatrix} & \begin{pmatrix} \sin \phi_1 \sin \phi_3 - \\ \cos \phi_1 \sin \phi_2 \cos \phi_3 \end{pmatrix} \\ -\cos \phi_2 \sin \phi_3 & \begin{pmatrix} \cos \phi_1 \cos \phi_3 - \\ \sin \phi_1 \sin \phi_2 \sin \phi_3 \end{pmatrix} & \begin{pmatrix} \sin \phi_1 \cos \phi_3 + \\ \cos \phi_1 \sin \phi_2 \sin \phi_3 \end{pmatrix} \\ \sin \phi_2 & -\sin \phi_1 \cos \phi_2 & \cos \phi_1 \cos \phi_2 \end{bmatrix}$$

The angles ϕ_1 , ϕ_2 , and ϕ_3 are the gimbal angles with respect to their null position.

The matrix $[M_F]$ is the fixed relationship (neglecting craft flexure) between the craft and the platform gimbals when they are caged to a null position.

1.2.5 Computer Function C_4 (Local Vertical Determination)

The purpose of computer function C_4 is to process the Horizon Sensor output to improve the accuracy of the local vertical determination. Some of the functions performed by the computer would be averaging of the Horizon Sensor output over several orbits, to compensate for errors due to weather and climatic effects, and determination of the local

vertical, allowing for the earth oblateness and other horizon anomalies. The two-axis gimbal system is slaved to the Horizon Scanner output such that the orbital gyro compass is maintained in a vertical position with respect to the earth's surface. The local vertical vector (\overline{LV}) is defined by:

$$\overline{LV} = \cos \theta_1 \overline{i_c} + \cos \theta_2 \overline{j_c} + \cos \theta_3 \overline{k_c} \quad (1.104)$$

1.2.6 Computer Function C_5 (Craft Position Determination)

Computer function C_5 is used to compute the craft's position with respect to earth.

The local vertical vector (\overline{LV}) may be written in terms of the craft triad as given by the Horizon Scanner (see Equation 1.104) or in terms of earth coordinates, $GHA\gamma$, and the inertial triad ($\overline{\gamma}$, \overline{n} , \overline{p}) as follows:

$$\overline{LV} = \cos L \cos(L_0 + GHA\gamma) \overline{\gamma} - \cos L \sin(L_0 + GHA\gamma) \overline{n} + \sin L \overline{p} \quad (1.105)$$

where:

L = latitude

L_0 = longitude measured west of Greenwich

$GHA\gamma$ = angle between the Greenwich meridian and the meridian that passes through the first point of Aries. This quantity would be supplied by a clock aboard the space-craft that reads absolute time.

Now we can solve for the craft triad ($\overline{i_c}$, $\overline{j_c}$, $\overline{k_c}$) in terms of the inertial triad ($\overline{\gamma}$, \overline{n} , \overline{p}) by inverting the matrix relationship in Equation 1.102.

$$\begin{bmatrix} \overline{i_c} \\ \overline{j_c} \\ \overline{k_c} \end{bmatrix} = \begin{pmatrix} [M_1] & [M_F] \end{pmatrix}^{-1} \begin{bmatrix} \overline{\gamma} \\ \overline{n} \\ \overline{p} \end{bmatrix} \quad (1.106)$$

Substituting Equation 1.106 into 1.105 yields,

$$\overline{LV} = f_1 \overline{\gamma} + f_2 \overline{n} + f_3 \overline{p} \quad (1.107)$$

where: f_1, f_2 , and f_3 = functions of $\theta_1, \theta_2, \theta_3$ and the transformation angles between the craft and inertial space.

Now equating coefficients of $\bar{\gamma}$, \bar{n} , and \bar{p} for Equations 1.105 and 1.107 results in the following expressions:

$$\cos L \cos(L_0 + GHAY) = f_1 \quad (1.108a)$$

$$-\cos L \sin(L_0 + GHAY) = f_2 \quad (1.108b)$$

$$\sin L = f_3 \quad (1.108c)$$

Solving these equations for latitude (L) and longitude (L_0) yields the subpoint of the spacecraft or earth:

$$L = \sin^{-1} f_3 \quad (1.109)$$

$$L_0 = \tan^{-1} \left[\frac{\tan GHAY + f_2 / f_1}{\tan GHAY - 1} \right] \quad (1.110)$$

1.2.7 Computer Function C_6 (Spacecraft Altitude)

The angular subtense of the earth as measured by the Horizon Scanner is a direct measure of the instantaneous altitude of the spacecraft with respect to earth. The basic relationship between altitude and angular subtense is given by:

$$\text{Altitude} = R \left(\frac{1 - \sin \psi/2}{\sin \psi/2} \right) \quad (1.111)$$

where: R = radius of the earth

ψ = angular subtense of the earth as measured by the horizon scanner

If an accurate altitude reading is necessary, then R and ψ must be corrected for any geophysical distortion effects.

1.2.8 Computer Function C_7 (Initial Conditions For Horizon Scanner)

Since the Horizon Scanner gimbal system cannot position itself until after it has acquired the earth, it is necessary to initially position it with inputs from the Inertial Platform. These inputs are processed by computer function C_7 .

1.2.9 Computer Function C_8 (Spacecraft Attitude With Respect To Earth)

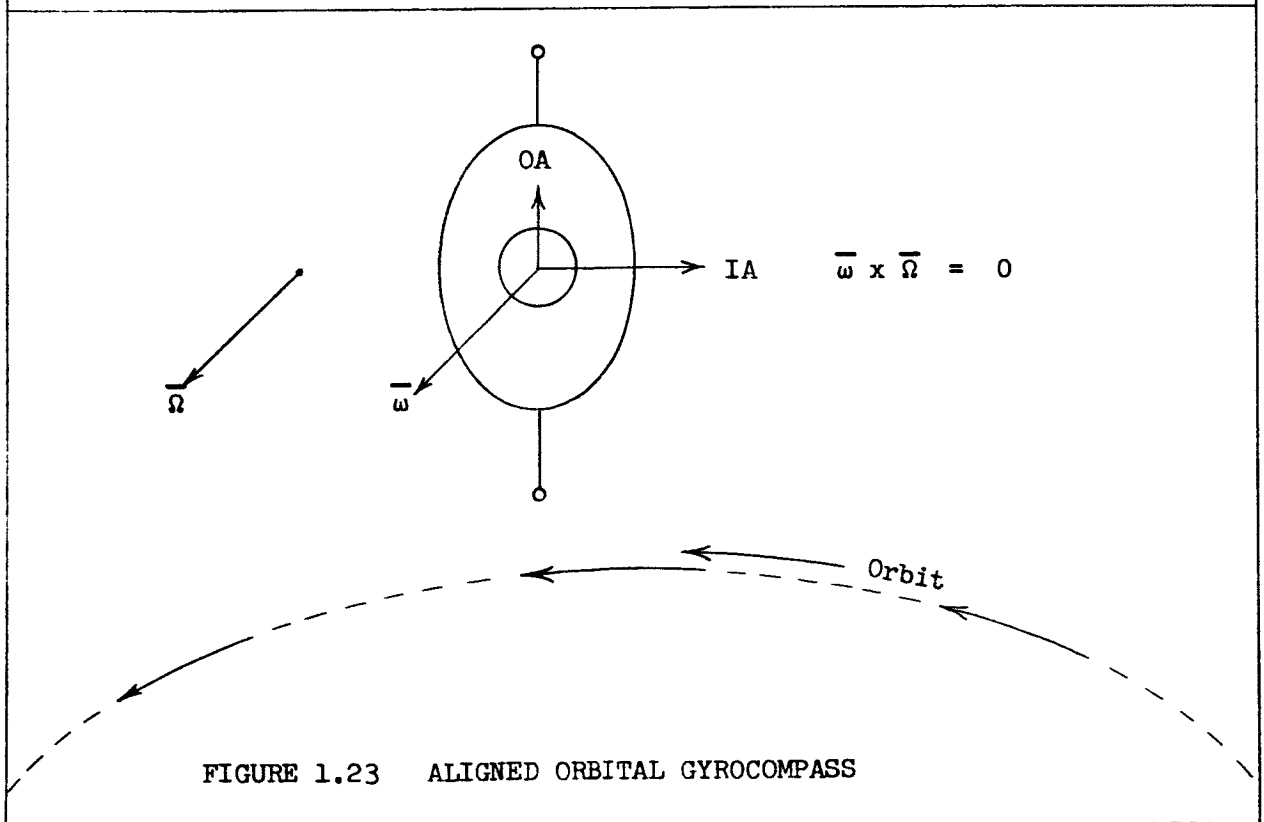
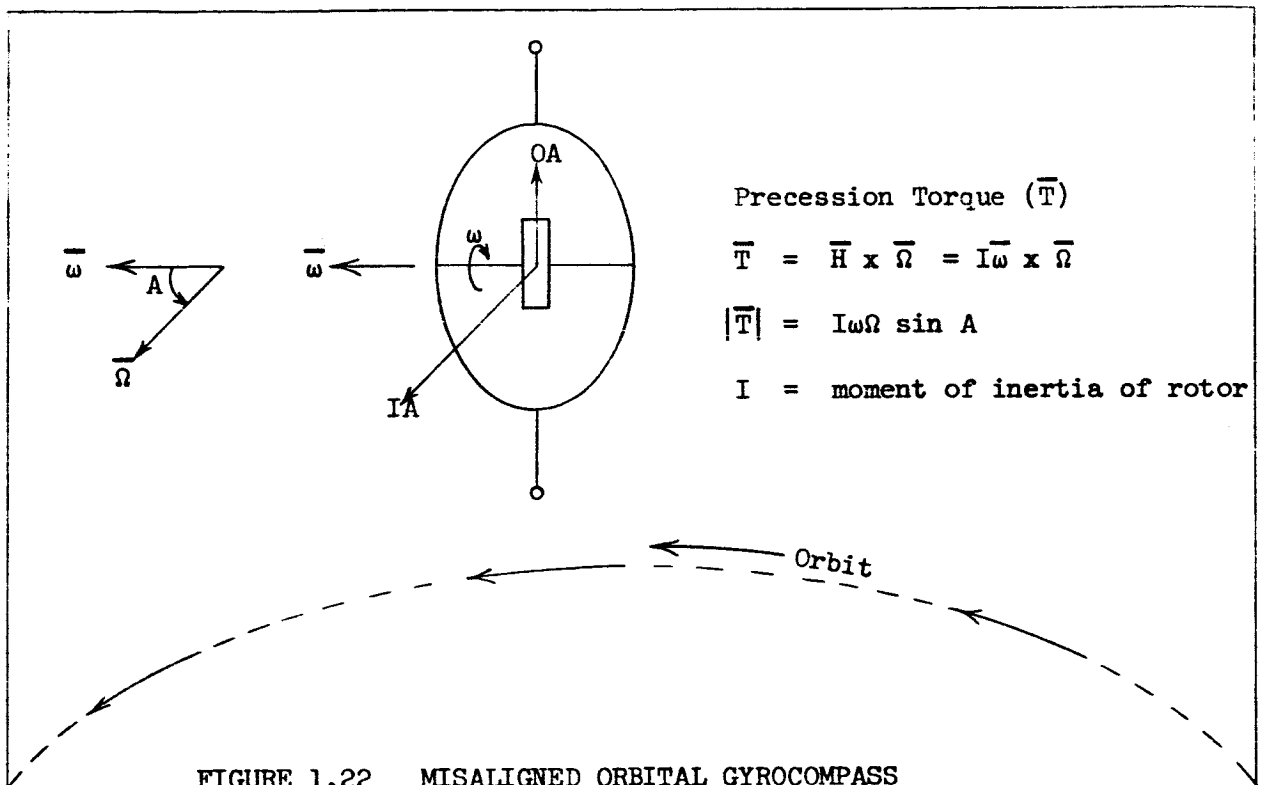
Since the Horizon Scanner effectively defines the orientation of the spacecraft with respect to a line connecting the center of the earth and the spacecraft, the only other information required to completely specify the attitude of the spacecraft with respect to earth is the heading angle. An orbital gyro compass may be used to determine the attitude of the spacecraft with respect to its trajectory.

1.2.9.1 Orbital Gyrocompass

The orbital gyrocompass consists of a rate integrating gyro whose gimbal axis is slaved to the local vertical. This is accomplished by mounting the gyro on a two-gimbal servo that is slaved to the local vertical by outputs from the Horizon Scanner. Now, if the spin axis (SA) of the gyro rotor is misaligned with the orbital angular velocity vector $\bar{\Omega}$, then a torque about the gyro output axis (OA) will cause the gyro to precess until its spin axis coincides with the orbital angular velocity vector $\bar{\Omega}$. The gyro senses the orbital angular velocity because the Horizon Scanner output causes a rotation about the gyro input axis, when the gyro is misaligned, in order to maintain gyro gimbal axis parallel to the local vertical. Figures 1.22 and 1.23 show a misaligned and an aligned gyro respectively.

Note that Ω is the time derivative of the orbit angle.

If the gyro is just allowed to precess until $\bar{\omega}$ is parallel to $\bar{\Omega}$, the gyro will oscillate about null. Thus the gyro output is used to torque a platform gimbal to null. A block diagram of a gyro precessing to null without a gimbal is shown in Figure 1.24.



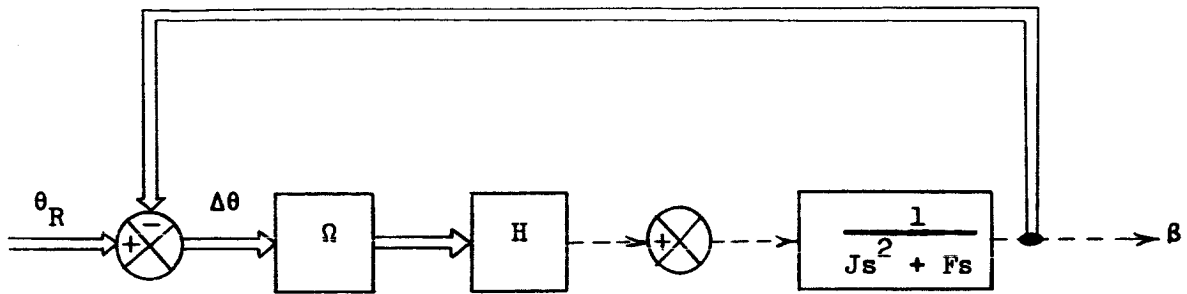


FIGURE 1.24 BLOCK DIAGRAM OF ORBITAL GYROCOMPASS
(NOT GIMBAL MOUNTED) PRECESSING TO NULL

where:

Ω = magnitude of orbital angular velocity

θ_R = orbit heading reference angle

β = gyro gimbal angle

$\Delta\theta = \sin \Delta\theta = \sin (\theta_R - \beta)$

The transfer function $\Delta\theta/\theta_R$ (assuming the system to be near null so that $\sin \Delta\theta \approx \Delta\theta$) is given by:

$$\frac{\Delta\theta}{\theta_R} = \frac{\Omega H/J}{s^2 + s \frac{F}{J} + \frac{\Omega H}{J}} \quad (1.112)$$

If F is small as is the case for a gas bearing gyro, then the loop will oscillate about null with a period given approximately by:

$$T_{\text{Oscillation}} = 2\pi \sqrt{\frac{J}{\Omega H}} \quad (1.113)$$

In order to damp the oscillation the gyro is mounted on a heading gimbal which is torqued by the signal from the gyro pickoff. Thus the heading gimbal pickoff indicates the direction of the spacecraft heading axis with respect to the orbit trajectory. Figure 1.25 shows a block diagram of an orbital gyrocompass with the gyro mounted in a heading gimbal. Note that the counter torque (βH) about the input axis due to the precession of the gyro about its output axis is not shown since it is assumed that the Horizon Scanner overrides this torque and maintains the gyro vertical.

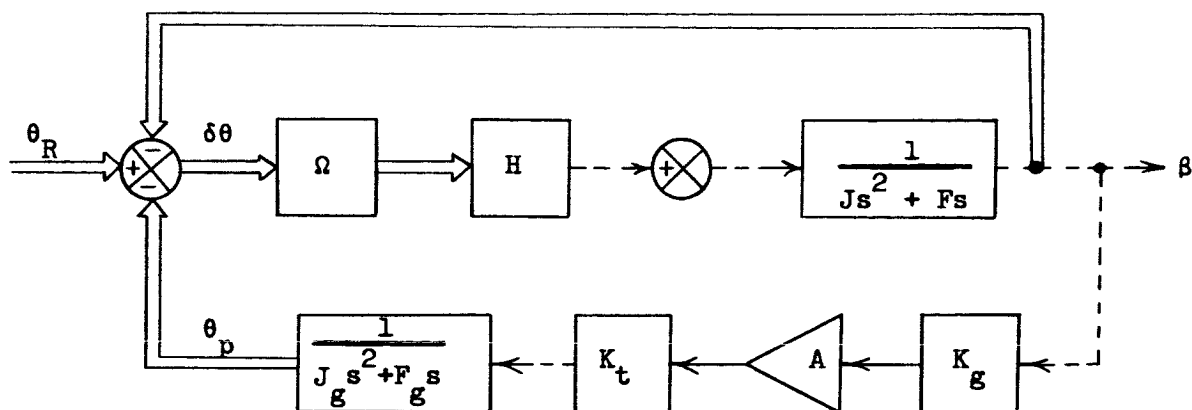


FIGURE 1.25 BLOCK DIAGRAM OF GIMBAL MOUNTED ORBITAL GYROCOMPASS

where:

- θ_p = heading gimbal angle
- $\delta\theta = \theta_R - \beta - \theta_p = \sin(\theta_R - \beta - \theta_p)$
- K_g = gyro pickoff
- A = amplifier gain
- K_t = heading gimbal torquer scale factor
- J_g, F_g = heading gimbal inertia and friction respectively

The signal flow graph for the system shown in Figure 1.25 is given in Figure 1.26.

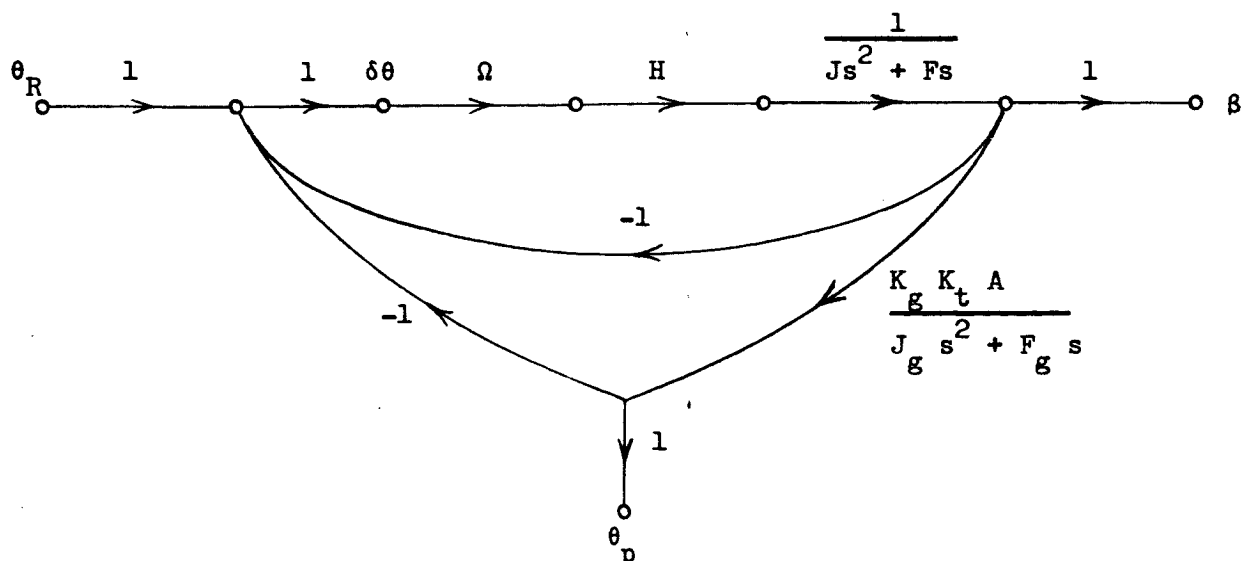


FIGURE 1.26 SIGNAL FLOW GRAPH FOR GIMBAL MOUNTED ORBITAL GYROCOMPASS

The following transfer functions may be written directly from Figure 1.26.

$$\frac{\delta\theta}{\theta_R} = \frac{s^2 (s + F/J)(s + F/J)}{s^4 + s^3 \left(\frac{F}{J} + \frac{F}{J} \right) + s^2 \left(\frac{FF}{JJ} + \frac{\Omega H}{J} \right) + s \frac{\Omega HF}{JJ} + \frac{\Omega H K K_t A}{JJ}} \quad (1.114)$$

$$\frac{\beta}{\theta_R} = \frac{\Omega H s (s + F/J) / J}{s^4 + s^3 \left(\frac{F}{J} + \frac{F}{J} \right) + s^2 \left(\frac{FF}{JJ} + \frac{\Omega H}{J} \right) + s \frac{\Omega HF}{JJ} + \frac{\Omega H K K_t A}{JJ}} \quad (1.115)$$

$$\frac{\theta_p}{\theta_R} = \frac{\frac{\Omega H K K_t A}{JJ}}{s^4 + s^3 \left(\frac{F}{J} + \frac{F}{J} \right) + s^2 \left(\frac{FF}{JJ} + \frac{\Omega H}{J} \right) + s \frac{\Omega HF}{JJ} + \frac{\Omega H K K_t A}{JJ}} \quad (1.116)$$

Now letting $\theta_R(s)$ be a step function, which corresponds to a difference between the heading gimbal angle and the craft heading, and using the final value theorem to obtain the steady-state values of $\delta\theta$, β , and θ_p :

$$\delta\theta \text{ (steady state)} \left| \begin{array}{l} \theta_R(s) = \frac{\theta_R}{s} \end{array} \right. = 0 \quad (1.117a)$$

$$\beta \text{ (steady state)} \left| \begin{array}{l} \theta_R(s) = \frac{\theta_R}{s} \end{array} \right. = 0 \quad (1.117b)$$

$$\theta_p \text{ (steady state)} \left| \begin{array}{l} \theta_R(s) = \frac{\theta_R}{s} \end{array} \right. = \theta_R \quad (1.117c)$$

The heading gimbal angle corresponds to the craft heading angle as shown in Equation 1.117c. The heading angle together with the local vertical vector (\bar{LV}) define the attitude of the spacecraft with respect to earth.

1.2.10 Summary and Conclusions - Orbital Guidance and Navigational System

In the foregoing analysis it was shown that an inertial platform referenced to an inertial triad together with one or two star trackers can provide a navigational or guidance inertial reference whose error is bounded. An inertial system with no star tracker, on the other hand, has an error characteristic that is unbounded. Thus for long term missions, such as the earth orbital type intended for this system, a star tracker is necessary unless other means of position fixing such as earth-based trackers are employed. Note, however, that position fixes derived from earth-based tracking systems cannot provide any attitude information.

The inertial platform gimbal angle errors are shown to be in the range between approximately 10 to 20 arc seconds, depending upon the particular system configuration, if no craft flexure exists between the inertial platform and the star tracker. Different astro-inertial system configurations that are feasible include locating the star tracker on or off the platform and having one or two star trackers. In addition, if a star tracker capable of rapid acquisition such as the vidicon star tracker is used, then the errors due to random and fixed gyro drift are small, compared to the gimbal pickoff errors and the star tracker error.

The addition of a horizon sensor and a gyro compass to the inertial platform and star tracker provides a capability to permit the determination of the position and attitude of the spacecraft with respect to earth.

1.3 COMPARISON OF STATIC POINTING ACCURACY FOR STAR TRACKER MOUNTED ON AND OFF THE PLATFORM

The static pointing accuracy of a star tracker used as an alignment reference for a stellar monitored inertial measurement unit is considered for three star tracker mounting configurations. These include:

1. Star tracker mounted directly on the platform
2. Star tracker mounted on the spacecraft superstructure, adjacent to the platform, so that no craft flexure error is introduced.
3. Star tracker mounted on the spacecraft superstructure, remote from the platform, so that craft flexure errors are significant.

The equations that relate the different sources of error for the three different cases are derived, then the static pointing accuracy is determined for a representative stellar-inertial system. Assumptions made in this system are:

1. Star tracker accuracy -- 5 arc-sec. rms
2. Resolver (platform and star tracker gimbals)
Accuracy -- ± 10 arc-sec. peak-to-peak
Excitation frequency -- 1016 hz
Multipole element -- 64-pole; 32 cycle
Phase readout -- Double angle encoding
3. Digital angle quantizing
Clock rate -- 2.048 M.hz.
4. Platform initial alignment error, and platform drift corrected by closing the platform control loop about the star tracker.
5. Star sightings made at several different angles relative to the platform triad.

1.3.1 Derivation of Error Equations

1.1.3.1 Preliminary Definitions

$\phi_{1a}, \phi_{2a}, \phi_{3a}$ = true platform gimbal angles (ϕ_{1a} = outer gimbal, ϕ_{2a} = middle gimbal, and ϕ_{3a} = inner gimbal.)

$\delta_1, \text{SHA}_1 (A_1)$ = first star's angles as read out by the star tracker

$\delta_2, \text{SHA}_2 (A_2)$ = second star's angles as read out by the star tracker

$\Delta\delta_1, \Delta\delta_2, \Delta A_1, \Delta A_2$ = difference between commanded and star tracker output star pointing angles

$\Delta\phi_{1c}, \Delta\phi_{2c}, \Delta\phi_{3c}$ = star tracker corrections to platform gimbal angles

The following sets of equations relating the star tracker outputs to the platform correction angles are derived in Section 1.1.

$$\Delta\delta_1 \approx \Delta\phi_{1c} \cos A_1 - \Delta\phi_{2c} \sin A_1 \quad (1.118a)$$

$$\Delta A_1 \approx (\Delta\phi_{1c} \sin A_1 + \Delta\phi_{2c} \cos A_1) \tan \delta_1 - \Delta\phi_{3c} \quad (1.118b)$$

$$\Delta\delta_2 \approx \Delta\phi_{1c} \cos A_2 - \Delta\phi_{2c} \sin A_2 \quad (1.118c)$$

$$\Delta A_2 \approx (\Delta\phi_{1c} \sin A_2 + \Delta\phi_{2c} \cos A_2) \tan \delta_2 - \Delta\phi_{3c} \quad (1.118d)$$

Solving these equations for $\Delta\phi_{1c}$, $\Delta\phi_{2c}$, and $\Delta\phi_{3c}$ yields:

$$\Delta\phi_{1c} = - \frac{\sin A_2}{\sin(A_1 - A_2)} \Delta\delta_1 + \frac{\sin A_1}{\sin(A_1 - A_2)} \Delta\delta_2 \quad (1.119a)$$

$$\Delta\phi_{2c} = - \frac{\cos A_2}{\sin(A_1 - A_2)} \Delta\delta_1 + \frac{\cos A_1}{\sin(A_1 - A_2)} \Delta\delta_2 \quad (1.119b)$$

$$\Delta\phi_{3c} = [- \Delta\delta_1 \cot(A_1 - A_2) + \Delta\delta_2 \csc(A_1 - A_2)] \tan \delta_1 - \Delta A_1 \quad (1.119c)$$

OR:

$$\Delta\phi_{3c} = [- \Delta\delta_1 \csc(A_1 - A_2) + \Delta\delta_2 \cot(A_1 - A_2)] \tan \delta_2 - \Delta A_2 \quad (1.119d)$$

1.3.1.2 Case 1 - Tracker on Platform

The sources of static system error with the tracker mounted on the platform are 1) inherent tracker error and 2) tracker gimbal pickoff errors. Defining the following:

$\epsilon\delta$ and $\epsilon A \sec \delta$ = tracker error in declination and SHA(A) respectively

ϵ_{tp} = tracker gimbal pickoff error

Thus let:

$$\Delta\delta_1 = \Delta\delta_1' + \epsilon\delta_1 + \epsilon_{tp_1} \quad (1.120a)$$

$$\Delta\delta_2 = \Delta\delta_2' + \epsilon\delta_2 + \epsilon_{tp_2} \quad (1.120b)$$

$$\Delta A_1 = \Delta A_1' + \epsilon A_1 \sec \delta_1 + \epsilon_{tp_3} \quad (1.120c)$$

$$\Delta A_2 = \Delta A_2' + \epsilon A_2 \sec \delta_2 + \epsilon_{tp_4} \quad (1.120d)$$

where $\Delta\delta_1'$, $\Delta\delta_2'$, $\Delta A_1'$, $\Delta A_2'$ = the true angular differences between computed and measured δ and SHA

Also let:

$$\Delta\phi_{1c} = \Delta\phi_{1c}' + \epsilon\phi_1 \quad (1.121a)$$

$$\Delta\phi_{2c} = \Delta\phi_{2c}' + \epsilon\phi_2 \quad (1.121b)$$

$$\Delta\phi_{3c} = \Delta\phi_{3c}' + \epsilon\phi_3 \quad (1.121c)$$

where $\Delta\phi_{1c}'$, $\Delta\phi_{2c}'$, $\Delta\phi_{3c}'$ = the true platform correction angles

$\epsilon\phi_1$, $\epsilon\phi_2$, $\epsilon\phi_3$ = the errors in platform gimbal angles due to tracker error and tracker gimbal pickoff error

Now substituting equations 1.120a, b, c, d and 1.121a, b, c into equations 1.119a, b, c, and solving for $\epsilon\phi_1$, $\epsilon\phi_2$, and $\epsilon\phi_3$ yields:

$$\epsilon\phi_1 = -\frac{\sin A_2}{\sin(A_1-A_2)} (\epsilon\delta_1 + \epsilon_{tp_1}) + \frac{\sin A_1}{\sin(A_1-A_2)} (\epsilon\delta_2 + \epsilon_{tp_2}) \quad (1.122a)$$

$$\epsilon\phi_2 = -\frac{\cos A_2}{\sin(A_1-A_2)} (\epsilon\delta_1 + \epsilon_{tp_1}) + \frac{\cos A_1}{\sin(A_1-A_2)} (\epsilon\delta_2 + \epsilon_{tp_2}) \quad (1.122b)$$

$$\epsilon\delta_3 = \left[-(\epsilon\delta_1 + \epsilon_{tp_1}) \cot(A_1-A_2) + (\epsilon\delta_2 + \epsilon_{tp_2}) \csc(A_1-A_2) \right] \tan \delta_1 - (\epsilon A_1 \sec \delta_1 + \epsilon_{tp_3}) \quad (1.122c)$$

It is seen from equations 1.122a, b, c that the platform errors ($\epsilon\phi_1$, $\epsilon\phi_2$, $\epsilon\phi_3$) are dependent upon the declination (δ) and SHA(A) of the star (i.e., the pointing angles of the star tracker). Thus to simplify the equations and obtain numerical results, the following typical pointing angles are assumed:

$$\delta_1 = \delta_2 = 45^\circ$$

$$A_1 = 90^\circ$$

$$A_2 = 45^\circ$$

Substituting these values into equations 1.122a, b, c yields

$$\epsilon\phi_1 = -(\epsilon\delta_1 + \epsilon_{tp_1}) + \frac{2}{\sqrt{2}} (\epsilon\delta_2 + \epsilon_{tp_2}) \quad (1.123a)$$

$$\epsilon\phi_2 = -(\epsilon\delta_1 + \epsilon_{tp_1}) \quad (1.123b)$$

$$\epsilon\phi_3 = \left[-(\epsilon\delta_1 + \epsilon_{tp_1}) + \frac{2}{\sqrt{2}} (\epsilon\delta_2 + \epsilon_{tp_2}) \right] - \left(\frac{2}{\sqrt{2}} \epsilon A_1 + \epsilon_{tp_3} \right) \quad (1.123c)$$

Note that $\epsilon\delta_1$ and $\epsilon\delta_2$ are different samples of the same error source and not different error sources. The same is true of ϵ_{tp_1} , ϵ_{tp_2} , ϵ_{tp_3} , and ϵ_{tp_4} (assuming the same accuracy pickoff is on both star tracker gimbals) and of ϵA_1 and ϵA_2 . Thus, the mean-squared values of the samples are identical to the mean-squared value of the error source. This is expressed by:

$$\overline{\epsilon_{tp}^2} = \overline{\epsilon_{tp_1}^2} = \overline{\epsilon_{tp_2}^2} = \overline{\epsilon_{tp_3}^2} = \overline{\epsilon_{tp_4}^2} \quad (1.124a)$$

$$\overline{\epsilon_{\delta}^2} = \overline{\epsilon_{\delta_1}^2} = \overline{\epsilon_{\delta_2}^2} \quad (1.124b)$$

$$\overline{\epsilon_A^2} = \overline{\epsilon_{A_1}^2} = \overline{\epsilon_{A_2}^2} \quad (1.124c)$$

Now assuming no cross-correlation to exist between the various error sources or between different samples of the same error source, the root-mean-squared (rms) errors in gibal angles are given from equations 1.123a, b, and c as:

$$\sqrt{\overline{\epsilon_{\phi_1}^2}} = (\epsilon_{\phi_1})_{RMS} = \left[\left((\epsilon_{\delta_1} + \epsilon_{tp_1})^2 - \frac{4}{\sqrt{2}} (\epsilon_{\delta_1} + \epsilon_{tp_1})(\epsilon_{\delta_2} + \epsilon_{tp_2}) + 2(\epsilon_{\delta_2} + \epsilon_{tp_2})^2 \right)_{AVG} \right]^{1/2}$$

The rms errors $\sqrt{\overline{\epsilon_{\phi_2}^2}}$ and $\sqrt{\overline{\epsilon_{\phi_3}^2}}$ are similar in form, but will not be included for brevity.

After the average is taken, all the cross-product terms drop out. From the relationships given by Equations 7a, b, c, the expressions for the RMS platform gibal errors are obtained.

$$(\epsilon_{\phi_1})_{RMS} = \sqrt{3(\overline{\epsilon_{\delta}^2} + \overline{\epsilon_{tp}^2})} \quad (1.125a)$$

$$(\epsilon_{\phi_2})_{RMS} = \sqrt{\overline{\epsilon_{\delta}^2} + \overline{\epsilon_{tp}^2}} \quad (1.125b)$$

$$(\epsilon_{\phi_3})_{RMS} = \sqrt{3\overline{\epsilon_{\delta}^2} + 5\overline{\epsilon_{tp}^2} + 2\overline{\epsilon_A^2}} \quad (1.125c)$$

1.3.1.3 Second Case - Tracker off Platform but no Flexure Errors

When the star tracker is mounted off the platform, the position of the platform gimbals (i.e., the inertial triad) are referenced to the tracker by means of pickoffs mounted on the platform gimbals. The platform gibal pickoff errors are directly coupled from the platform through the star tracker back into the platform gibal angles. This direct coupling may be seen by assuming a platform pickoff error in equations 1.118a, b, c, d, determining the star tracker misalignment error from the platform pickoff error and then substituting the star tracker error into equations 1.119a, b, c, d. The result is a direct coupling. Thus, the platform gibal angle errors due to

star tracker error, star tracker pickoff error and platform gimbal pickoff error are given by:

$$(\epsilon\phi_1)_{\text{RMS}} \left| \begin{array}{l} \text{OTPT} \\ \text{NF} \end{array} \right. = \sqrt{3(\epsilon\delta^2 + \epsilon_{tp}^2) + \epsilon\phi_{1p}^2} \quad (1.126a)$$

$$(\epsilon\phi_2)_{\text{RMS}} \left| \begin{array}{l} \text{OTPT} \\ \text{NF} \end{array} \right. = \sqrt{\epsilon\delta^2 + \epsilon_{tp}^2 + \epsilon\phi_{2p}^2} \quad (1.126b)$$

$$(\epsilon\phi_3)_{\text{RMS}} \left| \begin{array}{l} \text{OTPT} \\ \text{NF} \end{array} \right. = \sqrt{3\epsilon\delta^2 + 5\epsilon_{tp}^2 + 2\epsilon A^2 + \epsilon\phi_{3p}^2} \quad (1.126c)$$

where

OTPT = Off The Platform Tracker

NF = No Flexure of the craft

$\epsilon\phi_p^2$ = mean-squared platform gimbal pickoff error
(includes quantization error for digitized pickoffs).
Subscripts 1, 2 and 3 refer to the gimbals
(1 = outer gimbal, 2 = middle gimbal, 3 = inner gimbal)

1.3.1.4 Third Case - Tracker off Platform with Craft Flexure

Craft flexure between platform and star tracker will cause platform misalignment in exactly the same manner as platform gimbal pickoff error. That is, flexure is a directly coupled error. Thus, the platform gimbal angle errors due to tracker error, tracker pickoff error, platform gimbal pickoff error and craft flexure are given by:

$$(\epsilon\phi_1)_{\text{RMS}} \left| \begin{array}{l} \text{OTPT} \end{array} \right. = \sqrt{3(\epsilon\delta^2 + \epsilon_{tp}^2) + \epsilon\phi_{1p}^2 + \epsilon\phi_{1f}^2} \quad (1.127a)$$

$$(\epsilon\phi_2)_{\text{RMS}} \left| \begin{array}{l} \text{OTPT} \end{array} \right. = \sqrt{\epsilon\delta^2 + \epsilon_{tp}^2 + \epsilon\phi_{2p}^2 + \epsilon\phi_{2f}^2} \quad (1.127b)$$

$$(\epsilon\phi_3)_{\text{RMS}} \Big|_{\text{OTPT}} = \sqrt{3 \overline{\epsilon\delta^2} + 5 \overline{\epsilon_{tp}^2} + 2 \overline{\epsilon_A^2} + \overline{\epsilon\phi_{3p}^2} + \overline{\epsilon\phi_{3f}^2}} \quad (1.127c)$$

where $\overline{\epsilon\phi_{1f}^2}$, $\overline{\epsilon\phi_{2f}^2}$, $\overline{\epsilon\phi_{3f}^2}$ = mean-squared craft flexure rotations reflected into the three gimbal axes.

1.3.2 Numerical Evaluation of Platform Gimbal Errors - Platform Gimbal Pickoff Errors

The ST 124-M platform uses multispeed, digitally encoded resolver pickoffs. The pickoff parameters are:

64 pole resolvers

1016 hz excitation frequency

2.048 mega hz clock rate

+10 arc-second mechanical accuracy

The quantizing error is given by computing the least significant bit (LSB) as follows:

For a double angle encoding system:

$$\text{LSB} = \frac{360^\circ (3600 \text{ sec/deg}) (1016 \text{ hz})}{2 \times (64 \text{ poles}) (2.048 \times 10^6 \text{ hz})} = 5.03 \text{ arc-sec.}$$

Since the quantizing error is uniformly distributed, its RMS value is given by:

$$(\text{LSB})_{\text{RMS}} = \frac{5.03}{\sqrt{3}} \text{ sec} = 2.9 \text{ sec.}$$

Also assuming the mechanical accuracy of the resolver to be uniformly distributed yields:

$$\text{RMS Resolver Error} = \frac{10 \text{ sec}}{\sqrt{3}} = 5.8 \text{ sec RMS}$$

Thus, the net gimbal pickoff error is given by:

$$\sqrt{\overline{\phi_{1p}^2}} = \sqrt{(2.9)^2 + (5.8)^2} \text{ sec} = 6.5 \text{ sec.}$$

Tracker Error - A typical star tracker error for this type of application is:

$$\sqrt{\epsilon_{\delta}^2} = 5 \text{ sec}$$

$$\sqrt{\epsilon_A^2} = 5 \text{ sec}$$

Assuming that the pickoffs on the tracker gimbals are of the same type as that on the platform gimbals, the mean-squared pickoff error for the tracker gimbals will be:

$$\sqrt{\epsilon_{tp}^2} = 6.5 \text{ sec.}$$

Table 1.6 below summarizes the RMS gimbal angle errors for the above specified tracker error, tracker pickoff error, and platform gimbal pickoff error.

TABLE 1.6 SUMMARY OF PLATFORM GIMBAL ANGLE ERRORS
FOR THREE DIFFERENT MOUNTING CONFIGURATIONS

Mounting Configuration	Outer Gimbal Error (ϵ_{ϕ_1}) rms	Middle Gimbal Error (ϵ_{ϕ_2}) rms	Inner Gimbal Error (ϵ_{ϕ_3}) rms
	sec	sec	sec
Star Tracker Mounted on Platform	14.2	8.2	18.3
Star Tracker Mounted Off Platform with No Craft Flexure	15.6	10.5	19.5
Star Tracker Mounted Off Platform Including Craft Flexure	$\sqrt{244.2 + \epsilon_{\phi_{1f}}^2}$	$\sqrt{109.6 + \epsilon_{\phi_{2f}}^2}$	$\sqrt{378.8 + \epsilon_{\phi_{3f}}^2}$

The gimbal angle errors were calculated assuming two star fixes at angles of $\delta_1 = \delta_2 = 45^\circ$, $A_1 = 90^\circ$, and $A_2 = 45^\circ$. The first star shot was chosen at an angle of 90° to one gimbal axis and 45° to the other two gimbal angles. The purpose of this choice was to simplify the expression relating the error sources in the gimbal readout and control loop. The gimbal angle errors calculated for the outer and the middle gimbal also determine the random alignment error that would be introduced when a single star tracker tracking a star that is 45 degrees to the normal to the two control axes, is used to correct drift in two axes of a practical system. A star shot normal to the control axis is desired since the scale factor of the detected error increases proportionately to the sine of the angle of the line of sight to the star from the control axis. The star tracker line of sight error with respect to the platform will be 16.4 arc-seconds rms when the star shot is made at an angle of 45 degrees to the normal to the two control axes.

The second star shot is assumed to be made at an angle of 45 degrees to all of the platform axes, which represents the worst case conditions for a second star shot. The gimbal angle errors calculated would decrease with a better choice of navigational stars.

No specific values have been assumed for craft flexure moments. However, if the distance between the platform and the tracker is in the order of 10 to 15 feet, and the rigidity of the structure is similar to that of an aircraft, flexure of several minutes of arc can be produced, under different environmental conditions. Optical methods to detect and compensate for flexure of the spacecraft are feasible. An optical line of sight is required between the star tracker and the platform if this method is utilized. The angular deviation of the line of sight from the star tracker to the platform and the angular rotation of the star tracker with respect to the platform must be determined and introduced into the platform control loop as an error. Two separate instruments would be necessary to monitor the magnitude of the craft flexure in three axes. Since the craft flexure errors will not be nulled out, the optical instrumentation would have to have a uniform accuracy over the total useful range. Assuming an accuracy of ± 1 percent for the craft flexure instrumentation, craft flexure of ± 2 arc-minutes will produce an additional error of ± 2.4 arc-seconds. This flexure error will increase the overall gimbal angle error to:

- 1) $(\epsilon\phi_1)_{\text{rms}} = 15.8 \text{ arc-sec.}$
- 2) $(\epsilon\phi_2)_{\text{rms}} = 10.7 \text{ arc-sec.}$
- 3) $(\epsilon\phi_3)_{\text{rms}} = 19.6 \text{ arc-sec.,}$

The error due to craft flexure would then be negligible provided instrumentation with the given accuracy is attainable.

1.3.3 Pointing Angle Errors

The pointing angle error due to the misalignment of the platform gimbals with respect to the true inertial triad will be computed in this section.

Denote the true inertial triad by the three vectors $\bar{\gamma}$, \bar{n} , and \bar{p} as shown in Figure 1.27 below.

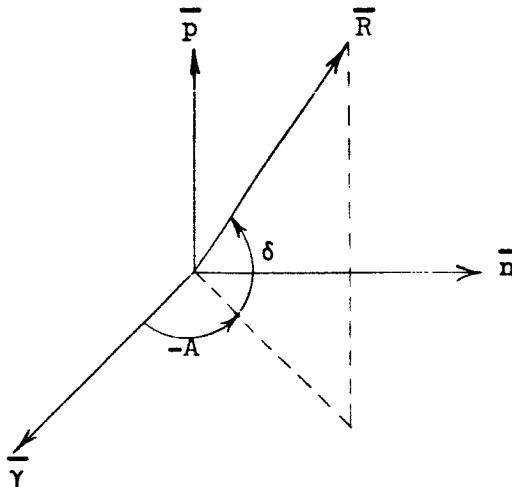


FIGURE 1.27 LOCATION OF POINTING VECTOR \bar{R} WITH RESPECT TO TRUE INERTIAL TRIAD

The pointing vector \bar{R} may be written as:

$$\bar{R} = a_1 \bar{\gamma} + a_2 \bar{n} + a_3 \bar{p} \quad (1.128)$$

Where a_1 , a_2 , and a_3 are given in terms of the pointing angles (δ, A) as:

$$\begin{aligned} a_1 &= \cos \delta \cos A \\ a_2 &= -\cos \delta \sin A \\ a_3 &= \sin \delta \end{aligned} \quad (1.129)$$

Now the triad defined by the position of the platform gimbals is rotated with respect to the true inertial triad by the gimbal angles $\epsilon\phi_1$, $\epsilon\phi_2$, and $\epsilon\phi_3$. Since these error angles are small, the small angle approximation for the sine and cosine functions are applicable. Thus, the relationship between the two triads is given by:

$$\begin{bmatrix} \overline{\gamma'} \\ \overline{n'} \\ \overline{p'} \end{bmatrix} = \begin{bmatrix} 1 & \epsilon\phi_3 & -\epsilon\phi_2 \\ -\epsilon\phi_3 & 1 & \epsilon\phi_1 \\ \epsilon\phi_2 & -\epsilon\phi_1 & 1 \end{bmatrix} \begin{bmatrix} \overline{\gamma} \\ \overline{n} \\ \overline{p} \end{bmatrix} \quad (1.130)$$

Where $\overline{\gamma'}$, $\overline{n'}$, and $\overline{p'}$ represent the triad formed by the platform gimbals.

The pointing vector from the platform gimbals triad ($\overline{R'}$) is given by:

$$\overline{R'} = a_1 \overline{\gamma'} + a_2 \overline{n'} + a_3 \overline{p'} \quad (1.131)$$

Substituting equation 1.130 into equation 1.131 yields the equation for $\overline{R'}$ in terms of the true inertial triad:

$$\overline{R'} = (a_1 - a_2 \epsilon\phi_3 + a_3 \epsilon\phi_2) \overline{\gamma} + (a_1 \epsilon\phi_3 + a_2 - a_3 \epsilon\phi_1) \overline{n} + (-a_1 \epsilon\phi_2 + a_2 \epsilon\phi_1 + a_3) \overline{p} \quad (1.132)$$

The pointing angle error is defined as the angle between pointing vector from the true inertial triad (\overline{R}) and the pointing vector from the triad formed by the platform gimbals ($\overline{R'}$). This angle is given approximately by:

$$\Delta\theta = | \overline{R} \times \overline{R'} | \quad (1.133)$$

where $\Delta\theta$ = pointing angle error.

Substituting equations 1.128 and 1.132 into equation 1.133 and simplifying,

$$\Delta\theta = \left| \begin{bmatrix} (a_2^2 + a_3^2) \epsilon\phi_1 - a_1 a_2 \epsilon\phi_2 - a_1 a_3 \epsilon\phi_3 \\ -a_1 a_2 \epsilon\phi_1 + (a_1^2 + a_3^2) \epsilon\phi_2 - a_2 a_3 \epsilon\phi_3 \\ -a_1 a_3 \epsilon\phi_1 - a_2 a_3 \epsilon\phi_2 + (a_1^2 + a_2^2) \epsilon\phi_3 \end{bmatrix} \begin{bmatrix} \overline{\gamma} \\ \overline{n} \\ \overline{p} \end{bmatrix} \right| \quad (1.134)$$

The values of a_1 , a_2 , and a_3 are dependent upon the specific pointing angles.

Therefore three typical sets of pointing angles will be chosen and the pointing error computed. The three sets chosen are:

- a) $\delta = 0, A = 0, a_1 = 1, a_2 = a_3 = 0$
- b) $\delta = 45^\circ, A = -90^\circ, a_1 = 0, a_2 = \frac{\sqrt{2}}{2}, a_3 = \frac{\sqrt{2}}{2}$
- c) $\delta = 60^\circ, A = 0, a_1 = 1/2, a_2 = 0, a_3 = \frac{\sqrt{3}}{2}$

The RMS pointing angle errors for these three cases (assuming no cross-correlation between gimbal angle errors) are given by:

a) $(\Delta\theta)_{\text{RMS}} = \left[\overline{\epsilon\phi_2^2} + \overline{\epsilon\phi_3^2} \right]^{1/2}$

b) $(\Delta\theta)_{\text{RMS}} = \left[\overline{\epsilon\phi_1^2} + \frac{1}{2} \overline{\epsilon\phi_2^2} + \frac{1}{2} \overline{\epsilon\phi_3^2} \right]^{1/2}$

c) $(\Delta\theta)_{\text{RMS}} = \left[\frac{3}{4} \overline{\epsilon\phi_1^2} + \overline{\epsilon\phi_2^2} + \frac{1}{4} \overline{\epsilon\phi_3^2} \right]^{1/2}$

Table 1.7 summarizes the pointing angle errors for the cases outlined in Table 1.6.

TABLE 1.7 SUMMARY OF RMS POINTING ANGLE ERRORS WITH RESPECT TO
AN ABSOLUTE REFERENCE FOR THREE DIFFERENT POINTING VECTORS

	POINTING VECTOR		
	$\delta = 0, A = 0$	$\delta = 45^\circ, A = -90^\circ$	$\delta = 60^\circ, A = 0$
MOUNTING CONFIGURATION	Gimbal angle error ($\Delta\theta$) _{rms}		
	$\overline{\text{sec}}$	$\overline{\text{sec}}$	$\overline{\text{sec}}$
STAR TRACKER ON PLATFORM	20.0	20.0	17.4
STAR TRACKER OFF PLATFORM, NO FLEXURE	22.2	22.2	19.7
STAR TRACKER OFF PLATFORM, WITH FLEXURE	$\left[448.4 + \epsilon\phi_{2f}^2 + \epsilon\phi_{3f}^2 \right]^{1/2}$	$\left[448.4 + \epsilon\phi_{1f}^2 + \frac{1}{2}\epsilon\phi_{2f}^2 + \frac{1}{2}\epsilon\phi_{3f}^2 \right]^{1/2}$	$\left[387.5 + \frac{3}{4}\epsilon\phi_{1f}^2 + \frac{1}{4}\epsilon\phi_{3f}^2 \right]^{1/2}$

1.4 COORDINATE TRANSFORMATION FOR STAR TRACKER MOUNTED OFF THE PLATFORM

A star tracker in a 2-gimbal mount that is to be used to monitor the alignment of a stable platform mounted in a 3-gimbal system is separated from the stable platform by 5 gimbals. Resolvers attached to the gimbals read out the gimbal angles, and the angle between the line of sight (LOS) of the star tracker and a given inertial reference vector can be computed using these gimbal angles. The following analysis describes the coordinate relationship between the stable platform reference and the LOS of the star tracker.¹ Equations 1.33 and 1.35 were derived using similar transformation equations.

Figure 1.28 illustrates a three-gimbal stable platform mounted on an unstabilized vehicle base, with a star tracker in a two-gimbal system also mounted on the unstabilized vehicle base. Movement of the vehicle base with respect to the stable platform will produce a rotational transformation of the coordinate system. Consider a counterclockwise rotation about the outer gimbal of the stable platform on the ϕ axis as shown in Figure 1.29.

The quantities x_1 , x_2 and x_3 are the components of the vector \bar{r} in the original coordinate system. The terms x_1' , x_2' and x_3' are the components of \bar{r} in the rotated coordinate system. The new coordinates are related to the original coordinates by a set of simultaneous equations:

$$\begin{aligned} x_1' &= x_1 \cos \phi + x_2 \sin \phi \\ x_2' &= -x_1 \sin \phi + x_2 \cos \phi \\ x_3' &= x_3 \end{aligned} \quad (1.135)$$

These equations can be expressed in the following matrix equation:

$$\begin{bmatrix} x_1' \\ x_2' \\ x_3' \end{bmatrix} = \begin{bmatrix} \cos \phi & \sin \phi & 0 \\ -\sin \phi & \cos \phi & 0 \\ 0 & 0 & 1 \end{bmatrix} \begin{bmatrix} x_1 \\ x_2 \\ x_3 \end{bmatrix} \quad (1.136)$$

The first column matrix represents the vector in terms of the rotated coordinate system, and the last column matrix represents the vector in terms of the original coordinates.

The matrix that relates rotation of the outer gimbal of the stable platform to the rest of the system is:

$$[\phi] = \begin{bmatrix} \cos \phi & \sin \phi & 0 \\ -\sin \phi & \cos \phi & 0 \\ 0 & 0 & 1 \end{bmatrix} \quad (1.137)$$

¹Saul Moskowitz, "Simplifying Resolver Chain Design with Matrix Notation," Electronic Design, March 2, 1964, pp 28-33.

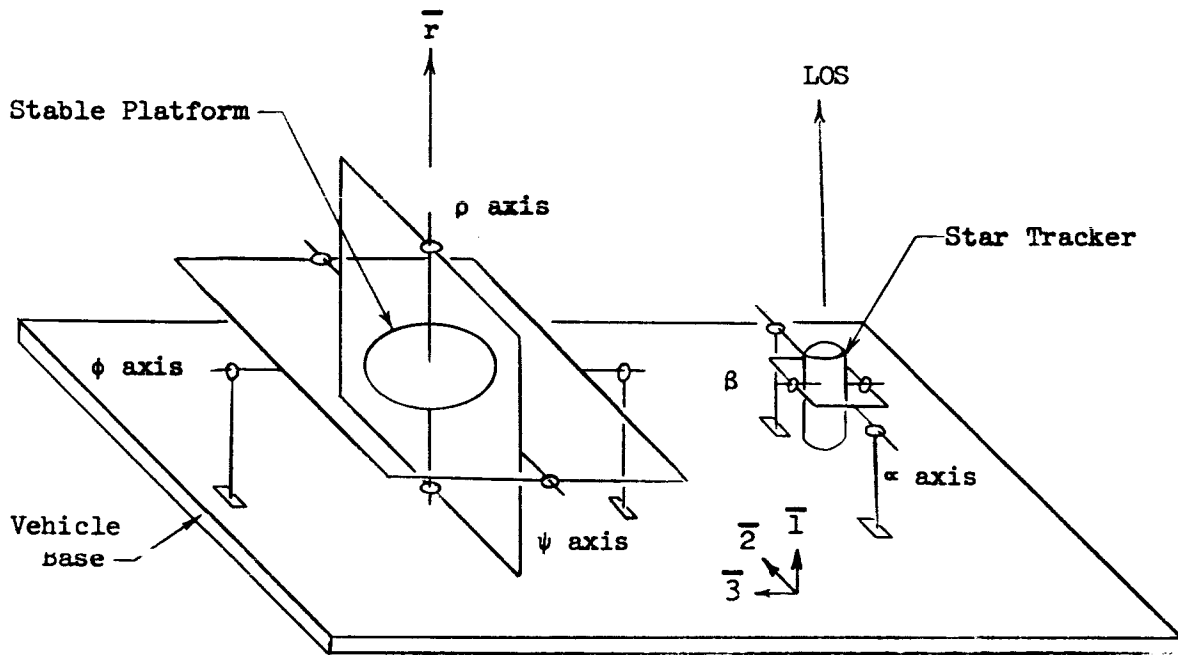


FIGURE 1.28 GIMBAL ARRANGEMENT FOR 3-AXIS STABLE PLATFORM AND TWO-AXIS STAR TRACKER MOUNT

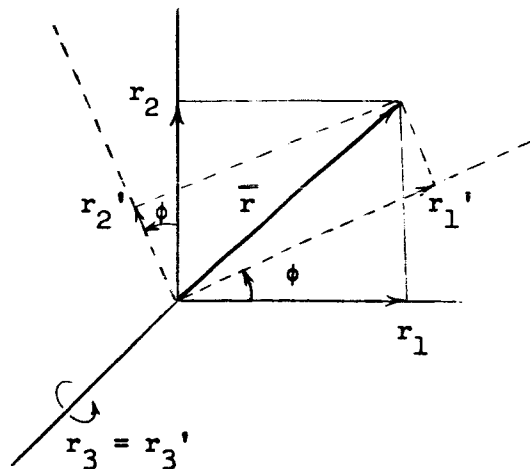


FIGURE 1.29 COORDINATE CHANGE DUE TO ROTATION ABOUT ϕ AXIS OF PLATFORM GIMBAL

The matrix for the middle gimbal of the stable platform is:

$$[\psi] = \begin{bmatrix} \cos \psi & 0 & -\sin \psi \\ 0 & 1 & 0 \\ \sin \psi & 0 & \cos \psi \end{bmatrix} \quad (1.138)$$

The matrix for the inner gimbal of the stable platform is:

$$[\rho] = \begin{bmatrix} 1 & 0 & 0 \\ 0 & \cos \rho & \sin \rho \\ 0 & -\sin \rho & \cos \rho \end{bmatrix} \quad (1.139)$$

The matrix for the outer gimbal of the tracker is:

$$[\alpha] = \begin{bmatrix} \cos \alpha & 0 & -\sin \alpha \\ 0 & 1 & 0 \\ \sin \alpha & 0 & \cos \alpha \end{bmatrix} \quad (1.140)$$

The matrix for the inner gimbal of the tracker is

$$[\beta] = \begin{bmatrix} \cos \beta & \sin \beta & 0 \\ -\sin \beta & \cos \beta & 0 \\ 0 & 0 & 1 \end{bmatrix} \quad (1.141)$$

To determine the relationships between the different gimbal angles, the reference vector \bar{r} will be transformed into a vector along the axis of the tracker by means of the transformations $[-\rho]$, $[-\psi]$, $[-\phi]$, $[\alpha]$ and $[\beta]$ in that order. The first three matrices are negative since the transformations are clockwise. If the angles α and β are set so that the LOS of the tracker is aligned with the reference vector \bar{r} , this alignment condition can be represented by the following matrix equation:

$$\begin{bmatrix} 1 \\ 0 \\ 0 \end{bmatrix} = [\beta] [\alpha] [-\phi] [-\psi] [-\rho] \begin{bmatrix} r_1 \\ r_2 \\ r_3 \end{bmatrix} \quad (1.142)$$

The reference vector is normalized to unity since only the direction not the magnitude of the vector is of interest. Therefore the components r_1 , r_2 and r_3 of the reference vector are:

$$r_1^2 + r_2^2 + r_3^2 = 1 \quad (1.143)$$

Since the LOS of the star tracker must initially be pointed at the star to be tracked, using the stable platform as a reference, the gimbal angles α and β of the tracker mount must be known in terms of the gimbal angles of the stable platform. Multiplying both sides of equation 1.142 by the transformation $[-\alpha]$, $[-\beta]$

$$[-\alpha] [-\beta] \begin{bmatrix} 1 \\ 0 \\ 0 \end{bmatrix} = [-\phi] [-\psi] [-\rho] \begin{bmatrix} r_1 \\ r_2 \\ r_3 \end{bmatrix} \quad (1.144)$$

Substituting equations 1.137 through 1.141 into equation 1.144, and performing the matrix multiplications indicated

$$\begin{bmatrix} \cos \alpha \cos \beta \\ \sin \beta \\ -\sin \alpha \cos \beta \end{bmatrix} = \begin{bmatrix} \cos \phi [r_1 \cos \psi + \sin \psi (r_2 \sin \rho + r_3 \cos \rho)] \\ -\sin \phi [r_2 \cos \rho - r_3 \sin \rho] \\ \sin \phi [r_1 \cos \psi + \sin \psi (r_2 \sin \rho + r_3 \cos \rho)] \\ + \cos \phi [r_2 \cos \rho - r_3 \sin \rho] \\ -r_1 \sin \psi + \cos \psi (r_2 \sin \rho + r_3 \cos \rho) \end{bmatrix} \quad (1.145)$$

From rows 1 and 3 of equation 1.145:

$$-\tan \alpha = \frac{-r_1 \sin \psi + \cos \psi (r_2 \sin \rho + r_3 \cos \rho)}{\begin{pmatrix} \cos \phi [r_1 \cos \psi + \sin \psi (r_2 \sin \rho + r_3 \cos \rho)] \\ -\sin \phi [r_2 \cos \rho - r_3 \sin \rho] \end{pmatrix}} \quad (1.146)$$

From row 2 of equation 1.145:

$$\sin \beta = \sin \phi [r_1 \cos \psi + \sin \psi (r_2 \sin \rho + r_3 \cos \rho)] + \cos \phi [r_2 \cos \rho - r_3 \sin \rho] \quad (1.147)$$

Equations 1.146 and 1.147 can be implemented through a resolver chain or the tracker gimbal angles computed using the given equations. For purposes of checking platform drift through launch, all five gimbal angles can be telemetered to the ground. The LOS of the star tracker with respect to the platform can then be computed and the platform drift determined from this LOS computation.

2. BASIC OPTICAL TRACKING SYSTEM DESIGN CONCEPTS

The basic functions of an optical tracking system can be represented by the block diagram shown in Figure 2.1.

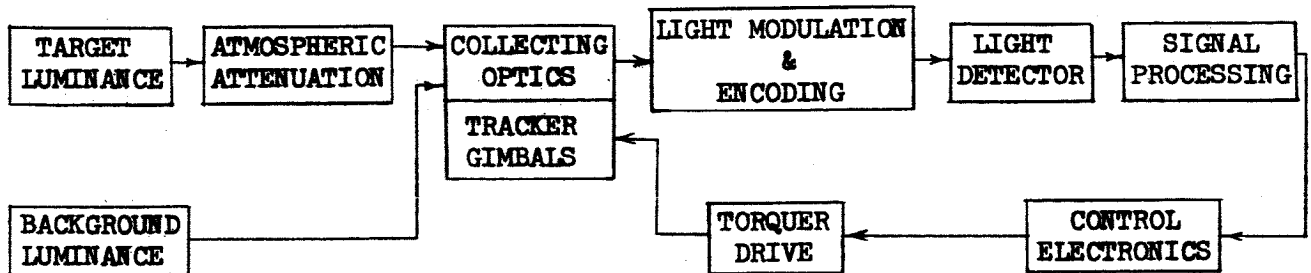


FIGURE 2.1 REPRESENTATIVE OPTICAL TRACKING SYSTEM BLOCK DIAGRAM

The block diagram of an optical tracking system is applicable for an ultra-violet, visible or infrared tracking system, but only visible tracking systems will be considered in this discussion. The mechanical modulation methods described can be used for any system by selecting the proper detector for a given spectral region. The characteristics of the different optical detectors influences the tracking system design, and in some detectors, the signal encoding function is performed by the detector itself so this portion of the block diagram may be combined in a single block.

Schematically, light from the target and the background that is incident on the tracker is collected by an optical system, optically modulated to encode the collected energy to separate the target and background information, then is detected by an optical detector whose function is to convert the optically encoded signal into an electrical signal. The signal processing electronics consist of amplification and demodulation of the target signal to derive a track error signal. The track error signal is used to drive the tracker gimbal torquers, to reposition the tracker so that the optical bore-sight of the tracker is aligned with the line-of-sight to the target.

The target and background radiance characteristics and the atmospheric attenuation of the target energy are parameters that are determined by the particular application in which the tracking system is utilized and will not be considered. In addition the control electronics and the gimbal drive will not be discussed in this consideration of optical tracking systems.

2.1 OPTICAL SYSTEM

The optical system collects the radiation from a given field of view and either produces an image of the area within the field of view or concentrates the total collected energy in a spot of higher flux density. In the majority

of applications of optical tracking systems, an imaging optical system is desired, though a non-imaging optical system such as an ellipsoid of revolution, or a cone channel can be used to track point sources under specific conditions.

The most important factors considered in the design of an optical tracking system are:

1. The physical size
2. The focal length and collecting aperture
3. The image quality
4. The angular field of view
5. The spectral response
6. Reflective or refractive optics.

In general, all the parameters must be considered with respect to each other in arriving at the optimum optical design for a given system. The physical size of the optical system is a function of the focal length, the aperture, and the mechanical arrangement of the individual elements in the optical system. The frontal cross section of the lens is fixed by the required lens aperture, but the length of the optical system can be compressed by proper design. A summary of typical optical systems and the good and bad features of the different systems are shown in Table 2.1.

The ratio of the focal length of the lens to the diameter of the collecting aperture is the geometrical f /number of the lens. An optical system with a small f /number is termed a fast system while an optical system with a large f /number is termed a slow optical system. Typical fast optical systems have f /numbers of approximately unity while a system with an f /number over eight is regarded as slow. Since the apex angle of the convergent rays is inversely proportional to the f /number, the optical design of a slow system is simplified since the lens can be designed for a smaller range of convergent light rays.

The f /number is an index of the light gathering power of an optical system with a given focal length. In the past, the f /numbers quoted by lens manufacturers have related strictly to the geometrical dimensions of the lens. Since a portion of the light collected by the lens may be absorbed by the lens material, as in the case of a refractive lens or obscured by one of the optical elements as in the Cassegrainian system, a T /number is sometimes used rather than an f /number to provide a more representative figure of merit in regard to light gathering power of the lens. To determine the T /number, the geometrical aperture is reduced to an effective aperture by multiplying the area of the aperture by the lens transmission, and the T /number is then determined by the ratio of the focal length of the lens to the effective aperture.

The image quality of a lens is a measure of the sharpness of the image that is produced by the lens. For a photographic lens this image quality is determined by using standard charts and standardized optical measuring

TABLE 2.1 REPRESENTATIVE OPTICAL SYSTEMS

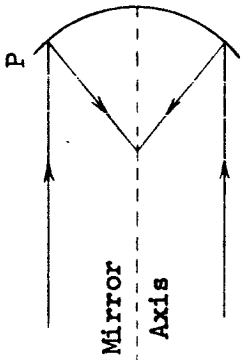
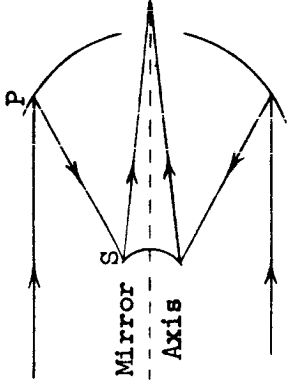
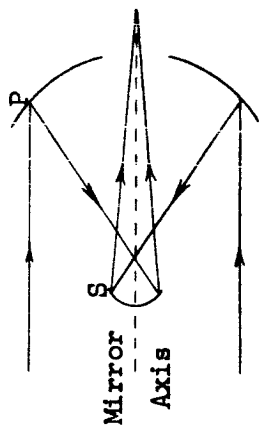
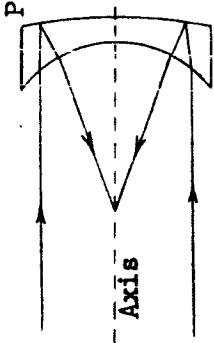
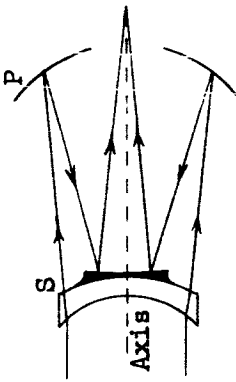
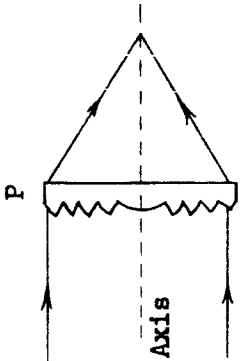
LENS TYPE	OPTICAL SCHEMATIC	LENS CHARACTERISTICS
PARABOLOID		<p>P = Parabolic mirror</p> <p>No spherical or chromatic aberration</p> <p>Off-axis image subject to coma</p> <p>Detector plane located in optical system</p>
CASSEGRAIN		<p>P = Spherical or parabolic mirror</p> <p>S = Hyperbolic mirror</p> <p>No spherical or chromatic aberration</p> <p>Image formed past primary mirror permitting detector to be located behind optical system</p> <p>Blocking of entrance aperture by secondary lens reduces transmission</p> <p>Non-vignetted field limited by mirror arrangement</p>
GREGORIAN		<p>P = Spherical or parabolic mirror</p> <p>S = Ellipsoidal mirror</p> <p>Lens characteristics similar to Cassegrain but longer in length due to difference in the optical path.</p>

TABLE 2.1 (CONT'D) REPRESENTATIVE OPTICAL SYSTEMS

LENS TYPE	OPTICAL SCHEMATIC	LENS CHARACTERISTICS
NEWTONIAN		<p>P = Parabolic mirror S = Plane mirror or reflecting prism Commonly used in astronomical telescopes Suffers from coma for off-axis images Prism or mirror obscures a portion of entrance aperture</p>
HERSCHELIAN (off-axis parabola)		<p>P = Inclined parabolic mirror No central obscuration by secondary lens Subject to coma</p>
SCHMIDT		<p>P = Spherical mirror C = Aspheric refractive corrector plate Capable of high resolution over large field-of-view Free of spherical aberration and coma Produces a curved focal plane Detector assembly obscures portion of entrance aperture</p>

TABLE 2.1 (CONT'D) REPRESENTATIVE OPTICAL SYSTEMS		
LENS TYPE	OPTICAL SCHEMATIC	LENS CHARACTERISTICS
MANGIN MIRROR		P = Refractor with mirrored back surface Free of spherical aberration and coma Restricted to small apertures and small fields of view Permits greater correction than simple spherical mirror Aperture blocking by detector assembly
MAKSUTOV		P = Meniscus reflector S = Meniscus refractor-reflector Free of coma, spherical and chromatic aberration Compact Relatively large aperture Central obscuration by mirror on secondary
FRESNEL		P = Sectioned refractor Reduced weight, axial space requirement, lower absorption than simple refractor Difficult to fabricate

techniques. The maximum number of lines ruled on a standard chart that can be resolved by the lens determines the resolution of the lens.

This resolution criteria however does not yield a complete definition of the energy distribution of the image of a point source such as a star. Assuming that the aperture of the lens is circular, the star image formed is a bright central disk surrounded by a series of fainter rings. The bright central disk is known as the "Airy" disk and the diameter of this disk is the figure which is also quoted as the resolution of the lens. The radius of the disk for a perfect lens can be determined by the following equation:

$$\theta = 1.220 \frac{\lambda}{a} \quad (2.1)$$

where θ is the angular radius of the ring, λ is the wavelength of light and a is the diameter of the objective lens. The linear diameter of the Airy disk is then

$$d = 2\theta f \quad (2.2)$$

where d is the diameter of the Airy disk, and f the focal length of the optical system. From the previous equations the size of the Airy disk is shown to be inversely proportional to the diameter of the lens, so an extremely high resolution lens must be large to reduce the diffraction effects from the edges of the lens.

In Table 2.2 is shown the dimensions of the diffraction pattern of a star image that is produced by a perfect lens.

TABLE 2.2 ENERGY DISTRIBUTION OF STAR IMAGE

RING	m	I_{\max}	I_{total}
Central maximum	0	1	1
First dark	1.22		
Second bright	1.638	0.01745	0.084
Second dark	2.233		
Third bright	2.666	0.00415	0.033
Third dark	3.238		
Fourth bright	3.694	0.00165	0.018
Fourth dark	4.241		
Fifth bright	4.722	0.00078	0.011
Fifth dark	5.243		

The angular separation of the different rings from the center of the pattern can be calculated by the relationship,

$$\theta = \frac{m\lambda}{a} \quad (2.3)$$

where θ is the angular separation and m the value given in Table 2.2. The values of I_{\max} in the table are the relative intensity of the different rings and I_{total} is the total amount of light in the ring, both compared to the brightness of the central disk.

The instantaneous field of view of the optical system is set by the focal length of the lens and the size of the active area of the photodetector. The total field coverage is the field that is swept by the detector during a scan cycle of the optical tracker and is a function of the design of the scanning mechanism rather than the optical system.

Reflective and refractive elements are reflecting surfaces and transmitting elements that are used to focus the collected optical rays. The choice of refractive or reflective elements or a combination of the two (catadioptric system) in the optical system design are parameters that are available to the optical designer to achieve the size, speed, image quality, and spectral response desired. In general a reflective optical system has the advantage of being free of chromatic aberration so the lens can be used in the design of ultra-violet, visible and infrared tracking systems by interchanging the optical detector.

The Cassegrainian optical system is the most commonly used reflective optical system. In this design, the convergent rays in the optical system are reflected off two mirrors, essentially folding the optical path, so that the length of the telescope can be shortened by a factor of two over a simple lens.

The optical efficiency of a reflective system, in a design where the optical axis is concentric to the entrance aperture, is reduced due to blocking of a portion of the entrance aperture by one of the reflecting surfaces as in the case of the Cassegrainian system, or by the detector assembly as in the case of the parabolic optical system. By utilizing only a portion of the primary mirror (off-axis parabola), the loss in optical efficiency due to blocking of the entrance aperture can be eliminated. However, one of the prime advantages of the reflective system, that of compactness in mechanical design, must be sacrificed.

The refractive optical system almost always forms an image at a plane which is beyond the last element in the optical system. This allows easy access to the image plane, so the optical design can proceed separately from the mechanical design of the tracker. With the reflective system, the image plane may fall within the optical system, so the optical modulation

mechanism and the detector must be located within the optical system. The Cassegrainian system provides an image plane that is beyond the primary mirror, permitting easy access to the image plane. However, due to the arrangement of the reflectors in the Cassegrainian system, the usable field of view in which no vignetting occurs is limited.

The materials used in a refractive optical system must be selected considering its optical transmission properties, index of refraction and mechanical properties. Since the optical transmission and the index of refraction of most optical materials vary as a function of the wavelength of light, the performance of a refractive optical system is normally optimized for two wavelengths, somewhere towards the ends of the desired spectral band. To minimize the degradation of the image quality beyond and between these design points, multiple elements with different indices of refraction are utilized to compensate for the change in the dispersive power of the different elements as a function of wavelength.

Combinations of refractive and reflective elements in an optical system are useful in applications where a fast lens with high resolution over a large field of view is required. The Schmidt optical system is the best known catadioptric system. The feature of this system is the aspheric refractor corrector plate. The corrector plate provides variable zone correction of spherical aberration, so that lens resolution close to the theoretical limit can be obtained over a field of view of 60×60 degrees. The image plane produced by a Schmidt lens is spherical, so the detector or light modulation mechanism must also be curved to properly utilize this lens design.

2.1.1 Field Lens

Certain photodetectors such as photomultipliers and photodiodes, produce the same output regardless of the location of the target image on the sensitive area of the photodetector. An optical tracking system utilizing a detector of this type frequently will be used in the optical configuration illustrated in Figure 2.2.

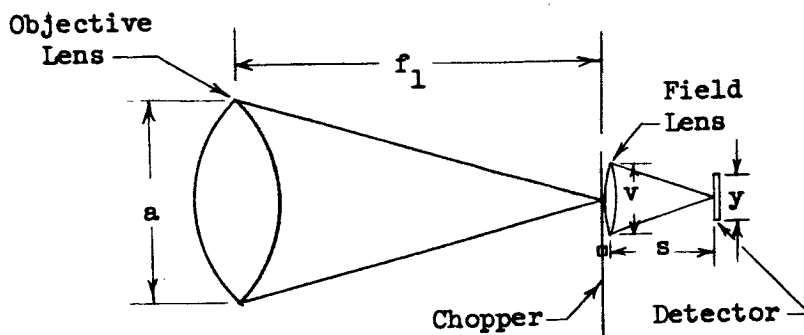


FIGURE 2.2 FIELD LENS SYSTEM

The objective lens forms an image of the scene at the plane in which the light chopper is located. The objective lens is defined as the lens closest to the object being viewed. A field lens, or a lens that subtends the field of view is placed close to the focal plane of the objective lens to refocus the light collected by the objective onto the detector.

The field lens forms an image of the entrance aperture at the detector plane. With this optical arrangement, the collected light is spread uniformly over the sensitive area of the detector and eliminates the effects of sensitivity variations over the detector area. The use of a field lens provides a second advantage in that the size of the detector required to cover a given field of view with an optical system of a given focal length can be reduced.

In the optical system shown in Figure 2.2, the diameter of the objective lens is a , and the focal length f_1 . The field lens has a focal length of f_2 .

The location of the image produced by the field lens can be calculated using the lens formula

$$\frac{1}{f_2} = \frac{1}{f_1} + \frac{1}{s} \quad (2.4)$$

where s is the distance of the image from the nodal point of the lens

$$s = \frac{-f_1 f_2}{(f_2 - f_1)} \quad (2.5)$$

The size of the image (y) produced by the field lens is given by

$$\frac{y}{s} = \frac{a}{f_1} \quad (2.6)$$

$$y = \frac{-af_2}{f_2 - f_1} \quad (2.7)$$

The quantity V is the linear dimension of the field of view (θ) of the objective lens, and is also the required diameter of the field lens.

$$V = f_1 \tan \theta \quad (2.8)$$

and

$$\frac{f_2}{V} = f_{no2} \quad (2.9)$$

where f_{no2} is the f /number of the field lens

$$f_2 = V f_{no2} = f_1 \tan \theta f_{no2}$$

The factor by which the size of the detector required to subtend a given field of view can be reduced using a field lens is given by the ratio of

$$\frac{Y}{V} = \frac{-a f_2}{(f_2 - f_1) f_1 \tan \theta} \quad (2.10)$$

Substituting for f_2 ,

$$\frac{Y}{V} = \frac{-a f_{no2}}{f_1 (\tan \theta f_{no2} - 1)}$$

Since

$$\frac{f_1}{a} = f_{no1} \quad (2.11)$$

where f_{no1} is the f/number of the objective lens,

$$\frac{Y}{V} = \frac{-f_{no2}}{f_{no1} (f_{no2} \tan \theta - 1)} \quad (2.12)$$

For typical star tracker applications,

$$8 < f_{no1} < 64$$

$$0.75 < f_{no2} < 1.5$$

$$0.5 \text{ deg.} < \theta < 5 \text{ deg.}$$

The reduction of the size of the detector used with an optical system with an f/16 objective lens, an f/1 field lens and a field of view of 1 degree, is from Equation 2.12,

$$\frac{Y}{V} = \frac{-1}{16(0.0174 - 1)} = 0.0635 \text{ times}$$

For a very fast objective lens, in the order of f/1, the use of a field lens is not advantageous, since the image produced by the field lens will not be substantially reduced over the size of the image produced by the objective.

2.2 BASIC DETECTOR TYPES

The detectors which are employed in star tracking systems fall into three general classifications. The first type is a single element or "point" detector which provides an electrical output signal which is independent of the location of the incident radiant energy on the sensitive surface of the photodetector. With this type of photodetector, the incoming radiation must be modulated by a mechanical scanning device to encode the star location information and to provide rejection of background radiance. The photomultiplier and the photodiode are examples of this type of detector.

The second type of detector is an extended area detector, whose output is a function of the distribution of radiant energy over the sensitive area of the detector. The image dissector is one example of an extended area detector, and can be considered as a matrix of single element detectors which are individually interrogated to determine the radiation distribution. Another example of an extended area detector is the Radiation Tracking Transducer (RTT), made by Micro-Systems Incorporated. This detector is essentially a four-terminal device which determines the position of the incident radiation by the relative amplitude of the photovoltaic signal produced by the incident energy at the four terminals of the detector. The two detectors differ, however, since an image of the scene being viewed can be reproduced using an image dissector, but the RTT can only indicate the centroid of the energy incident on the detector surface.

The third type of detector is an extended area detector which, in addition to the properties of the second type of detector, is also capable of integrating the incident radiant flux over a period of time to increase the effective target signal. Two examples of this detector type are the vidicon and the image orthicon. In the vidicon, storage of the electron image is provided through the extremely high capacitance of the photoconductive surface which comprises the faceplate of the vidicon. In the image orthicon, storage is provided by means of an electrostatic image created within a special-image section of the tube. In both of these detectors, an electron beam is used to read out the stored image.

2.2.1 Single Element Detectors

The majority of the optical detectors manufactured fall into the single element category. Among these are included photodiodes, photomultipliers, the semiconductor elements, silicon and germanium, and a number of photoconductive, photovoltaic and photomagnetic compounds.

2.2.1.1 Photomultipliers

Photodiodes have a photoemissive surface which emits electrons when illuminated by light. The emitted electrons are then collected by an anode which is biased at a higher voltage than the photosensitive emissive surface. The photomultiplier is a modification of the photodiode, in which the emitted electrons are electrostatically accelerated then allowed to strike a specially prepared surface called a dynode. The dynodes are coated with a substance which releases secondary electrons upon being bombarded by high velocity electrons. This process can be iterated until the electron flux is increased many orders of magnitude. As a circuit element, the photomultiplier can be analyzed as a high impedance current generator, whose performance limits are determined by the efficiency of the photosensitive surface, compared to the thermionic emission of this surface and the leakage currents in other parts of the photomultiplier.

The spectral response of the materials that exhibit photoemissive properties fall primarily in the visible portions of the spectrum. The different types of photoemissive materials classified with respect to spectral response exceeds 21 in number, but basically there are four to five different photoemissive materials that are of interest. These include the materials that provide S1, S11, and S20 response, and a new material with ultraviolet response, for which an "S" number has not yet been assigned. The materials used to create an S1 photocathode response are Ag-O-Cs; the S11 response, Cs-Sb; the S20 response, Sb-K-Na-Cs; and the UV response Cs-Te. See Figure 2.3.

The spectral response of the S1 photocathode extends past 1.0 microns, and it has the best red response of any of the photoemissive materials. However, its quantum efficiency, or the ability to convert incident photons to free electrons, is very low. At 0.8 microns, which is the peak of the S1 red response, the quantum efficiency is 0.4 percent.

The S11 spectral response extends from 0.3 to 0.6 microns. The quantum efficiency of this material that provides this response exceeds 13 percent at the peak of its response curve, providing a very efficient photocathode. To increase the quantum efficiency of this material, the material is deposited on a mirrored surface to permit a second pass of the incident light through the photosensitive material. The quantum efficiency is increased to greater than 20 percent at the peak of the spectral response. The Cs-Sb photocathode with this greater quantum efficiency is designated as having an S17 response. The material comprising the S11 photocathode is translucent, permitting design of photomultipliers with the photocathode deposited on the rear of the entrance window of the photomultiplier, a configuration referred to as end-on photomultiplier. To achieve the S17 response, the photocathode is deposited on an opaque substrate, requiring a different mechanical arrangement of the entrance window, the photocathode and the dynodes. The net effects of this mechanical

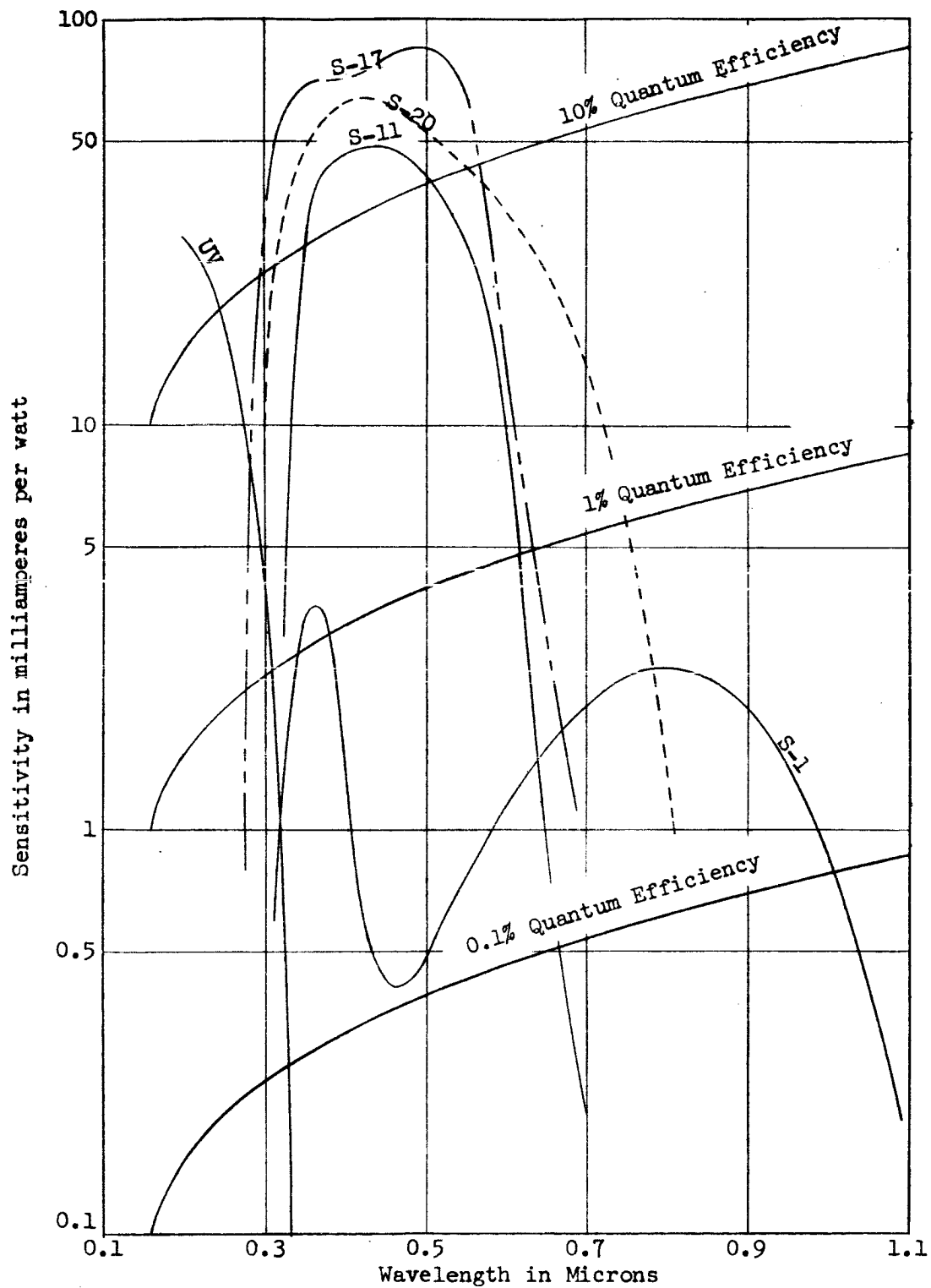


FIGURE 2.3 SPECTRAL RESPONSE OF FIVE REPRESENTATIVE PHOTOEMISSIVE SURFACES

arrangement of the photomultiplier components on the design of an optical tracking system, are that the optical system used with the S17 photomultiplier must have a longer back focal length, and the optical tracker cannot be designed with the detector package symmetrical with respect to the optical axis.

The spectral response of the Cs-Sb surface can be extended into the ultraviolet region, by the utilization of a photocathode window that has good ultraviolet transmission. Photomultipliers having S5 and S21 responses are examples of detectors utilizing this manufacturing technique. Some of the visible response of the Cs-Sb surface is sacrificed to achieve sensitivity out to 0.2 micron.

The S-20 photocathode has a very high quantum efficiency and an excellent red response. In comparison with the S17 photocathode, the S20 quantum efficiency at the peak of its response curve is lower, but its spectral response extends farther into the red region of the spectrum. The S20 can also be utilized in a head-on configuration, so the choice between these two detectors in a star tracking system is dependent upon the mechanical design of the star tracker as well as the radiant characteristics of the star.

The Cs-Te photocathode has a long wavelength cutoff at about 0.32 microns. The spectral response is limited to the ultraviolet region, and a photomultiplier with this response of this type is useful for making daytime ultraviolet measurements and experiments, since the photomultiplier is unaffected by solar radiation.

The performance of a star tracking system utilizing a photomultiplier can be calculated from the following expression:

$$S/N = \frac{F_c C B}{\sqrt{2q(i_d + I a b)(1 + 1/G)\Delta f}}$$

where F_c is the effective star flux incident on detector (lumens)
 C is the detector response to the incident star flux (amp per lumen)
 B is the electronic transfer characteristics of the signal amplifier
 q is the charge of an electron (coulomb)
 i_d is the photocathode dark current (amp)
 I is the illumination on the detector due to background radiance (foot-candles)
 a is the area of the scanning aperture (square feet)
 b is the detector response to background flux (amp per lumen)
 G is the gain per dynode stage in the photomultiplier
 Δf is the electronic bandwidth (cycles)

2.2.1.2 Semiconductor Detectors

There are a number of photosensitive compounds and elements that change their electrical characteristics when illuminated by radiation in the optical region of the spectrum. The more common of these that are used as detectors of optical radiation include silicon, germanium, selenium, lead sulfide, lead selenide, lead telluride, lead arsenide, gallium arsenide, indium antimonide, cadmium sulfide, and cadmium selenide. In general these detectors provide a change in electrical characteristics across a two-terminal network, which is proportional to the total radiant flux on the detector regardless of the location and the concentration of the radiant flux on the sensitive area of the detector. The various detectors may be photovoltaic, photoconductive, or photo-magnetic, and in some cases can exhibit all three characteristics. Of the detectors listed, the detectors that show the most promise for use in a star tracker are silicon and cadmium sulfide. The other detectors are either sensitive to infrared energy alone, have too low a responsivity, or are similar in characteristics to silicon and cadmium sulfide.

2.2.1.2.1 Silicon

A silicon detector is a photovoltaic cell which is manufactured as shown in Figure 2.4. A diffused p-n junction is formed between a thin layer of P type silicon and a thicker layer of N type silicon. Nickel electrodes are plated to the silicon to provide electrical contact.

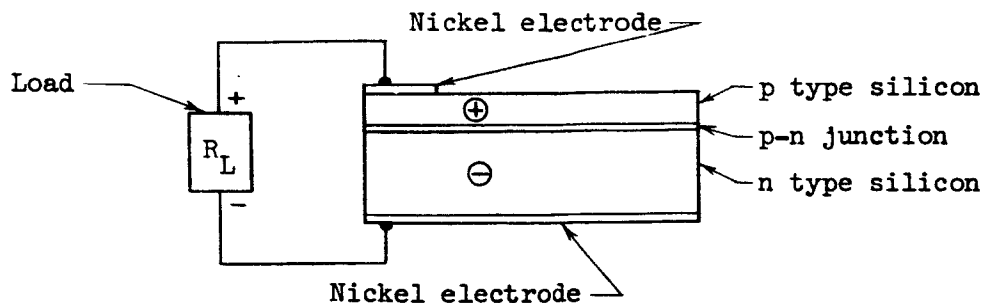


FIGURE 2.4 SILICON PHOTOVOLTAIC DETECTOR

When light strikes the p type silicon, hole-electron pairs are created in both the p and n regions, but the electrostatic field at the junction sweeps the holes into the p region and the electrons into the n region. The unbalanced charge carrier produces a voltage difference across the output terminals.

The sensitivity of a silicon detector is expressed in terms of D^* where D^* is defined as the detectivity of the cell for a detector of unity area and unity bandwidth. The detectivity can also be expressed as the signal-to-noise ratio produced with a radiant flux of unity incident on the detector.

$$D^* = A^{1/2}/P_N \text{ (cm-cps}^{1/2}\text{/watt)}$$

The quantity A is the area of the detector, and P_N is the radiant flux required to provide a signal-to-noise ratio of one, when the electronic bandwidth is unity.

$$P_N = JNA/V-\Delta f^{1/2} \text{ (watts)}$$

where

- N is the rms noise voltage (volts)
- J is the radiant flux density (watts/cm²)
- V is the rms signal voltage (volts)
- Δf is the electronic bandwidth (cycles)

The detectivity of silicon is in the order of 10^{12} cm - cps^{1/2}/watt, and the time constant is 300 μ sec. The spectral response is shown in Figure 2.5.

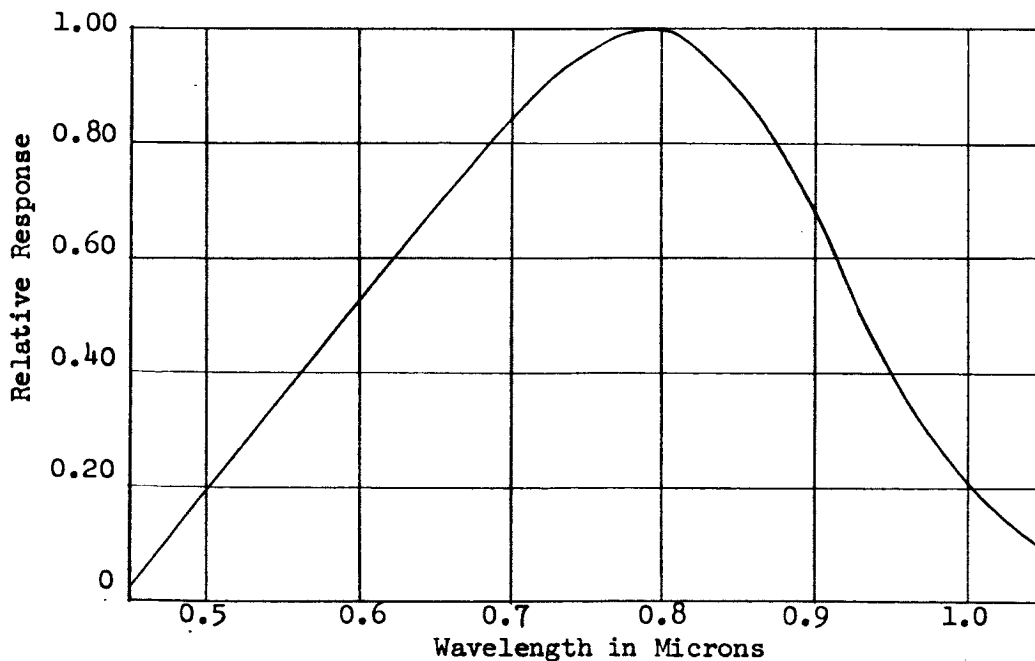


FIGURE 2.5 SPECTRAL RESPONSE OF SILICON PHOTOVOLTAIC DETECTOR

2.2.1.2.2 Cadmium Sulfide

Cadmium sulfide and cadmium selenide are primarily photoconductive materials, though it is possible to manufacture detectors of these materials with photovoltaic properties. These detectors have a very high responsivity, and are capable of an impedance change of three orders of magnitude when the incident radiant flux is changed from zero to 10,000 foot-candles. These materials are affected by humidity and temperature, and are subject to fatigue. Detector fatigue is evidenced by the loss or reduction of detector response at low light levels after prolonged use, or after being exposed to intense light. For use in a star tracker, the detector would have to be enclosed in a sealed, temperature controlled chamber, and also be provided with a sun protection device. The spectral response and the responsivity curves of CdS and CdSe are illustrated in Figure 2.6.

2.2.2 Extended Area Detectors

2.2.2.1 Image Dissector

The image dissector utilizes a photoemissive cathode in which the electrons emitted by the photosensitive surface are accelerated and deflected by means of electrostatic or electromagnetic fields. The electron emission from a given area of the photocathode is proportional to the flux density of the light on the cathode, so an electron "image" is produced. This electron image is scanned across a mechanical aperture by changing the beam deflection fields. The electrons that enter the mechanical aperture are then multiplied in a dynode chain.

The image dissector is identical in function to the photomultiplier with the exception that a small area of the photocathode can be sampled with the image dissector, rather than the complete cathode with the photomultiplier. The need for a separate scanning mechanism to encode the optical signal is thus eliminated. The performance of a star tracker utilizing an image dissector can be analyzed in the same manner as a photomultiplier system.

2.2.2.2 Radiation Tracking Transducer

The sensitive area of the radiation tracking transducer (RTT) consists of an extended photovoltaic p-n layer. The photoeffect produced is similar to that of the silicon photovoltaic cell. The excess electrons in the n region of the RTT spreads out laterally and, due to the forward bias conditions, recrosses the junction and combines with the holes. The potential difference measured between various points on the n layer

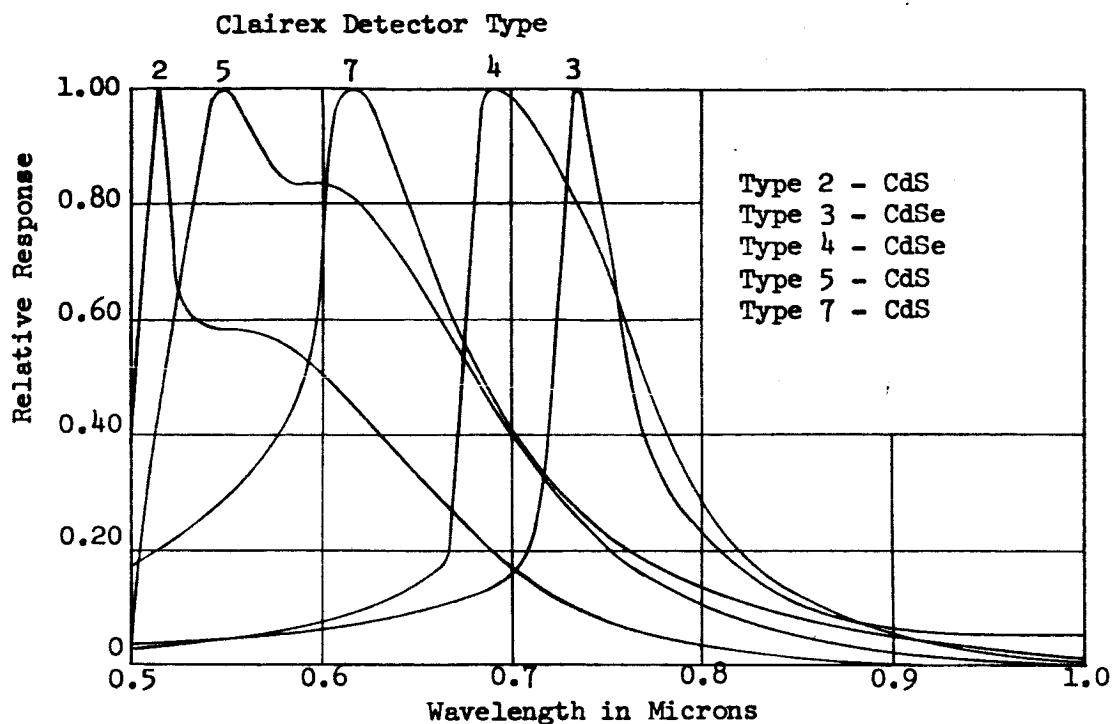


FIGURE 2.6a. SPECTRAL RESPONSE OF SEVERAL TYPES OF CLAIREX CdS and CdSe DETECTORS

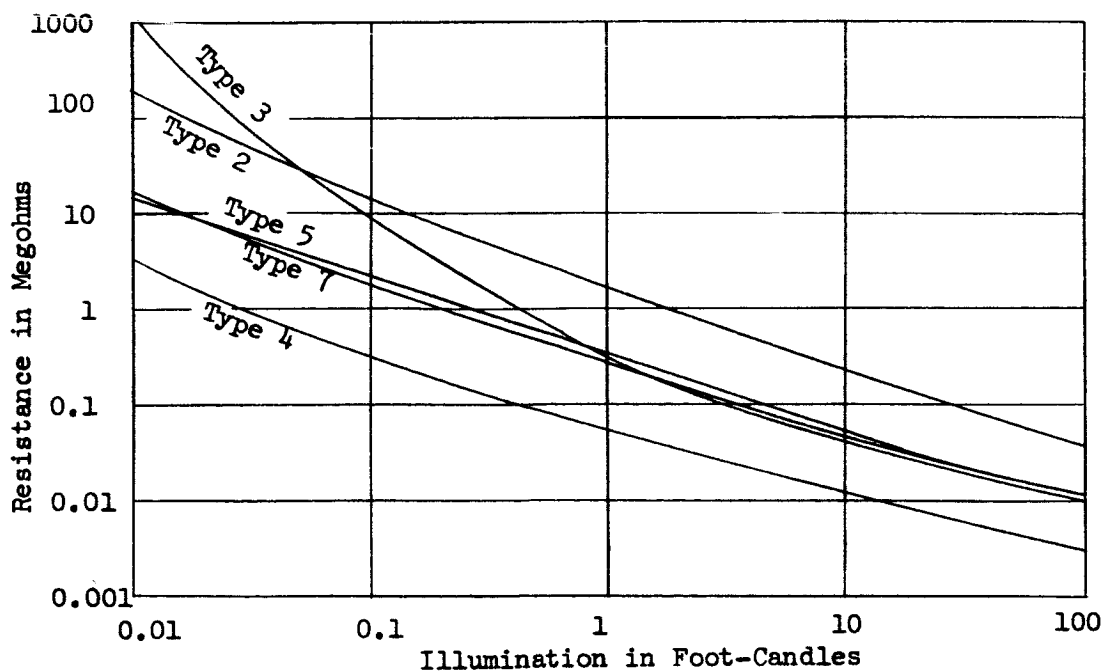


FIGURE 2.6b. VARIATION OF RESISTANCE OF CdS and CdSe WITH ILLUMINATION

provides a distribution that is radially symmetrical about the light spot. By placing electrodes at four points on the n layer, the position of the light spot relative to these four points can be determined.

The RTT provides an output that is a function of the total flux on the detector as well as the location of the centroid of the illumination on the detector. If the device is utilized in a tracking system, the voltage across the cell must be measured to determine the intensity of the detected light and this information used to normalize the gain of amplifiers used to measure the four lateral voltages in the detector.

The single advantage of this detector is the elimination of moving parts when utilized in an optical tracking system. However, as pointed out, accurate radiometry is required to provide off-axis pointing information, which is required for proportional control in a closed loop tracking system. In the presence of background radiation, the radiometric data would be erroneous, since only a small portion of the total radiometric signal would represent the star flux. Compensation of the background flux by biasing the radiometric output is feasible, but under dynamic tracking conditions the background flux will be variable and this technique cannot be utilized. The silicon cell used as a two-terminal device utilizes most of the electron-hole pairs that are created to provide a star signal. With the RTT, most of the electron-hole pairs are lost through recombination, and the signal is further reduced by the requirement for four output channels rather than one.

The NEP of the detector is 5×10^{-10} watts for a 5 cps bandwidth, and the detector provides an output ranging from 100 to 1000 volts per inch per watt for an off-axis spot of light. The D^* of the detector is 6.7×10^9 cm-cpw^{1/2}/watt compared to a D^* of 10^{12} cm-cps^{1/2}/watt for a photovoltaic silicon detector used as a two-terminal device. The detector sensitivity is thus compromised to provide positional information.

2.2.3 Extended Area Detectors With Storage

2.2.3.1 Vidicon

In the RCA C-73496 vidicon, which is a miniature vidicon developed for high sensitivity in slow scan applications, a thin-film composed of compounds of antimony and sulfur is vacuum-deposited on the back of the entrance window. This photoconductive layer which is about four microns thick, is called a target. The spectral response illustrated in Figure 2.7, peaks at 0.52 microns, and the quantum efficiency at the spectral peak is close to unity. The high capacitance and resistivity of the photocathode provides electronic charge storage capability, and the combination of high quantum efficiency and storage capability yields a sensitivity of 650 microamperes per lumen under moderate lighting conditions.

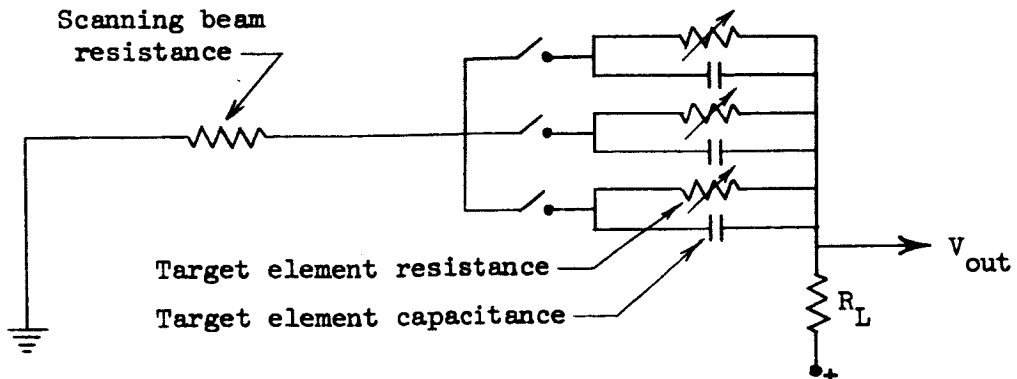
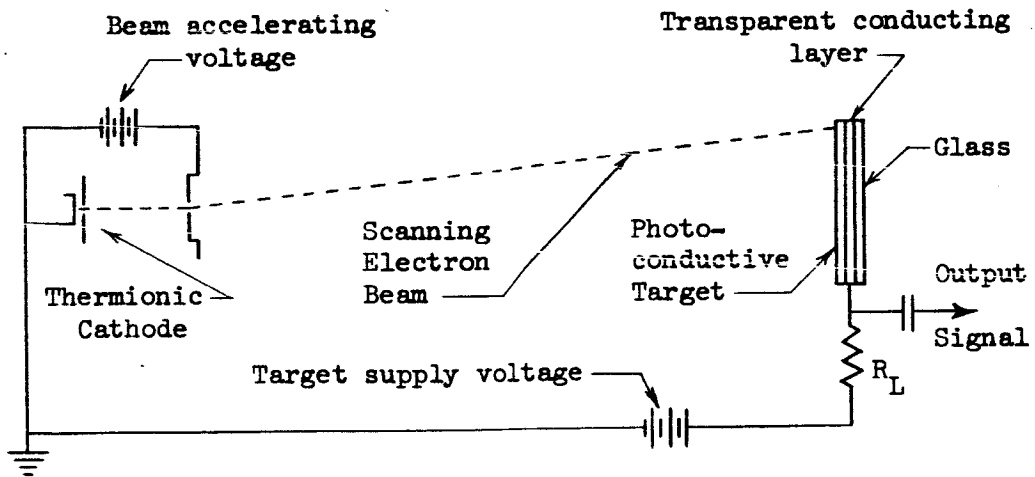
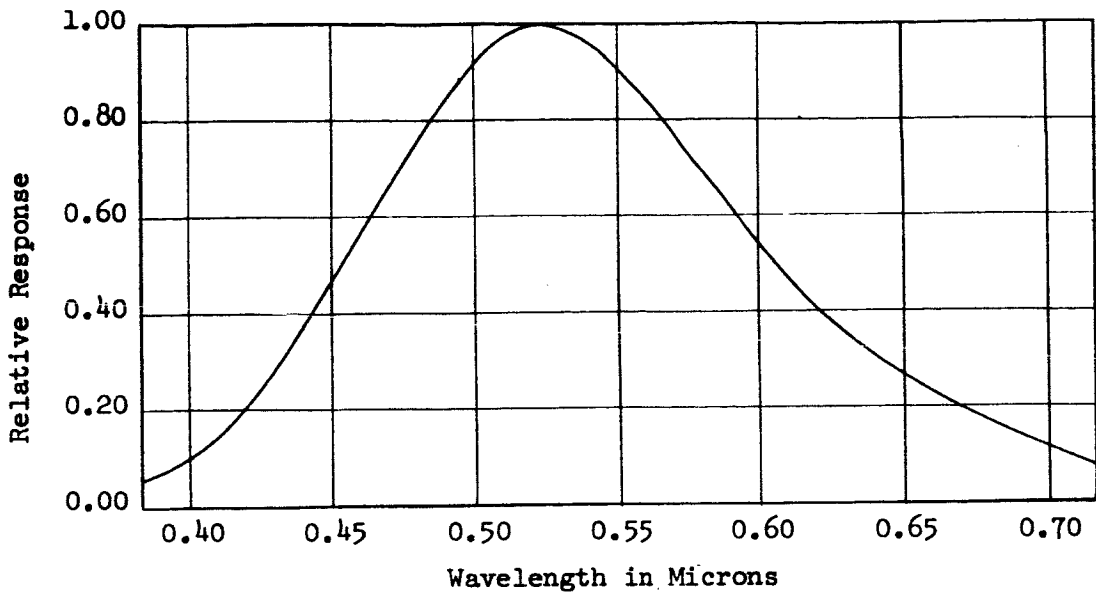


FIGURE 2.7 SPECTRAL RESPONSE (RCA C-73496) AND EQUIVALENT CIRCUIT OF VIDICON

The equivalent circuit of the vidicon is illustrated in Figure 2.7. The scene being viewed is imaged on the target, which is biased positively with respect to the electron gun cathode by 10 to 15 volts. If the target is unilluminated, the potential on the back of the target will be reduced to that of the electron gun cathode after several scans. Subsequent to this initial target charging period, the beam will deposit sufficient electrons to compensate for the leakage current through the target layer in the preceding frame period. If the target is then illuminated, its resistivity decreases and the current flow from the back to the front surface of the target is increased. Since the target potential is reduced, the number of electrons deposited on the target by the scanning beam will increase. This increase in deposited electrons is reflected in the load resistor, R_L , as a current flow. The current in the load resistor comprises the output video signal.

The resistivity of the target is a function of the illumination on the target, and at low light levels, the change in resistivity is also cumulative over the frame period. In an image dissector, electrons are continuously emitted from the photocathode, but all are discarded except those from a limited sampled area. This storage characteristic of the vidicon becomes useful when the star tracker is operated in the presence of high sky background. Since both the star and the background radiance are averaged over a frame period, if the total star flux incident on the vidicon is greater than the statistical average of the background radiance, the star can be detected.

The performance of the vidicon star tracking system can be calculated from the following expression:

$$S/N = \frac{F_c C S B r_a}{\sqrt{2q(i_d + IAbS)\Delta f}}$$

where S is the gain in sensitivity due to storage

r_a is the amplitude response of the scanning beam to small electrostatic charges

A is the area of the photoconductive target (square feet)

The storage gain S is equal to the number of scanned elements in the raster. Since the star image falls on one line of the raster, the star image will be scanned once per frame, and the star signal is allowed to accumulate between successive scans.

If the horizontal resolution is made equal to the vertical resolution, where the vertical resolution is determined by the number of scanning lines used in the raster, the number of elements in the raster will be the square of number of raster lines.

2.2.3.2 Image Orthicon

Four separate functions are performed in the image orthicon tube to produce a video output signal (figure 2.8). The image orthicon utilizes an image section, a target mesh storage section, a scanning section and a multiplier section to perform the four functions. In the image section, electrons emitted by the photocathode, are linearly accelerated providing an electron image of the scene being viewed. This electron image is then directed onto a target composed of a glass disk which is in close proximity to a fine mesh screen. When a target of insulating material is bombarded by high velocity electrons, secondary electrons are excited at the surface. An electrostatic charge pattern is established on one side of the glass target which corresponds to the optical image on the photocathode. The opposite side of the glass target will become charged positively with respect to the equilibrium potential of the target. In the scanning section the target is scanned by an electron beam, and electrons are deposited on the target in direct proportion to the electrostatic charge pattern on the rear side of the target. The electrons that are not deposited on the target are collected then amplified in a multiplier section. The output of the multiplier becomes the video output signal.

By coupling the noise-free gain of the electron multiplier and the storage gain provided by the glass target, a highly sensitive detector is produced. The image orthicon is best suited for low light level applications. Due to the low capacity of the target, and the limited magnitude of the electrostatic charge that can be accumulated on the target due to the natural physical limitations of the target and mesh combination, the output of the image orthicon saturates when the illumination on the faceplate increases by two orders of magnitude. For daytime operation against a bright sky background, the image orthicon does not perform as well as a vidicon, though for a given diameter collecting optics, the image orthicon is capable of detecting a star that is five star magnitudes dimmer than with the vidicon.

Since the impedance of the target is very high, the mesh is used to establish the target equilibrium voltage. If the photocathode is dark, the scanning electron gun will bring the rear of the target to the electron gun cathode potential. The front of the target should then be at the equilibrium potential, but since the mesh and the target are capacity rather than direct coupled, this equilibrium cannot be achieved. If the mesh is brought closer to the target, the potential of the front surface of the target can be brought closer to the equilibrium potential. However, the positioning of the mesh with respect to the target must be compromised to permit the build-up of electrostatic charge under normal operating conditions, so essentially minimum sensitivity is a compromise with dynamic range.

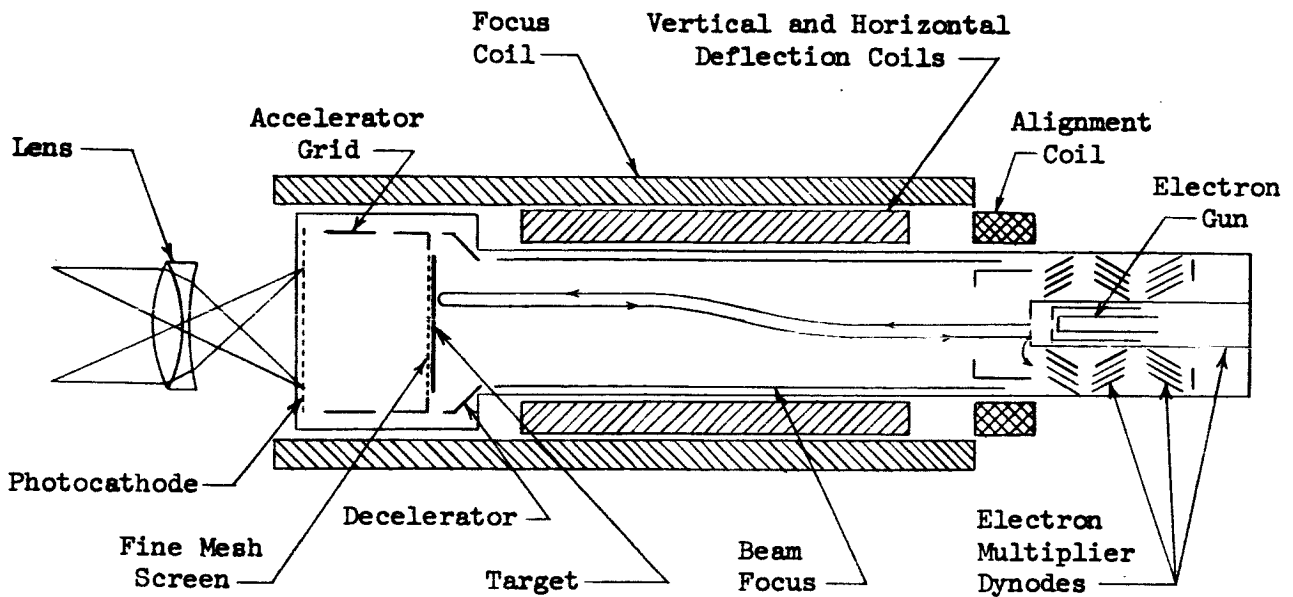


FIGURE 2.8a. IMAGE ORTHICON SCHEMATIC ARRANGEMENT

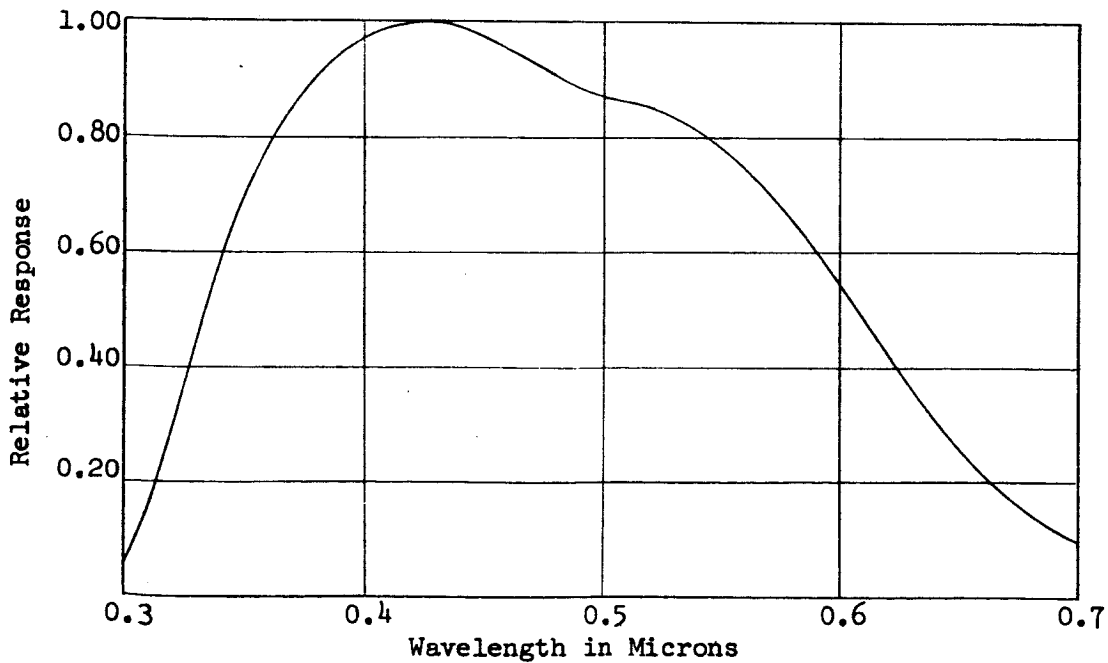


FIGURE 2.8b. SPECTRAL RESPONSE OF WESTINGHOUSE WL-7611 IMAGE ORTHICON

The performance of an image orthicon star tracker can be calculated from the following expression:

$$S/N = \frac{F_c t CSB r_a}{g_m \sqrt{2q (i_d + tIAbS)(1 + 1/G)\Delta f}}$$

- where
- F_c is the effective star flux incident on detector (lumens)
 - t is the transmission of the fine mesh screen which is in front of the target in the image section
 - C is the detector response to the incident star flux (amp. per lumen)
 - S is the gain in sensitivity due to storage
 - B is the electronic transfer characteristics of the signal transfer
 - r_a is the amplitude response of the scanning beam to small electrostatic charges
 - g_m is the increase in beam noise due to incomplete modulation of the scanning beam
 - q is the charge of an electron (coulomb)
 - i_d is the photocathode dark current (amp.)
 - I is the illumination on the detector due to background radiance (foot-candles)
 - A is the area of the photoconductive target (square feet)
 - b is the detector response to background flux (amp per lumen)
 - G is the gain per dynode stage in the photomultiplier
 - Δf is the electronic bandwidth (cycles)

2.3 MECHANICAL MODULATION METHODS

The single element "point" detectors provide an output signal that is independent of the location of the flux concentration on the sensitive area of the detector. When this type of detector is used in an optical tracking system, some mechanical method of modulating the incident radiation must be utilized to provide an indication of the location of the luminous flux relative to the center of the field of view of the optical tracker. Some of the mechanical modulation techniques that have been used to encode the optical signal to provide error information include radiation balance, optical field dither, amplitude-modulated reticle and frequency-modulated reticle systems.

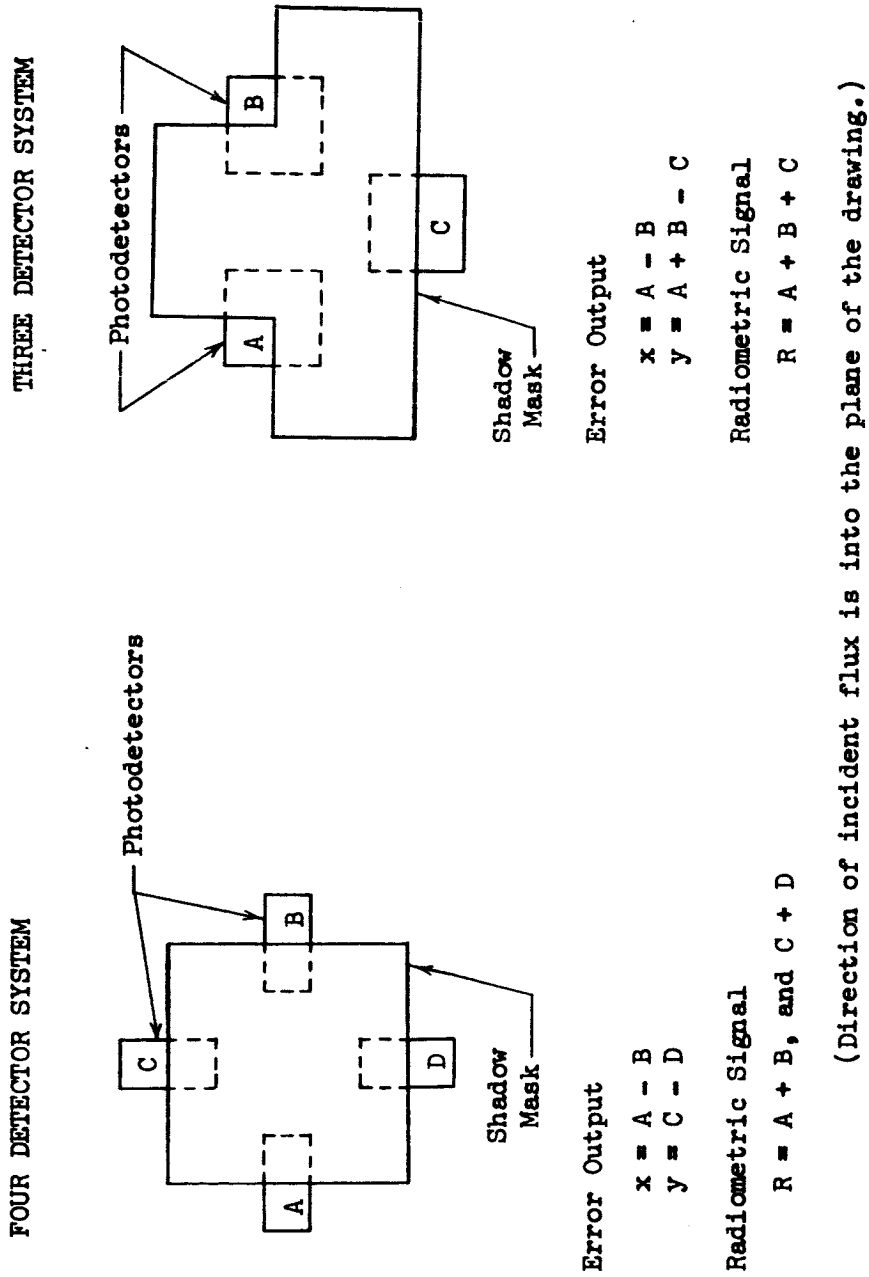
2.3.1 Radiation Balance System

In a radiation balance system, the radiant flux from the object that is to be tracked is divided optically into two or more channels. The optical tracker is designed so that it will be aligned with the target when the signal from all the channels are equal. Different system implementations have been used in operational systems, and while the most common configuration is an arrangement of four detectors utilized in pairs to provide pointing information in two orthogonal axes, a system using three detectors to provide two-axis control is feasible. In Figure 2.9 is illustrated a typical four-detector radiation balance system, and a three-detector system, both using shadowing masks to change the total flux on the different detectors as a function of the angle between the target and the line of sight of the optical tracker. The three-detector design was implemented by the Jet Propulsion Laboratory in their Earth Sensor, which was used to provide an attitude reference relative to the earth in the Ranger series of space flights.

The X and Y axes errors in the four-detector configuration is derived by comparing the outputs from two detectors (A-B and C-D), and the total signal or the radiometric value (R) of the target is determined by adding the signals from two opposing detectors. The X axis error for the three-detector configuration is derived by comparing the outputs from two detectors, and the Y axis error is obtained by comparing the outputs from all three detectors. The radiometric signal is the sum of all three signals.

The reliability of the three detector system is greater than the four-detector system since the component count in the system is reduced. For good linearity and resolution, highly sensitive, matched detectors are required in both systems. The three-detector system requires three detectors that are matched to each other, while the four-detector system requires two pairs of matched detectors. In the three-detector system, the outputs of the three detectors cross-couple, so nonlinearity in detector response will add an offset error to the sensor error transfer curve.

FIGURE 2.9 THREE AND FOUR DETECTOR RADIOMETRIC BALANCE SENSORS



The radiometric balance type of sensor does not use scanning or moving mechanisms to modulate the optical signal. The advantage of this system is the high reliability due to the simplicity of the basic design. However this design has no background discrimination capability, and any nonuniformity in the background radiance will produce an error output. In addition, the background signal from the detector is produced by the sum of the background flux on the detector, so the instantaneous field of view of the detector must be very small if a dim target is to be acquired and tracked in the presence of background radiance. Defining the minimum detectable star for a background limited star tracking system as the star magnitude that will provide an illuminance at the entrance aperture of the sensor that is equal to the background luminance within the solid angle defined by the sensor field of view, then

$$F_s = \frac{B' \Omega}{\pi}$$

where F_s is the star illuminance in lumens/ft²

B' is the background or sky brightness in foot-lamberts

Ω is the sensor field of view in steradians

The minimum detectable star for a background-limited optical system is thus a function only of the background brightness and the field of view of the sensor. The size of the aperture of the sensor or the ultimate sensitivity of the detector are unimportant when the background radiance is the primary noise source. The luminance from a one foot-lambert sky background will provide an effective background illuminance at the entrance aperture of the optical system of 2.67×10^{-6} lumens/ft² for a sensor with a 10 arc-minute by 10 arc-minute field of view. A -1.64 magnitude star will provide this illuminance, so only celestial bodies brighter than -1.64 magnitude are detectable under the given conditions. Since the daytime sky brightness at sea level is approximately 500 to 1000 foot-lamberts under low sky background conditions, and Sirius, the brightest star in the heavens is a -1.47 magnitude star, a radiation balance star tracker is only usable as a nighttime star tracker.

2.3.2 Mechanical Optical Field Dither

The radiation balance star tracker is operated in a dc mode, so the collected star flux must be greater than the total background flux for the star to be detectable. Since the sky background in a limited region, say one degree square is quite uniform, the sky background can be used to establish a threshold to permit detection of a star by comparison of one portion of the sky to another. If this comparison is performed cyclically, the star signal will be encoded at a given frequency. The background signal out of the detector for a uniform sky background will

be a high level signal with a frequency distribution resembling noise. A narrow electronic bandpass centered about the repetition frequency of the star signal can be used to attenuate the background signal. Since the background signal is a function of the characteristics of the detector utilized in the optical detection system, parameters such as the modulation frequency and the electronic bandwidth will also influence the system performance, so systems of this type must be considered individually to determine performance limits.

If the star signal is correlated in the frequency domain and the background signal is uncorrelated, increasing the aperture of the optical system will increase the target signal to background noise ratio. The collected star and the background flux both increase proportionately to the square of the aperture, but if the background signal out of the detector has a "white" noise distribution, the rms value of the background signal in a given bandwidth will increase as the square root of the background signal. Thus the star signal with a given background will increase linearly with the aperture size.

Instead of taking discrete samples of finite areas, the instantaneous field of view can also be mechanically dithered to modulate the star flux. The dither can be produced by oscillating a mirror in the optical path of the star tracker, or by moving the entire sensor head. By scanning the dither pattern, a large field of view can be searched.

A star tracker utilizing this dither scanning principle was designed by Nortronics for the SM 62A Snark missile, and contained a two-inch diameter optical system with a 20-inch focal length, an RCA 7029 photomultiplier as the detector, and a circular instantaneous field of view of 40 arc-seconds. The system was capable of tracking third magnitude stars in the daytime. Demonstrated tracking capability included tracking of a +1.93 magnitude star against a 1350 foot-lambert background with a peak signal to rms noise ratio of 22:1, and tracking of a +2.75 magnitude star against a 410 foot-lambert background with a peak signal to rms noise ratio of 22:6. These results were obtained with very narrow electronic bandwidths, so long search acquisition times are required, and the information rate is low, producing a star tracker with a limited tracking rate capability.

2.3.3 Amplitude and Frequency Modulated Reticule Systems

A common technique in the design of optical tracking systems is the use of a reticle placed at the focal plane of the optical system to modulate the focused optical energy and to encode the target error information. The reticle is composed of an intricate pattern of opaque and clear segments, that combined with the proper scanning motion is capable of providing target signal modulation and at the same time attenuating the signal caused by background flux.

In Figure 2.10 is illustrated two reticle systems that provide an amplitude modulated (AM) and a frequency modulated (FM) target error signal. The information processing circuitry in these systems make use of demodulation techniques common to communication circuitry to derive the track error signal.

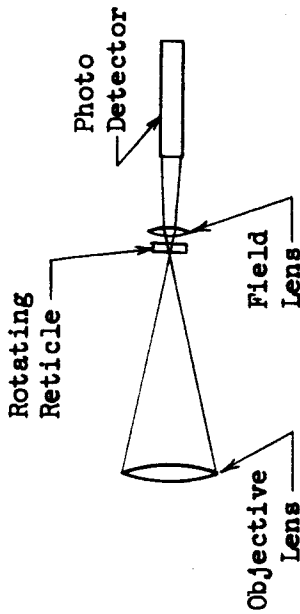
In the AM system, a "rising sun" reticle is rotated to modulate the target signal. The rays of the "sun" are composed of alternate clear and opaque segments, and the other half of the reticle composed of a 50 percent transmitting surface. When the target is off-axis, the target signal will be an AM carrier signal that is 100 percent modulated at the reticle rotation frequency. The target error information is encoded in two side bands about the carrier frequency. The carrier frequency is the reticle rotation frequency times twice the number of spoke pairs in the reticle pattern, and the side bands are equal in width to the reticle rotation frequency. The phase and the amplitude of the envelope of the target signal are compared with a reference signal to determine the direction and magnitude of the track error.

In the FM system, rotation of a wedge placed in the convergent light path of a refractive optical system, (off-axis mirror in a reflective optical system), will cause the target image to move in a circular path at the focal plane of the lens. The scanning motion of the target image is called nutation. For the AM system, the reticle is rotated, but the reticle is stationary in the FM system and the target image is scanned over the reticle pattern. When the target is on-axis, the nutation circle will be symmetrical with respect to the center of the reticle and the target signal modulation produced by the reticle will be an FM carrier signal. The frequency of the FM carrier is the product of the nutation rate and the number of spoke pairs in the reticle. When the target moves off-axis, the nutation circle will be displaced with respect to the center of the reticle, and the target signal will be frequency modulated as the nutated image scans over the reticle pattern. The target signal is amplified, limited, then demodulated to provide a track error signal. The phase of the track error signal is a function of the phase relationship of the high and low frequency components in the target signal and its amplitude is a function of the frequency deviation components in the target signal.

The advantage of a reticle system is that a relatively large instantaneous field of view can be scanned using a simple mechanical motion. The scanning is provided by rotation of an optical element, which is superior to the dither scan system, considering the drive power requirements, and the reaction force created by oscillating elements or movement of the entire sensor head. An ideal reticle has an average transmission of fifty percent, so that a uniform background will produce no ac components when scanned by the reticle.

FIGURE 2.10 OPERATIONAL DIAGRAM - AMPLITUDE AND FREQUENCY MODULATED SCANNING SYSTEMS

AM RETICLE SYSTEM



FM RETICLE SYSTEM

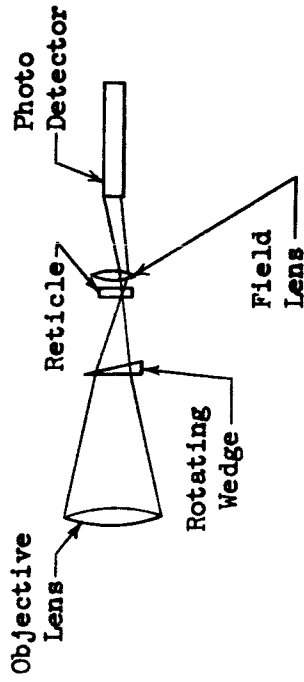
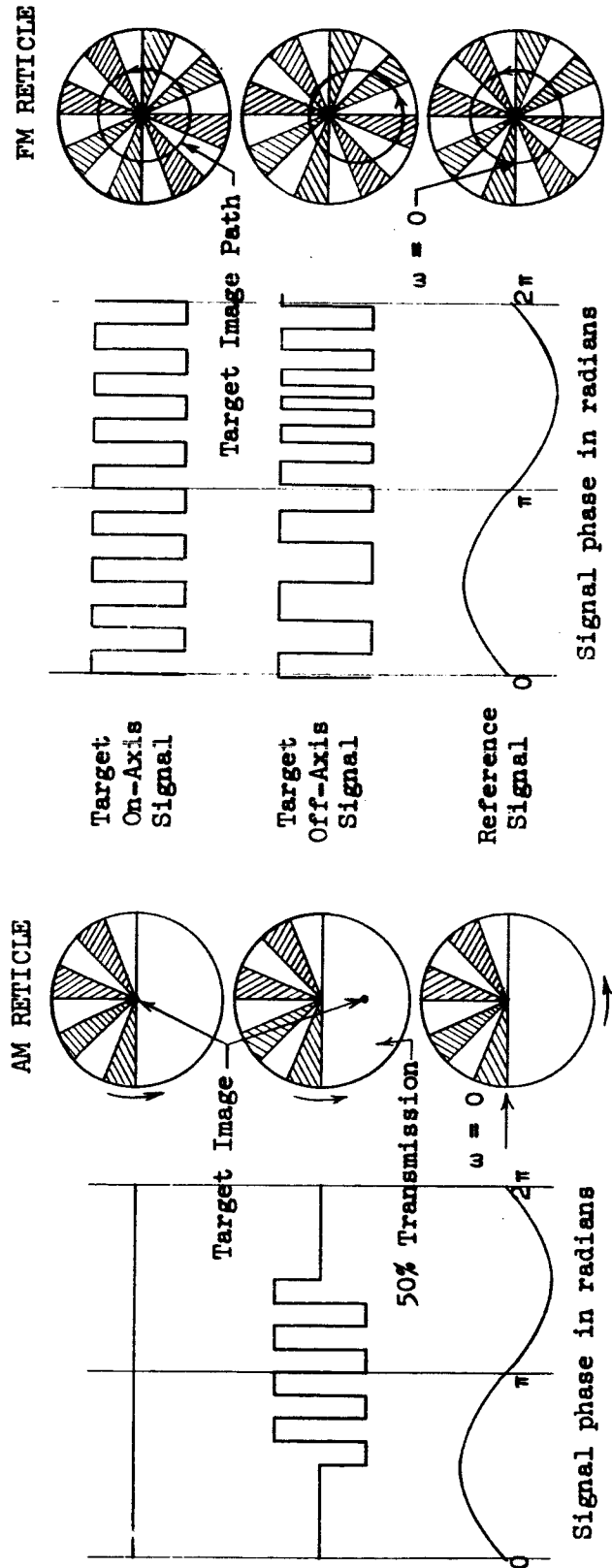


PHOTO DETECTOR AND REFERENCE SIGNAL WAVEFORMS



Large background gradients will produce modulation components at the basic scan frequency, but since the system carrier frequency is much higher, only the lower amplitude harmonics of this signal will be within the system bandpass. The reticle, however, cannot provide discrimination against fine background details. In addition, manufacturing defects in the fabrication of the reticle will produce modulation components even with a perfectly uniform background.

With the rotating AM reticle system, the modulation efficiency of the reticle decreases when the target image falls in the area of the reticle where the detail in the pattern is smaller than the image size. This effect causes the track error signal to decrease proportionately as the target image approaches the center of the reticle. When the target is aligned with the optical axis of the telescope, the modulation efficiency is zero. There are two disadvantages in this loss of signal at null. First, the system cannot provide a positive indication that the target is being tracked, since the signal from the optical detector is the same when the target is on-axis, as when there is no target within the field of view. Second, the target error signal must exceed the system input noise before the target error signal is detectable. Since every system has a finite amount of noise, the tracking system will have a dead band about the null point, producing a system that tends to "hunt" when the target is on-axis.

In the FM system, a track indication signal is always present whenever the target is within the field of view. With the target on-axis, the detector output is an FM carrier, which can be used as a track indicator. Since the amount of frequency modulation in the target error signal is a function of the location of the target nutation circle with respect to the center of the reticle, the demodulated error signal will provide a track error signal that is proportional to the deviation of the line of sight to the target from the optical axis of the tracker. The FM system has superior tracking capability over the AM system in the presence of noise, since the optical detector signal is limited, and high amplitude noise pulses will not saturate the system. However, the AM system utilizes a narrower system bandwidth, and has a higher system sensitivity, and is capable of detecting dimmer targets under zero background conditions.

SECTION 3

UTILIZATION OF OPTICAL SENSING ELEMENTS
IN A SPACE VEHICLE

3.1 MONITORING OF PLATFORM DRIFT WITH A STAR TRACKER

The performance of the platform under a high gravity environment and for extended periods in a zero gravity field can be monitored by means of celestial sightline determinations. Platform drift can be determined and the platform updated from information obtained from several star sightings. The same star tracker would also be capable of providing an accurate reference for platform realignment should the platform be tumbled in a mission, or in the event the platform is deactivated to conserve power in an extended mission.

3.1.1 Platform Drift During Launch

To check platform drift during launch, a star tracker capable of tracking dim stars in the presence of a relatively high ambient sky background is required. Daytime star tracking capability is desirable so that the experiment does not place unnecessary restrictions on the launch window. For this experiment, the tracker window must be positioned on the vehicle so that the tracker can look upwards as the vehicle is pitched over in the boost phase. The magnitude of the pitch maneuver and the size of the optical window place restrictions on the tracking capability of the sensor, and it is doubtful that a single star can be tracked continuously during the complete boost period unless the trajectory and vehicle attitude is chosen specifically to achieve this result. The star tracker must be capable of high slew rates and rapid star acquisition capability to provide a good celestial reference during the launch phase. A single star sighting cannot be used to determine drift in three axes due to cross coupling effects, so multiple star trackers or sequential star sightings within the drift limitations of the platform are required. A single star sighting, however, can establish the error limits in two axes, assuming that the sighting is made at a small angle to the third axis.

3.1.2 Platform Drift in Earth Orbit or in Deep Space

To check platform drift in earth orbit or in deep space, sightings on two or three stars can be used to obtain an inertial fix which can be compared with the platform alignment. For earth orbiting vehicles, two star sightings are sufficient if vertical determination from auxiliary equipment is sufficiently accurate to be used as the third reference vector. The star sightlines should be mutually perpendicular to each other to minimize cross coupling but the window size restrictions and star availability may preclude this desired feature.

To realign the platform in earth orbit when the inertial reference is lost, rough vehicle alignment can be made by means of horizon sensors and sun sensors. Orbital information plus the orbital time must be available to calculate star coordinates.

The vehicle alignment using horizon and sun sensors will be sufficiently accurate so that the star will fall in the instantaneous field of view of a star tracker with a field of one degree by one degree. The platform alignment can then be corrected by comparing the star shot with the platform orientation.

For a vehicle in solar orbit, an inertial reference can be reestablished by rotating the vehicle about an axis that is aligned with the sun and searching a segment of space for an easily detectable and easily recognizable star such as Canopus. Canopus is well suited for this application since it is close to the south ecliptic pole and this star provides a reference vector at a large angle to the sun line. Methods by which Canopus can be identified include color, magnitude, and relative angles between detectable stars in the search volume. For this method to be effective, the vehicle trajectory and the mission time must be available since the angle between the sun and the star line is a function of these two variables.

3.1.3 Equipment Required for Platform Drift Measurements

The equipment required to accomplish most of the applications delineated include a star tracker capable of tracking dim stars against a high sky background, mounted in a two gimbal, gyro-stabilized platform. The star tracker will be capable of automatic tracking of a star within its field of view. The sightline to the star will be read out using precision resolvers, and this information can be either telemetered to the ground or fed to an on-board computer for comparison with the inertial platform alignment. Star ephemerides must be available from an on-board storage and a computation made to convert this data to gimbal angles, or this information telemetered to the vehicle.

A star tracker utilizing a vidicon as the sensing element is capable of acquiring and tracking stars against a bright sky background. This vidicon star tracker will be considered for the platform alignment reference check during the vehicle boost period because of this capability. The other applications for which a star tracker is suited, such as in-orbit platform alignment, or platform realignment following loss of the inertial reference, can be handled by a star tracker such as the Quadrant Photomultiplier Star Tracker developed under Contract No. NAS 8-5393.

3.1.3.1 Use of the Vidicon Star Tracker to Monitor Platform Drift During Launch

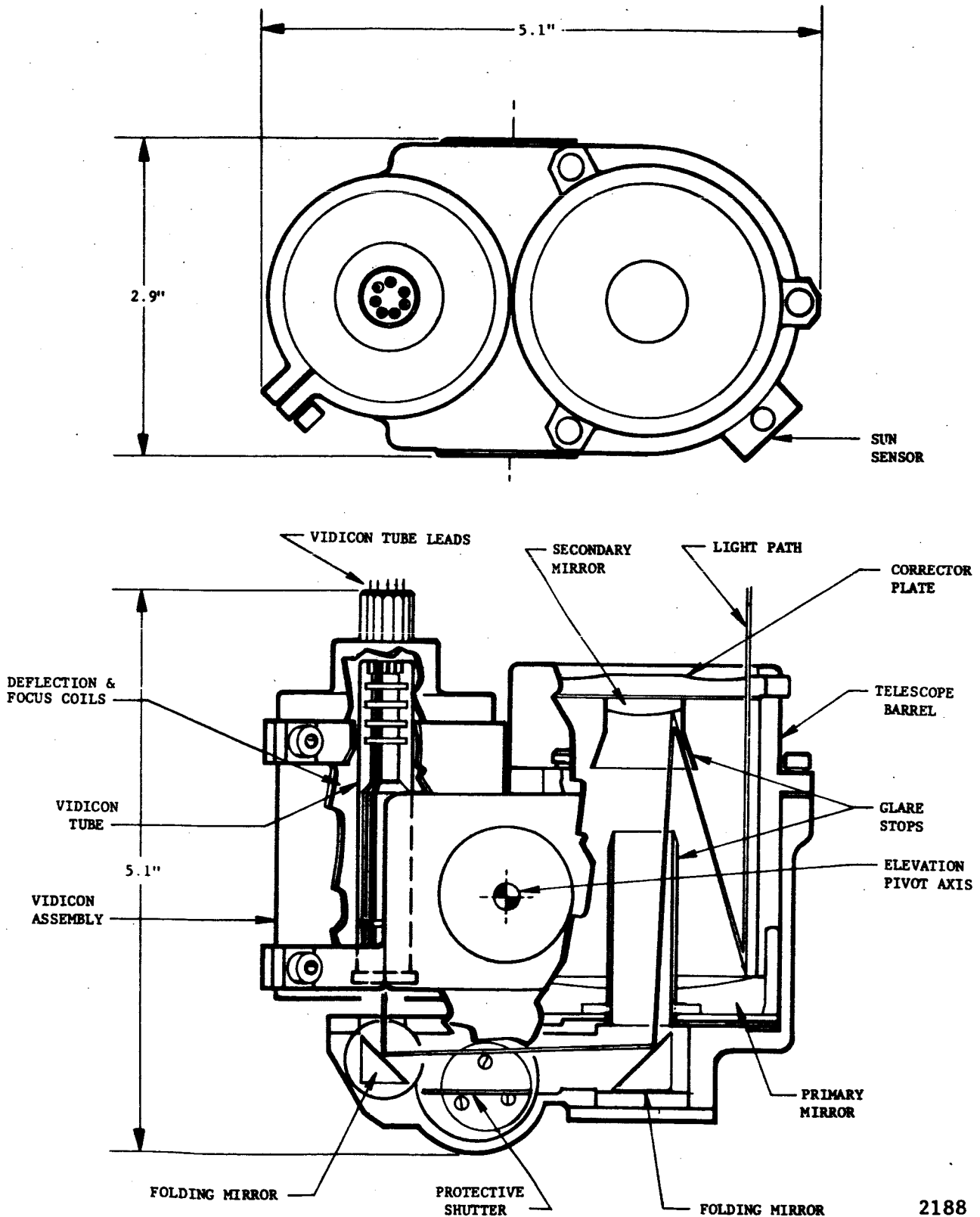
The use of a star tracker to monitor platform drift that may be caused by the increased gravitational force that occurs during the vehicle boost period, imposes the most severe test of a star tracker performance capability. First, the star tracker must be capable of tracking accuracies higher than the tracking accuracy of the platform, under the vibration environment produced by the boosters, for the tests to be meaningful. Second, the star tracker must be able to acquire and track a star in the presence of a bright sky background, since most space launches are daytime launches. Third, the star tracker must be capable of rapid star acquisition, since the tracker window limitations may not permit continuous tracking of one star during the total boost period, as the vehicle is pitched over in its downrange trajectory profile. In addition, performance degradation may be caused by the plume exhaust products or by ablative materials in the vehicle shroud.

The vidicon star tracker is well suited to this mission since it is capable of rapid star acquisition under daytime conditions, and in addition can track a star that is located anywhere within its field of view. The star image does not have to be aligned with the optical axis to provide good tracking accuracy, so a control system with a high response rate is not required for the monitoring tasks.

3.1.3.2 Star Tracker Description and Accuracy

A miniature vidicon optimized for slow scan operation is used as the detector for the star tracker. The outline of a vidicon star tracker is illustrated in figure 3.1. A cassegrainian optical system with a long back focal length is used as the collector, and provides a long focal length lens that requires a relatively small volume. The long back focal length (separation of the focal plane from the last element in the optical system) permits the optical path to be folded, resulting in a compact sensor head design.

If the sun is close to the field of view of the sensor, stray radiation that is diffusely reflected off portions of the telescope housing may raise the ambient illumination level to a point where the star signal cannot be detected. Empirical determinations of this pointing limitation indicate that the background illumination level becomes excessive for proper operation, when the sun is within 20 degrees of the optical line of sight. Protection for the vidicon faceplate from direct solar illumination is required to prevent permanent damage to the photosensitive surface. For the vidicon star tracker, this protection is provided by means of a sun sensor which actuates a shutter in the optical system whenever the sun is within 20 degrees of the line of sight.



2188

FIGURE 3.1 OPTICAL HEAD OF VIDICON STAR SENSOR

NORT 65-126

The number of stars that can be detected against a daytime sky background must also be considered. The net effect of the sky background radiance is an increase in the random noise level at the output of the vidicon. As the sky background level increases, proportionately brighter stars are required to produce a signal-to-noise ratio sufficient to discriminate the star signal from the background signal. The number of stars that can be tracked will thus be inversely proportional to the sky background level.

Star brightness itself cannot be used as the sole star availability criterion since the presence of two stars in the field of view that cannot be distinguished from each other on the basis of brightness is a possibility. Therefore, star brightness and star separation, both angular and with respect to magnitude, are used to determine star availability.

The number of stars that can be tracked by a vidicon star tracker system is determined by the characteristics of the optical system, the active area of the vidicon, and the background radiation level. The system considered has an entrance aperture of 3.5 inches or a corrected aperture of 3.2 inches, considering optical blocking losses due to the secondary mirror and the spider supporting the mirror in the cassegrainian optical system. A focal length of 57 inches and an active vidicon target area of 0.16 by 0.16 inch produces an instantaneous field of view of 10 x 10 arc-minutes. A 2.5 visual magnitude star can be tracked with this star tracker, against a 1000 foot-lambert background.

The accuracy of the star tracker system is distributed as shown in Table 3.1.

TABLE 3.1
VIDICON STAR TRACKER ACCURACY

	<u>rms arc-seconds</u>
Vidicon resolution	3.0
Vidicon linearity (0.5%)	3.0
Angle pickoffs	3.0
Total rms error	5.2 arc-seconds

The system accuracy may be improved by modifying some of the system parameters. For example, the field of view of the tracker, which for the system considered is 10 x 10 arc-minutes can be narrowed by extending the focal length of the optical system. With a small field of view, the ability of the tracker to function in the presence of a high ambient background is improved. The accuracy will be improved proportionately to the reduction in the field size if the rest of the star tracker design parameters remain the same. This expediency places a more stringent requirement on the accuracy with which the star tracker must initially be pointed, unless time is available to perform a programmed search by moving the instantaneous field of view over a larger search field of view. The star tracker accuracy can also be improved by the use of more accurate resolvers to read out the gimbal angles in the star tracker mount.

The telescope of the star tracker must be equipped with a window allowing a wide field of view. The size of the window will depend upon the physical parameters of the telescope and the gimbal system. A system with a field of view of ± 55 degrees would require a window approximately 13 inches in diameter.

The optical head complete with a two-axis gimbal assembly can be mounted in a cylindrical space 13 inches in diameter by 10 inches long. A volume of 1350 cubic inches; a weight of 28 pounds; and an average power of 20 watts, is required for the star tracker. The size of the associated electronics is about 350 cubic inches and has a weight of 18 pounds with a power consumption of 19 watts.

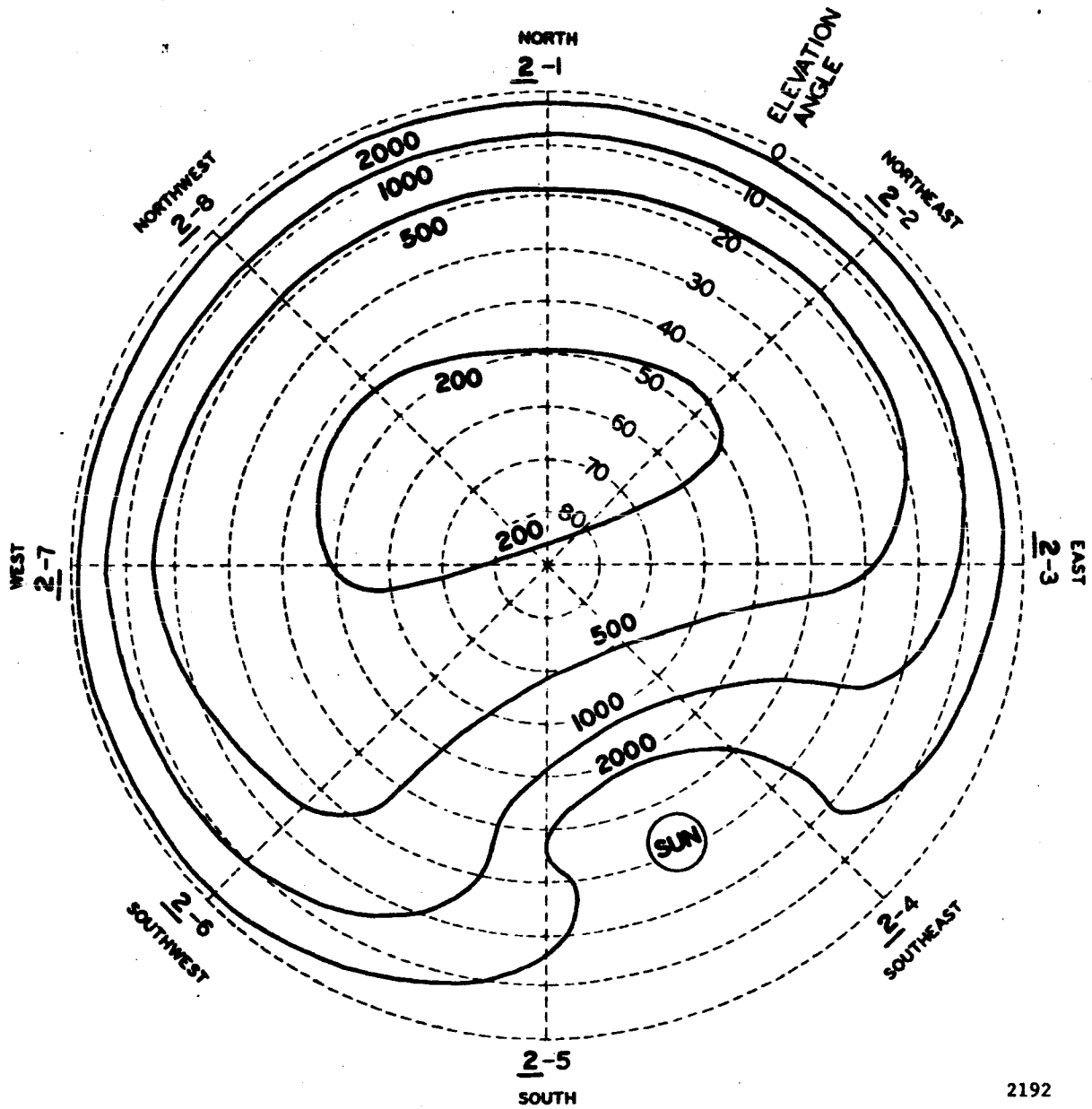
3.1.3.3 Brightness of the Daytime Sky Background

Further information on the sky brightness problem can be obtained from a report on the "High Altitude Daytime Sky Background Radiation Measurement Program, Sky Luminance, Polarization, Infrared Radiance and Albedo Data from Research Vehicle No. 1," Part 1 and Part 2, Technical Documentary Note No. AL TDR 64-134, U. S. Air Force Avionics Laboratory, Research and Technology Division, Wright-Patterson Air Force Base, Ohio - May 1964 (Unclassified). Representative curves of daytime sky brightness at altitudes of 20,000 and 40,000 feet taken from this report are presented in Figures 3.2 and 3.3. These curves show the magnitude of the sky brightness that will be seen by the star tracker during the launch profile.

The brightness of the sky background increases sharply in regions close to the horizon. In order to keep the background level below 1000 foot-lamberts, the sensor field-of-view must be restricted to look angles greater than 20 degrees above the horizon.

Isolumes in Foot-Lamberts

Albedo = 15%



2192

FIGURE 3.2 ISOLUME PLOT SHOWING BRIGHTNESS OF SKY
AT 20,000-FOOT ALTITUDE

Isolumes in Foot-Lamberts

Albedo = 12%

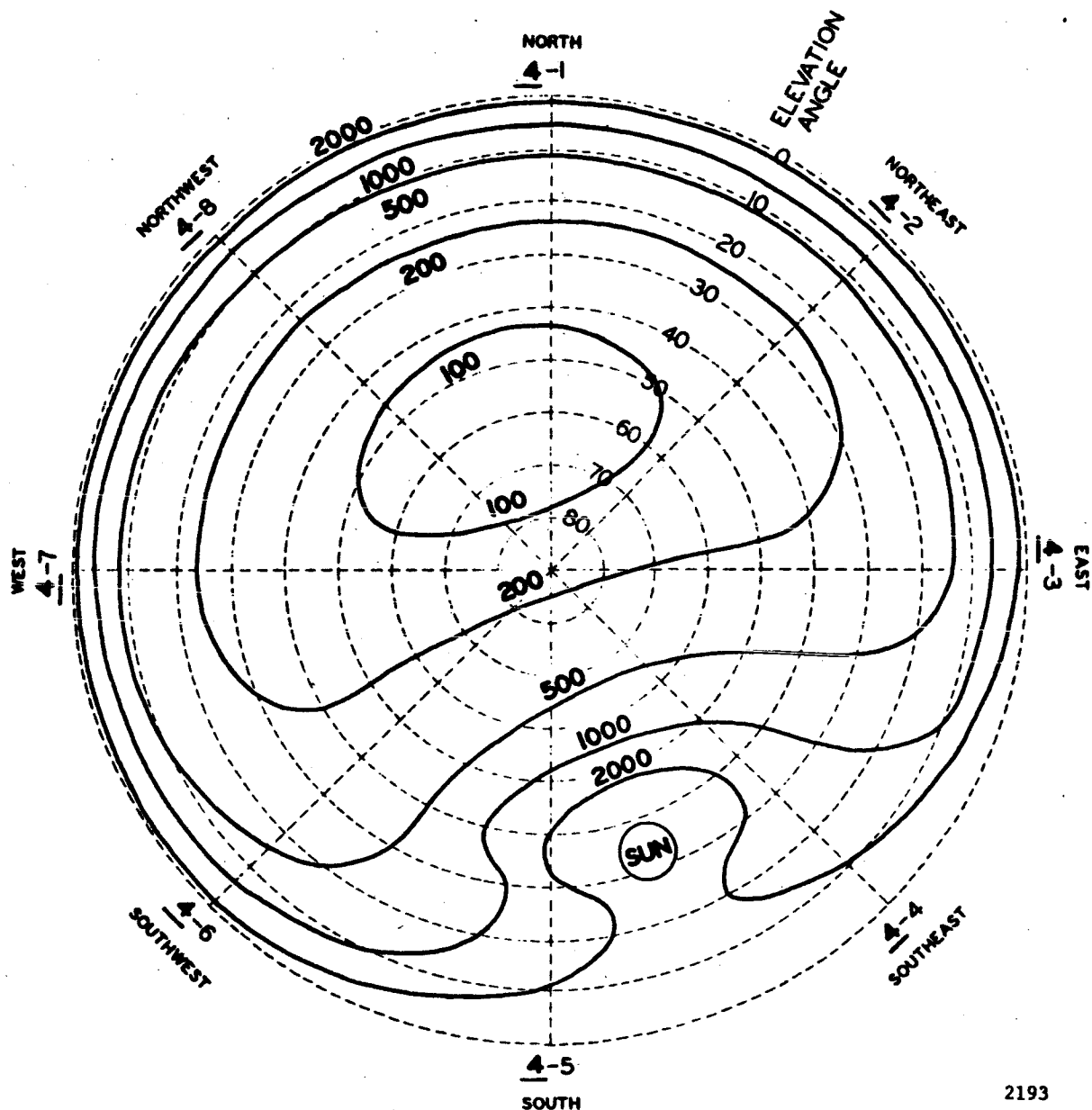


FIGURE 3.3 ISOLUME PLOT SHOWING BRIGHTNESS OF SKY
AT 40,000-FOOT ALTITUDE

NORT 65-126

3.1.3.4 Star Availability During Launch Period

The number of stars that can be tracked from either a stationary point on the ground or from earth orbit is dependent upon a number of parameters. The location of the horizon and the sun within the celestial sphere, the brightness of the sky background, the limits of the search field of view of the star tracker and the sensitivity of the star tracker are some of the parameters involved with star availability determination. Star availability should properly be determined by a computer program, but a quick estimate can be made using a star chart if the star tracking requirements can be defined. For the case where the star tracker is used to monitor platform alignment during the launch period, the problems involved are the location of the zenith, the horizon, the sky background and the sun with respect to the vehicle during launch. A method is outlined to show how the star chart with three overlays can be used to determine star availability for a Saturn type launch from Cape Kennedy.

The star chart (Figure 3.4) depicts the location of the stars in the celestial sphere in terms of hour angle and declination. Rotation of the earth on its axis causes the star pattern to rotate with respect to a given point on the ground at the rate of one revolution per day. In addition, the orbital motion of the earth about the sun causes the relative location of the sun with respect to the stars to precess approximately one degree per day, so the location of the sun and the stars in the celestial sphere is a function of the time of the day and the day of the year. Due to the inclination of the axis of rotation of the earth, the sun traces a path in the celestial sphere which is designated as the ecliptic, when the path of the sun is plotted over a period of a year.

The right ascension of a star is measured eastward along the celestial equator from the first point of Aries to the meridian passing through the star. This measurement is made in terms of time, and is commonly referred to as the hour angle of the star. At the autumnal equinox, the path of the ecliptic crosses the plane defined by the equator of the earth, as the path of the ecliptic moves from the northern to the southern hemisphere. The Right Ascension Hour will correspond to the time of the day that the star will be overhead during the autumnal equinox. For other days of the year, the right ascension hour of the stars at the zenith at midnight must be estimated, so that the stars that will be overhead at a given time can be determined.

The simplified Right Ascension Schedule (Table 3.1) lists the Right Ascension Hour of the stars that will be at the zenith at midnight on the dates indicated. The astronomical day begins at midnight of the calendar date and continues through 24 hours. To determine the zenith with respect to the star chart at the launch date, the time of launch computed on a sidereal time basis must be added to the right ascension hour for midnight on the launch date. Should the right ascension hour exceed 24, then 24 hours

WORLD STAR CHART

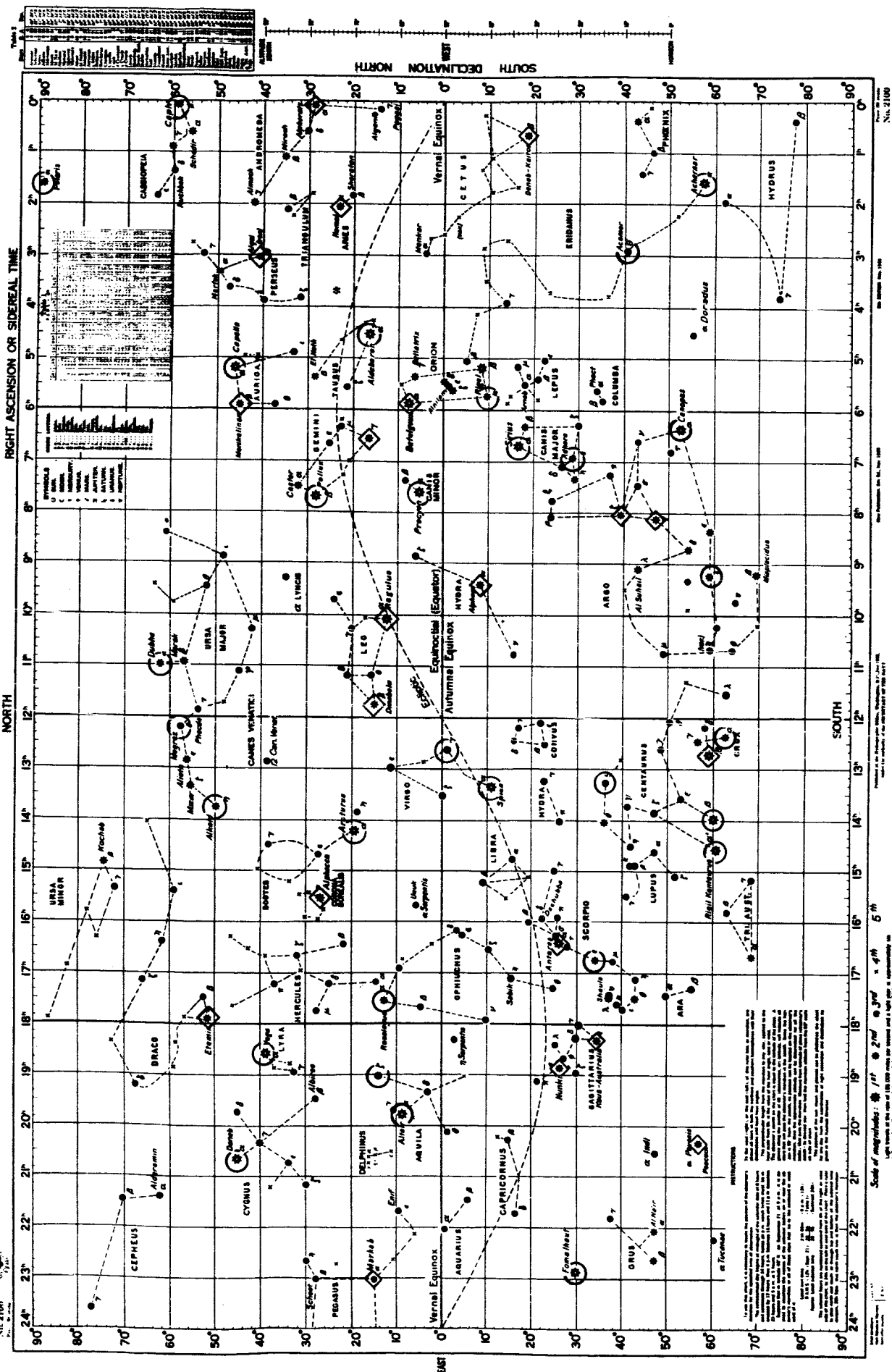


FIGURE 3.4 STAR CHART SHOWING PRIMARY AND SECONDARY NAVIGATIONAL STARS

must be subtracted from this number to determine the hour angle of the zenith stars at the zenith.

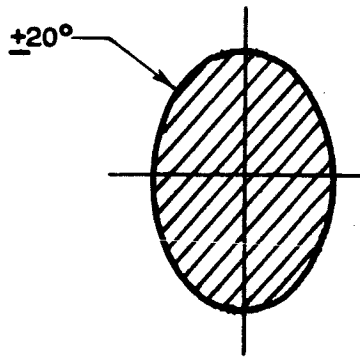
TABLE 3.2 RIGHT ASCENSION MONTHLY SCHEDULE

DATE	JANUARY		FEBRUARY		MARCH		APRIL	
	h	m	h	m	h	m	h	m
1	6	39	8	41	10	32	12	34
10	7	14	9	17	11	07	13	09
20	7	54	9	56	11	47	13	49
	MAY		JUNE		JULY		AUGUST	
1	14	32	16	54	18	33	20	35
10	15	08	17	10	19	08	21	10
20	15	47	17	49	19	48	21	50
	SEPTEMBER		OCTOBER		NOVEMBER		DECEMBER	
1	22	37	0	35	2	38	4	36
10	23	13	1	11	3	13	5	11
20	23	52	1	50	3	52	5	51

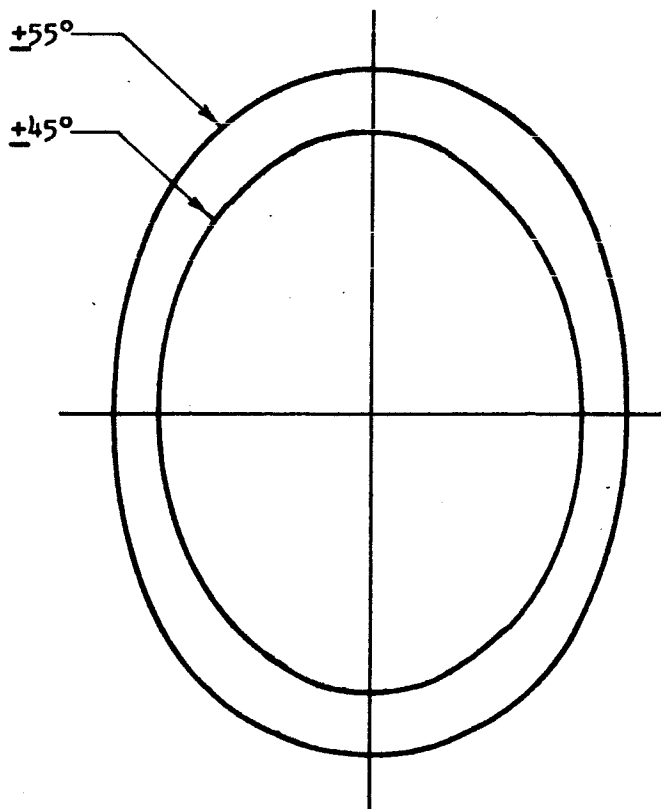
The declination angle of a star is the angle between an imaginary line drawn from the center of the earth to the star and the plane that passes through the equator of the earth. Positive declination angles denote stars in the northern hemisphere and negative declination angles, stars in the southern hemisphere.

The latitude of the launch site, Cape Kennedy, corresponds to the declination angle of the star ephemeris coordinates. Thus all launches from Cape Kennedy will originate from a line drawn through the 26th parallel which is approximately the latitude of Cape Kennedy. For a more accurate determination, the latitude must be corrected to compensate for the location of the different launch pads.

The field of view of the star tracker is assumed to be circular, but project as ellipse on the star map since the coordinates of the star map are asymmetrical. Two ellipses representing fields of view of $+45^\circ$ and $+55^\circ$ are illustrated in overlay number 1, Figure 3.5. The major horizontal divisions on the star chart are 15 degrees apart, while the



OVERLAY #2 SOLAR EXCLUSION ZONE



OVERLAY #1 STAR TRACKER FIELD OF VIEW

FIGURE 3.5 STAR TRACKER FIELD OF VIEW AND SOLAR EXCLUSION ZONE

vertical divisions are 10 degrees apart. This field of view will be aligned normal to the zenith on the launch pad and pointed in a westerly direction, so that when the booster is pitched over in its downrange trajectory, the field of view of the star tracker will be pointed towards the zenith. The field of view of the star tracker will thus be pointed at a meridian which is six hours from the zenith. The field of view of the star tracker at launch will be centered about the intersection of the meridian and the parallel which denotes the latitude of the launch pad.

On the launch pad, the earth will obscure half of the field of view of the star tracker. The horizon of the earth projects as a vertical line through the center of the field of view of the star tracker. The sky background luminance further restricts the usable field to look angles that are greater than 20 degrees above the horizon. This restriction was determined from considerations of sky brightness and star tracker performance characteristics.

The sun is located in the celestial sphere at a right ascension angle that is twelve hours different from the right ascension hour of the stars at the zenith at midnight. The intersection of the meridian that corresponds to the right ascension of the sun and the ecliptic determines the location of the sun with respect to the star chart for any day of the year. The stray solar radiation that is specularly or diffusely reflected off portions of the telescope housing places a limit as to the angle with which the star tracker can be operated with respect to the sun. Empirical determinations of this pointing limitation indicates that the background illumination from stray solar energy becomes excessive when the sun is within 20 degrees of the optical line of sight. In overlay number 2, Figure 3.5, this sun exclusion zone is illustrated in the proper scale for use with the star chart. When center of the ellipse depicting the sun exclusion zone is positioned as described, all the stars falling within this zone must be excluded from the list of available stars.

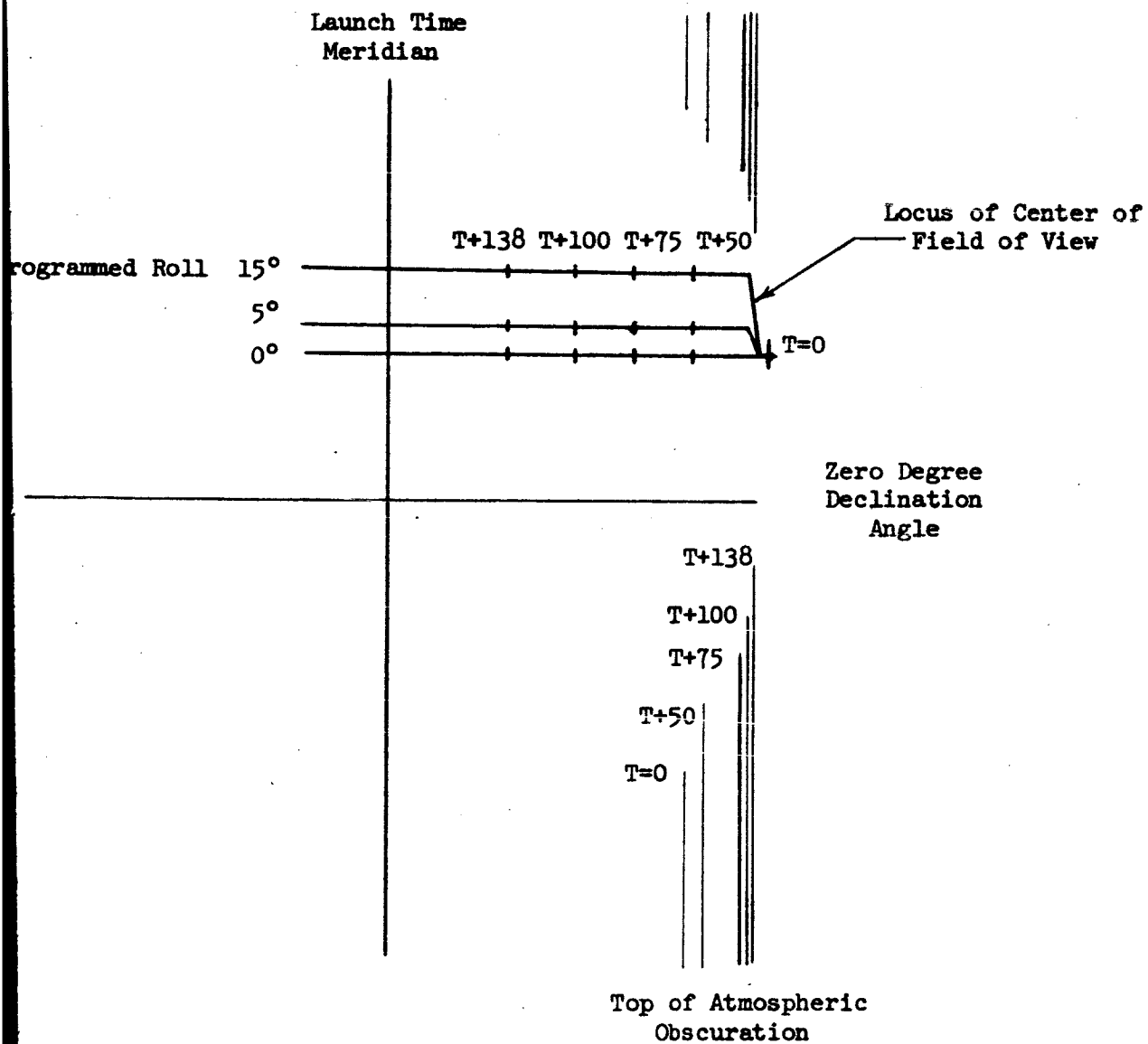
For most star tracker applications, the criteria used to determine the suitability of a particular star as a navigational star are the brightness of the star and the separation of the star from other stars in terms of relative brightness and in angle. For specific applications, the star selection criteria may be extended to include the declination of the star and also the color, for example, Polaris and Canopus, which are often used as the reference star for terrestrial and interplanetary navigation respectively. On the star chart, the thirty stars that are best suited for used as navigational stars are circled. An additional twenty stars that could be used as navigational stars in the event that the window size allotted for the star tracker is limited, or if two or more stars with a minimum angular separation are desired within a limited field of view, are enscribed with a diamond outline.

Shortly after launch, the Saturn is rolled to correct the azimuth alignment, so that the pitch and the yaw axes will be properly aligned with respect to the chosen trajectory. For smaller missiles, this azimuth alignment can be

accomplished on the pad by rotating the whole spacecraft, but this procedure is impractical for the Saturn. The magnitude of this roll maneuver will be from zero to fifteen degrees depending upon the chosen trajectory. The star tracker is assumed to be pointed west at launch and this roll maneuver will cause the line of sight of the star tracker to rotate northward. On overlay number 3, Figure 3.6, the loci of the line of sight of the star tracker for three different roll maneuvers, zero, five and fifteen degrees are plotted. The location of the centers of the field of view of the star tracker as a function of time after launch are delineated for several discrete intervals. By positioning the center of the ellipses that denotes the field of view of the star tracker on these loci, star availability can be determined for different intervals during the vehicle launch. The location of the horizon and the field of view limitation imposed by the brightness of the sky background are also illustrated on overlay number 3. The location of the horizon relative to the celestial sphere will vary as a function of the vehicle altitude, but the change is insignificant for the 138 second launch interval considered. However, the sky brightness changes rapidly as a function of vehicle altitude, so the change in the field obscuration caused by the brightness of the sky background is also shown on overlay number 3 for several intervals after vehicle launch. All stars to the right of a vertical line through the sky background obscuration limit cannot be tracked.

To reiterate, the procedure for locating the overlays and determining the stars in the system field of view is as follows:

1. From Table 3.2 determine the right ascension hour for midnight of the calendar date of the launch.
2. Find the meridian for the hour of the flight by adding the hour of launch to the right ascension hour found in Table 1.
3. Locate Overlay number 1 on the World Star Chart by aligning the Zero Declination Angle and Launch Time Meridian on the overlay to the zero degree declination angle and hour meridian on the star chart.
4. Determine the position of the sun (approximately 12 hours from the hour found in Table 3.2 and on the ecliptic plane).
5. Determine the system field of view ($\pm 45^\circ$ or $\pm 55^\circ$).
6. Determine the roll program from 0 degrees through 15 degrees.
7. Those selected stars that fall within the system conical field of view and to the east or to the left of the atmospheric obscuration line are stars capable of being tracked at $T = 0$.



RE 3.6 OVERLAY NUMBER 3 ORIENTATION OF CENTER OF THE FIELD OF VIEW WITH WORLD STAR CHART RIGHT ASCENSION AND DECLINATION PLUS UPPER ATMOSPHERIC OBSCURATION

3.1.3.5 Vented Gases and Plume Effects

A vehicle rising through the atmosphere can be expected to produce turbulence and shock waves that will affect the operation of the star tracker. Refraction of the incoming stellar radiation will be produced that will cause the star to appear displaced from its true position. The star tracker will sense this change as a vehicle attitude error unless corrective inputs are supplied. The refractive error can be predicted to a given extent, provided certain facts are available. Some of the necessary data needed to calculate this effect are: 1) the vehicle velocity; 2) the altitude; 3) the air density; 4) the air temperature, and 5) the angular relationships between the vehicle, star, and shock wave. The magnitude of the refractive error will decrease as the altitude increases, and will completely disappear as the craft leaves the atmosphere.

There is one further potential source of refractive error that may cause erroneous star position information. This potential error source is caused by the passage of vented gases across the field of view of the tracker. Oxygen, hydrogen, and helium are often used as coolants or as fuel for the booster, and the boil-off requires venting to the atmosphere during the vehicle countdown period. Location of the boil-off vents relative to the star tracker window plus air turbulence will determine if the gases will enter the field of view while on the launch pad. Refractive errors are caused by changes in the index of refraction over the star radiation path. The errors caused by the vapors are random in nature and, thus cannot be programmed out. During flight through the atmosphere, the effects of the vented gases are minimized. However, once in orbit, the boil-off of material may again become of some concern. The gases, when they are vented, will be traveling at the same speed as the vehicle and may produce deleterious effects.

In addition to the vented gases, there has been some indications that all exhaust products from the engines are not thrown backward away from the vehicle. It is likely that during the first few seconds of engine firing, exhaust products, as well as dirt and dust, may be thrown up to obscure the star tracker field of view, and may also be deposited on the star tracker window. As the vehicle rises through the atmosphere, paint or other materials that ablate the nose cone may also be deposited on the window. These particles act as diffuse reflectors when illuminated, raising the effective background radiance presented to the star tracker. The "fireflies" described by the astronauts in the Mercury flights are ascribed to sunlight reflected off particles on the window in the capsule. If the star tracker is not used during the boost phase, the window can be covered with a protective dome, which would be discarded after booster cutoff. However, coating of the window may also be caused by exhaust products from the attitude control engines, or other engines which may be used to modify the spacecraft orbit or trajectory, so other preventive measures may be required.

3.2 OPTICAL INSTRUMENTATION FOR ORBITAL NAVIGATION AND FOR ATTITUDE CONTROL

The use of optical instrumentation as part of the attitude control, vehicle alignment and orbital navigation system for a spacecraft is considered for a number of different applications. The actual type of optical instrumentation that would be utilized for attitude control or orbital navigation would be dependent upon the intended application and the accuracy requirement. Typical utilization of optical instrumentation while in an earth orbit would include attitude control of an earth oriented satellite, attitude control of a solar oriented, inertially stabilized vehicle, orbital navigation, vehicle realignment after loss of inertial reference and the use of a star tracker to provide a stellar reference to correct the drift of the inertial platform during an extended mission.

3.2.1 Earth-Oriented Orbital System Using a Horizon Sensor and a Gyro Compass

For a satellite whose orientation must be maintained with respect to the ground, a horizon sensor is the most practical device to use to provide a vertical reference. The horizon sensor will provide attitude error information about two of the spacecraft axes, but the attitude error about the third axis must be provided by an additional instrument. In a coordinate system where the axis aligned with the orbital path is the roll axis, the axis aligned with the local vertical is the yaw axis and the third axis is the pitch axis, the horizon sensor will provide roll and pitch control. However, currently no easily implemented and simple device is available to provide a direct measure of vehicle yaw alignment. The most practical method of yaw control of an earth oriented satellite is by gyro compassing. In the gyro compass, the gyro rotor is constrained relative to the vehicle frame so that its spin axis tends to align itself normal to the orbital plane. With vertical established by the horizon sensor, rotation about the yaw axis will be sensed by this gyro. The attitude control accuracy attainable is a function of the accuracy of the horizon sensor and the accuracy of the gyro compassing technique. A brief consideration will be given to horizon sensors but the accuracy attainable by gyro compassing will not be considered.

Of the devices that have been proposed for vertical sensing, the horizon sensor is the most practical. In the past an infrared detector was used to sense the thermal gradient between the planetary disk of the earth and space. Accuracy of the horizon determination was affected by weather conditions, season of the year, cloud cover and other climatic effects. Accuracy of the local vertical determination was limited to 0.2 to 0.5 degree r.m.s. with devices that operated in this manner. A major breakthrough in infrared horizon sensor technology was achieved with the decision to track the atmospheric carbon dioxide emission rather than the earth itself. The concentration of CO₂ in the upper atmosphere is relatively constant and the greatest variation that is detectable is the temperature rather than the distribution of the gas. Carbon dioxide has an intense absorption band at 15 microns and can easily be distinguished

from other radiating or scattering sources. The tracking technique used is to detect the inflection point of the CO₂ radiation gradient by scanning an infrared detector across the gradient. Vertical determination accurate to greater than 0.1 degree r.m.s. has been achieved using this method. The actual accuracy attainable is classified. At orbital altitudes of 150 n.mi., the earth oblateness itself is sufficient to cause vertical determination errors in the order of 0.1 degree, so to obtain higher accuracy than this, a computer program must be utilized to subtract the earth oblateness effects. With use of the computer the accuracy of the vertical determination can be further improved by averaging the horizon sensor output for a number of orbits.

3.2.2 Inertially Oriented System Using Solar-Inertial or Sun-Star Alignment

The most straightforward method of attitude control of a solar oriented, inertially stabilized vehicle is by means of a sun sensor and a strap down inertial measurement system. Sun sensors are relatively easy devices to design since the sun is such an intense source, but can become fairly complex if the sun must be tracked to a high degree of accuracy. Measured from the earth, the sun subtends approximately 30 minutes of arc, and 6 minutes to one minute tracking accuracy can readily be achieved by tracking the sun using radiation balance techniques.

Several methods of vehicle realignment after loss of inertial or celestial reference are feasible. In the JPL Mariner spaceflight to Mars, a sun-Canopus reference system was utilized. This information in addition to the orbital time and orbital parameters can be used to reorient the spacecraft. The choice of the sun and Canopus as the prime references in an interplanetary vehicle is quite obvious. The sun is easily located and can also be used as the prime source of power for the vehicle. Since all the orbits of the planets are close to the ecliptic plane, flights to the moon, Mars or Venus will be in the plane of the ecliptic. The line of sight to the sun can be used to control two axes of the spacecraft and a second celestial sighting, orthogonal to these two axes would provide the third axis control. Canopus is chosen as the second reference since it is close to the south ecliptic pole, and is the second brightest star in the heavens. In addition it is unique in color class, being fairly cool relative to the majority of the stars in the celestial sphere. To erect the spacecraft using these two references, the sun is first acquired, and the vehicle oriented with respect to the sun. The vehicle is then rolled about this sun line. The Canopus tracker is offset at an angle to permit acquisition of Canopus, as the field of view of the tracker is scanned over the sky. Several methods of Canopus identification are feasible, such as

brightness and color. Sirius is the brightest star in the heavens and is more than two times brighter than Canopus. The third brightest star is almost two times dimmer than Canopus, so Canopus is readily identifiable by brightness alone. Verification of Canopus acquisition can also be made by mapping the stars in the conical segment that is scanned as the vehicle is rotated about the sun line.

3.2.3 Earth-Oriented Orbital System Using Horizon Sensor and Star Field Scanner

For an application such as an orbiting space station, rotation of the spacecraft about the sun line may not be feasible. Lack of sufficient thrust to perform maneuvers of large magnitude may be one of the deterrents. In addition while in orbit, the sun may be obscured by the earth for a large portion of the orbit. If the orbit is out of the ecliptic plane, Canopus may also be obscured during a large portion of the orbit. With these two effects, the interval when both references are available to the spacecraft may be very limited. The rotation rate of the Mariner spacecraft was two revolutions per hour. Thus in the time required for one Canopus search revolution, the vehicle would complete one-third of its orbit assuming a 90 minute orbit. If the rotational rate utilized for vehicle re-erection were in this order of magnitude, a high probability would exist that one or both of the celestial references would be eclipsed during this interval.

A horizon sensor and a star field scanner has been proposed as an alternate vehicle re-erection system. The star field scanner would map the stars in its field of view as the scanner is rotated. A computer would then be required to compare the star field signature obtained to determine the orientation of the vehicle in yaw. For applications where the yaw error is small, as in the case where the celestial reference is lost with the two star tracker, horizon sensor system, the attitude reference can readily be re-established. The star field scanner can also be used as the prime spacecraft yaw reference if desired.

3.2.4 Autonomous Navigation System Using Horizon Sensor and Star Trackers

If the location of the satellite relative to the earth is desired, additional instruments to those necessary simply to maintain vehicle attitude control are required. Assuming that radar nets and beacons will not be utilized, an autonomous navigation system using a horizon sensor and a star tracker as the basic components are capable of determining the vehicle position relative to the earth to an accuracy in the order of ± 20 n.mi. A fairly low orbit, a horizon sensor accuracy of 0.1 degree, and a star tracker accuracy of 20 arc seconds are assumed under these conditions. If greater accuracy is desired, filtering and smoothing of the horizon

sensor and the star tracker data could reduce the error. The star tracker location and field of view aboard the vehicle is an important question, since these factors in part determine the star availability and the interval over which a star can be tracked. The computer requirements are also important since the star ephemeris must be stored in the computer memory, then converted to yield the star tracker line-of-sight to the star relative to the orbital position. To perform these functions, the orbital information must be known to a certain degree of accuracy, and the star tracker will then be used to upgrade the navigational computation.

Several permutations of instruments and methods of implementing an autonomous orbital navigation system are feasible. The actual choice of a given system would be dependent upon mission and accuracy requirements. Two of the most common system mechanizations include first, the use of a horizon sensor and an inertial platform with a star tracker used to update the platform alignment, and second, the use of a horizon sensor with two star trackers.

For extended orbital operation, the gyro drift will eventually cause the attitude control errors to develop to the point where the errors will be intolerable. To provide an orientation reference for space navigation, the commonly proposed solution is to supplement the gyro-stabilized platform with a star tracker system. The platform then is used to provide stability under relatively high frequency disturbances, such as docking and maneuvering, and the star tracker prevents any long term drift of the inertial reference. The problem of operational lifetime of the gyros in the platform still exists, and one of the proposed solutions is to turn off the platform when the vehicle will be orbiting under quiescent conditions, then re-erect the platform prior to the time when a major change in vehicle attitude or orbit is made.

The use of two star trackers and a horizon sensor has been proposed as an alternate system for space navigation. The two star trackers will continuously acquire and track different stars as the vehicle orbits, and thus a celestial reference will always be provided. Since the star trackers are constantly slewing, acquiring, then tracking different stars, the computational requirements necessary to provide the slewing commands and to relate the star tracking data to the orbital parameters are large. In concept, one star tracker will be tracking while the other is slewed to the next navigational star. If the vehicle is tumbled about the primary control axis of the star tracker that is being slewed, star acquisition and lock-on may be delayed or even lost if the motion is greater than the instantaneous field-of-view of the star tracker. Since the interval over which a star can be tracked while in orbit is limited, both star trackers may be rendered ineffective, and the attitude reference will be lost.

3.2.5 Precision Orbital Navigation System Using a Landmark Tracker

For precision orbital navigation, sightings on distant bodies such as stars limit the accuracy with which the navigational accuracy can be determined. An angular sighting error to a star of a 20 seconds of arc will result in a large orbital position error. In an effort to obtain a more accurate orbital navigational system, the tracking of objects on the ground has been proposed. Different sensors and methods are feasible, such as the use of visual, infrared and microwave sensors and the tracking of known and unknown landmarks. The problems involved with the concept are sensor limitations, accuracy of the geodetic surveys, and computer requirements. Cloud cover, landmark identification, and the accuracy with which a landmark can be tracked are problems germane to the sensor. The location of the landmarks themselves are not precisely known. The basic geodetic references have been found to be as much as several thousand feet in error from data obtained from orbiting vehicles. Tracking of unknown landmarks would provide data points in the trajectory that can be used to solve for an unknown in a matrix. By iteration and the accumulation of multiple data points, such as local vertical, star sightings and others, the navigational accuracy can be improved. Orbital navigation systems utilizing landmark tracking could substantially improve the navigational accuracy over the horizon sensor-star tracker system.

One function that can be performed by a manned orbital satellite is the mapping of terrestrial landmarks to improve the accuracy of the geodetic surveys and in turn the accuracy of autonomous orbital navigation systems utilizing landmarks. The radiation signatures of landmarks, notably, volcanoes, islands, lakes, snow-covered peaks, hot springs and others as viewed from space would help in the design of sensors for landmark detection.

3.2.6 Attitude Control of A Space Vehicle

The purpose of attitude control of a space vehicle is to stabilize the spacecraft to a desired accuracy from a reference on the vehicle to an external reference. External references that can be utilized include the local vertical of a planet; optical sightings to celestial bodies such as the sun, the planets and the stars; an inertial reference; and gravity gradients and the magnetic field of the earth. The accuracy of attitude stabilization is dependent upon the spacecraft mission, and the attitude control can be fairly crude for applications such as a communications satellite, but must be highly accurate for a vehicle such as the Orbiting Astronomical Laboratory. Typical methods of attitude control that are presently being utilized, include spin-stabilization, gyro compassing with a horizon sensor to provide local vertical direction, horizon sensors used with sightings on celestial bodies, and multiple celestial body sightings. Gravity gradients and magnetic field effects are being investigated and are scheduled for testing on one of the geophysical satellites in the near future. In Table 3.3, the attitude control techniques utilized by different spacecraft are listed for comparison.

3.2.6.1 Spin Stabilization

The majority of vehicles launched prior to 1963 were spin stabilized. Spin stabilization is simple to implement and is quite effective, being capable of short term stability within ± 1 degree about two axes. The spin was imparted to the vehicle by rotating the entire top stage of the launch vehicle prior to injection into orbit. The advantages of spinning the payload are that the center of gravity of the payload will lie on the axis of rotation, simplifying the problem of alignment of the thrust axis of the booster with the c.g. of the payload, and the spinning motion of the satellite can also be used to generate the scanning motion for the sensors and other instruments.

A spin stabilized satellite will be oriented with respect to inertial space and if the satellite must be maintained at a given orientation with respect to the earth, the vehicle must be continuously precessed at a given rate to maintain the alignment with respect to the earth. Other disadvantages to spin stabilized satellites are disturbing torques which cause the spacecraft to wobble, and also the difficulty of making observations from a rotating spacecraft.

3.2.6.2 Celestial Body Tracking

The trajectory of a space vehicle in the midcourse phase of its flight between two planets may vary from the nominal precomputed trajectory due to errors in the injection velocity and due to inaccuracies of the knowledge of the different astronomical constants. An on-board optical system to measure angles between lines of sight to celestial bodies to determine the position of the spacecraft at a specified time in the trajectory was described by Robert Stern.¹ Three or more measurements of the angle subtended by a pair of celestial bodies are made in a relatively short time, and compared to the precomputed angle for the specific time in the trajectory. Since all the angular measurements are subject to some degree of uncertainty, the sightings were chosen in such a manner that the smallest uncertainty in the computed estimate of the spacecraft position is produced.

The trajectory of an interplanetary flight will lie in, or be close to the ecliptic plane, and all the relatively close celestial bodies, such as the planets, the sun and the moon are located close to the ecliptic plane. Sightings on celestial bodies should be made to the closest celestial bodies available, to maximize the accuracy of the navigation information that can be obtained with each sighting. In addition, it is desirable to choose the sightings so that the sight-lines to the celestial body form an orthogonal

¹Proceedings of the National Aerospace Electronics Conference, May 11-13, 1964, Selection of Optical Sightings for Position Determination in Interplanetary Space, Robert G. Stern.

VEHICLE	MISSION	REFERENCE COORDINATE SYSTEM	SENSORS	SENSOR ACCURACY
OA0	Celestial body observation	Sight-line to celestial body under observation, plus star sighting normal to prime sight-line	6 Star Trackers 6 Sun Sensors	+0.1 arc sec. to observed object +1 arc minute rotation about this line of sight
OGO	Geophysical measurements	Local vertical Line of sight to sun	Horizon Sensor Sun Sensor	+2 degrees +20 degrees
OSO	Solar measurements	Spin stabilized with spin axis pointed to sun	Sun Sensor	+1 arc minute
Advanced OSO	Solar measurements	Three-axis stabilization Sun-star reference	Sun Sensor Star Tracker	+5 arc second
Nimbus	Meteorological Studies	Spin-stabilized (Attitude determined by correlating Horizon Sensor and TV output as both scan conically due to spacecraft rotation)	Horizon Sensor Television Camera	+1 degree
Midas and Samos	Reconnaissance Satellite	Local Vertical Gyro-Compassing	Horizon Sensor Single axis, rate integrating gyro	
Ranger	Lunar Probe	Sun-Planet (Earth) Orientation	Sun Sensor Earth Sensor	+6 arc minutes +12 arc minutes
Mariner R	Venus Probe	Sun-Planet (Earth) Orientation	Sun Sensor Earth Sensor	+6 arc minutes +12 arc minutes
Mariner C	Mars Probe	Sun-Star (Canopus) Orientation	Sun Sensor Canopus Tracker	

TABLE 3.3 (Continued)

VEHICLE	MISSION	REFERENCE COORDINATE SYSTEM	SENSORS	SENSOR ACCURACY
Mercury	Manned Orbital Missions	Local Vertical Gyro-Compassing	Horizon Sensor 3-axis platform	+30 arc minutes
Gemini	Manned Orbital Missions	Local Vertical Gyro-Compassing	Horizon Sensor 3-axis platform	+ 6 arc minutes
Apollo	Manned Lunar Mission	Stellar-Inertial plus Landmark Tracking	Star tracker 3-axis platform Manual sextant	
Lunar Orbiter	Lunar Photography from Lunar Orbit	Sun-Star (Canopus) Orientation	Sun sensor Canopus tracker	

set of vectors. The amount of near celestial bodies that are available are limited and lie in the same plane, so at least one sighting has to be made to a star that is normal to the ecliptic plane. Star availability also becomes a problem since there is no star normal to the ecliptic plane that exhibits characteristics that make it attractive for use as a navigational star. Canopus, which is close to the south ecliptic pole is the commonly chosen star for space navigation.

Due to the limited availability of near celestial bodies, and to the difficulty of locating good navigational stars that form an orthogonal reference coordinate system, Stern has proposed a system in which three to six measurements are made of the angles between a number of celestial bodies. The six measurements would include measurements of the angles between Venus-Canopus, Venus-Spica, Earth-Sun, Venus-Earth, Earth Pollux, and Earth-Regulus. The uncertainties in all angular measurements are assumed to be 50 microradians or approximately 10.3 arc-seconds. With this measurement technique, the positional uncertainty volume would form an ellipsoid with the dimensions shown in Table 3.4.

TABLE 3.4 AXES OF EQUI-PROBABILITY ELLIPSOID

	Largest Axis (Miles)	Middle Axis (Miles)	Smallest Axis (Miles)
3 Sightings	3780	1140	594
6 Sightings	3350	610	533

An earth orbiting vehicle utilizing only celestial body tracking for navigation purposes would be subject to errors of approximately the same order of magnitude. An orbiting satellite, that utilizes optical instrumentation in its navigation system, should use a guidance system similar to those described in the next section on Autonomous Navigation Systems.

3.2.7 Accuracy of Autonomous Navigation System

Autonomous space guidance and control systems that require no assistance from ground aids have been proposed.² One type of earth-orbital navigation and/or guidance system would include star trackers, infrared horizon sensors and inertial references. The accuracy of this system would be limited by the

²Advanced Guidance Concepts, James A. Fusca, Space/Aeronautics, December 1964.

performance of the horizon sensor. Errors in horizon determination develop from basic instrument errors and horizon phenomenology. Random errors are caused by the fluctuations of the apparent horizon detection point, which is influenced by weather and climatic conditions, and also by the instrument errors. Design of the horizon sensor to operate in the 15 micron wavelength band to detect the atmospheric carbon dioxide band has tended to reduce the apparent horizon detection point fluctuations. These random errors as well as systematic errors caused by factors such as the earth oblateness, can be reduced by the use of on-board data processing to average the random errors and to compensate for the systematic errors. An estimate of the accuracy with which the position of the vehicle can be determined with this technique is shown in Table 3.5.

TABLE 3.5 AUTONOMOUS NAVIGATION ACCURACY ESTIMATE

	Operational 1965	Operational 1970	Operational 1975
Horizon Sensor (Position)	12 miles	4 miles	2 miles
Stellar Tracker (Axis attitude)	9 arc minutes	3 arc minutes	1.5 arc-min.
Landmark Tracker (Position)		1.5 miles	1.0 miles
Stellar Tracker (Axis Attitude)		1.5 arc minutes	1.0 arc-min.

A second type of autonomous navigation and guidance concept would utilize the detection of known landmarks in conjunction with the stellar and the horizon data. High positional accuracy is attainable, but a large data storage and computation capability for this type of system is required. In addition, the navigational accuracy obtained is dependent upon the orbit, weather conditions, night level and contrast conditions. Gerald M. Levine³ has shown that the major source of error in this navigation system is the lack of knowledge of

³Application of Midcourse Guidance Technique to Orbit Determination, G. M. Levine, AIAA Journal, Vol. 3, No. 1, January 1965.

the exact position of the landmark, particularly when multiple landmark observations are made. The larger the landmark uncertainty, the less worthwhile are added observations. Results using linear filtering techniques to reduce the positional error has shown that two observations of a given landmark are sufficient unless the landmark position is precisely known. Using a landmark tracker with a tracking accuracy of 1 milliradian, the spacecraft position can be determined to an accuracy of 1.5 miles as shown in Table 3.5.

The basic sensor capability of current instruments and the projected accuracy that can be attained in the future is shown in Table 3.6. The star tracker capability is not being fully utilized in the autonomous navigation system since the basic accuracy is limited by the horizon sensor.

TABLE 3.6 SENSOR PERFORMANCE CAPABILITY ESTIMATE

	Operational 1965	Operational 1970	Operational 1975
Star Tracker	20 arc seconds	10 arc seconds	5 arc seconds
IR Horizon Sensor	6 arc minutes	2 arc minutes	1 arc minute
Landmark Tracker	--	1.0 milliradian	0.7 milliradian
Gyroscope	0.1 deg. per hr.	0.03 deg. per hr.	0.01 deg. per hr.

3.3 CONSIDERATIONS OF EXPERIMENTS THAT CAN BE PERFORMED FROM AN ORBITING SATELLITE

The type of experiments that would be considered in an orbiting satellite would fall into two general categories. The first would include scientific research and engineering experiments that cannot be performed except under space conditions. The second would be determination of the geophysical phenomena that can be detected from space and the accuracy with which these detections can be made.

The use of the Saturn IV booster as a space workshop would permit extensive testing of components and instruments designed to operate in a space environment, but whose environmental testing had been limited due to shortcomings of space chambers. The testing would include the performance evaluation and the reliability of different instruments and the effects of gamma and ultraviolet radiation on different materials.

Components that are affected by gravitational attraction include gyros, accelerometers, and gravimeters. Instruments that are affected by atmospheric gases include horizon sensors, sun sensors and star trackers. For gyros and accelerometers, the errors caused by gravity can thus be separated from the errors caused by spring stiffness, rotor suspension and frictional effects. For a number of years, the accuracy of horizon sensors and the cause of the sensor errors has been difficult to define. Observation of the weather conditions and other phenomena, in the region where the horizon detection is being made would permit correlation of the horizon detection point with the atmospheric effects. Sun sensor accuracy is normally tested on the earth with a simulated source or by using the sun itself. Simulated sources sacrifice either collimation or intensity of the simulated solar radiation. If the sun itself is used, atmospheric absorption reduces the intensity of the solar radiation. Thus the performance of sun sensors must be extrapolated to space conditions. Experiments performed with star trackers could include the amount of background that is caused by the star tracker window.

The testing of bearings, solar cells, torquers, resolvers and other materials and components in a vacuum environment would produce data on the characteristics of these components under vacuum conditions that cannot be reproduced and maintained in a space chamber.

Some of the geophysical phenomena that may be observable from an orbiting satellite would be the temperature and direction of ocean currents, the velocity and location of the jet streams in the upper atmosphere, the formation and movement of weather fronts, the position and radiation signature of terrestrial landmarks, and atmospheric refraction effects. The type of experiments that would be performed would be determined by the phenomena that is being examined. Spectrometers or radiometers in a number of spectral bands would be needed to determine whether ocean currents and jet streams could be detected. These instruments would also be used to study weather fronts to determine the best method to detect hurricanes and other weather disturbances, and also to determine the signature of terrestrial landmarks. The surveying of landmarks to improve the accuracy of the geodetic surveys could be accomplished by manual tracking using a sextant, or by photographic mapping techniques. The effects of atmospheric refraction can be measured by tracking a star in the vicinity of the horizon, and measuring the deviation of the line of sight to the star that is caused by the atmosphere of the earth.

3.3.1 Thermal Ocean Mapping

Thermal mapping of the ocean would be beneficial to oceanographic studies, and would permit the plotting of ocean currents, and also yield data that can be used by the fishing industry. Several methods of determining the wavelength at which the radiation peaks and comparing the amount of energy in two different spectral bands. The peak of the blackbody radiation curve moves to shorter wavelengths for warmer bodies, and this peak can be plotted

by the use of a sensitive spectrometer with high resolution. For objects that radiate as blackbodies, the ratio of the radiant emittance in two spectral bands can be used to determine the temperature of the body. With two measurements only, an ambiguous result is obtained, since one of the spectral regions chosen may lie before or after the spectral peak of the blackbody curve, and a given ratio between the radiant emittance from the two spectral regions can be produced by blackbodies of two different temperatures. For thermal mapping of the ocean, the range of temperatures of interest is bounded and so one of the possibilities can be eliminated as being extraneous.

3.3.1.1 Scanning Spectrometer

To define the operating range of the instruments needed to thermally map the ocean, assume that the temperature of the ocean may range from 40°F to 70°F; that the ocean has an emissivity of 0.9 or greater, in the region about the spectral peak; and the average atmospheric transmission in this spectral region is greater than 80 percent. In Table I, the shift of the spectral peak for bodies of different temperatures is shown. For temperature increments of 5°F the spectral peak shifts approximately 0.1 micron. To attempt to resolve this spectral peak, the spectral resolution of the spectrometer must be better than 0.02 micron. The trade-off that is of importance here is system resolution and weight versus system sensitivity. The infrared detectors have a basic detectivity limit, and if the detector irradiance is reduced by narrowing the spectral bandwidth, the collecting optic must be enlarged to increase the amount of collected energy.

TABLE 3.7 PEAK OF BLACKBODY CURVE FOR DIFFERENT TEMPERATURES

Temperature		λ max.
°F	°C	Microns
70	21.1	9.850
65	18.3	9.945
60	15.6	10.038
55	12.8	10.136
50	10	10.237
45	7.22	10.339
40	4.4	10.443

For the spectrometer, assume that the optical system consists of an objective lens that focuses the incoming energy, a condenser lens that recollimates the energy, a monochromator that separates the energy spectrally, and a field lens to refocus the energy onto an infrared detector. The infrared detector is a thermistor bolometer; chosen since it does not require special cooling for operation. This detector is not as sensitive as other infrared detectors that are available, but the complexity and maintainability of the cooling systems required for the other infrared detectors make the choice of the thermistor bolometer attractive when long term operation without maintenance is contemplated.

Table 3.8 summarizes the basic parameters in the design of the scanning spectrometer to measure ocean temperature. All parameters listed are conservative, so an instrument to satisfy the system requirements specified can be built with readily available components.

TABLE 3.8 DESIGN PARAMETER FOR SCANNING SPECTROMETER
TO MEASURE OCEAN TEMPERATURES

1. Radiation Characteristics of Water	
Radiation type	Blackbody
Temperature	273° K (32° F)
Emissivity	0.9
Radiance	$1 \times 10^{-2} \text{ w/cm}^2$ - steradian
2. Instrument Parameters	
Spectral resolution	0.02 micron
Optical efficiency	0.5
Electrical efficiency	0.35
Detector	Thermistor bolometer
Size	0.1mm x 0.1mm
Sensitivity	5×10^{-11} watt (25 cps bandwidth, $\tau = 6$ msec)
Detector threshold	S/N of 7:1
Field of view	1×10^{-6} steradian
Lens diameter	17 cm
Resolution	0.1 mile at 100 miles
3. Miscellaneous	
Atmospheric transmission	0.8
Volume	1400 cubic inches
Weight	40 pounds
Power	20 watts

The radiance in a 0.02 micron bandwidth at approximately 10 microns is 0.12 percent of the total energy emitted by a 273°K body. The effective radiance (F) is the product of the radiant intensity (W), the emissivity (E), and the percentage of the energy in the spectral bandwidth ($\Delta\lambda$), or

$$F = W E \Delta\lambda \quad (3.1)$$

$$F = 10^{-2} \times 0.9 \times 0.0012$$

$$F = 1.1 \times 10^{-5} \text{ w/cm}^2 - \text{steradian}$$

The effective irradiance (R) at the detector plane is a function of the field of view of the optical system (Ω), the optical efficiency (ϵ_e), the electrical efficiency (ϵ_e), the atmospheric transmission (A_t), and the signal threshold (S/N).

$$R = \frac{F \Omega \epsilon_e \epsilon_e A_t}{S/N} \quad (3.2)$$

$$R = \frac{1.1 \times 10^{-5} \times 10^{-6} \times 0.5 \times 0.35 \times 0.8}{7}$$

$$R = 2.2 \times 10^{-13} \text{ w/cm}^2$$

The collecting aperture (C) required to produce this detector irradiance is a function of the detector sensitivity (S) and is given by the following equation;

$$C = \frac{S}{R} \quad (3.3)$$

$$C = \frac{5 \times 10^{-11}}{2.2 \times 10^{-13}}$$

$$C = 2.27 \times 10^2 \text{ cm}^2$$

The lens diameter (D) required is then;

$$D = \left(\frac{4C}{\pi} \right)^{1/2} \quad (3.4)$$

$$D = \left(\frac{4 \times 227}{\pi} \right)^{1/2}$$

$$D = 17.0 \text{ cm}$$

The estimate of weight, size and power for a spectrometer with a 0.02 micron resolution is given in Table 3.8. These estimates do not include the gimbals, control system and mounting fixtures required to keep the spectrometer pointed at a specific location as the spectral scanning is being accomplished.

The field of view of 10^{-6} steradian chosen for the instrument has an angular coverage of approximately one milliradian by one milliradian. At an altitude of 100 miles this system will be capable of resolving objects that are 0.1 mile in length. The two radiometer system described in the next section is capable of much better resolution since the angular coverage is much less. For the comparison, the weight and power requirements of the two instruments were taken to be the important factors. The differences in the design parameters chosen for the two instruments are caused by the utilization of the instrument. For the radiometer, a much better signal to noise ratio and bandwidth is desired for output stability, since the temperature determination is a function of the absolute value of the signal rather than the relative value of the signal as in the case of the spectrometer. However, since the radiometers use a wide spectral band with 50 times more energy than the spectrometer, the higher signal to noise and electronic bandwidth required do not penalize the system.

3.3.1.2 Dual Radiometer

The spectral peak of the blackbody radiation of a 273°K blackbody is at 10.6 microns, so the percentage of the radiated energy in a given bandwidth for wavelengths longer than the peak will remain relatively constant as shown in Table 3.9. A fairly long wavelength, say 11.5 - 12.5 microns could be used to establish the baseline for the temperature determination, and a second band chosen at 6.5 - 7.5 micron could be used to provide a large differential in effective irradiance as a function of temperature. Selecting a spectral band with wavelengths shorter than 6.5 microns is not desirable since the amount of energy in a given bandwidth drops rapidly for wavelengths shorter than 6.5 microns.

The dual radiometer design for this system is simple in concept, consisting of duplicate sets of optics, mechanical modulators or choppers, and infrared detectors. The infrared detectors again are thermistor bolometers. Interference filters with different spectral bandpass are placed in the optical path of the two systems to provide the difference in spectral response of the systems. The primary system parameters are outlined in Table 3.10.

TABLE 3.9 PERCENTAGE OF BLACKBODY ENERGY IN DIFFERENT SPECTRAL BANDS AS A FUNCTION OF TEMPERATURE

TEMP.	SPECTRAL BAND (MICRONS)					
°F	6.5 - 7.5	7.5 - 8.5	8.5 - 9.5	9.5 - 10.5	10.5 - 11.5	11.5 - 12.5
	%	%	%	%	%	%
70	4.84	5.94	6.52	6.67	6.48	6.11
65	4.70	5.82	6.42	6.60	6.46	6.10
60	4.56	5.70	6.35	6.53	6.42	6.09
55	4.42	5.58	6.25	6.47	6.38	6.08
50	4.29	5.45	6.14	6.40	6.34	6.06
45	4.15	5.33	6.04	6.33	6.29	6.04
40	4.02	5.19	5.92	6.26	6.25	6.02
Change over temp.range	17	12.6	9.2	6.15	3.5	1.5

TABLE 3.10 DESIGN PARAMETERS FOR DUAL RADIOMETER
OCEAN TEMPERATURE DETERMINATION SYSTEM

1. Radiation Characteristics of Water

Radiation type	Blackbody
Temperature	273°K (32°F)
Emissivity	0.9
Radiance	1×10^{-2} w/cm ² - steradian

2. Instrument Parameters

Spectral bandwidth	1 micron
Optical efficiency	0.5
Electrical efficiency	0.35
Detector	Thermistor bolometer
Size	0.1 mm x 0.1 mm
Sensitivity	1×10^{-10} watt (100 cps bandwidth, $\tau = 6$ m.sec.)
Detector threshold	S/N of 10:1
Field of view	1.6×10^{-7} steradian
Focal length (optics)	25 cm
Lens diameter	10.25 cm
Resolution	0.04 mile at 100 mile

3. Miscellaneous

Atmospheric transmission	0.8
Volume	800 cubic inches
Weight	40 lbs.
Power	25 watt

The effective radiance for each radiometer is from equation 3.1,

$$F = 10^{-2} \times 0.9 \times 0.06$$

$$F = 5.4 \times 10^{-4} \text{ w/cm}^2 - \text{steradian}$$

From equation 3.2, the effective detector irradiance is

$$R = \frac{5 \times 10^{-4} \times 1.6 \times 10^{-7} \times 0.5 \times 0.35 \times 0.8}{10}$$

$$R = 1.21 \times 10^{-12} \text{ w/cm}^2$$

From equation 3.3, the collecting aperture required is

$$C = \frac{10^{-10}}{1.21 \times 10^{-12}} = 82.5 \text{ cm}^2$$

From equation 3.4, the lens diameter is

$$D = \left(\frac{4 \times 82.5}{\pi} \right)^{1/2}$$

$$D = 10.25 \text{ cm}$$

The angular coverage of the radiometer pair is 0.4 milliradian by 0.4 milliradian. At an altitude of 100 miles the system is capable of resolving objects 0.04 miles in diameter on the ground.

3.3.1.3 Choice of System for Thermal Ocean Mapping

Both systems are capable of accomplishing the specific task for which the design is intended. Were this task the sole function desired for instrumentation of this type, the dual radiometer system would be desirable since the system is extremely simple, and is very sensitive. However, the scanning spectrometer is adaptable for determination of the signature of landmarks in the infrared and the infrared spectral characteristics of storm and weather fronts.

3.3.2 Geophysical Background Information

Geodesy is the branch of geophysics that is involved with the size and shape of the earth, the exact position of different points on the earth surface and gravitational phenomena. When a small area is surveyed for the purpose of producing a map, the area can be assumed to be located on a plane. For geodetic surveys, or surveys of large areas of the earth surface, the curvature of the earth must be considered.

Geodetic surveys are referenced to the geoid, or the equipotential surface of the earth. In practice, the mean sea level determines the geoid. The gravitational attraction of a body is a function of its mass and due to local variations of the topography of the earth, the direction of the gravity vector may be shifted from the true vertical to the center of the earth. The difference in the mass of a continent compared to the mass deficiency of the ocean will cause the gravitational vector to be rotated toward the direction of the land mass. The surface of the ocean which forms the equipotential surface will be normal to this gravitational vector. Thus the geoid is influenced by surface irregularities.

For the purposes of geodetic surveys, the earth is considered to be an ellipsoid of revolution. Due to the variations in the geoid and the ellipticity of the earth, different ellipsoids that match the geoid of the particular terrain have been adopted in various countries as a reference. Standard surveying techniques cannot be used over the expanse of the oceans, so other methods must be utilized to relate the different reference ellipsoids to each other. Some methods attempted have been the occultation of stars by the moon, and the position of a rocket or satellite with respect to the star pattern. The star occultation technique is capable of locating the point at which the measurement is made precisely in terms of longitude and latitude of the earth. However, the radius of the earth at the point of measurement is still a variable and considerable error between reference ellipsoids can be introduced depending upon the assumptions made regarding the radius of the earth at the point of measurement. The problems concerned with this measurement is that time exposures must be made to obtain sufficient light to photograph the star at the moment of occultation. The image of the moon will be blurred if the telescope is slewed to track the star. This image blurring plus the requirement for precise measurement of the time when occultation occurs limits the accuracy of the determination. Tracking of the moon and the stars separately has been used to obtain sharp images of both bodies on one photographic plate, but this method has only recently been attempted and its use is not common.

Simultaneous photograph of a flash of light from a rocket against a star background has been used to locate several points on the earth with respect to each other. In this case, seven observation sites at Sitka, Alaska; Spokane, Washington; Lincoln and El Centro, California; and Mauna Loa, Hawaii and Kaeno, Oahu, Hawaii were used. A flare was ignited at three points during the trajectory of a ballistic missile, the first at 900 miles altitude, at 1400 miles (apogee), and at 920 miles altitude during the rocket descent. The relative position of the rocket to the star background in the different photographs determines the direction to the rocket for the different sites, and the coordinates of all the observation sites can be determined by using the distance between two observation sites as a baseline. The accuracy of the given measurements are limited by the accuracy with which the baseline can be determined.

A much more sophisticated geodetic surveying system, the Sequential Collation of Range System (SECOR) has been built and test flown in a satellite. The SECOR system measures range from a satellite to four ground stations.

A series of modulated signals is transmitted from the ground station to the satellite. A transponder on the satellite detects the phase of the signals and retransmits the phase information to the ground station. By using triangulation methods, the geodetic position of one of the ground stations can be determined if the position of the other three stations are known. If the ground points are close to each other, the triangulation computation is simple, but if the unknown point is too far apart for simultaneous observation, the satellite orbit must be plotted and the unknown position determined by measuring range to the satellite for a number of orbits of the satellite. It is planned to establish geodetic reference points over the entire world by sequentially determining the position of a fourth station from three known stations.

3.3.3 Mapping by Photographic Techniques

Once reference points have been established by the use of geodetic surveying techniques such as SECOR, a more accurate map of the world could be produced using photographs of the local terrain made from a satellite. The photographs would be indexed to the established reference points so that the map would be a true representation of the surface of the earth rather than a compromise based on a spheroidal earth. This map would precisely locate landmarks that are recognizable from orbital altitude such as islands, lakes, volcanoes and other features that may be used as references for a self-contained orbital navigation system.

A complete photographic system consisting of several cameras and automatic film processing equipment would weigh approximately 800 lbs. and require 200 watts of power. Other uses for the photographic system would be repeated photography of given areas to collect statistical information pertaining to cloud cover, weather and storm formation and location of the atmospheric jet stream.

3.3.4 Cold Star Detection

Atmospheric absorption, and the background caused by atmospheric radiance, limit the detection of cold stars by an observer on earth to stars with a color temperature of over 1000°K. A sensitive, broad-band, infrared radiometer could be used in a satellite to detect cold stars. Since optical windows for infrared radiation are difficult to fabricate, this instrument would have to be operated outside the spacecraft in a space environment. This system would have to be cryogenically cooled to achieve its maximum sensitivity, and a closed-cycle, cryogenic cooling system would be required to cool the sensor for extended periods without maintenance. An infrared radiometer with an eight-inch aperture, and a spectral response of 8 to 24 microns, would weigh approximately 50 pounds and require 100 watts of power. The cryogenic system, however, would weigh an additional 150 pounds and require 500 watts of power. Weight estimates do not include a gimbal mounting system for automatic scanning.

3.3.5 Atmospheric Refraction Measurements

Optical experiments that look through the atmosphere of the earth are affected by atmospheric refraction. The index of refraction of air is a function of its density and changes from a value of 1.000276, measured at the Fraunhofer C line (6562.816Å) at one standard atmosphere, to 1.000000 in a vacuum. For accurate measurements where optical sightings through the atmosphere are required, the atmospheric refraction effects must be considered. One method of obtaining data concerning atmospheric refraction would be to measure the deviation of a sight-line to a star from the time that the star is close to the horizon of the earth, until it is occulted by the earth. Refraction effects would then be determined using a model of the atmosphere of the earth. The equipment required for this task is a precision star tracker mounted in an accurate gimbal system.

3.3.6 Contamination of Spacecraft Window

An observation window in a spacecraft can be contaminated in a number of ways. Atmospheric constituents such as dust, haze and salt spray may coat the window, either by electrostatic attraction or the self-adhesive properties of the contaminants. The lift-off splash and the exhaust products from the booster rockets may also deposit foreign matter on the window. A retro-rocket is sometimes used in the staging phase to insure separation of the different stages before the second stage engines are fired. The exhaust from this retro-rocket will be directed toward the payload stage and may deposit debris and solid exhaust particles directly onto an observation window located on the upper stage. In addition, atmospheric heating of the nose cone and the shroud causes ablation of the paint and other materials comprising the forward section of the vehicle, and these ablative products may also be deposited on the window.

If the observation port is not used during the launch period, it can be covered so it will not be contaminated in the early phases of the mission. However, if the spacecraft is to be maneuvered after achieving orbit, the secondary booster engines, or the attitude control engines will also be contaminant sources, so a protective window covering, that is discarded after launch, may not be completely successful in preventing window contamination.

The optical transmission characteristics of a dirty window are degraded due to absorption and scattering of light by the contaminant coating. However, the more serious effect is caused by particles or other matter which act as diffuse reflectors when illuminated, causing glare, or an overall increase in the background radiance level. This glare, coupled with the absorption and scattering effects produced by a dirty window,

may affect the accuracy and capability to make visual observations and perform optical experiments from a spacecraft. The magnitude and the possible sources of window contamination in the command module and the payload package of the Saturn missile, should be determined if optical observations such as star tracking, photography, spectrophotometric and radiometric measurements are contemplated.

4. REDUCTION OF EFFECTS OF OFF-AXIS AND BACKGROUND ILLUMINANCE IN A STAR TRACKER

The detection capability and tracking accuracy of a star tracker operating against a bright background is reduced due to the system noise caused by the background. To enable the star tracker to operate under these conditions, the star tracker design parameters such as the field of view and type of optical detection method utilized must be chosen to minimize the effects of background illumination.

Care also must be taken in the design and fabrication of the optical system, to attenuate and not to accentuate glare caused by a bright sky background. Methods of reducing glare include specifying the quality of the optical material used in the manufacturing of refractive elements, controlling the quality of workmanship in the fabrication of the optical elements, and the use of baffles and traps in the optical system design to reduce the amount of stray light in the optical cavity. In some cases, it may be possible to remove the cause of background radiance. An optical window, which is a potential source of background radiance if contaminated, could be eliminated, by designing the star tracker to operate in a space environment, so a window is not required.

Another source of stray radiation is off-axis illumination from an intense source such as the sun or the moon. A sunshade can be used to prevent off-axis light rays from striking the entrance aperture, and the baffles used to attenuate glare, should also be designed to be effective against spurious off-axis illumination that does enter the optical system. The sunshade may be a simple hollow tube, or can be a complex array of small glass cells, which functions simultaneously as an optical window and as a sun shield.

4.1 SUNSHADE

A long cylindrical, lens shade can be used to reduce the effects of off-axis illumination, by restricting the light rays that are permitted to strike the entrance aperture of the lens, to those that are within the field of view of the optical system. For an optical system with a two-inch aperture and a one-degree field of view, the length of the sunshade would have to be longer than 100 inches, to provide effective shielding. The length of the sunshade can be reduced by compromising the ability of the sunshade to eliminate off-axis illumination, and if the effectiveness of the sunshade is limited to rays with angles of incidence of greater than 10 degrees, the length of the sunshade can be reduced to 11 inches. However, if the aperture of the optical system is increased, the length of the sunshade must also be increased to provide the same off-axis illumination rejection capability. In Figure 4.1, is plotted the sunshade length that is required for optical systems with different apertures, as a function of the minimum angle at which the sun shade will be effective.

The effectiveness of a simple sunshade, however, is normally degraded long before the off-axis light is allowed to directly illuminate the

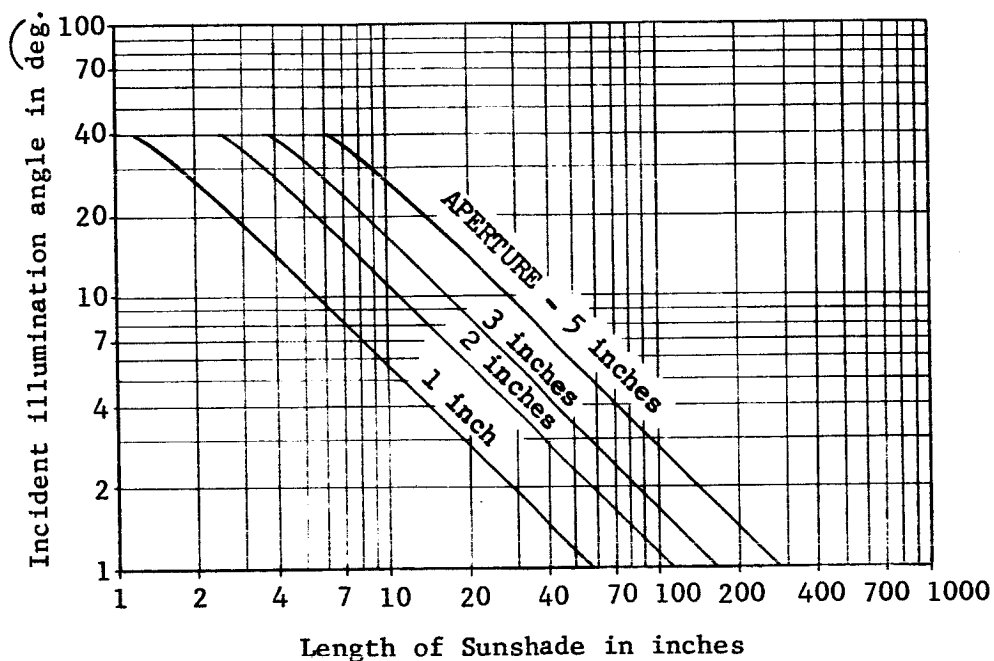


FIGURE 4.1 SUNSHADE LENGTH AS A FUNCTION OF ANGLE OF INCIDENCE OF STRAY ILLUMINATION

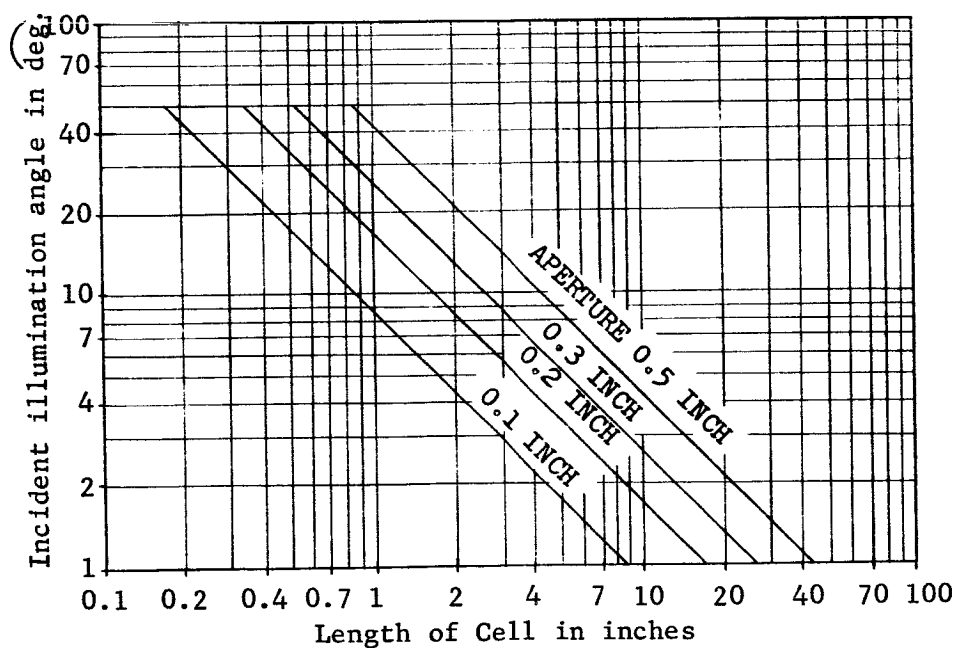


FIGURE 4.2 CELL LENGTH OF MULTI - CELLED SUN SHIELD AS A FUNCTION OF ANGLE OF INCIDENCE OF STRAY ILLUMINATION

aperture. When the angle of the incident illumination is less than the critical or grazing angle of the material comprising the inner walls of the sunshade, the light will be totally reflected off the walls, and may be directed into the field of view of the star tracker. The incident angle for glass with an index of refraction of 1.5 is 42 arc-degrees. For materials with high indices of refraction, the critical angle is smaller, but to be effective at angles of 10° , the index of the wall material must be greater than 5.8. The only materials exhibiting indices of this value are certain metals, which are not usable in a sunshade due to its high reflectivity. A practical material for the inner housing of the lens shade would be carbon black, which is an effective light absorber, until the angle of the incident light becomes smaller than 25 arc-degrees.

4.2 MULTIPLE-CELLED SUN SHIELD

A method to reduce the length of the sunshade, and also to attenuate light incident on the walls of the sunshade, is the use of a multi-celled glare reducing shield placed immediately in front of the entrance aperture of the optical system. The shield is composed of small glass cells that are coated with a light absorbing material, whose index of refraction matches that of the glass. The length of each cell, in this application, is determined by the minimum angle between the optical axis of the sunshade and the sun line, for which the sunshade must be effective, the index of refraction of the glass comprising the cells, and the cell diameter. The geometrical relationships between different parameters of the glare shield are plotted in Figure 4.2, assuming that the glass that comprises the cells has a refractive index of 1.5, and the cell diameters are 0.1, 0.2, 0.3, and 0.5 inch. Depending on the cell diameters used, the length of the multi-celled glare shield is greatly reduced as compared to the normal sunshade. A sketch of the multi-celled sunshade is shown as Figure 4.3. The light absorbent material used between cells absorbs off-axis radiation and is capable of attenuating light reflected off the cell walls by factors of ten thousand.

The effect on system performance of the multi-celled light shield approach is twofold:

- a) A reduction in transmission of the overall system due to the obscuration of a portion of the entering beam by the light absorbent material between the cells of the sun shield.
- b) A redistribution in energy and appearance of the diffraction image, due to the multiplicity of apertures in the entrance pupil.

Both these effects will be dependent on the cell size, the shape of each cell (circular, square, hexagonal, etc.) and the arrangement of the cells across the aperture. The appearance and distribution of the resultant diffraction image may be determined by the method outlined below:

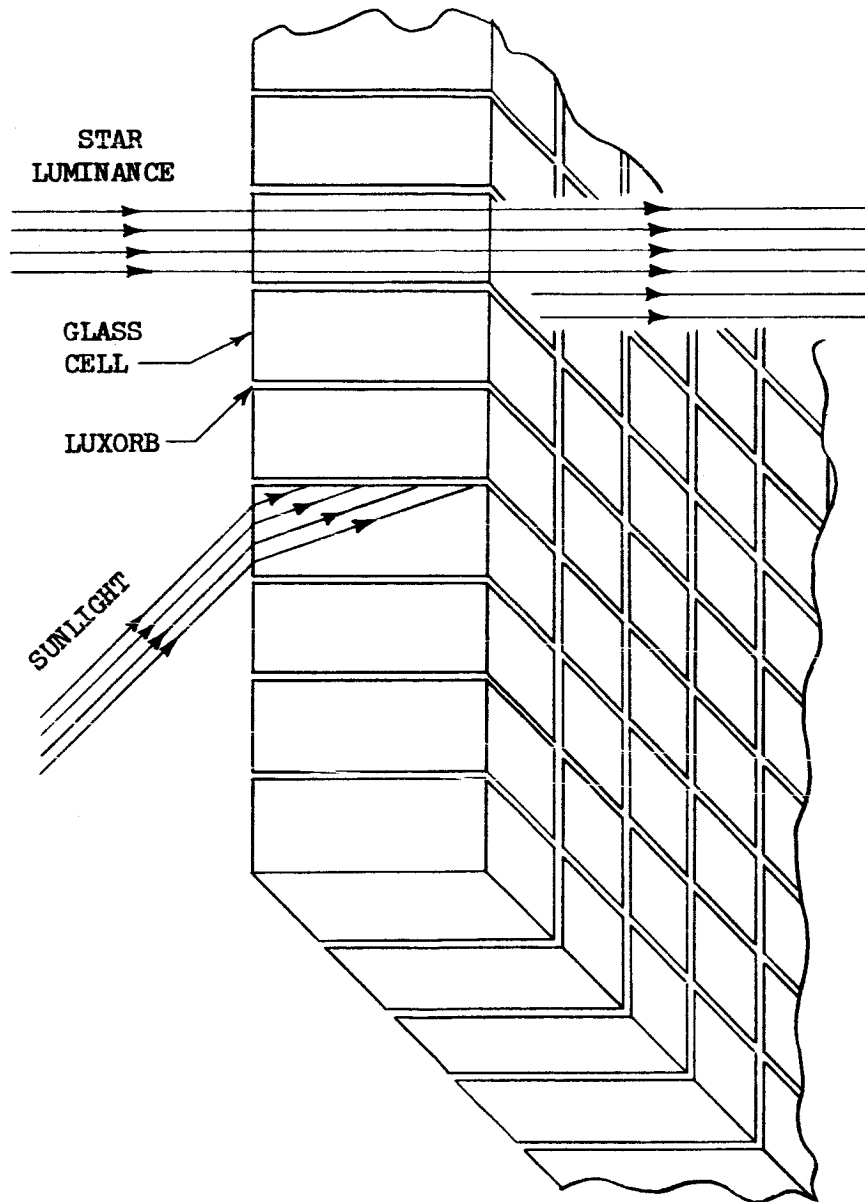


FIGURE 4.3 MULTIPLE CELL SUN SHIELD

The general expression for the intensity, I , at a given point in the focal plane caused by diffraction of the wavefront emanating from a point source by an aperture, is given by

$$I = A'^2(C^2 + S^2) \quad (4.1)$$

where: A'^2 is a constant proportional to the original amplitude

$$C = \int \cos(ux + vy)dw$$

$$S = \int \sin(ux + vy)dw$$

x, y are the rectangular coordinates of any point in the aperture

w (origin in the plane of the diffracting aperture)

$$u = 2\pi\lambda (\alpha_1 + \alpha_0)$$

$$v = 2\pi\lambda (\beta_1 + \beta_0)$$

and α_1, β_1 and α_0, β_0 are the direction cosines with respect to the x, y axis of a line from the origin to the source Q and the point P_0 , respectively (for a telescope system, the point source Q is effectively at infinity, and if the light falls perpendicularly on the diffracting aperture, $\alpha_1 = \beta_1 = 0$).

To derive the intensity function for a multiplicity of diffracting apertures, two coordinate references are established:

ξ, η are the coordinates of any point in one of the apertures referred to a local origin contained within the individual aperture

x, y are the coordinates of the local origin with reference to the main origin established for the entire array of diffracting apertures.

The coordinates of any point in one of the diffracting apertures with reference to the array origin may be expressed as:

$$X = x_i + \xi; \quad Y = y_i + \eta$$

The final intensity function for the multiplicity of diffracting apertures is given by Equation 4.1, where

$$C = \sum_i \int \cos[u(x_i + \xi) + v(y_i + \eta)] d\xi d\eta \quad (4.2)$$

and
$$S = \sum_i \int \sin[u(x_i + \xi) + v(y_i + \eta)] d\xi d\eta$$

Positions of zero intensity in the pattern are given when $C = 0$ and $S = 0$ simultaneously.

The use of two reference coordinates in the solution of the intensity function allows a further simplification by dividing the solution into two parts:

- a) Denote the integrals C and S by c and s when they are extended over a single diffracting aperture:

$$c = \int \cos(u\xi + v\eta) d\xi d\eta; \quad s = \int \sin(u\xi + v\eta) d\xi d\eta$$

- b) Denote the summation over the array of apertures by c' and s' :

$$c' = \sum_i \cos(ux_i + vy_i); \quad s' = \sum_i \sin(ux_i + vy_i)$$

The intensity function can now be expressed by

$$I = A'^2(c^2 + s^2)(c'^2 + s'^2) \quad (4.3)$$

Since $A'^2(c^2 + s^2)$ is the intensity due to a single diffracting aperture, the final intensity of a multiplicity of diffracting apertures is given by the intensity due to one elemental aperture times a factor dependent on the number and arrangement of the multiple apertures in the array $(c'^2 + s'^2)$. An example of the type of diffraction images to be expected from an array of apertures is shown in Figure 4.4.

Use of the multi-celled sun shield, then, must be analyzed from diffraction theory to establish the appearance and distribution of the resultant image as a function of final cell shape, cell size and cell arrangement established by the requirements of a particular application. The effect on system performance of the final appearance of the diffraction image may limit the use of the multi-celled sun shield approach. Its excellent shielding properties, however, would be most useful in those applications where system requirements and performance would be insensitive to the diffraction effects produced by the multiple cells in the sun shield.

4.3 REDUCTION OF GLARE

For the purpose of analysis, the glare produced in telescope systems has been divided into two categories:

- a) Optical Glare: Glare that is produced from the active optical elements, such as from scattering within glass elements or from imperfections such as bubbles, digs, scratches, or dust on the optical surfaces.

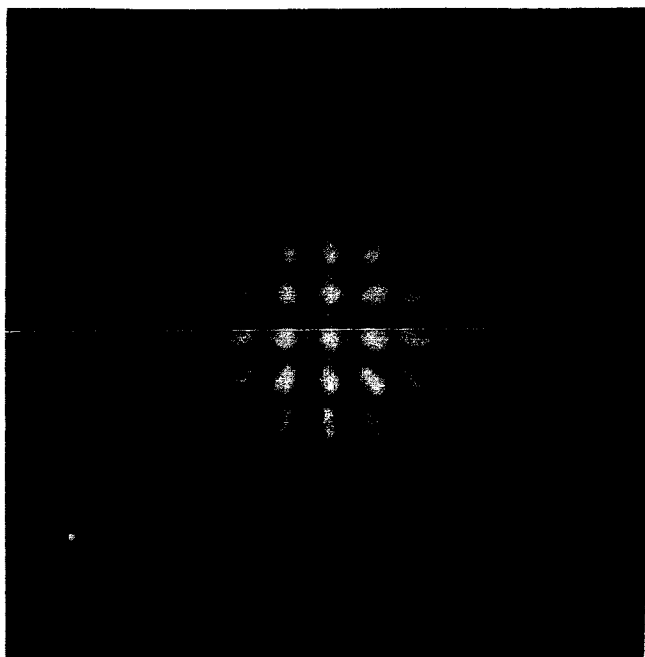
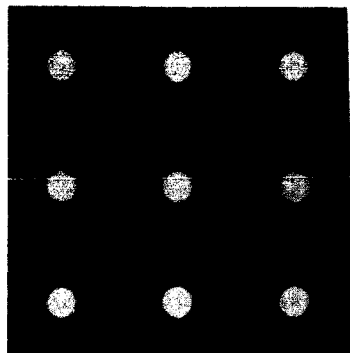
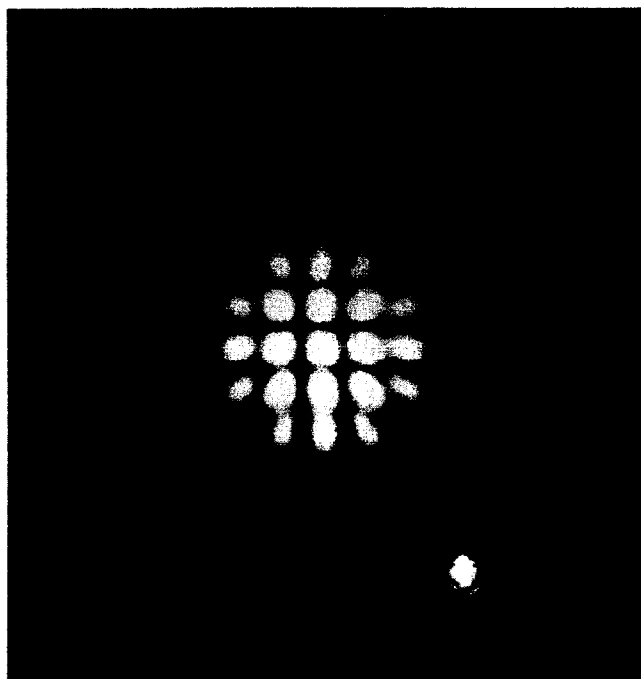
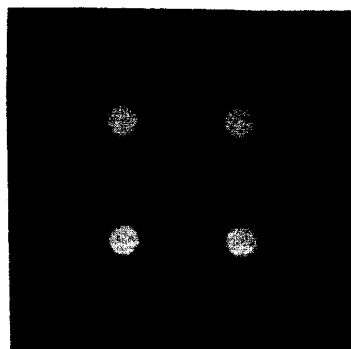


FIGURE 4.4 DIFFRACTION PATTERNS PRODUCED BY MULTIPLE APERTURES



- b) Mechanical Glare: Glare that is produced by reflection and/or diffusion from the mechanical structure of the optical system such as the housing walls and lens mounts.

4.3.1 Optical Glare

Since the effect of optical glare is produced by defects that are present within the active optical diameter of the system, this effect can be minimized by specifying the required quality of optical materials and workmanship. Bubbles, scratches, digs, and other imperfections will, to some extent, always be present in the finished optical elements. A careful analysis of system performance requirements must be performed to set acceptable limits on the maximum optical defects to be allowed.

4.3.1.1 Bubbles

If a bubble within the field of view of the telescope has sunlight incident on it, light will be reflected off the bubble and into the telescope. Part of this reflected light will reach the focal plane within the limits defined by the field of view. The area of the bubble that reflects light directly into the telescope field is given by the relation:

$$A_B = \frac{\pi \omega^2 r^2}{16} \quad (4.5)$$

where A_B = area of bubble

ω = angle defining telescope field of view (radians)

r = radius of bubble

The effective reflecting area (A_{EB}) of the bubble is the area of the bubble projected in the plane that is perpendicular to the rays from the sun.

$$A_{EB} = \frac{\pi \omega^2 r^2}{16} \left(\cos \theta + \frac{\omega}{4} \right) \quad (4.6)$$

where θ = Incident angle of the solar radiance

Since we are dealing with internal reflection of sunlight at the air-glass interface of the bubble ($n_B = 1$), the minimum value of θ for internal reflection is given by the critical angle.

The luminous flux entering the telescope from a bubble is given by

$$F_B = A_{EB} L_s \quad (4.7)$$

where F_B = Luminous flux entering telescope

L_s = Irradiance from the sun

Alternately, this can be expressed by

$$F_B = \frac{\pi \omega^2 r^2}{16} \left(\cos \theta + \frac{\omega}{4} \right) L_s \quad (4.8)$$

The maximum size and the number of bubbles that can be tolerated in the optical system can now be specified from Equation 4.8 by determining the maximum extraneous flux allowable from this type of defect.

4.3.1.2 Scratches

When a scratch on the optical surface is in a position such that the scratch is illuminated by direct sunlight, it is assumed that all the sunlight that falls upon the scratch will be radiated as a diffuse source over a 2π steradian field. The amount of flux that will reach the telescope focal plane is given by

$$F_R = A_s L_s \frac{\omega}{2\pi} \quad (4.9)$$

where F_R = luminous flux in telescope field caused by a scratch

A_s = area of scratch

Allowable scratches on the optical surfaces may be specified by Equation 4.9 in the same manner as used above to specify bubble content.

4.3.2 Mechanical Glare

By baffling the interior walls of the optical system, stray radiation that enters the optical system can be trapped and absorbed and not affect the system performance. Present design techniques for optical baffles favor the use of specular rather than diffuse reflection in the baffling chambers so that the path of off-axis radiation in the optical cavity can be predicted and the stray radiation be more effectively trapped. However, specularly reflective baffles can only be designed to be effective for a given range of incident illumination, so if the stray radiation will be incident over a wide range of angles, diffuse baffling surfaces with low reflectances will provide more satisfactory attenuation of the off-axis illumination.

With a diffuse reflector, each point in the optical cavity acts as an illumination source, and the intensity of the diffuse illuminance from an off-axis source such as the sun can be sufficient to render the system inoperative. Under these conditions, a design combining optical cavity baffling and a multiple-celled window may be required to reduce the off-axis illumination to a tolerable level.

4.4 OPERATION OF A STAR TRACKER WITHOUT A WINDOW

Operation of a star tracker in a pressurized controlled environment for a space mission has many advantages. Some of the advantages are protection of the instrument from contamination during handling, launch and while in orbit, convection cooling capability for components in the instrument that operate at elevated temperatures, and capability of testing and check-out of the instrument in the laboratory without special space environmental chambers. However, the pressurized chamber must be specially designed with a sealed flat window mounted in the housing. This design increases the weight and complexity of the star tracker housing, and adds fabrication difficulties in the manufacturing and coating of the optical window required.

If the star tracker were capable of operating in a space environment, a simple protective covering could be used to prevent contamination of the star tracker optics during the initial launch period. Mounting freedom would also be realized, and the star tracker could be positioned on the exterior of the vehicle to provide a larger search field. A larger search field would allow greater freedom in the choice of navigational stars, without resorting to expedencies such as rolling of the vehicle, or the use of multiple star trackers to extend the total look angle of the star tracker. However, operation of a star tracker in a space environment requires special preparation of the bearings and brushes that are exposed to the space environment, to prevent excessive wear and cold welding of the sliding surfaces due to inadequate lubrication. These factors must all be considered in the choice of operating environment for a star tracker. The problems associated with the operation of bearings in a space environment are outlined to describe the nature of the issue.

4.4.1 Bearing and Brush Wear Under Space Conditions

The prime problem encountered in the operation of gears, bearings and electrical contacts in space is excessive friction and wear of the rubbing or sliding surfaces due to inadequate lubrication. The proposed solution is the development of a lubricant that will function in a space environment. Some of the lubricants proposed are silicone oils and greases or vacuum oils with low vapor pressures, laminar solids such as molybdenum disulfide, soft metals, and plastics.

4.4.1.1 Oils and Greases

Silicone oils and greases, and high vacuum oils and other materials used to provide fluid lubrication of a bearing, form a thin film between the sliding surfaces of the bearing. An insufficient amount of lubricant or too high a bearing load will cause a partial breakage in the lubricating film thickness and the bearing surfaces will come into direct contact with each other, increasing the friction and the surface wear, eventually causing bearing failure. The problems involved with the use of oils and greases as lubricants are the loss of lubricating fluid by evaporation, polymerization, and oxidation of the lubricant.

The evaporation rate of lubricating fluids that were tested by Lockheed Aircraft to determine a suitable lubricant for use under vacuum conditions is typically in the order of 1×10^{-4} gm/cm²/hr., with the oil heated to 110° C and a pressure in the test chamber of 2×10^{-7} Torr. This evaporation rate of 1×10^{-4} gm/cm²/hr., is approximately equivalent to evaporation of a 1 mm thickness of oil in 1,000 hours. This evaporation rate is greatest during the initial period of exposure to a vacuum. Part of this accelerated lubricant loss is due to entrainment of droplets of air in the escaping gas stream when the pressure in the assembly is decreasing. Sealed bearings would serve to reduce the lubricant loss by entrainment in the gas stream, by reducing the flow rate of the gas stream. Creepage of the oil from the bearing surfaces to adjoining surfaces is enhanced by vacuum conditions. The net effect of this creepage is that the area over which evaporation can occur is increased, thus increasing the lubricant loss. The proposed solution to this problem is to coat the bearing shafts and other surfaces with a non-wetting material to minimize creepage of the lubricant.

Lubricant failures are sometimes accompanied by the formation of a very heavy residue on the sliding surface of the bearing. This formation is due to polymerization of the lubricant and is promoted by catalytic action by bare metal surfaces exposed by frictional wear. This lubricant polymerization increases the oil viscosity and the bearing drag, and for applications where the bearing drag is critical such as in a gyro bearing, catastrophic failure of the component can occur. For motors and other mechanisms where bearing torque is less critical, frictional polymerization would not limit the use of oils and greases in space.

Some materials provide effective lubrication by reacting with the surface to be lubricated and forming a thin film attached to the rubbing surfaces. The lubrication in this case is not provided by the material itself but by the film formed by the chemical reaction. Since the film in many cases is a metal oxide, the reaction will not occur in absence of oxygen and the material will be ineffective as a lubricant in space. This point must be considered when selecting a lubricant for space.

Labyrinth sealing techniques have been proposed for bearing lubrication in a vacuum. The labyrinth seal consists of a reservoir of oil or grease to replenish the lubricant on the sliding surfaces. The labyrinth seal requires more weight, volume and power than an unsealed bearing, and in addition since the lubricant is continuously evaporating, a gas cloud is created which may affect some scientific experiments such as ion concentration which may be performed during a space mission. The advantage of the labyrinth seal is that oils and greases which are compounded for use as lubricants in an atmospheric environment can be utilized, so the behavior of the lubricant can be predicted. Silicone and vacuum oils have low vapor pressures and have been used successfully with unsealed bearings. Due to the higher viscosity of these oils, in particular the high vacuum oils, the driving torque required is greater when these lubricants are used rather than normal lubricants.

4.4.1.2 Laminar Solid

Molybdenum disulfide (MoS_2) forms a surface film which functions as a lubricant. The film can either be burnished onto the surface or bonded to the surface with an organic resin or an inorganic adhesive. It can also be used as an impregnant in solids or as an additive to oils and greases.

The crystal structure of MoS_2 is laminar, and consists essentially of planes of molybdenum atoms alternating with planes of sulfur atoms. The atomic arrangement in each MoS_2 layer is hexagonal, and the forces that hold the atoms together in each layer are stronger than those between adjacent layers of sulfur atoms. This arrangement permits the planes to slide readily over one another with low frictional resistance without breaking down the molecular structure.

Molybdenum disulfide particles are platelets which tend to orient themselves with the surface on which they are placed. The cleavage planes of the particles or the plane of low frictional resistance will thus be parallel to the sliding surface to be lubricated. Rubbing or burnishing increases the degree of orientation and lowers the coefficient of friction slightly.

Graphite is a laminar solid that is widely used in normal environmental conditions as a lubricant. Graphite contains adsorbed water vapor which is essential to the properties of graphite used as a lubricant. In space the adsorbed water vapor is lost and graphite no longer performs as a lubricant. Molybdenum disulfide functions equally well under atmospheric conditions as in a vacuum. In addition the coefficient of friction of MoS_2 is about one-half that of graphite.

The method in which laminar solid lubricants such as MoS_2 is applied to a bearing to be lubricated is important since the amount and distribution of MoS_2 in the bearing has a direct effect on the degree and nature of the lubricant buildup in the ball track of the bearing during operation. The formation of sizable discrete isolated patches of MoS_2 can cause rough running of the bearing and a generalized buildup of MoS_2 will reduce the bearing clearance and require a higher driving torque. With proper application of MoS_2 , a thin, smooth coating is formed in the ball track.

4.4.1.3 Soft Metals

The most highly polished metal surfaces will appear to be quite rough when viewed under a high powered microscope. Two metal surfaces that are placed together will touch only at the points where the high spots of the two surfaces coincide. Therefore the effective contact area between the two plates is much smaller than the overlapping areas of the surfaces. If pressure is applied to force the surfaces together, the high spots will be crushed and will suffer plastic deformation. The number and the size of the contact area supporting the load will be increased with this plastic deformation.

Moving the two surfaces with respect to each other will add frictional heating and the combination of intense local heating and high pressure will cause abrasion and seizure of the metals. The localized adhesion or the cold welding of the metal surfaces forms junctions which must be sheared to permit the surfaces to slide with respect to each other. The frictional force in the sliding surface is thus proportional to the product of the shear strength of the junctions and the effective contact area between the two surfaces.

Assume that a spherical object is in contact with a flat surface. If the spherical object were composed of a hard material and the flat surface of a soft material, the soft material will be deformed by the hard spherical object and the area of contact between the two surfaces becomes large. The frictional force between the two surfaces would be high because of the large contact area.

If both objects were composed of hard materials, the contact area between the two surfaces is small, but the strength of the junction that is formed is large, so the frictional force is still relatively high. However a film of soft material with a low shear strength can be placed between the two hard bodies to combine the beneficial characteristics of both materials. The hard substrate material supports the load and keeps the contact area small while the film of soft metal reduces the junction strength.

Films of gold, silver, barium and lead have been used as lubricants due to their low shear strength. The major problem in securing long wear life with a metal-film lubricant is obtaining good adhesion between the substrate and the film. Cleaning of the surface and the method by which the film is deposited on the substrate is important. In general, however, the use of soft metals as lubricants is most effective for applications where the bearing loads are small, and the electrical conductivity of the lubricating metal is advantageous for the desired application.

4.4.1.4 Plastics

The use of plastics for lubrication purposes is quite attractive for many applications. The plastic itself can be self-lubricating as in the case of teflon. Teflon also has very little tendency to cold-weld to metals even under high vacuum conditions. Plastics tend to absorb vibration and will provide quieter running gears and bearings. Some plastics have very good impact strength and can survive heavy shock loads without appreciable signs of wear or brinelling. Plastics will also deform to compensate for lower tolerances in manufacture of balls, bearing races and gear teeth, and for inaccuracies in mounting and alignment. Contamination of a bearing by dust or other debris is less of a problem since the plastic is soft and the contaminant will more likely become embedded in the plastic rather than score the mating surface. Plastics in addition are relatively free of corrosion effects by the atmosphere.

However, plastics have poor thermal conductivity and plastic parts will run hotter than similar parts made of steel. Their thermal coefficient of expansion is also ten times higher than steel, and most plastics cannot function at elevated temperature since they will soften then melt if the temperature is raised. Plastics are also weaker than steel and therefore have a much lower load carrying capacity than an identical steel part.

One practical use for plastics in a precision bearing would be as a thin film over a metal surface to act solely as a lubricant and not as part of the supporting structure. However, plastics reinforced with fibers to provide structural strength have been employed successfully in precision ball bearings. In this application, the balls and the races were made of steel, but the retainers were made of teflon reinforced with glass fiber and coated with molybdenum disulfide. These bearings were run dry, and the only noticeable wear after considerable running time was wear of the retainer.

Impregnating of a porous metal substrate with teflon has been attempted. The lubricating action is similar to that of oil-impregnated bronze, in that the frictional heating causes the teflon to flow to the surface of

the substrate and form a thin film at the sliding surface. This combination of materials takes advantage of the low coefficient of friction of teflon and of the high thermal conductivity, low thermal expansion and the mechanical strength of the metal substrate.

Plastics tend to decompose when subjected to hard radiation and for applications where the spacecraft is exposed to radiation for extended periods of time, the use of plastics may not be warranted.

4.4.1.5 Ceramics and Cermet Materials

Hard brittle materials that have a very low tendency to cold-weld to the metal parts with which they come in contact have been considered for use in bearings. Typical materials that can be used would be sapphire, glass, cemented carbides and pyroceram. In general these materials are limited to low speed and light load applications. For some of the material such as sapphire and glass, special precautions must be taken at launch to support the load carried by the bearing since sapphire and glass tend to shatter under heavy loads.

4.4.2 Space Lubrication Suppliers

4.4.2.1 Vac-Kote Process By Ball Brothers

A number of different techniques are available for space lubrication of bearings and brushes. The Vac-Kote process was developed by Ball Brothers Research Corporation in Boulder, Colorado, and is a conductive lubricant that can be used for either bearings or brushes. The Vac-Kote processes involve the application of fluid and/or solid lubricant coatings by various methods, depending upon the device treated and its operational requirements. The fluid lubricants are normally applied in a vacuum, and solid lubricant coatings applied to metallic surfaces by molecular bonding.

The Vac-Kote process permits the use of standard commercial components in the design of an instrument for space application. To prepare the component for use in the instrument, the component is disassembled, cleaned, then coated with the special lubricant. The lubricant has a low vapor pressure and does not outgas in sufficient quantities to cause contamination of other spacecraft instrumentation. The fluid lubricant used is an organic compound containing long chain hydrocarbon molecules, and the solid lubricant is molybdenum disulfide.

Vac-Kote has been used successfully for many slip-ring, motor and bearing applications. However, it is not a solution for all vacuum lubrication problems. Each application is unique and must be considered separately.

4.4.2.2 Columbia Broadcasting System

A space lubricant of a proprietary nature is manufactured by CBS. Bearings coated with this material were tested by Thompson Ramo Woolridge under simulated space conditions. The material was described as being very slippery, and bearings coated with this material require no break-in period as contrasted to coatings containing MoS_2 which require a run-in period to achieve proper running conditions. However, over extended periods of time, the torque required to drive the bearings coated by CBS increased slowly while bearings coated with MoS_2 stabilized after the run-in period and operated satisfactorily for the length of the tests conducted by TRW which was 39 days. A conclusion can be made that the CBS lubricant would fail if the tests were extended, but no evidence of failure could be determined for the MoS_2 coated bearings.

4.4.2.3 Electrofilm Incorporated

Electrofilm prepares a number of solid film lubricants for different applications. Most of these are mixtures of graphite and molybdenum disulfide, that are bonded to the part to be lubricated with a resin. The resin binds the graphite and molybdenum disulfide particles together, forming a thin solid film with a low shear strength over the surface to be lubricated. The application method is to spray, dip, tumble, or spray-tumble the parts to be lubricated in a resin-lubricant mixture, then bake the parts to polymerize the resin.

For space applications, Electrofilm proposes using molybdenum disulfide as the lubricant, and sodium silicate as the bonding material. This product is being evaluated at present for performance in a vacuum environment.

4.4.2.4 Lubeco, Inc.

Lubeco use a chemical binder to bond a dry lubricant to the part to be lubricated. The proprietary binder and bonding material is named Lubeco 905, and is a completely inorganic solid dry film lubricant. The binder is established by electrodeposition of colloids in a suspension under the influence of an electric field, which in the case of Lubeco 905 is generated by an intrinsic electrolytic system. The binder serves to form a thin film that contains particles of the actual lubricant, which for space applications would be molybdenum disulfide.

4.4.3 Summary of Applications of Bearing Lubrication for Space

Adequate lubrication of bearings and brushes under space conditions can be accomplished in a variety of ways. The particular lubrication method chosen would be dependent upon the particular application and there is no universal solution to the space lubrication problem. For a star tracker, the critical components which require lubrication are the brushes in the torquers, the sliding surfaces in the bearings and the slip rings used for signal and power transfer. Tests conducted by Ball Brothers indicate that their Vac-Kote process is satisfactory for coating brushes and slip rings and can provide thousands of hours of trouble-free operation. Precision bearings are required for the star tracker gimbals to provide the desired alignment accuracy. Close manufacturing tolerances and pre-loading of the bearings become necessary to achieve this degree of accuracy. The tests conducted and the experience obtained with vacuum lubricants were with bearings of lower accuracy and smaller pre-loading force so that operation of precision bearings for a given period cannot be specified as having been demonstrated. However, Ball Brothers feel that with proper coating, precision bearings could be operated satisfactorily for extended periods in a space environment.

The differences in the solid dry film lubricants made by the different manufacturers would lie in the properties of the binder rather than the actual lubricant, since for space applications, the different manufacturers all recommend molybdenum disulfide. However the characteristics of the binder is important since the thickness, uniformity and wear properties of the film would determine the bearing accuracy and running life that can be expected.

APPENDIX A

MODIFICATION OF ELECTRONIC CIRCUITRY TO IMPROVE PERFORMANCE
OF QUADRANT PHOTOMULTIPLIER CELESTIAL BODY TRACKER

In accordance with Contract NAS8-20193, preliminary redesign of certain circuits in the electronics subsystem of the celestial body tracker produced by Northrop-Nortronics (under Contract NAS8-5393) has been accomplished.

Design cannot be finalized until all modifications and redesigned circuits have been constructed and tested in the laboratory (at MSFC).

If successful, the redesign will eliminate the apparent (warm-up) time delay, decrease the error signal cross talk, and improve tracker accuracy, as per paragraph (amended) 1.4.3 of Exhibit A in subject contract.

This description and block diagram of the proposed modifications is intended to supplement the necessary circuit diagrams and component lists.

Basically the modified system includes changes in the following areas:

1. The switching means for commutating the four photocathodes of the Quadrant Photomultiplier Tube (QPMT) is modified to allow grounded operation of the cathodes. The desired result is to eliminate the time delay (warm-up) due to interelectrode and stray circuit capacitances charging when negative high voltage is applied to the cathodes.
2. The high voltage power supply is polarity-reversed so that the high positive voltage may be applied to the dynodes and collector, thus allowing the cathodes to be operated at or near ground, in accordance with the desire to eliminate warm-up time.
3. An improved ac-coupled preamp is designed to allow operation with the positive collector anode supply, and to improve signal-to-noise ratio.
4. A new synchronous detector circuit is designed to provide error-reduced operation in both signal channels.
5. The A.G.C. Amplifier is modified to make it compatible with the reversed high voltage supply.
6. A synchronous A.G.C. rectifier is provided to generate an A.G.C. error signal, since the signal processing chains are no longer dc coupled and a dc amplitude dependent error signal is no longer available.

7. Diode logic and transistor drivers are provided to properly activate the synchronous detectors.
8. A new flip-flop counter chain is substituted for the previous design in order to generate the required new timing and gating waveforms.

Included in this circuitry are modifications for the master oscillator to change its frequency and to provide outputs for both polarities of its waveform.

It is worthwhile at this point to discuss each modification in detail. Consider first the high-voltage QPMT cathode switching circuit.

For correct operation each cathode must be switched on separately in a pre-arranged order, as contrasted with the old system wherein the cathodes were activated in pairs.

Furthermore, since the new system includes ac coupling between the QPMT anode and the preamp, a "dead time" is necessary between the active "on" periods of each consecutive pair of cathodes.

During the "on" period, each cathode must be held at ground potential; conversely, during the "off" period of a cathode, it must be maintained at the potential of the first dynode, which is approximately +150 V. When a cathode is at the same potential as the first dynode, no signal current will flow from it.

Since circuit resistances are very high (in the megohm range), inter-electrode and stray parasitic capacitances present a charge-discharge time constant problem which could seriously lengthen switching rise and fall times if means were not provided to eliminate the problem.

In the new design, this difficulty is overcome by utilizing a differential switch arrangement, which at all times charges and discharges stray circuit capacitances through a high conductivity path; the high conductivity is provided by complementary pairs (NPN-PNP) of switching transistors which alternately connect each QPMT cathode to either +150V or ground.

Each switching transistor differential pair is driven from a single ended signal source. Coupling into the switching transistors is by capacitor, and diodes are connected between base and emitter of each transistor to prevent the coupling capacitors from charging and thereby adversely biasing the transistors.

Each switching circuit receives a signal which is formed by "anding" together waveforms from each transistor flip-flop in the counter chain. The switching circuit driving signal is comprised of pulses having 12.5 percent duty cycle with sufficient amplitude to cycle the switch transistors between saturation and cutoff.

Isolation resistors (R5, R6, R7, R8) are provided between each "and" gate and its associated switching circuit to prevent excessive loading by the switches.

To operate in the new mode, a positive high voltage is required rather than the negative high voltage previously used.

In order to convert the present power supply to a positive voltage supply it is merely necessary to remove the present silicon rectifiers and reverse their connections in the circuit. However, it is believed desirable to replace the present rectifier diodes with improved diodes of Type 1N649.

An improved preamp circuit has been designed for the celestial body tracker system. This circuit features low noise, high input impedance, and double ended (push-pull) output.

In order to achieve high input impedance and low noise, a field effect transistor is used as an input stage. This stage couples into a grounded-base stage so that the combination forms a cascode circuit; this preserves bandwidth by reducing the effect of Miller capacitance in the FET stage.

The cascode output feeds a differential amplifier with emitter follower output. Heavy negative feedback from one side of the differential stage to a resistor in the source circuit of the FET linearizes the amplifier and reduces input loading (R and C).

Signal pulses from the QPMT are amplified approximately 60 db in the preamp; the exact gain (which can be varied by changing R7) will depend on parameters in the signal processing electronics.

The A.G.C. amplifier must be modified to take into account the positive high voltage supply, a sample of which is applied through R2 to the summing junction at the base of input transistor Q1. The sample of high voltage is taken from the 150 volt tap on the QPMT high voltage bleeder and voltage divider. An error signal, negative-going with an increase in star signal amplitude, is applied to the same summing junction.

Resistor R1 (nominally 500K) is chosen to limit the A.G.C. amplifier output swing over the range of expected star signal amplitudes. This is the only modification required in the A.G.C. amplifier circuit; otherwise, all components remain the same as the old circuit.

No change is required in the high voltage power supply oscillator, or in its connection to the A.G.C. amplifier output.

The synchronous A.G.C. rectifier together with its transistor driver circuit is used for rectifying the raw composite ac signal which appears at the proper output terminal the the preamp. This circuit achieves rectification by clamping action.

The clamp uses an FET which grounds the output terminal of C1 between signal pulses, thus charging C1 to the peak instantaneous value of the signal. Resistor R1 and C2 form a low-pass smoothing filter which eliminates the ac waveform from the A.G.C. error signal.

The clamp FET is turned on by a negative-going pulse applied to its gate electrode by the action of transistor driver Q2. The input of Q2 is connected to terminal A on the first flip-flop through capacitor C3 and isolation resistor R4.

Each error signal synchronous detector is comprised of five FET switches. Two of these (F3, F4) are used for dc restoration or clamping of the ac waveforms which couple through C1 and C2 into the synchronous detectors from the two output terminals of the preamp. F3 and F4 are driven by the same negative-going pulse which drives Q1 in the A.G.C. rectifier circuit (terminal X).

F1 and F2 are series switches. When keyed on by signals on D and F respectively, EO 1 and EO 2 are alternately connected to the loop integrator.

F5 is a dc clamp which grounds the integrator input terminal between signal pulses in order to eliminate the effects of stray pickup interference on the error signal. It is activated by a keying signal (E) on its gate electrode.

The advantage of using FET's in a synchronous detector is that there is negligible offset due to currents which flow by virtue of parasitic sources such as switching signals coupled to the signal path through leakage and stray capacitance. Thus offset and drift errors are reduced and system accuracy is improved.

Signals D, E, and F are derived from the synchronous detector drivers, which comprise driver transistors Q1, Q2, and Q3 and associated wave shaping logic.

Each driver transistor supplies a large negative-going pulse to its respective FET gate circuit.

The waveform shaping logic comprises a pair of four-input "and" gates; three input terminals are driven by signals from the flip-flop binary counter chain, so that a "1" (ON) appears on the respective driver transistor base whenever the proper coincidence occurs between counter chain flip-flop waveforms. The fourth input is supplied by the master oscillator multivibrator (terminal 0). The purpose of this pulse is to delay the instant of turn-on of F1 and F2 by an amount sufficient to eliminate leading edge transients.

The output clamp F5 is driven by a signal from driver Q3; the input of Q3 comprises the sum or composite of the signals from Q1 and Q2.

The signals at D, E, F, and X are all negative-going turn-on pulses; pulse amplitudes should lie between 10 and 15 volts.

In the old configuration there was a 50 percent overlap between signals from adjacent cathodes. The QPMT was dc coupled to the preamp. In the new configuration, each cathode is separately and individually interrogated and a 50 percent time gap is retained between interrogations to allow the use of ac coupling.

In the old system, the master oscillator coupled to a flip-flop divider, each of whose outputs drove an additional flip-flop divider, thus generating gating signals whose phase differed by 90. degrees.

In the new system, a synchronous binary counter chain generates individual signals which combine in "and" gate logic to form keying pulses, similar to those which would be obtained from a ring-counter chain or shift register with a single stored and shifted pulse.

The flip-flop circuits which comprise the counter chain are identical to those in the old system and in fact the old circuit boards can be used in the modified system.

The logic which interconnects the flip-flops in the counter chain is, of course, different from that of the old system. In general, the logic comprises "and" gates which allow synchronous triggering of all three flip-flops.

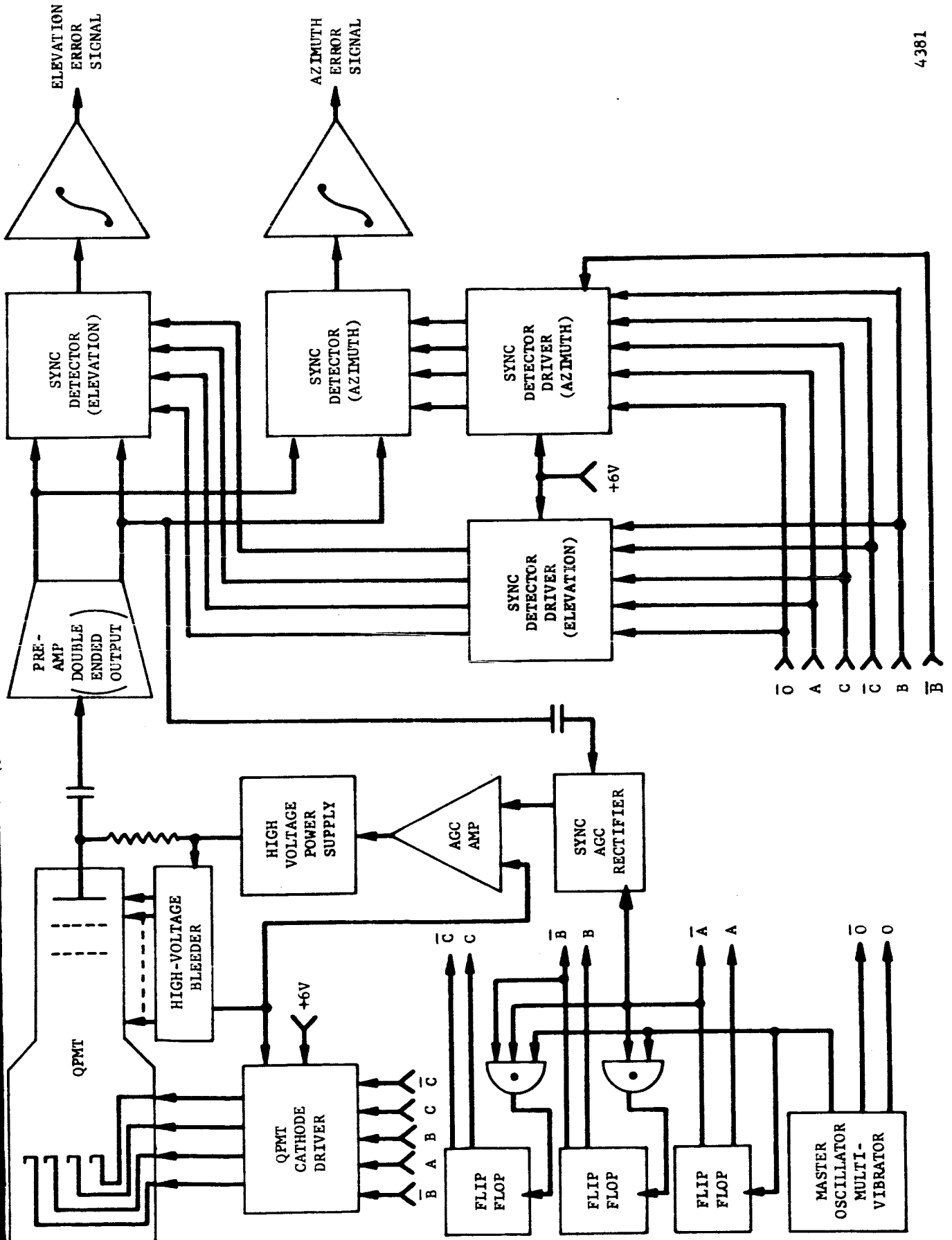
The master oscillator multivibrator is modified in two respects: its free running frequency is doubled, and isolation amplifiers are provided to allow external use of its waveforms.

Figure A1 is a block diagram of the new system showing its interconnections.

Figure A2 is a waveform diagram showing the inter-relationships in time of waveforms at various parts of the system.

Figures A3 - A10 are circuit diagrams of the new and modified circuits. All existing circuits in the old system which are not discussed here are retained and used as is.

Bear in mind that all circuits and modifications are tentative and cannot be finalized until verified in the laboratory. Furthermore, laboratory construction and test may indicate the necessity for modification or replacement of parts of the system not contemplated at this time.



1 FIGURE A1 ELECTRONIC BLOCK DIAGRAM

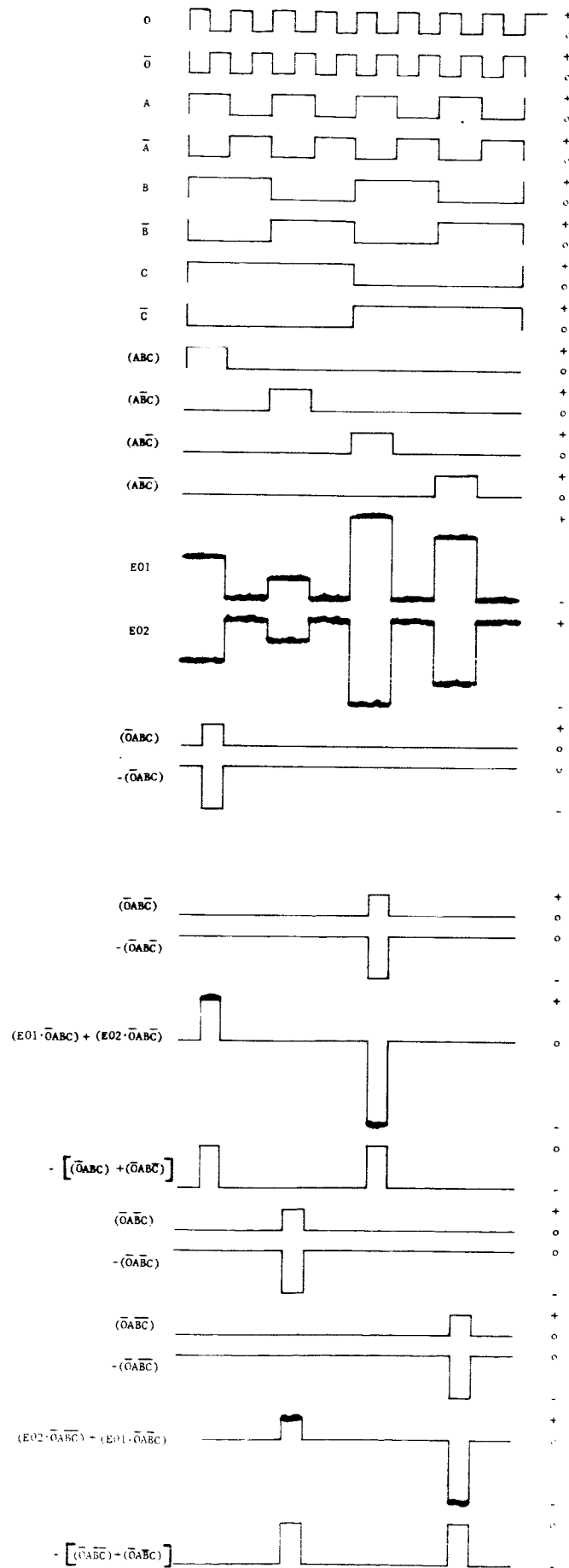


FIGURE A2 IMPORTANT WAVEFORMS

4373

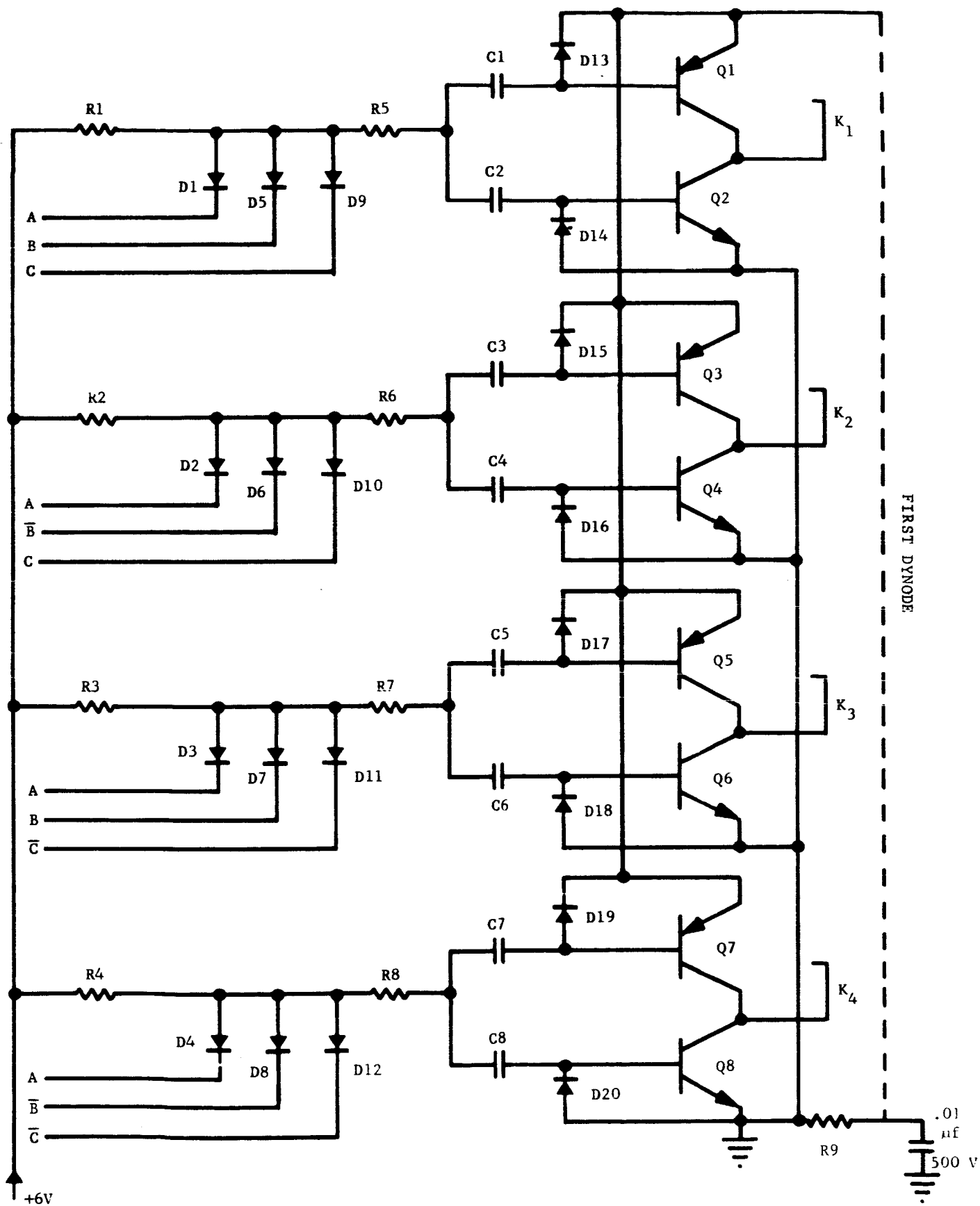
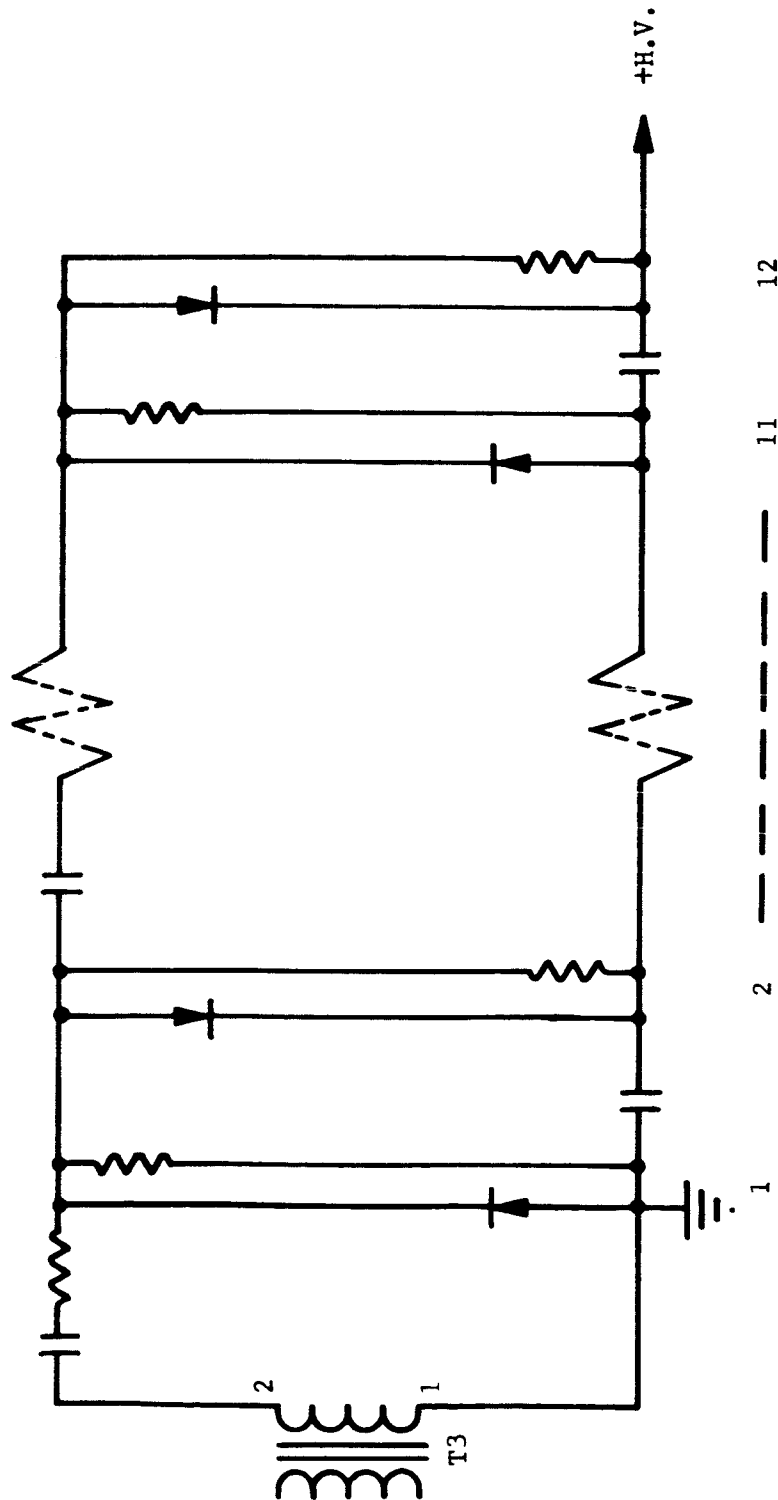


FIGURE A3 CATHODE SWITCH ARRAY

4372



COMPONENTS SAME AS ON 50630956, EXCEPT
DIODES, WHICH ARE 1N649's

4374

FIGURE A4 HIGH-VOLTAGE RECTIFIER

4378

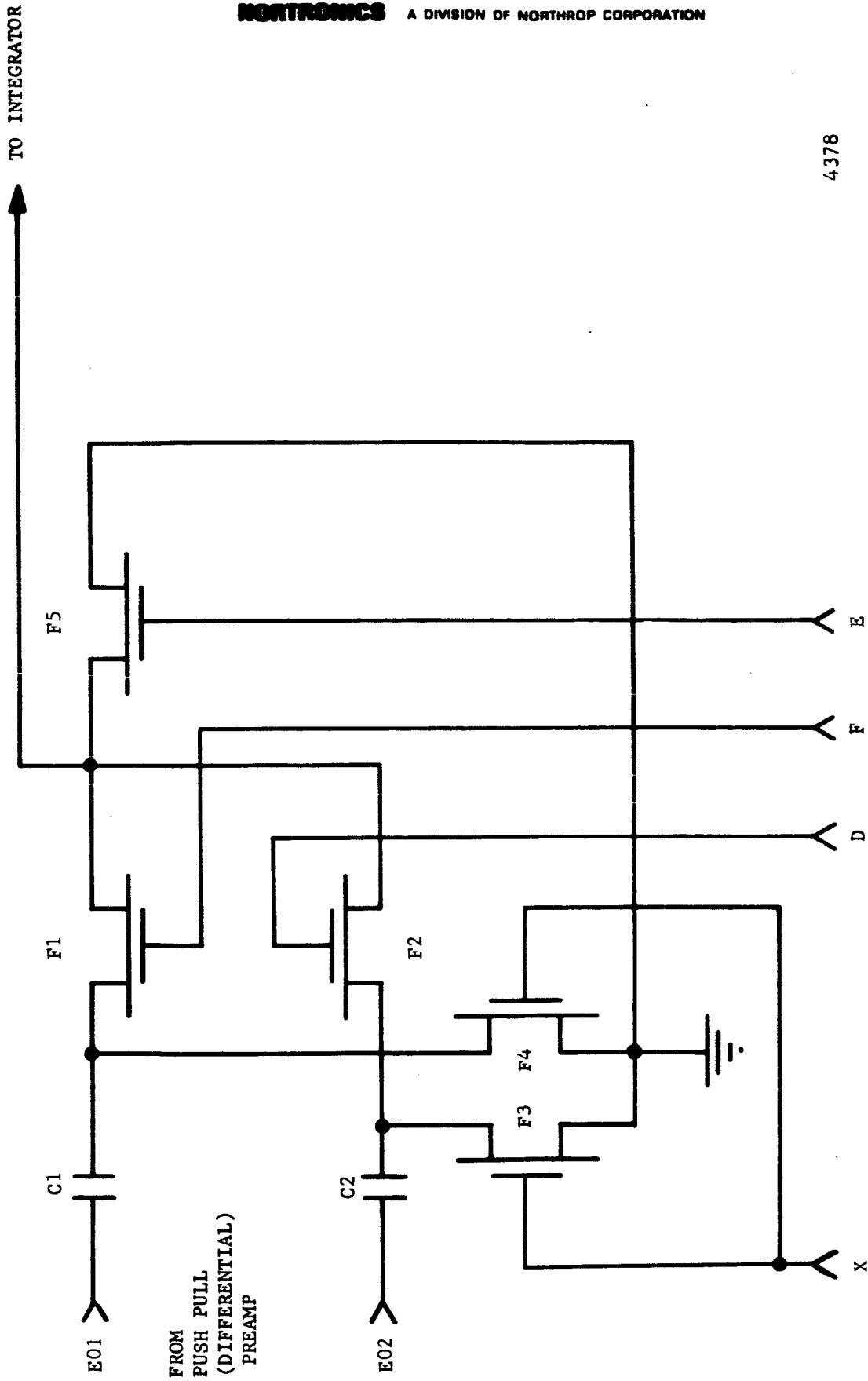


FIGURE A5 SYNCHRONOUS DETECTOR
(2 REQ'D)

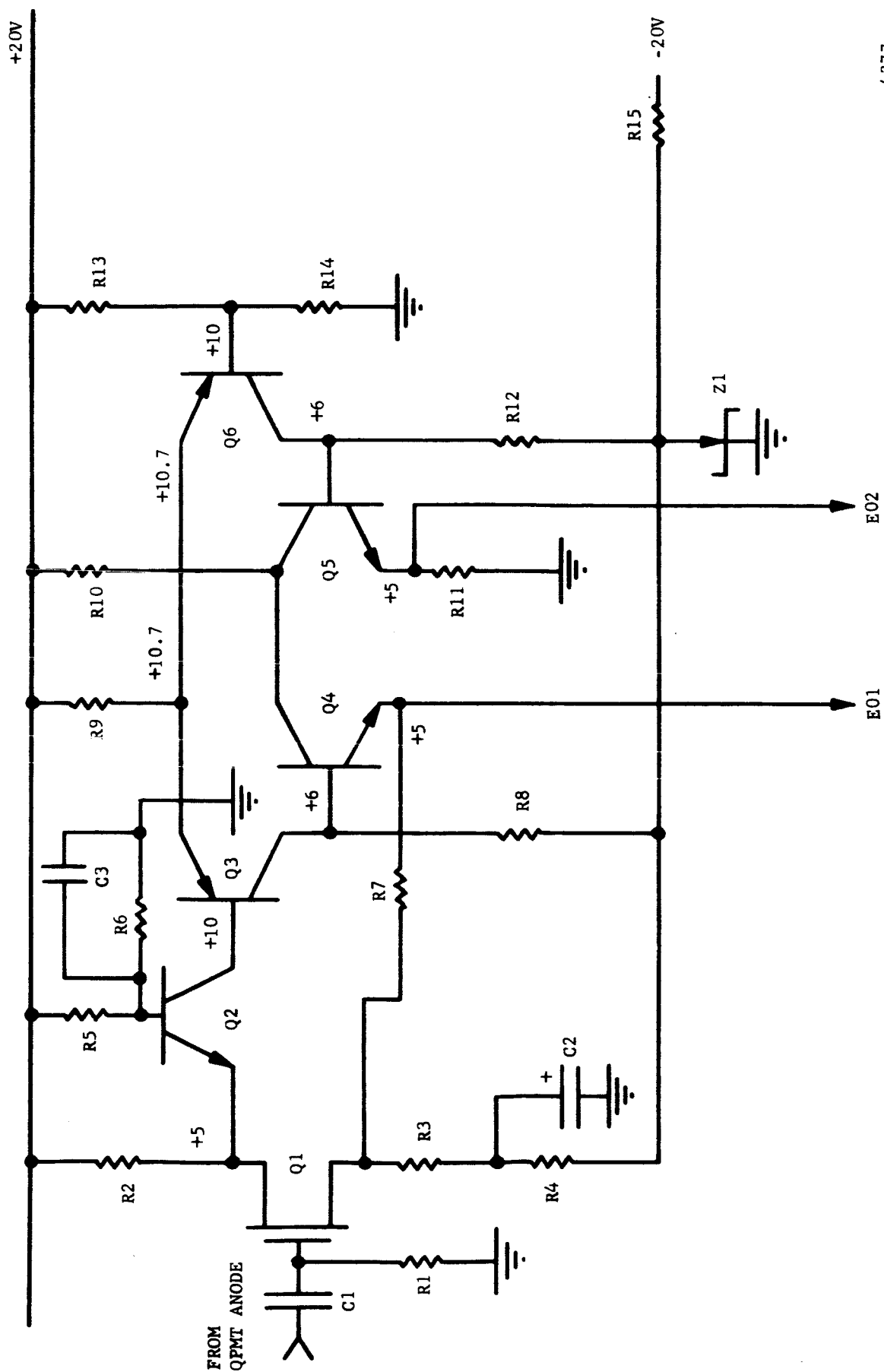
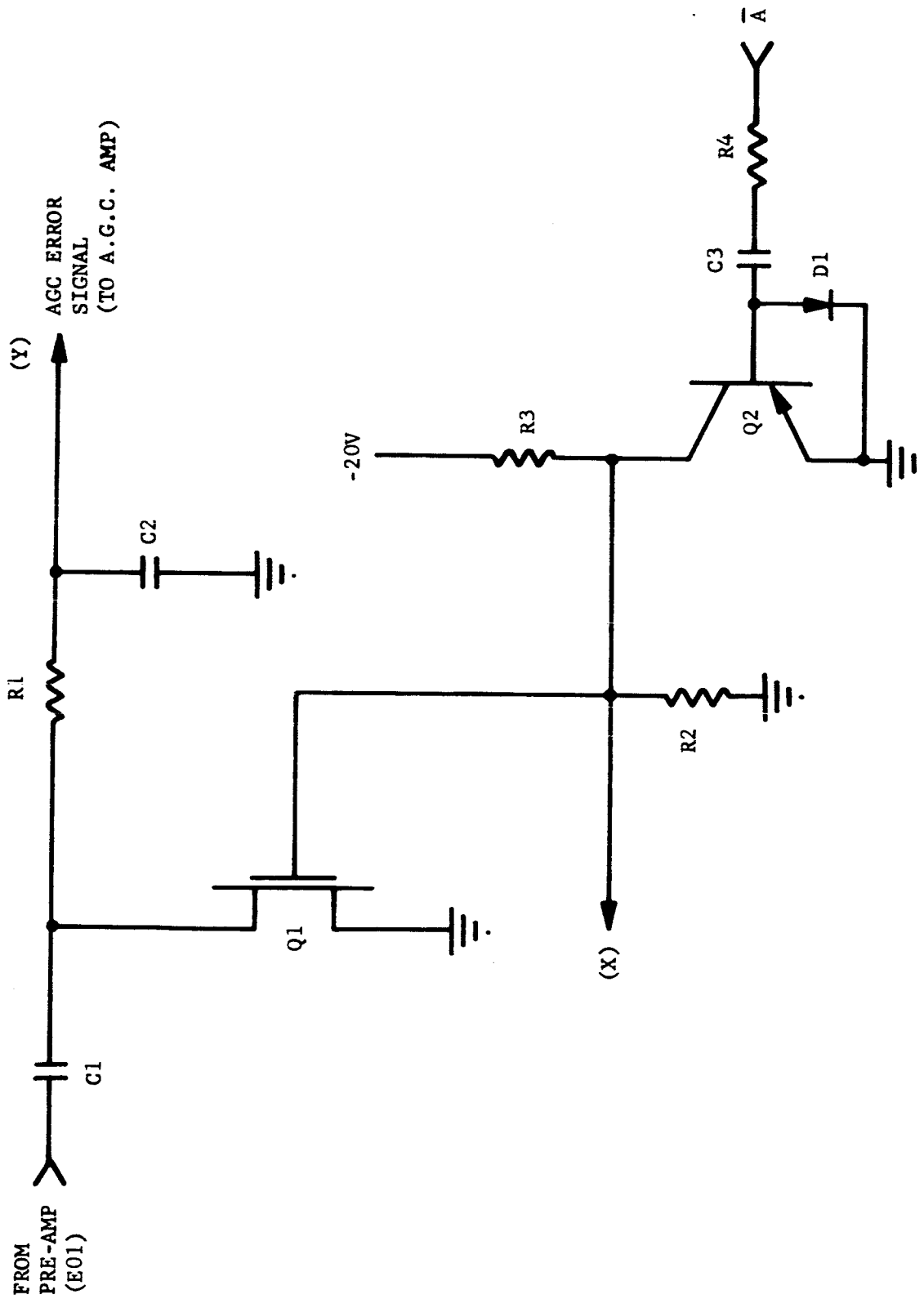


FIGURE A6 PRE-AMPLIFIER

4377



4375

FIGURE A7 A.G.C. RECTIFIER

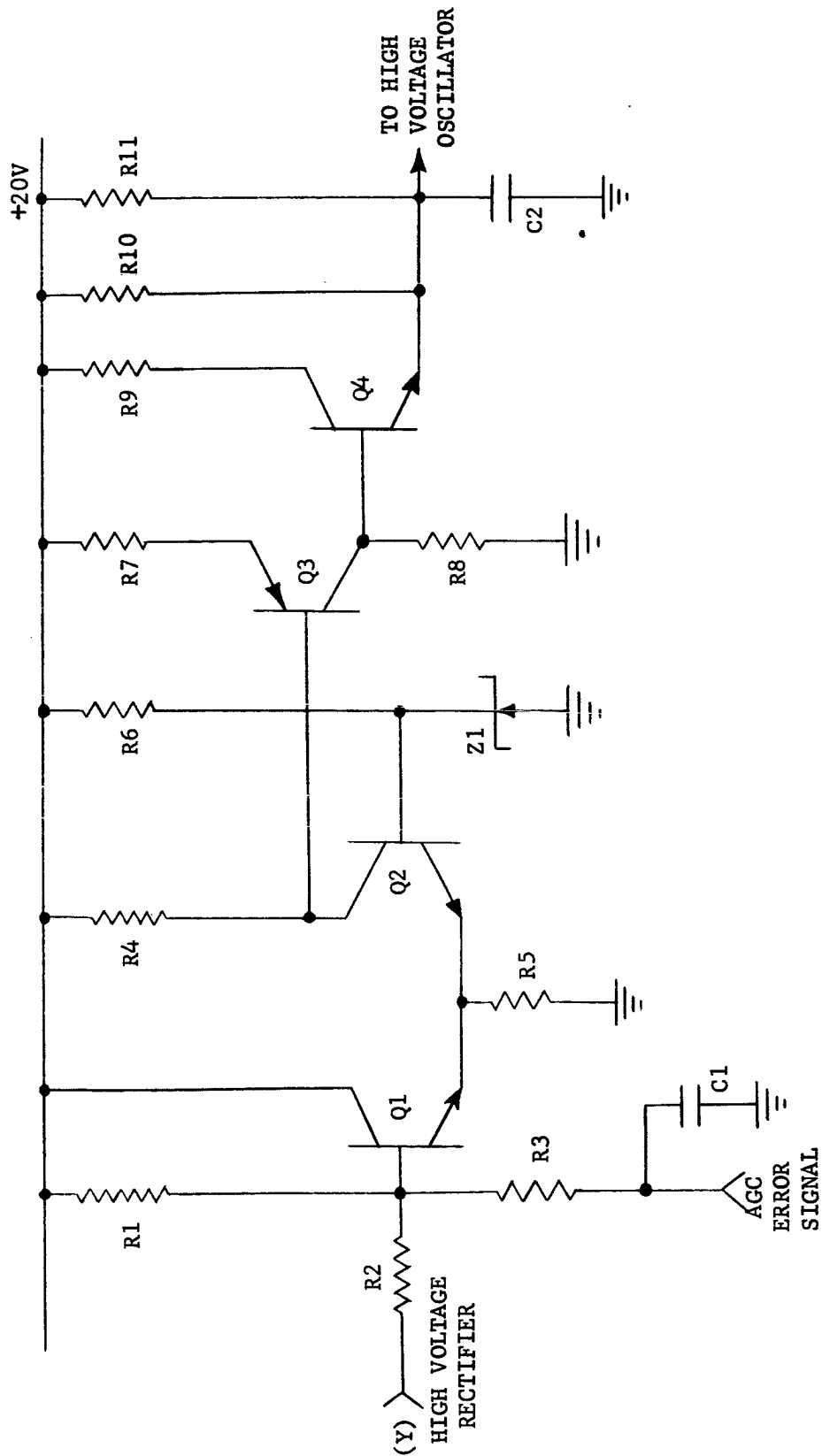


FIGURE A8 A.G.C. AMPLIFIER

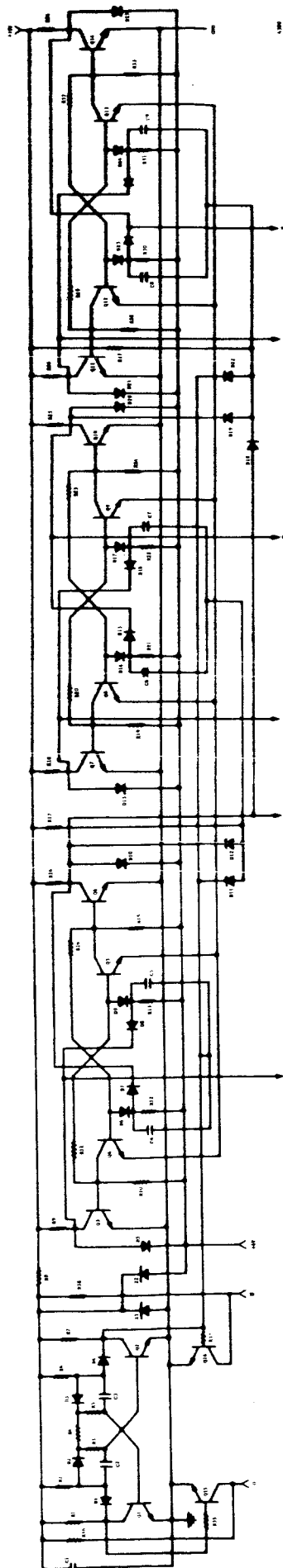
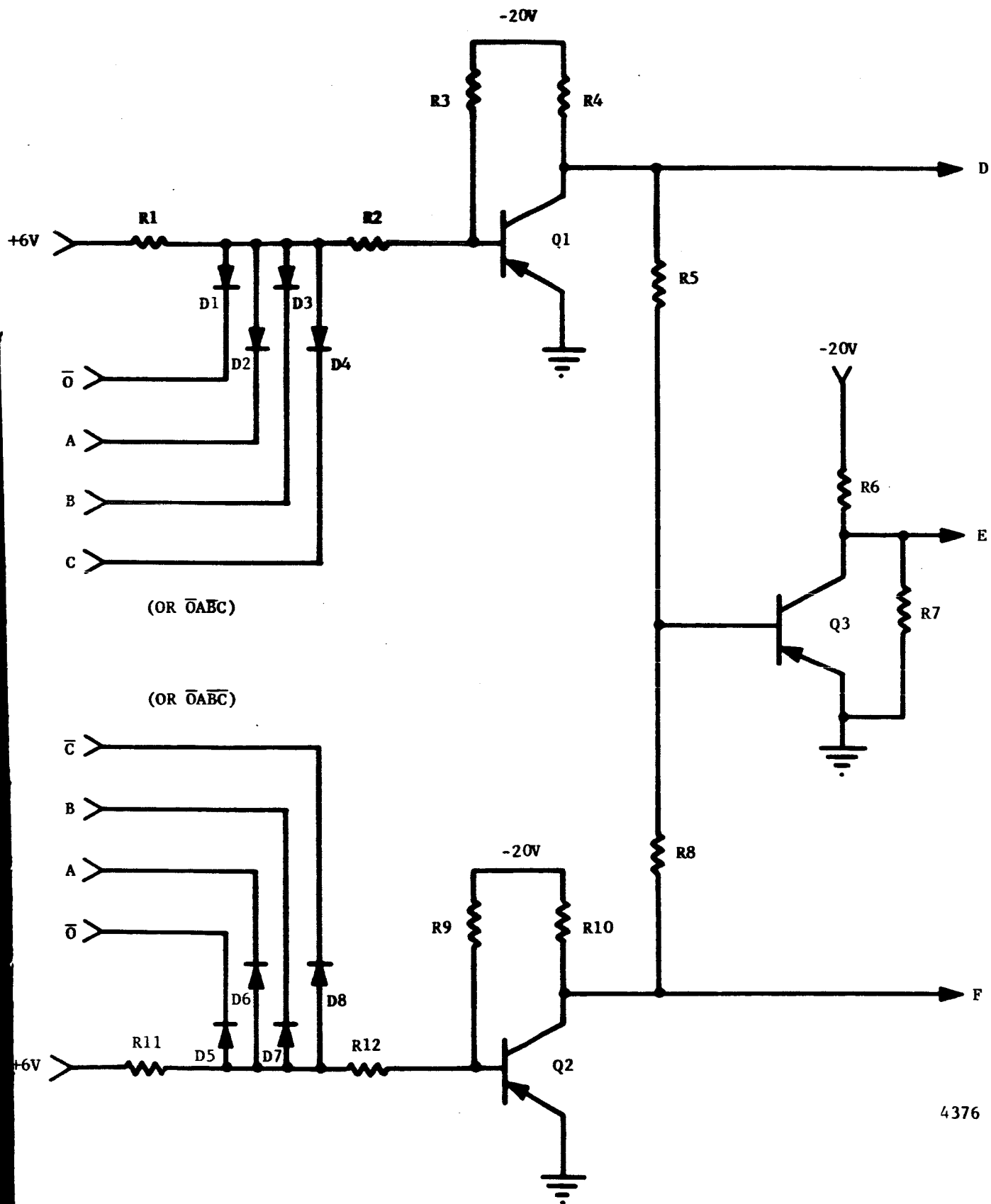


FIGURE 1 - WATER DETECTION AND CONTROL SYSTEM



4376

FIGURE A10 SYNC DETECTOR DRIVER
(2 REQ'D)

COMPONENT PARTS LIST FOR CELESTIAL BODY TRACKER
ELECTRONIC MODIFICATIONS

FIGURE A-3 QUADRANT PHOTOMULTIPLIER CATHODE SWITCH ARRAY

<u>PART DESIGNATION</u>	<u>QTY.</u>	<u>PART DESCRIPTION</u>	<u>MANUFACTURER</u>
C1 thru C8	8	0.1 μ f capacitors	
D1 thru D20	20	1N916A Diodes	Texas Instr.
Q1, Q3, Q5, Q7	4	2N3743 Hi-Voltage PNP Transistors	Motorola
Q2, Q4, Q6, Q8	4	2N3742 Hi-Voltage NPN Transistors	Motorola
R1 thru R8	8	100K Resistors	
R9	1	3.9 meg. Resistor	

FIGURE A-4 HIGH VOLTAGE RECTIFIER

D1 thru D12	12	1N649 Rectifiers	Texas Instr.
-------------	----	------------------	--------------

FIGURE A-5 SYNCHRONOUS DETECTOR (2 required)

F1 thru F5	10	FI-100 MOS FET Transistors	Fairchild
C1, C2	4	0.01 μ f Capacitors	

FIGURE A-6 PREAMPLIFIER

R1	1	20 meg	
R2	1	68 K	
R3	1	300 Ω	
R4	1	30 K	
R5	1	15 K	
R6	1	6.2 K	
R7, R11	2	300 K	
R8, R12	2	56 K	
R9	1	22 K	
R10	1	100 K	
R13, R14	2	51 K	
C1	1	0.001 μ f, 3 KV	
C2, C3	2	10 μ f, 20 V	
Q1 (FET)	1	2N3438	AMELCO
Q2, Q4, Q5	3	2N3565	
Q3, Q6 (Dual)	1	2N3801	Motorola

FIGURE A-7 HIGH VOLTAGE A.G.C. RECTIFIER

<u>PART DESIGNATION</u>	<u>QTY.</u>	<u>PART DESCRIPTION</u>	<u>MANUFACTURER</u>
C1, C3	2	0.1 μ f Capacitors	
C2	1	0.22 μ f Capacitor	
D1	1	1N916A Diode	
R1	1	133K, 1% Precision Resistor*	
R2, R4	2	100K Resistors	
R3	1	20K Resistor	
Q1	1	FI-100 Field Effect MOS Transistor	Fairchild
Q2	1	2N1132 Transistor	

FIGURE A-8 HIGH VOLTAGE A.G.C. AMPLIFIER

R1	1	500K, 1% Precision Resistor	
----	---	-----------------------------	--

FIGURE A-9 MASTER OSCILLATOR AND BINARY COUNTER CHAIN**

C1	1	1 μ f Capacitor	
C4 thru C9	6	68 pf Capacitors	
C2, C3	2	680 pf Capacitors	
D1 thru D25	25	1N916A Diodes	
Q1 thru Q16	16	2N2369A Transistors	Texas Instr.
R1, R7, R9, R12, R13, R16, R18, R21, R22, R24, R25, R29, R30, R33	14	10K Resistors	
R2, R6	2	2.67K, 1%, Prec. Resistors	
R8	1	420 Ω Resistor	
R4	1	39.2K, 1% Prec. Resistor	
R3, R5	2	47.5K, 1% Prec. Res.	
R10, R15, R19, R24, R27, R32	6	2.7K Resistors	

*Salvageable from old system.

**Most of the components in this list are salvageable from the old system.

FIGURE A-9 MASTER OSCILLATOR AND BINARY COUNTER CHAIN (Cont'd)

<u>PART DESIGNATION</u>	<u>QTY.</u>	<u>PART DESCRIPTION</u>	<u>MANUFACTURER</u>
R11, R14, R20 R23, R28, R31	6	2.2K Resistors	
R17, R26	2	20K Resistors	
Z1		CD3814 Zener Diodes	
Z2		CD2699 Zener Diodes	

FIGURE A-10 SYNCHRONOUS DETECTOR DRIVER (2 required)

D1 thru D8	16	1N916A Diodes
R1, R2, R5, R7 R8, R11, R12	14	100K Resistors
R3, R9	4	680K Resistors
R4, R6, R10	6	20K Resistors
Q1, Q2, Q3	6	2N1132 Transistors

APPENDIX B BIBLIOGRAPHY

1. Pitman, George, Inertial Guidance, John Wiley and Sons, 1962
2. Stearns, Edward V., Navigation and Guidance in Space, Prentice-Hall, 1963
3. Fernandez, M. and Macomber, George R., Inertial Guidance Engineering, Prentice-Hall, 1962
4. Leondes, Cornelius T., Guidance and Control of Aerospace Vehicles, McGraw-Hill, 1963
5. Kuo, Benjamin C., Analysis and Synthesis of Sampled-Data Control Systems, Prentice-Hall, 1963
6. Friedman, A. L., Rushman, A., Gelb, A., "Optimization of Sampling Long-Term Inertial Navigation Systems," IEEE Trans. on Aero. and Nav. Elec., Sept. 1964, pp. 142-150
7. Swerling, P., Reich, E., "Statistical Theory of Navigation Employing Independent Inertial and Velocity Measurements," The Rand Corp., Santa Monica, California, Rept. RM-1220, March 1954.
8. Kalman, R. E., "A New Approach to Linear Filtering and Prediction Problems," ASME J. Basic Engineering, pp. 35-45, March, 1960
9. A. A. Michelson, Studies in Optics, University of Chicago Press, 1927
10. Jenkins & White, Fundamentals of Optics, McGraw-Hill, 1950
11. N. P. Laverty, "The Comparative Performance of Electron Tube Photo-detectors in Terrestrial and Space Navigation Systems," IEEE Trans. on Aerospace and Nav. Elec., Sept. 1963.
12. Saul Moskowitz, "Simplifying Resolver Chain Design with Matrix Notation," Electronic Design, March 2, 1964, pp 28-33
13. James A. Fusca, "Advanced Guidance Concepts," Space/Aeronautics Dec. 1964, Vol. 42, No. 7, pp. 46-55
14. Robert G. Stern, "Selection of Optical Sightings for Position Determination in Interplanetary Space," Proc. of Natl. Aerospace Elec. Conf., May 11-13, 1964, pp. 254-271
15. Gerald M. Levine, "Application of Midcourse Guidance Technique to Orbit Determination," AIAA Journal, Vol. 3, No. 1, Jan. 1965, pp 137-139

16. James Holahan, "Attitude Control for Unmanned Spacecraft," Space/Aeronautics, Feb. 1963, pp 78-86
17. J. D. Welch, "An Optical-Inertial Space Navigation System," Astrodynamics & Aeronautics, June 1965, pp 90-94
18. F. J. Clauss, "Lubricants and Self-Lubricating Materials for Spacecraft Mechanisms," Lockheed Missiles and Space Division, LMSD-894812, 18 April 1961
19. J. C. Heindl and R. J. Belanger, "OGO Solar Array Drive and Shaft Support Bearing Tests," Space Technology Laboratories, TR2311-6026-RU 00, 20 Sept. 1962
20. "Vac-Kote - - - A Vacuum Lubrication Process," Technical Memorandum 22.0, Ball Brothers Research Corporation, Feb. 1965
21. "Vac-Kote Capabilities," Technical Memorandum 22.1, Ball Brothers Corp., July 1965.
22. "Vac-Kote Lubrication Technology for Long Space Life Bearing Applications," TN66-35, Ball Brothers Research Corp., March 4, 1966
23. R. Adamczak, R. Benzing, H. Schwenker, "Advanced Lubricants and Lubrication Techniques," Industrial and Engineering Chemistry, Vol. 56, No. 1, Jan. 1964, pp 40-47
24. F. J. Clauss, W. C. Young, "Materials for Lubricated Systems," Space Materials Handbook, 2nd Edition, Tech. Documentary Report No. ML-TDR-C4-40, Lockheed Missile and Space Company, Contract No. AF33(657)-10107 for A. F. Matl. Lab., Wright-Patterson AF Base, Ohio
25. Technical Bulletins on Solid Film Lubricants from Electrofilm Inc.
26. B. D. McConnell, "Air Force Materials Laboratory Solid Film Lubrication Research," Tech. Doc. Report No. ML-TDR 64-46 A.F. Matl. Lab, Wright-Patterson Air Force Base, Ohio, Apr. 1964
27. R. L. Johnson, D. Buckley, "Studies of Lubricating Materials In Vacuum" presented at Southwest Research Institute Aerospace Bearing Conf., San Antonio, Texas, Mar. 1964
28. T. Spalvins, D. Buckley, "Vacuum Deposited Gold Thin Films as Lubricants in Vacuum (10^{-11} mm hg)," presented at 12th Annual Vacuum Symposium, Oct. 1965
29. T. L. Ridings, "Tests of Dry Composite Lubricated Bearings for Use in an Environmental Chamber," Aerospace Environmental Facility, Arnold Engineering Center, Arnold Air Force Station, Tenn., Mar. 1965

30. V. Hopkins, D. Gladdis, "Development of Solid Film Lubricants for Use in Space Environments," presented at 1963 USAF Aerospace Fluids and Lubricants Conf., San Antonio, Texas, Apr. 1963
31. R. D. Brown, R. A. Burton, P. M. Ku, "Long-Duration Lubrication Studies in Simulated Space Vacuum," ASLE Transactions 7, (1964) pp 236-248
32. M. Devine, E. Lamson, J. Bowen, "Inorganic Solid Film Lubricants," Journal of Chem. and Eng. Data Vol. 6, No. 1, Jan. 1961, pp 79-82
33. "Lubeco 905 Technical Manual," Lubeco, Inc.
34. E. Bisson, W. Anderson, Advanced Bearing Technology, Office of Scientific and Tech. Inf., National Aeronautics and Space Administration, NASA SP-38, 1964
35. F. F. Fischbach, M. E. Graves, P. B. Hays, R. G. Roble, "Satellite Measurement of Atmospheric Structure by Stellar Refraction," U. of Mich., Dept. of Aeronautical and Astronautical Eng., High Alt. Eng. Lab. Tech. Report for NASA, Goddard Space Flight Center, Contract NASr-54(08), Apr. 1965
36. P. B. Hays, F. F. Fischbach, "Analytical Solution for Atmospheric Density from Satellite Measurements of Stellar Refraction," U. of Mich., Dept. of Aeronautical and Astronautical Eng., High Alt. Eng. Lab. Tech. Report for NASA, Goddard Space Flight Center, Contract No. NASw-140.
37. "SECOR, Sequential Collation of Range System," Status Report U. S. Army Corps of Eng., Apr. 1964
38. "High Altitude Daytime Sky Background Radiation Measurement Program, Sky Luminance, Polarization, Infrared Radiance and Albedo Data from Research Vehicle No. 1," Part 1 and Part 2, Technical Documentary Note No. AL TDR 64-134, U.S.A.F. Avionics Lab., Research and Technology Div., Wright-Patterson Air Force Base, Ohio, May 1964
39. R. J. Orange, "Autonomous Space Navigation," Space/Aeronautics Vol. 45, No. 5, May 1966, pp 86-94.
40. T. E. Rodgers, "Luxorb - A Novel Approach to the Reduction of Off-Axis Light in Astro-Inertial Systems," paper presented at Optical Society of America Meeting, April 3, 1959.